



Publicly Accessible Penn Dissertations


1-1-2015

Liquid Cell Electron Microscopy With the Nanoaquarium: Radiation and Electrochemistry

Nicholas M. Schneider

University of Pennsylvania, schneider.nicholasm@gmail.com

Follow this and additional works at: <http://repository.upenn.edu/edissertations>

 Part of the [Chemistry Commons](#), and the [Mechanical Engineering Commons](#)

Recommended Citation

Schneider, Nicholas M., "Liquid Cell Electron Microscopy With the Nanoaquarium: Radiation and Electrochemistry" (2015). *Publicly Accessible Penn Dissertations*. 1993.

<http://repository.upenn.edu/edissertations/1993>

This paper is posted at ScholarlyCommons. <http://repository.upenn.edu/edissertations/1993>

For more information, please contact libraryrepository@pobox.upenn.edu.

Liquid Cell Electron Microscopy With the Nanoaquarium: Radiation and Electrochemistry

Abstract

The advent of the electron microscope has fostered major advances in a broad spectrum of disciplines. The required vacuum environment of standard electron microscopy, however, precludes imaging of systems containing high vapor pressure liquids. The recent development of liquid cells like the Penn nanoaquarium overcomes this limitation, enabling imaging of temporally evolving processes in liquids with nanoscale resolution at video frame rates. We used Liquid Cell Electron Microscopy to investigate the morphological evolution of the electrode-electrolyte interface during electroplating, the onset of diffusive instabilities in electrodeposits, beam-mediated nucleation, growth, and dissolution of metallic nanoparticles, the nucleation and growth of nanobubbles, and the fundamentals of the electron-water interactions (Radiation Chemistry). The control of interfacial morphology in electrochemical processes is essential for applications ranging from nanomanufacturing to battery technologies. Critical questions still remain in understanding the transition between various growth regimes, particularly the onset of diffusion-limited growth. We present quantitative observations at previously unexplored length and time scales that clarify the evolution of the metal-electrolyte interface during deposition. The interface evolution during initial stages of galvanostatic Cu deposition on Pt from an acidic electrolyte is consistent with kinetic roughening theory, while at later times the behavior is consistent with diffusion limited growth physics. To control morphology, we demonstrate rapid pulse plating without entering the diffusion-limited regime, and study the effects of the inorganic additive Pb on the growth habit. The irradiating electrons used for imaging, however, affect the chemistry of the suspending medium. The electron beam's interaction with the water solvent produces molecular and radical products such as hydrogen, oxygen, and hydrated (solvated) electrons. A detailed understanding of the interactions between the electrons and the irradiated medium is necessary to correctly interpret experiments, minimize artifacts, and take advantage of the irradiation as a tool. We predict the composition of water subjected to electron irradiation under conditions relevant to liquid cell electron microscopy. We interpret experimental data, such as beam-induced colloid aggregation and observations of crystallization and etching of metallic particles as functions of dose rate. Our predictive model is useful for designing experiments that minimize unwanted solution chemistry effects, extend liquid cell microscopy to new applications, take advantage of beam effects for nanomanufacturing such as the patterning of nanostructures, and properly interpreting experimental observations.

Degree Type

Dissertation

Degree Name

Doctor of Philosophy (PhD)

Graduate Group

Mechanical Engineering & Applied Mechanics

First Advisor

Haim H. Bau

Keywords

Electrochemistry, Electron Microscopy, Image Processing, Nanoscience, Radiation, Radiolysis

Subject Categories

Chemistry | Engineering | Mechanical Engineering

LIQUID CELL ELECTRON MICROSCOPY WITH THE NANOAQUARIUM:
RADIATION AND ELECTROCHEMISTRY

Nicholas M Schneider

A DISSERTATION

in

Mechanical Engineering and Applied Mechanics

Presented to the Faculties of the University of Pennsylvania

in

Partial Fulfillment of the Requirements for the

Degree of Doctor of Philosophy

2015

Supervisor of Dissertation

Dr Haim H Bau, Professor of Mechanical Engineering and
Applied Mechanics

Graduate Group Chairperson

Dr Prashant K Purohit, Associate Professor of Mechanical Engineering
and Applied Mechanics

Dissertation Committee

Daniel S Gianola, Assistant Professor, Mechanical Engineering and
Applied Mechanics, Materials Science and Engineering
David J Srolovitz, Professor, Mechanical Engineering and Applied Mechanics,
Materials Science and Engineering, Computer and Information Science
Frances M Ross, Research Scientist, IBM T.J. Watson Research Center
Haim H Bau, Professor, Mechanical Engineering and Applied Mechanics

LIQUID CELL ELECTRON MICROSCOPY WITH THE NANOAQUARIUM:
RADIATION AND ELECTROCHEMISTRY

© COPYRIGHT

2015

Nicholas Matthew Schneider

ACKNOWLEDGEMENTS

I would like to start, as we should start all things in science, by thanking those who have made our being here possible. First, I would like to thank Dr Joseph M Grogan. He is the one who paid most of the scientific debt to make this work possible. When we introduce the nanoaquarium - the device at the heart of this work - you can image Dr Joe pressing two silicon wafers together for years on end, until, by sheer force of will, they stuck, creating a hermetic seal, making this [nearly] impossible field, possible. I was lucky enough to have my time overlap with Joe for over three years. A time spent stealing his hard earned knowledge and experience in both science and life. Joe was and is more than generous with his time, consideration, and friendship - a true gift. Next I would like to thank Dr Frances M Ross, our collaborator from IBM T.J. Watson, who has essentially served as a second advisor to me. She has been extremely giving of her time, talents, and resources throughout the core of this work. Her guidance, discussions, and example have formed me as a scientist and professional. I would like to thank my advisor, Dr Haim H Bau, for being the one to ensure that my work is always new and exciting. His example as a passionate researcher combined with his support and guidance through the last five years has made my experience at Penn one of discovery, growth, and joy. I am particularly grateful for the freedom he has granted me to pursue my work and passions. His blessing to take on outside activities, travel, and dedicate time to side projects as often as I have was unwarranted. The life lessons, growth in world view, and friendships forged during these times have brought great joy to my life - I cannot thank him enough for the opportunities.

Many thanks to my committee members, Dr Daniel S Gianola and Dr David J Srolovitz, for the feedback and encouragement received throughout the dissertation process helping to shape my thesis and prepare me for my post-Penn world. Several hands contributed to this body of work and its experiments that are very difficult to

perform and analyze. Particularly I would like to thank Dr Jeung Hun Park and (Dr to be) Michael M Norton as they were the ones in the trenches with me turning the knobs and levers to perform our studies. Additionally, I appreciate Drs Jamie Ford (Penn), Suneel Kodambaka (UCLA), Daniel A Steingart (Princeton), Mark C Reuter (IBM), Arthur W. Ellis (IBM), and Matthew Goff (Cornell) for their help and useful discussions throughout the project. I have also been very lucky to work directly with several undergrads that contributed to my work and experience, these include Sarah Badin, Elizabeth Reeves, Brian J Mendel, Camri Robinson, and Jennifer Bourlier.

The work and life for a PhD goes beyond the science. It is the people and community around us that make us successful in our journey. I would like to thank all of the members of the Bau and Hu groups, especially Drs Robert Hart, Jason Thompson, Changchun Liu, Tong Gao, Barukyah Shaparenko, Sean Anderson and Jinzhou Yuan, for making my time as a student stimulating and enjoyable. Thank you to the entire faculty and staff of the department of Mechanical Engineering and Applied Mechanics and throughout the School of Engineering and Applied Science. A special thanks is due to Maryeileen B Griffith and Susan Waddington-Pilder for their help and encouragement throughout the years. I very much appreciate the time spent as a TA with Dr Robert W Carpick, Dr Michael Carchidi and my advisor. The examples and opportunities they gave in the classroom have played a vital role in my time at Penn. I would like to thank the MEAM students and residents of Rodin College House that I have had the pleasure of knowing through my time as a TA and GA. The chance to work with so many talented and overall excellent members of the Penn community has been inspiring and extremely rewarding. I would be amiss not to mention my three years in Rodin. The people and experiences that came with being a GA are among some of the most important and memorable. Many of the most important people in my life have come from this community, but I would like to specially thank Justin Gelzhiser, Connie Jiang, Danielle Wolfe, Nicholas Boccardi, Emily Gao, Joan Chen, Bianca Datta, Vikram Bhargava, and Alon Witztum (of

Harry Potter fame).

Naturally we thank our funding sources. My time at Penn, opportunities to present, and the work done here has been made possible, in part, through the generous support of the MEAM department, by the National Science Foundation through grants 1129722 and 1066573, and the NSF IGERT program (Grant DGE-0221664). Device fabrication was carried out at the Cornell NanoScale Facility (NSF Grant ECS-0335765), a member of the National Nanotechnology Infrastructure Network. Travel awards and grants to conferences and workshops were supported by Penn, the NSF, the Materials Research Society, the Microanalysis Society, the Microscopy Society of America, the German Center for Research and Innovation, and the Office for Science and Technology of the Embassy of France in the USA.

Finally, I would like to thank the family and communities that made my being at Penn possible. A special thanks to the greater RIT community, especially Dr Steven J Weinstein, Julie Olney, Kathy and Bob Hall, Terry Bohling, Mary Lou and Darrel Knapp, and my close friends Chris Crowley, Paul Solt of iPhoneDev.tv, Stephanie Lenhardt, Brandon Pastuszek, All of the Perkins crew, Sam Huynh, Robert Piccirillo, Perry Young, and Phil Amsler. I am very lucky to have all four of my grandparents to love and support me in my endeavors, my parents, brothers and their wives, and my extended family. I would like to thank Aunt Me, Uncle Tim, Tanner, Tayler and Tess for so often making me apart of their immediate family. This accomplishment is not my own, but that of all that have helped me along the way. This is yours too - I could not have made it this far without your love and support.

ABSTRACT

LIQUID CELL ELECTRON MICROSCOPY WITH THE NANO-AQUARIUM: RADIATION AND ELECTROCHEMISTRY

Nicholas M Schneider

Dr Haim H Bau

The advent of the electron microscope has fostered major advances in a broad spectrum of disciplines. The required vacuum environment of standard electron microscopy, however, precludes imaging of systems containing high vapor pressure liquids. The recent development of liquid cells like the Penn nanoaquarium overcomes this limitation, enabling imaging of temporally evolving processes in liquids with nanoscale resolution at video frame rates. We used Liquid Cell Electron Microscopy to investigate the morphological evolution of the electrode-electrolyte interface during electroplating, the onset of diffusive instabilities in electrodeposits, beam-mediated nucleation, growth, and dissolution of metallic nanoparticles, the nucleation and growth of nanobubbles, and the fundamentals of the electron-water interactions (Radiation Chemistry). The control of interfacial morphology in electrochemical processes is essential for applications ranging from nanomanufacturing to battery technologies. Critical questions still remain in understanding the transition between various growth regimes, particularly the onset of diffusion-limited growth. We present quantitative observations at previously unexplored length and time scales that clarify the evolution of the metal-electrolyte interface during deposition. The interface evolution during initial stages of galvanostatic Cu deposition on Pt from an acidic electrolyte is consistent with kinetic roughening theory, while at later times the be-

havior is consistent with diffusion limited growth physics. To control morphology, we demonstrate rapid pulse plating without entering the diffusion-limited regime, and study the effects of the inorganic additive Pb on the growth habit. The irradiating electrons used for imaging, however, affect the chemistry of the suspending medium. The electron beam's interaction with the water solvent produces molecular and radical products such as hydrogen, oxygen, and hydrated (solvated) electrons. A detailed understanding of the interactions between the electrons and the irradiated medium is necessary to correctly interpret experiments, minimize artifacts, and take advantage of the irradiation as a tool. We predict the composition of water subjected to electron irradiation under conditions relevant to liquid cell electron microscopy. We interpret experimental data, such as beam-induced colloid aggregation and observations of crystallization and etching of metallic particles as functions of dose rate. Our predictive model is useful for designing experiments that minimize unwanted solution chemistry effects, extend liquid cell microscopy to new applications, take advantage of beam effects for nanomanufacturing such as the patterning of nanostructures, and properly interpreting experimental observations.

TABLE OF CONTENTS

ACKNOWLEDGEMENTS	iii
ABSTRACT	vi
LIST OF TABLES	xi
LIST OF FIGURES	xxi
CHAPTER 1 : Introduction	1
CHAPTER 2 : Liquid Cell Electron Microscopy, A Dexterous Art	5
2.1 The Nanoaquarium	5
2.2 Device Loading	7
2.3 Device Pressure	9
2.4 Device Cleaning and Reuse	14
2.5 Failure Modes During Microscopy	15
2.5.1 Breaking Windows	15
2.5.2 Bubble Formation	17
2.5.3 Poor Electrical Connections	18
2.5.4 Collapsed Membranes and Leaking Devices	20
2.5.5 Beam Induced Deposition	20
CHAPTER 3 : Understanding Liquid Cell Results - Image Processing	23
3.1 Understanding Micrographs	23
3.1.1 What is a Micrograph? A Digital Image	23
3.1.2 Background Intensity	25
3.1.3 Intensity Consistency Between Image Regions	28
3.1.4 Beam Spatial Consistency	32
3.2 Automation of Image Processing	33
3.2.1 Raw Data	34
3.2.2 Unsupervised Edge Detection	34
3.3 Applications	41
3.3.1 Growth Front Tracking During Electrodeposition	41
3.3.2 Facet-Dependent Growth and Dissolution Rates in Nanoparticles	46
3.3.3 Bubble Nucleation, Growth, and Migration	47
CHAPTER 4 : Beam-Sample Interactions	52
4.1 Introduction	52
4.2 Electron Energy Loss in Liquids	52
4.2.1 Obtaining Dose Rate from Electron Trajectory Simulations	59

4.3	Electron Beam Heating	61
4.3.1	Calculating of Heating Profiles	61
4.3.2	Effect of Beam Current and Sample Thickness	64
4.4	Introduction to the Radiation Chemistry of Water	65
4.4.1	Energy transfer and short and long time kinetics	65
4.4.2	Formation, Diffusion, and Consumption Rates of Radiolysis Species	68
4.5	Kinetic Model	70
4.5.1	G-Values	73
4.6	Implementation of Homogeneous Model	74
4.7	Homogeneous Irradiation	74
4.7.1	Code Verification	79
4.8	Finite Beam Irradiation with Diffusion	82
4.8.1	Diffusion Coefficients	86
4.9	COMSOL Implementation	86
CHAPTER 5 : Effects of Radiolysis		88
5.1	Hydrogen and Bubble Formation	88
5.2	Radiolysis of Aerated Water	90
5.3	Changes in pH; Effect of pH on Radiolysis Yields	92
5.4	Hydrated Electrons; Particle Nucleation, Beam Writing, Etching vs. Growth	94
5.5	The Role of Hydrogen Peroxide on Liquid Cell Radiolysis	95
5.5.1	H ₂ O ₂ as an Additive	96
5.5.2	Varying Initial Concentration	97
5.5.3	Bubble Formation	97
5.6	Other Aqueous Solutions with Additional Chemistries	100
5.6.1	Beam Induced Gold Nanoprism Formation	100
5.6.2	Non-Aqueous Solvents	104
CHAPTER 6 : Electrochemistry with the Nanoaquarium		106
6.1	Geometry of Experimental Apparatus	106
6.2	Copper Growth Modes	106
6.3	2D Growth - Constant Height Assumption	108
6.3.1	Confirming Imaging Sensor is Not Saturated	108
6.4	Time for Growth to Become 2D	110
6.5	Copper Thickness Estimate	110
6.5.1	Liquid Thickness Estimate in Imaged Region	113
6.6	Control and Understanding Electrodeposit	114
6.7	Current Densities	116
6.8	Estimating Local Current Density from Average Growth Rate	116
6.8.1	Local Current Density from Experimental Observations	117
6.8.2	Relating Interface Normal Velocity to Point-Wise Current Density	119

6.9	Other Potential Mass Transport Mechanism	119
6.9.1	Full Supported Electrolyte (Negligible Electromigration) . . .	119
6.9.2	Electroosmosis Does Not Contribute Significantly	120
6.9.3	Surface Conduction	122
6.10	O ₂ Production at Counter Electrode	125
6.11	Etching By The Solution is Negligible	126
6.12	Ohmic Heating in the Electrode is Negligible	127
6.13	Ohmic Heating in the Electrolyte is Negligible	128
6.14	Sand Time	128
6.15	C-Rate	131
CHAPTER 7 : Morphological Evolution During Copper Electrodeposition . .		133
7.1	Copper Growth Regimes	134
7.2	Transition to Diffusion Limited Growth	134
7.3	Means of Morphology Control	146
7.3.1	Copper Electrodeposition Partial Conclusions	151
7.4	Methods	151
7.5	Electrical Data for Discussed Videos	152
7.5.1	Transition to Diffusion Limited Growth (400nA)	152
7.5.2	Low Current Density Deposition (75nA)	152
7.5.3	Pulse Plating (400 nA for 1 s, 0 nA for 5 s)	153
7.5.4	Lead Additive (300nA)	155
7.6	Ex Situ Hull Cell Experiments with Pb Additive	156
CHAPTER 8 : Conclusions and Outlook		159
8.1	Conclusions	159
8.2	Outlook	161
8.2.1	Automated Electron Beam Control	161
8.2.2	Electrochemical processes	163
APPENDIX		168
REFERENCES		191

LIST OF TABLES

TABLE 1 :	Water Radiolysis Kinetic Model	71
TABLE 2 :	G-Values for 300kV electrons in liquid water	74
TABLE 3 :	Steady State Concentration Power Law Parameters	78
TABLE 4 :	Diffusion Coefficients of Radiolysis Products	87
TABLE 5 :	Additional Reactions Required for Chloride	104
TABLE 6 :	Estimated Current Density Using Various Methods	118
TABLE 7 :	Physical Constants of Species in Solution.	120
TABLE 8 :	Sand Time in 2D Rectangular Channel with Elecotroosmotic Flow	124
TABLE 9 :	Sand Time given Butler-Volmer Kinetics with Constant Total Average Current on a Sinusoid and Flat Plate	131
TABLE 10 :	Hull Cell Results between Plain Copper and Lead Saturated Solutions	157

LIST OF FIGURES

FIGURE 1 :	Illustration of nanoAquarium	4
FIGURE 2 :	Top view of a completed single device (18 mm x 5 mm x 0.6 mm)	6
FIGURE 3 :	Schematic of nanoaquarium electrode layout	7
FIGURE 4 :	Time sequence of device filling. Empty, clean device (a). Initially filled device by placing solution on inlet associated with the top of the window (b) followed by the collapse of the membranes (c). Notice that liquid can be seen at the top of the window and along the silicon oxide on the left and right. The devices begins to fill the window region again and separate the membranes once solution is placed on the inlet associated with the bottom of the window image (d-g). An air bubble is trapped within the device (g), but then dissolves (h) leaving a filled device with no bulging (i). The device is then clamped resulting in a slight bulge that is irregular due to working pillars riding the two membranes (j).	10
FIGURE 5 :	Optical Image of partially filled device showing collapsed membranes, pillars, liquid, and a vapor bubble. (Same image as Figure 4d.)	10
FIGURE 6 :	Bowling Geometry as fitted to membrane deflection. Fitted liquid thickness (solid line) overlaid on intensity measures as scaled to thickness (a). Overall liquid thickness (b). 3D rendering of bowling windows (c).	13
FIGURE 7 :	Failed Device Window as Imaged in FEI Quanta STEM	16
FIGURE 8 :	Chamber pressure during breaking event in Hitachi H9000 at IBM	17
FIGURE 9 :	Large Bubble Blocking the Imaging Window: (a) STEM Bright Field (b) Optical Microscope Image	18
FIGURE 10 :	Etching of copper electrodeposit under galvanostatic conditions. Copper electrodeposition was performed around particles grown via beam deposition. The particles are not etched by the applied current and are instead left behind.	21
FIGURE 11 :	Advancing liquid vapor interface pushes particles toward the right, then receded and drags the particles back toward the left. A red dashed line illustrates the initial location of the bulk liquid phase.	22
FIGURE 12 :	Typical Nanoaquarium Micrograph	24
FIGURE 13 :	Typical Background Intensity	26

FIGURE 14 :	$\gamma(t)$ for Typical Electrodeposition Sequence	28
FIGURE 15 :	Best Fit Model to Background and Noise of sample frame from Figure 13 (Best fit: $\mu = 0.75$ and $\sigma = 0.04$)	29
FIGURE 16 :	Definition of Image Regions	30
FIGURE 17 :	Average Intensity of Image Regions where 0 and 1 correspond, respectively, to black and white grayvalues	30
FIGURE 18 :	Intensity Ratios during electrodeposition. (a) Intensity Ratio On and Off Electrodeposit (b) Intensity Ratio between Window and Silicon Regions	31
FIGURE 19 :	Vignetting is an optical aberration caused by geometry. . .	33
FIGURE 20 :	Single image vignette correction results showing the given image (a), the estimated vignetting (b), and the corrected image (c).	33
FIGURE 21 :	Example data of copper electrodeposition with a) overlaid crop indices (Red disks) and the defined angle of rotation and the b) resulting, cropped, rotated image. We refer to b) as the <i>sub image</i> throughout the rest of the text. Experimental methods for copper electrodeposition can be found later in the text.	35
FIGURE 22 :	The denoising column shows a) a nanocrystal sub image, b) the same image after TV filter application, c) and the difference between the two. The second column shows d) the image used as the background model, e) the frame of interest, and f) the foreground image. The edge detection column shows g) a thresholded foreground image (with TV filter), h) the extracted edges from the prepared foreground image, and i) the extracted edges without image preparation (undesired).	38
FIGURE 23 :	a) Stills from electrodeposition seen in Appendix Video B.6 . b) Maximum, minimum, and average growth height as a function of frame number. c) RMS roughness of growth as a function of time. d) Contours of the autocorrelation function of the surface roughness as a function of wavelength (spatial shift) and frame number. e) A heat map of the normal growth speed each frame. The green line represents the surface morphology at the transition time.	43
FIGURE 24 :	Illustrations of normal velocity extraction for a) a general surfaces, b) the moving least squares algorithm, and c) the minimum distance approach.	45

FIGURE 25 :	a) Image sequence of gold nanorod dissolution after image binarization and with the superposition of the minimum bounding box vertices (red) and connecting lines (green). b) Aspect ratio of particle as a function of frame. c) Perimeter of binarized convex hull. d) Right-handed rotation of particle from initial orientation.	48
FIGURE 26 :	a) Bubble radius as a function of frame. b) Comparison of Raw, Binary, and Masked image. c) Bubble intensity weighted centroid (squares) with bubble edge outline, color-coded in time.	51
FIGURE 27 :	Illustration of shape taken by electron trajectories (a). Schematic of cylindrical irradiated volume (b). Spurs as bead on a string following electron trajectory spaced, on average, by mean free path (c).	54
FIGURE 28 :	Collisional and Radiative Stopping Power for Electrons in Water.	55
FIGURE 29 :	Electron Mean Free Path in Water. Produce from data presented in LaVerne and Pimblott.	57
FIGURE 30 :	Electron trajectory simulation for nominal liquid cell with 200 nm of water sandwiched between two 50 nm silicon nitride windows illustrated in (a) and the resulting trajectories from Casino software (b).	60
FIGURE 31 :	Spatial dose rate (Gy/s) as calculated using electron energy loss and simulation parameters from Casino software.	62
FIGURE 32 :	Estimated temperature rise in a water layer as functions of beam radius and beam current due to electron beam-induced heating under typical TEM (left) and lower acceleration voltage STEM (right).	65
FIGURE 33 :	The concentrations of e_h^- , H^\bullet , H_2 , H_2O_2 , OH^\bullet , and O_2 as functions of time. Initially neat, deaerated water is irradiated continuously at a dose rate of 7.5×10^7 (Gy/s).	76
FIGURE 34 :	Steady state concentrations of e_h^- , H^\bullet , H_2 , H_2O_2 , OH^\bullet , and O_2 as functions of dose rate. De-aerated, neat water subjected continuous irradiation.	77
FIGURE 35 :	Temporal evolution of radiolysis products for γ radiolysis at 0.25 Gy/s of neat water.	79
FIGURE 36 :	Percent consumption of water as a function of dose rate.	81
FIGURE 37 :	Percent difference between COMSOL and MATLAB relative to Mathematica for H2 (a) and O3- (b) during homogeneous simulations.	81

FIGURE 38 :	Heterogeneous model predictions for the spatial and temporal evolutions of H_2 (a and b), e_h^- (c and d), O_2 (e and f), and H_3O^+ (H^+) (g and h). The left column depicts the concentrations of the selected radiolysis products of neat water as functions of the radial distance from the center of the irradiated region at various times. The right column depicts the concentrations of the same products at the center and edge of the irradiated region and at the perimeter of the liquid cell. The beam and liquid cell radii are, respectively, $1 \mu m$ and $50 \mu m$. The dose rate is $7.5 \times 10^7 Gy/s$	83
FIGURE 39 :	COMSOL Simulation Domain	87
FIGURE 40 :	Nucleation, growth, and migration of radiolytic bubbles at a serendipitous nucleation site.	89
FIGURE 41 :	The concentration of H_2 at the beam's center in the heterogeneous case for device radii sizes of $50 \mu m$ (red line) and $1000 \mu m$ (blue line) and the saturation concentration of H_2 in water at various pressures (horizontal lines). Initially neat, deaerated water is irradiated continuously at a dose rate of $7.5 \times 10^7 Gy/s$. The beam radius is $1 \mu m$	91
FIGURE 42 :	Ratio of aerated to deaerated steady state concentrations of e_h^- , H^\bullet , H_2 , H_2O_2 , OH^\bullet , and O_2 as functions of dose rate.	92
FIGURE 43 :	Steady state pH as a function of dose rate and initial pH prior to irradiation. Deaerated water.	93
FIGURE 44 :	(a) Steady state concentrations of e_h^- , H^\bullet , H_2 , H_2O_2 , OH^\bullet , and O_2 as functions of the pH value prior to irradiation for deaerated water under uniform irradiation (homogeneous case). (b) The ratio of radiolytic products concentrations in initially oxygen-saturated water ($C_{O_2}(0) = 0.255 mM$) and in deaerated water as functions of initial pH. The dose rate is $7.5 \times 10^7 Gy/s$	94
FIGURE 45 :	Ratios of steady state concentrations of select species as functions of initial H_2O_2 concentration compared to their neat water values during typical TEM imaging conditions ($7.5 \times 10^7 Gy/s$).	98
FIGURE 46 :	Estimated supersaturation of O_2 for homogeneous bubble nucleation "O" and for cases where no nucleation occurred under maximum possible dose rate "X" as a function of initial (pre-irradiation) H_2O_2 concentration.	99

FIGURE 47 :	Bright field TEM images of beam induced Au crystal growth in 20 mM HAuCl ₄ , acquired at times t indicated after irradiation began at t_0 . Dose rate of 6.0×10^8 Gy/s calculated with a beam current of 8.0 nA spread over 1 μ m radius. Figure generously provided by Dr Jeung Hun Park.	102
FIGURE 48 :	Growth rate dS/dt vs. beam current with each data point showing measured growth rate individual Au crystals. The beam current i varied from 0.1 nA to 8.0 nA over 1 μ m radius beam. The solid line is the least-squares fit and yields a growth exponent of $\beta \sim 0.76$	102
FIGURE 49 :	Schematic of electrode configuration with standard 3-electrode setup labeled with the Working (WE), Reference (RE), and Counter (CE) Electrodes. The gray area represents the nanochannel where the solution is loaded.	107
FIGURE 50 :	Illustration of Copper growth modes. The copper first nucleates at arbitrary sites, then forms a hard packed film which grows vertically until it reached the top of the device where it then grows perpendicular to the electrode in a essentially 2D fashion.	107
FIGURE 51 :	Sample frame from electrode deposition at 400 nA from Appendix Video B.10 indicating (a) image intensity extraction location as red vertical line. White dotted line represents electrode edge location. (b) Contour plot of extracted intensities as a function of distance from the electrode (along the vertical line in (a)) and time. The black line is located on the electrode, the red is off the electrode, the blue line is the background intensity, and the white dotted line represents the electrode edge. (c) Normalized intensities as functions of time for the points indicated in Figure 51b . Black and red points correspond to intensity normalized by the background intensity of each frame. Blue points represent the background intensity normalized by the initial frame intensity to illustrate the decay in the electron beam (due to the thermal emission source).	109
FIGURE 52 :	Further probing of intensities to ensure proper white balancing of image system (no saturation of detector). Identification of image regions (a) and their associated mean intensities and standard deviation as error bars (b).	110
FIGURE 53 :	Total required deposition time until growth becomes essentially 2D as a function of applied current as extracted from the bright field intensity in the electrode region.	111

FIGURE 54 :	Calculated liquid thickness in the imaged region (a) due to membrane bowing when nanoaquarium is loaded into microscope. Illustration of image region compared to entire window region as imaged in an optical microscope (b) where the small blue box is the region typically imaged during electron microscopy. The device is unfilled in the optical image. . . .	114
FIGURE 55 :	Measured Current Density as a function of applied current for Plain Copper deposition. The solid line is best-fit $i = aI$, where $a = 2.29 \times 10^9 (m^2)$	118
FIGURE 56 :	Resulting velocity profile from COMSOL for a slip velocity of $30 \mu m/s$ at the top and bottom walls. Deposition occurs on left wall ($y = 0$). The figures show the (a) magnitude of velocity, (b) x component, and (c) y component near the depositing wall.	123
FIGURE 57 :	Surface concentration of copper at peak and valley of half-wavelength sinusoid for total average current density of $500 A/m^2$. The amplitude is $500 nm$ and wavelength is $500 nm$	130
FIGURE 58 :	Concentration of copper near half-wavelength sinusoid after $0.01 s$ at total average current density deposition of $500 A/m^2$. The amplitude is $500 nm$ and wavelength is $500 nm$	131
FIGURE 59 :	Galvanostatic deposition and etching at $50 nA$ for $20 s$ each in $0.1 M CuSO_4$ and $0.18 M H_2SO_4$. This deposition results in island or nucleate growth. Insets: TEM bright field images recorded at time of A) 0, B) 10, C) 20, D) 27, and E) 40 s since the start of current flow. Each image is $1.8 \mu m$ horizontally.	134
FIGURE 60 :	Galvanostatic deposition and etching at $100 nA$ for $20 s$ each in $0.1 M CuSO_4$ and $0.18 M H_2SO_4$. This deposition results in compact growth. Insets: TEM bright field images recorded at time of A) 0, B) 7, C) 20, D) 22, and E) 40 s since the start of current flow. Each image is $1.8 \mu m$ horizontally.	135
FIGURE 61 :	Galvanostatic deposition and etching at $200 nA$ for $20 s$ each in $0.1 M CuSO_4$ and $0.18 M H_2SO_4$. This deposition results in dendritic growth. Insets: TEM bright field images recorded at time of A) 0, B) 7, C) 15, D) 23, and E) 36 s since the start of current flow. Each image is $1.8 \mu m$ horizontally.	135

FIGURE 62 :	Galvanostatic deposition with average current density of 288 A/m^2 and local average growth rate of 67 nm/s (equivalent to 1823 A/m^2) in 0.1 M $CuSO_4$ and 0.18 M H_2SO_4 . (a) Images recorded in bright-field conditions. Times in seconds since current flow began. The transition time is $\sim 3.1 s$. (b) Average, maximum, and minimum growth height as a function of time. (c) “Heat Map” of normal growth speed with white being fastest and blue/purple being slowest (d) Log-log plot of RMS roughness of interface as a function of time. Best fitting straight lines are shown with exponents indicated.	139
FIGURE 63 :	a) Current density normalized by average current density as a function of deviation from the mean height for growth of Figure 62 . b) Max, Min, and average current density normalized by limiting current for the experiment shown in Figure 62 . Percent of mass consumed by top quartile of points during growth during the experiments in c) Figure 62 and d) Figure 64	143
FIGURE 64 :	Galvanostatic deposition with average current density of 54 A/m^2 and local average growth rate of 1.3 nm/s (equivalent to 35 A/m^2) in 0.1 M $CuSO_4$ and 0.18 M H_2SO_4 . (a) Images recorded in bright-field conditions extracted from the video sequence found in the Appendix Video B.11 with detected edge as overlay. Times in seconds since current flow began. (b) Average, maximum, and minimum growth height as a function of time. (c) “Heat Map” of normal growth speed with white being fastest and blue/purple being slowest (need to redo with a color scale) (d) Log-log plot of RMS roughness of interface as a function of time. Best fitting straight lines are shown with exponents indicated.	145

FIGURE 65 :	Galvanostatic Pulsed deposition with average current density of $288 A/m^2$ and local average growth rate of $13 nm/s$ including off time (equivalent to $340 A/m^2$) in $0.1M CuSO_4$ and $0.18M H_2SO_4$. The local current density when only considering the pulse on time is $2040 A/m^2$. (a) Images recorded in bright-field conditions extracted from the video sequence found in the Appendix Video B.12 . Times in seconds since current flow began. (b) Average, maximum, and minimum growth height as a function of time. (c) “Heat Map” of normal growth speed with white being fastest and blue/purple being slowest (need to redo with a color scale) (d) Log-log plot of RMS roughness of interface as a function of time. Best fitting straight lines are shown with exponents indicated.	148
FIGURE 66 :	Galvanostatic deposition with average current density of $216 A/m^2$ for $10 s$ followed by $10 s$ of no current, repeated. Average local growth rate is $14 nm/s$ (equivalent to $381 A/m^2$) in $0.1 M CuSO_4$ and $0.18 M H_2SO_4$ saturated with $PbSO_4$ (a) Images recorded in bright-field conditions extracted from the video sequence found in the Supplemental Appendix Video B.13 with detected edge as overlay. Times in seconds since current flow began. (b) Average, maximum, and minimum growth height as a function of time. (c) “Heat Map” of normal growth speed with white being fastest and blue/purple being slowest (need to redo with a color scale) (d) Log-log plot of RMS roughness of interface as a function of time. Best fitting straight lines are shown with exponents indicated.	150
FIGURE 67 :	Potential as a function of time for deposition shown in Appendix Video B.10 . Total applied current of $400nA$ was turned on at time 0 and held constant.	153
FIGURE 68 :	Potential and applied current as a function of time for deposition shown in Appendix Video B.11 . Current is cycled on and off for a total of 35 periods with short pauses to restart the potentiostat after every 5 cycles (due to limitation in the software).	154
FIGURE 69 :	Potential and applied current as a function of time for deposition shown in Appendix Video B.12 . Current is cycled on for $1 s$ and off for $5 s$ and repeated.	155
FIGURE 70 :	Potential and applied current as a function of time for deposition shown in Appendix Video B.13 . Current is cycled on for $10 s$ and off for $10 s$	155

FIGURE 71 :	Schematic of Hull Cell design (a). Illustrative example of substrate in focus (b) compared to tips of dendrites in focus (c) at the same location. The circle represents the same location containing asperities that protrude out of the depth of field.	157
FIGURE 72 :	Illustration of beam-induced deposition (a). (Figure generously provided by Michael Norton) Exploitation of the fact that highly reducing species do not persist outside the beam region allows for mask-less patterning by the electron beam (b).	162
FIGURE 73 :	Galvanostatically deposited Copper-Nickel structure from 0.1 M NiSO ₄ 0.18 M H ₂ SO ₄ and 0.02 M CuSO ₄	165
FIGURE 74 :	Schematic illustration of a few electrode configurations: standard parallel (i); Hull cell design enabling deposition subject to varying current densities (ii); Hele Shaw (iii); sawtooth to study deposition on vertical structures and trench filling (iv); and bipolar (v). The entire exposed working electrode is in the viewing window (dashed line). Elongated window design to encourage bubble (shown as a gray ellipse) migration away from the electrode region (vi). Pillars next to the electrodes to simulate the presence of colloids (vii). A single photolithographic mask can be used to pattern the various electrode configurations, enabling the manufacturing of nanoaquariums with different electrode configurations in a single run with minimal added cost.	167
FIGURE 75 :	Illustration of wafer dicing steps	170
FIGURE 76 :	Illustration of inlet etching mask	172
FIGURE 77 :	Steps for lead production from copper foil	176
FIGURE 78 :	Gluing Leads to Nanoaquarium	177
FIGURE 79 :	IBM holder assembly. Asymmetry designed into nanoaquarium to aid in proper orientation (a). Standard orientation of IBM holder when loading (b.)	179
FIGURE 80 :	Top view of IBM holder with nanoaquarium prior to clamping. This holder is designed for the cartridge loading used by IBM's Hitachi H9000.	180
FIGURE 81 :	Photo of device loaded in STEM holder	182
FIGURE 82 :	Pixel size (<i>nm</i>) as a function of Magnification (1000's) in IBM's Hitachi H9000. Points represent measurements and solid line is a best fit giving $PixelSize = 15.17Mag^{-1}$, where <i>Mag</i> is the magnification is 1000's.	188

<p>FIGURE 83 : Pixel size (nm) as a function of Magnification (1000's) in Penn's FEI Quanta ESEM using STEM Detector. Points represent measurements and solid line is a best fit giving $PixelSize = 250.0Mag^{-1}$, where Mag is the magnification is 1000's.</p>	189
<p>FIGURE 84 : Beam current (nA) as a function of Spot Size in FEI Quanta ESEM using STEM Detector. Points represent measurements and solid line is a best fit giving $Current = 2.323 \times 10^{-3}Spot^{-1}$, where $Spot$ is software defined spot size.</p>	190

CHAPTER 1 : Introduction

The advent of the electron microscope (EM) has facilitated advances in a broad spectrum of scientific endeavors such as materials science, chemistry, and biology. The transmission electron microscope (TEM) introduced in the 1930's and later the scanning transmission electron microscope (STEM) have proven to be powerful means for imaging on the nano and even atomic scale, a scope far beyond the lengths made possible with standard light microscopy. The TEM and STEM afford not only high spatial resolution imaging, but allow for material characterization and manipulation due to the intrinsic interactions between the electron beam and the sample. These interactions provide qualitative information such as the relative atomic densities of the constituents in an inhomogeneous sample, as well as precise elemental analysis through characteristic x-ray emission (energy dispersive x-ray spectroscopy) and characteristic electron scattering (electron energy loss spectroscopy). For these reasons, the TEM and STEM have become standard analytical tools in both the physical and the biological sciences.

Standard electron microscopy suffers, however, from some limitations. The required high vacuum environment necessary for quality electron optics precludes the imaging of dynamical systems in many important fluids. Traditionally, systems of interest have been restricted to solid, frozen, or dried out samples, with very few EM studies focusing on the dynamical processes that take place in high vapor pressure liquids. The required vacuum of the electron microscope simply made the imaging of liquids impractical. P. G. de Gennes, who won the noble prize in physics for his work on liquid crystals, even states in his oft cited work (over 5000 citations), "Wetting: statics and dynamics," that our understanding of phenomena at the liquid-solid inter-

faces are limited because “solid/liquid interfaces are much harder to probe than their solid/vacuum counterpart; **essentially all experiments making use of electron beams become inapplicable when a fluid is present** [1].” That is to say, since imaging in standard electron microscopes requires one to maintain a high vacuum environment, liquids with high vapor pressures, especially water, will quickly evaporate and will not be accessible for observations. To study processes occurring in liquid media, one traditionally must fix (freeze or dry out) samples at various stages of the process and carry out *ex situ* imaging. Procedures for static sample preparation have resulted in major advances in many disciplines ranging from materials science to biology. However, imaging of fixed samples does not directly capture the dynamics of a process, it only grants static snapshots of states. This makes it difficult to select the “right” moment to fix the sample, and so, may preclude critical observations. This dictates the need to develop new techniques that grants the spatial and temporal resolution needed to study important dynamic systems.

Liquid Cell Electron Microscopy [2, 3] is a relatively new technique that makes it possible to view processes taking place in liquid media with a standard TEM, STEM, or SEM. This new method is producing new insights across many branches of science. For example, morphological instability, particularly dendrite formation, can cause potentially catastrophic failure in rechargeable batteries. Morphological instabilities can lower the quality of electroplated coatings, yet may also be useful in forming porous deposits. Thus, it is important to develop strategies to control these instabilities. Liquid cell electron microscopy allows us to image in real time and with nanoscale resolution the evolution of the solid-liquid interface during electrochemical deposition as a function of process conditions. This allows us to obtain insights into the mechanisms leading to instabilities and to investigate strategies for controlling

electrodeposited morphology. However, the role the electron beam plays by interacting with the sample must be understood both when designing experiments and interpreting experimental data. As ionizing radiation passes through the suspending medium, energy is transferred from the fast-moving electrons to the irradiated medium. This energy excites and dislodges orbital electrons, which results in the generation of radical and molecular species such as H_2 , O_2 , H_2O_2 , and hydrated electrons (e_{h}^-) [4–6]. The hydrated electrons and other strong reducers, oxidizing agents, and gaseous species can cause, respectively, reduction and precipitation of cations from solution, dissolution of metals, and nucleation and growth of bubbles [7–12]. A quantitative understanding of electron beam-induced effects is critical to assess whether the electron beam significantly affects the imaged phenomenon, to correctly interpret experiments carried out with liquid cells, to mitigate unwanted effects, and to take advantage of beam effects.

A home-brew liquid cell, the nanoaquarium (**Figure 1**) by Grogan and Bau at Penn [13,14], is used as a tool to investigate both the fundamental interactions between the electron beam and aqueous samples (Radiation Chemistry), and the morphological evolution of the electrode-electrolyte interface during copper electrodeposition (Electrochemistry). In this work, the basics of liquid cell electron microscopy as a technique and the interpretation of experimental results (particularly the micrographs) are first outlined. The electron-water interactions are then detailed followed by coverage of practical effects and their implications for liquid cell electron microscopy. Next, the results of copper electrodeposition experiments where we image, for the first time at the nanoscale, the transition from kinetic roughening through the onset of a diffusive instability are described along with general electrochemistry in a sealed liquid cell. Finally, we outline some promising new areas of research.

Liquid cell electron microscopy is often practiced as a qualitative science. Observations of the processes at the nanoscale provides insight into the fundamental nature of materials from their shortest length-scales to their device level dimensions. However, a more detailed picture is necessary to answer open questions and push material limits to new regimes. This work goes beyond the qualitative nature of our most basic result, the micrograph, and combines automated image processing with detailed understanding of beam induced phenomena to develop a quantitative world view in the context of liquid cell results. The explicit tracking of interfaces, phase dynamics, and solution chemistry lead to a deeper understanding of systems as they evolve morphologically and chemically - a step toward a full physical-chemical understanding at the nanoscale.

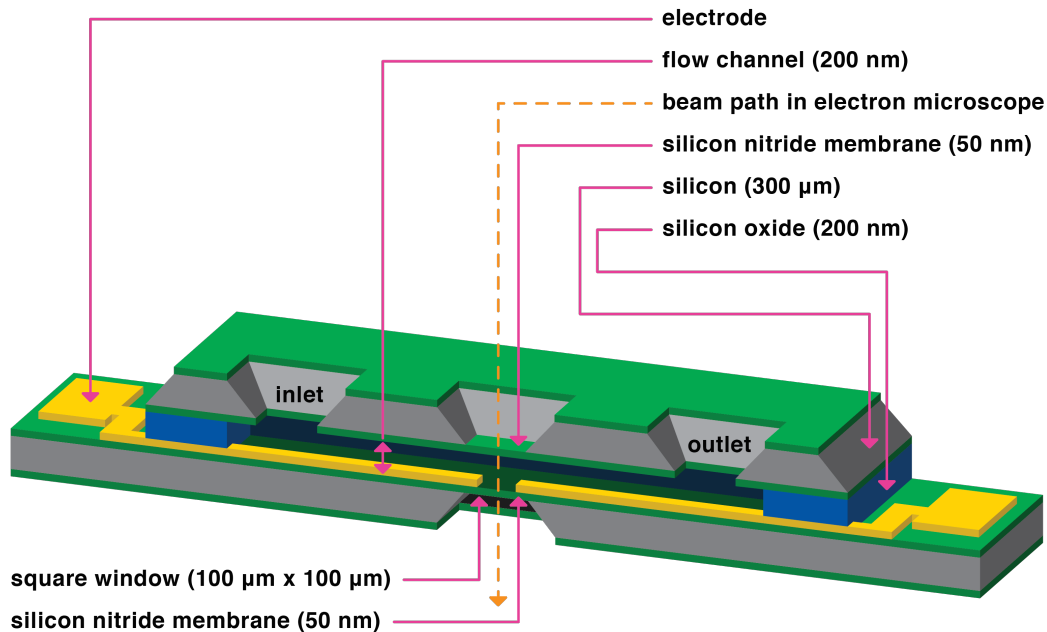


Figure 1: Illustration of nanoAquarium

CHAPTER 2 : Liquid Cell Electron Microscopy, A Dexterous Art

2.1. The Nanoaquarium

The nanoaquarium is a nanofluidic liquid cell device developed by Grogan and Bau at Penn [3, 13] for in situ (S)TEM of fluid samples. Standard microfabrication techniques are utilized with wafer level processing to create dozens of identical devices in each batch. The detailed fabrication protocol can be found in the works of Grogan [13, 14]. The general layout of an individual device is illustrated in **Figure 1** and a top-view photograph of a single chip is shown in **Figure 2**. The nanoaquarium is essentially two TEM grids with thin, electron transparent silicon nitride windows that have been wafer bonded - creating a completely hermetically sealed chamber. One wafer is coated with a thin film of patterned silicon oxide that defines the liquid cell geometry and height of the resulting nano channel prior to bonding. The thickness of the silicon oxide film that defines the liquid cell height, is well controlled and can be prescribed to be tens to hundreds of nanometers. The version of the nanoaquarium used in this work was manufactured with a silicon oxide film with 200 *nm* thickness, and the imaging windows were made of two 50 *nm* thick, low stress silicon nitride membranes, each measuring 100 by 100 μm . The device fits into a custom-made holder and can sustain the high vacuum environment of the electron microscope for many hours without any noticeable loss of liquid. Some of the nanoaquarium's highlights include [3, 14]:

- Thin sample cross-section that minimizes multiple scattering and improves resolution.
- The channel height of each device is highly controllable via the wafer bonding process and can be as thin as tens of nanometers.

- The wafer bonding and clean room assembly process ensures there is no risk of debris being trapped in the channels - a large risk in the commercial counterparts.
- Wafer scale processing allows high yield production.
- The hermetic seal provides leak-free operation and does not necessitate the use of potentially contaminating glues, epoxies, or polymer spacers.

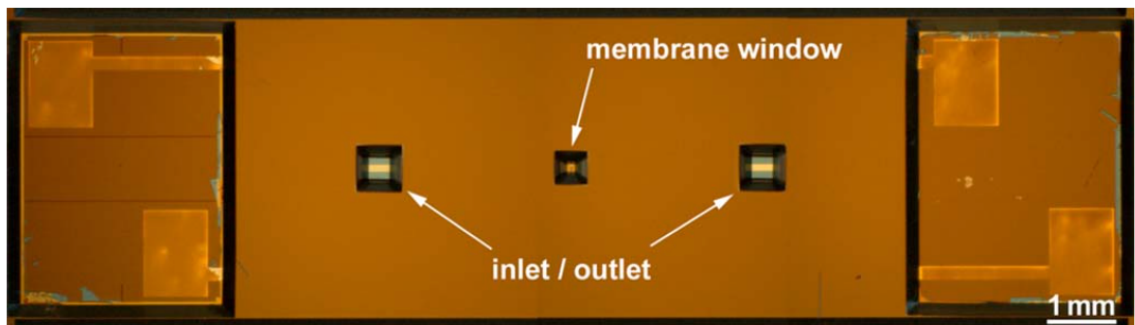


Figure 2: Top view of a completed single device ($18\text{ mm} \times 5\text{ mm} \times 0.6\text{ mm}$)

Two versions of the device are used throughout this work. The first version has electrodes within the channel and are primarily used in the electrodeposition experiments. The geometry of the electrodes can be seen in the to-scale schematic of **Figure 3**, where the electrode stack is made up of a 5 nm Ti adhesion layer with 25 nm of Pt on top. Metals were deposited via thermal evaporation, resulting in polycrystalline thin films. The lithography defines the electrode edges giving a well-controlled and known area exposed to introduced solutions. This precise control of geometry makes quantitative analysis of electrochemical experiments possible. The electrodes extending into the viewing window have a total exposed area of $2.4 \times 10^{-8}\text{ m}^2$, and the two distant electrode have an exposed area of $2.9 \times 10^{-7}\text{ m}^2$. The smaller electrodes that extend into the window are most often used as the working electrode (WE) with its pair being the reference electrode (RE) during electrochemical experiments. The distant, larger (12x by area) electrode is used as the counter electrode (CE).

A second version of the device employed during this work simply does not have any electrodes (the metals are never deposited). This is useful for experiments not requiring any electrical actuation or measurement, or when the platinum electrode would be problematic, which is the case in the study of hydrogen peroxide where Pt is a catalysis and can cause spontaneous bubble formation when H_2O_2 is sufficiently concentrated. Both sets of devices used in this work have nominal thicknesses defined by 200 *nm* of oxide. Further considerations, such as bowing of the membranes will be investigated later on.

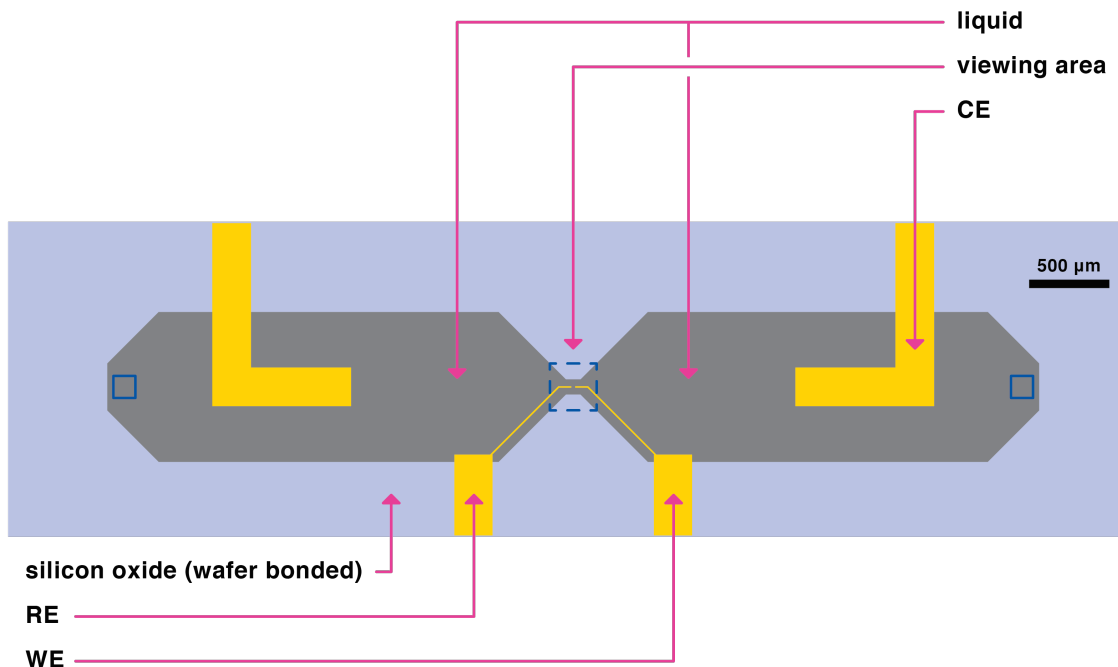


Figure 3: Schematic of nanoaquarium electrode layout

2.2. Device Loading

A fully prepared nanoaquarium can be filled via capillary forces when a droplet of solution is placed on an inlet. The thinness of the cell allows surface tension to pull wetting liquids into the device and fill the imaging chamber. Inspection of the nitride

window in an optical microscope is required before and after filling as a change in color will indicate the presence of the fluid. Placing a droplet on one inlet is often sufficient to fill the entire cell and is followed by placing another droplet on the second device inlet. Rubber O-rings (Markez-002 O-rings, Marco Rubber) should then be placed on the inlets so the device can be sealed in the custom-made fixtures for STEM at Penn and TEM at IBM as detailed in the appendix.

In cases where an air bubble appears in the window region, several steps can be taken to salvage the device and bring it into working order. For air bubbles, one can use filter paper to withdraw the fluid from the device and re-employ the droplet filling technique. If refilling is unsuccessful, a bubble can be removed from the device by applying a vacuum at one of the inlets. This can be practically achieved by placing an O-ring over an inlet without a droplet of solution (make sure the complementary inlet has solution so as to not dry out the device) and using a syringe that fits the O-ring in the fully dispensed portion and pulling out its plunger to create a vacuum. This “plunging” can be repeated multiple times until the bubble is removed. If the bubble is stubborn, the device should be cleaned and dried out and used for a later experiment. Details of cleaning are in **Section 2.4**.

Filling can also be hindered in cases where the two nitride windows collapse onto one another and exhibit a strong Van der Waals attraction. The first remedy is to wait for the fluid to slowly creep into the chamber and separate the membranes. If this fails, the refilling technique can be repeated several times to see if it is more successful. Alternatively, the device can be clamped in the holder to apply an additional pressure forcing the liquid into the window. However, care should be taken when employing this option as rapid clamping and over pressurizing the device can lead to the rupture of the windows. Clamping the device in its holder with one O-ring filled and one empty

is a good way to fill the device with low risk of window rupture. Once the device has been filled, and the membranes separated, the pressure can be reduced by loosening the set screws.

Figure 4 shows several stages from a typical filling event extracted from a video taken during filling available digitally **Appendix Video B.1**. The solution, in this particular case 3% wt H_2O_2 , was introduced on the inlet connected to the side of the window toward the top of the image. Capillarity pulls the fluid into the device and fills the entire window region. This can be seen by the subtle change in color in the shape of a bulge as seen by comparing **Figure 4b** to **Figure 4a**. Once the flow settles, the membranes begin to collapse and ultimately trap an air bubble around a pillar as seen in **Figure 4c**. Notice that the liquid is still seen near the top of the window and along the edge of the silicon oxide. Once a second drop of solution is added to the complementary inlet (toward the bottom of the image), the fluid begins to separate the collapsed membranes and refills the image region as illustrated by considering **Figure 4d** through **Figure 4g**. In this case, the air bubble dissolves and either remains as a dissolved gas, exits the device through the inlets, or migrates to another air pocket within the device. The dissolution can be seen in **Figure 4g** through **Figure 4i**. **Figure 4j** shows the final device after clamping where the entire window is filled with the solution, the pillars are working, and there is a small bulging.

2.3. Device Pressure

Given the nanoaquarium is a hermetically sealed device, it is possible to exploit the bowing of the observation window as a means to determine the pressure within the device. The silicon nitride membranes are relatively large, having been defined as a 100 μm square windows, and very thin, with a 50 nm thickness. The deposition

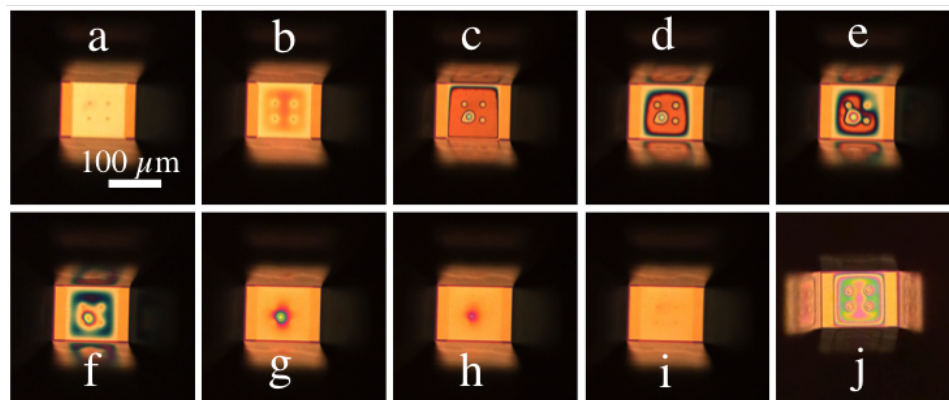


Figure 4: Time sequence of device filling. Empty, clean device (a). Initially filled device by placing solution on inlet associated with the top of the window (b) followed by the collapse of the membranes (c). Notice that liquid can be seen at the top of the window and along the silicon oxide on the left and right. The devices begins to fill the window region again and separate the membranes once solution is placed on the inlet associated with the bottom of the window image (d-g). An air bubble is trapped within the device (g), but then dissolves (h) leaving a filled device with no bulging (i). The device is then clamped resulting in a slight bulge that is irregular due to working pillars riding the two membranes (j).

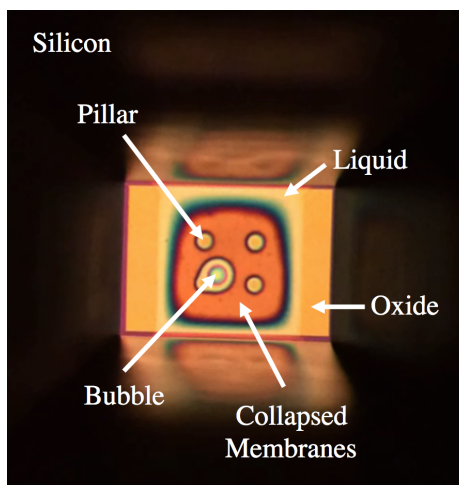


Figure 5: Optical Image of partially filled device showing collapsed membranes, pillars, liquid, and a vapor bubble. (Same image as **Figure 4d**.)

process results in very low residual stress (800 MPa), which, combined with the size of the membrane, allows for large deflection without rupture. This is a feature that grants great control over the initial clamped pressure within the device. When a loaded device is observed under an optical microscope, variations in thickness due to bowing are clearly visible. Adjusting the clamping pressure via set screws will alter the membrane deflection as it is a function of device pressure. The resulting light fringes, Newton's rings, are the direct result of constructive and destructive interference caused by the variations in liquid thickness and indirectly give the thickness of the device. Grogan *et. al.* [13,14] solved this optics problem for the nanoaquarium's materials and geometry in the absence of connecting pillars. If monochromatic light is used to measure the intensity of the bowing window in an optical microscope, the explicit gauge pressure of the device can be determined prior to pumping down within the electron microscope.

The pressure of a sealed device on the bench top is an important aspect of experimental design. The set screws can be adjusted to increase or decrease the pressure and the resulting number of fringes. Since multiple scattering events increase with liquid layer thickness, resolution is inversely related to liquid layer thickness. This means that keeping the liquid as thin as possible is optimal for the sake of resolution. However, additional clamping can be useful when studying systems where the formation of a gaseous species is expected, such as during electrochemical experiments. Higher pressures will lead to a larger saturation concentration require for the nucleation of a second phase, allowing for longer experiments before a bubble forms.

The pressure inside the device after it has been pumped down in the EM vacuum, however, will not necessarily be the same as the bench top pressure. One can imagine the sealed nanoaquarium system acting as a piston-cylinder with a non-linear spring

on top. The non-linear spring is the membrane and its mechanical ability to bulge. When the 1 *atm* of pressure is removed, the new state of the system will depend on the initial state. If the entire device is a liquid phase, say entirely liquid water, and we assume the final pressure does not drop below the saturation pressure (no phase change), there will be very little change in volume and pressure as the liquid water is nearly incompressible. However, if a second vapor phase, say trapped air, is present, then the pressure can drop significantly. The same is true in the cases where dissolved gases come out of solution and nucleate to form a second, vapor phase. This ultimately results in the pressure dropping within the device after being exposed to the vacuum. It is important to note that this is mainly due to having a sealed liquid cell. In commercial holders where the imaging chamber is often connected to atmosphere via tubing, the pressure will be maintained near the conditions outside of the microscope.

Imaging the shape of the membrane provides a simple means to estimate the pressure. Fortunately, the entire membrane can be imaged in the STEM, allowing for an *in situ* estimate of device pressure if we assume that the intensity in the image is linearly related to water thickness and that the intensity near the silicon edge is associated with the liquid thickness of 200 *nm*. To close this problem, we fit the intensity profile along a primary axis of the thin silicon nitride membrane (as illustrated in **Figure 6a**) to the Maier-Schneider *et. al.* [15] solution of the membrane deflection problem. The shape of the square membrane is given by

$$h(x, y = 0) = h_o \left(1 + 0.401 \frac{x^2 + y^2}{a^2} + 1.1611 \frac{x^2 y^2}{2a^4} \right) \cos \frac{\pi x}{2a} \cos \frac{\pi y}{2a} \quad (2.1)$$

where h is the height, h_0 is the maximum deflection at $(0,0)$ or the center of the membrane, a is the membrane half width, and (x, y) are coordinates measured from

the center of the membrane. **Figure 6b** and **c** show, respectively, the shape of the membrane at 1 *atm* applied pressure and a to-scale 3D rendering of how two membranes would look with the thin gap of our device. For convenience in estimating the pressure, we consider one axis of the membrane. In the case of its primary axis or the “midside-to-midside”, the membrane will take the shape of [15]

$$h(x, y = 0) = h_o \left(1 + 0.401 \frac{x^2}{a^2} \right) \cos \frac{\pi x}{2a}. \quad (2.2)$$

Since the membrane half length is known, we simply need to extract h_0 from the fitting.

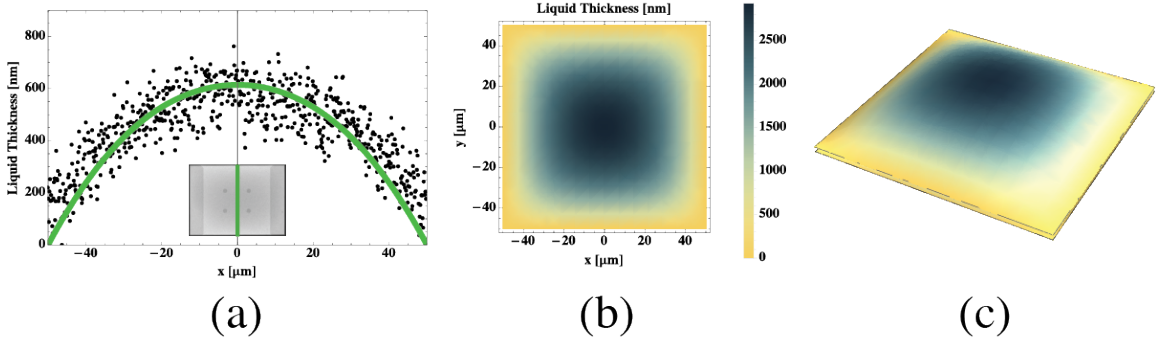


Figure 6: Bowing Geometry as fitted to membrane deflection. Fitted liquid thickness (solid line) overlaid on intensity measures as scaled to thickness (a). Overall liquid thickness (b). 3D rendering of bowing windows (c).

Once we have extracted the maximum height of the membrane, we can estimate the pressure within the device. Maier-Schneider *et. al.* [15] provide an analytical expression to directly relate the maximum deflection to an applied pressure as

$$p(h_0) = C_1 \frac{t\sigma}{a^2} h_0 + C_2(\nu) \frac{tE}{a^4} h_0^3, \quad (2.3)$$

where, a is the membrane half length, t is the membrane thickness, σ is the residual

stress in the film (800 MPa) [14], E is Young's modulus (325 GPa) [14],

$$C_1 = 3.45, \tag{2.4}$$

and

$$C_2(\nu) = 1.994 \frac{1 - 0.271\nu}{1 - \nu}. \tag{2.5}$$

The pressure given here is a gauge pressure (pressure drop across the membrane), meaning, if the membrane is completely flat, then the pressure internal to the device is equal to the pressure outside of the device (neglecting any additional forces such as surface tension pulling the membranes together in cases where the window is not fully wetted). In the case of a device loaded within the vacuum chamber of the microscope, we assume that the microscope chamber pressure ($< 10^{-5} \text{ torr}$) is negligible. For the case illustrated in **Figure 6**, we find the maximum deflection to be 614 nm associated with a pressure of 0.349 atm .

2.4. Device Cleaning and Reuse

With proper care, a nanoaquarium that has not failed irreversibly (see **Section 2.5**) can be reused. It is important to note that once a device has been filled, it should be considered contaminated and not be used with other systems. For example, a device that was used during copper electrodeposition with lead as an additive should not be refilled with a plain copper solution. However, if during the course of experiments, an undesired large bubble fills the viewing window, the following procedures may be used to reclaim the device for use with a compatible system.

When the holder is removed from the microscope and brought back to atmospheric

conditions, DI water should be available. Remove the cover plate and O-rings and place them in a DI Water wash container (or other appropriate solvent). Next, immediately place large droplets of DI water on the two inlets of the device. Using filter paper, withdraw the liquid from one side of the device at a time and replace the DI water in an alternating pattern. Repeat this process at least 10 times. Additionally, two droplets of different sizes can be placed on the inlets to force a flow from the smaller droplet into the larger one [16]. This flow is driven by the Laplace pressure in the smaller droplet being greater than that of the larger droplet - serving as an efficient means to flush the device over time. Note that this process also works as means of introducing solutions into the device, and can be exploited to replace solvents as an experimental method.

2.5. Failure Modes During Microscopy

There are several events that can lead to the failure of a device during the course of an experiment. In this section we will outline the most common modes of failure encountered during the course of this work. Some of the conditions leading to a failure can be mitigated, so we shall also outline procedures to aide in this end.

2.5.1. Breaking Windows

The first mode of failure is the most catastrophic - the rupture of the silicon nitride membrane window. A sample of a device with a failed window can be seen in **Figure 7** where the solution in the device is going through a phase change as it empties into the vacuum chamber. The video associated with this image is available in **Appendix Video B.2**, where a large bubble forms, and instead of delaminating the pillars, the silicon nitride membrane shatters. Windows will break most often for two different reasons. The first reason is the spontaneous formation of a large bubble in the win-

dow region. This can occur due to the nucleation of gaseous radiolytic byproducts or species created as part of electrochemical reactions. There is little that can be done to avoid this sudden event. The second condition leading to the rupture of a window is due to stresses associated with the passing of current through the built-in electrodes. With diligent care, these conditions can be avoided by performing galvanostatic (constant current) experiments where the current is started very low and slowly increased. In the second version of the nanoaquarium, the failure current is on the order of μA . This means that one can apply 10's or 100's of nA without destroying the device.

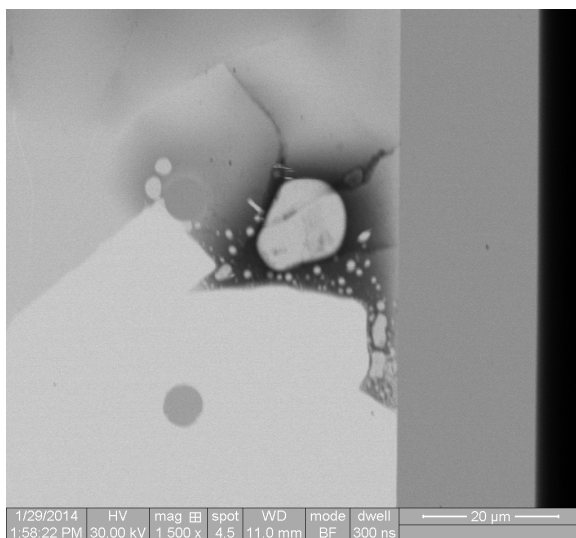


Figure 7: Failed Device Window as Imaged in FEI Quanta STEM

One advantage of using a sealed device with small liquid volume is that membrane breakage is less harmful to the microscope. When the membranes break, solution is released into the microscope chamber, which is at the very least a contaminant for other users. Additional damage can be done to the electron source and vacuum components if the pressure becomes too high. The small volume of the nanoaquarium leads to less than an order of magnitude increase in chamber pressure as measured *in situ* by the sensors on the Hitachi H9000 at IBM. Typically the column pressure is $\sim 10^{-6}$ torr with a loaded nanoaquarium. A device rupture will briefly increase

the column pressure to just less than $\sim 10^{-5}$ torr. This change only lasts for a few seconds where the column pressure returns to its initial base pressure. **Figure 8** shows a representative example of column pressure as a function of time during a catastrophic failure of the membrane when the device was loaded with copper solution. It is important to note that pressure is reported as the pressure in the microscope imaging chamber some distance from the device and that the explicit pressure near a ruptured window may vary from this measure. This means we do not know the pressure near the window accurately, but have a measure of the chamber as a whole.

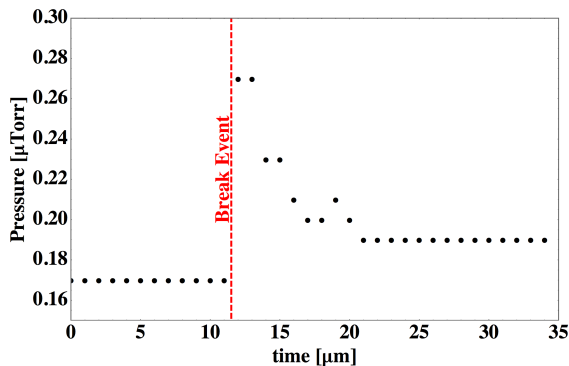


Figure 8: Chamber pressure during breaking event in Hitachi H9000 at IBM

2.5.2. Bubble Formation

The second and most common failure mode is the formation of a large bubble that fills the useful imaging area. **Figure 9** shows a STEM bright field image along with an optical microscope image with a large bubble consuming most of the imaging window. Gaseous bubbles can fill the imaging region by the simple migration of air that was trapped in the device during filling, nucleation of radiolytic byproducts, or nucleation of electrochemical products. The former most is the simplest to describe and the hardest to avoid once in the microscope. When the device is loaded, the membrane will deflect and bow outward into the vacuum (due to a new, larger ΔP across the nitride). A consequence of this additional bowing is the reduction of

pressure within the nanoaquarium. The details of pressure estimates can be found in **Section 2.3**. This reduction in pressure can dislodge trapped air that will often migrate into the center of the imaging window as it is energetically favorable to be in the larger thickness where the bubble can take smaller radii of curvature and lower Laplace pressure.

The nucleation and growth of large bubbles due to radiolysis or electrochemistry can be mitigated, but often arises out of necessity to perform a desired experiment. Radiolytic bubbles can be avoided by minimizing dose rate and total dose deposited in the sample. This topic is investigated in detail in the Radiolysis chapters. The bubbles generated via electrochemical processes, however, are unavoidable for many systems. In our copper electrodeposition experiments, the reaction at the counter electrode necessitates the formation of O_2 . Since this reaction is irreversible, oxygen will build up in the cell over time, and will eventually nucleate a bubble. Once a bubble has formed, newly produced O_2 will diffuse to the bubble causing continued growth. Eventually the bubble will consume the visible electrode and experiments will come to a halt.

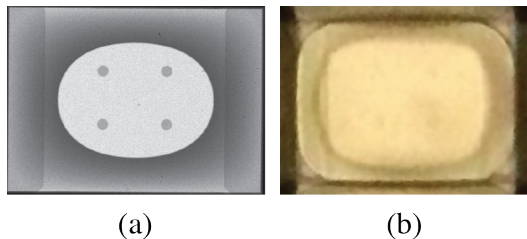


Figure 9: Large Bubble Blocking the Imaging Window: (a) STEM Bright Field (b) Optical Microscope Image

2.5.3. Poor Electrical Connections

During the loading process it is possible for a device to short to the holder. This results in a few possible outcomes. First, the electrical short circuit most often means

that no actuation will be possible since current will pass through the holder to the system ground instead of through the device. Precautions can be taken to avoid this outcome. Kapton tape has been added to the holder as a means to avoid device leads from contacting the side walls of the holder during the loading and clamping process. Additionally, ensuring the proper length of the electrical leads ensures that the short does not occur with the set screws. The second electrical failure is an open circuit. This arises in three predominate ways. If the silver epoxy used to glue the electrode is not properly prepared (the wrong ratio of the two components), then it can be left non-conducting. This is an irreversible failure, which is why the epoxy should be tested for mechanical strength and electrical conductivity prior to use. The next form of an open circuit is facilitated by a mechanical failure of the epoxy. If the holder is clamped too tightly, the epoxy bond can be broken. If this occurs, then leads can be re-glued only after the device has completely dried. (Windows in devices with liquids will break on hotplates.) The final electrical failure is when a device rotates during clamping and a electrical lead loses contact with a copper beryllium tab. This can simply be remedied by reassembling the holder.

Electrical issues can, in general, be mitigated with proper preparation. A multimeter may be employed to check for electrical connections from the holder to the device. However, a multimeter should never be used to check the electrical connection through a solution as the current used is often strong enough to break the windows within the device. Practically speaking, this means one should never place the two multimeter pins on two of the device leads at the same time. Otherwise, checking the connection from a single lead to the holder or any non-device lead component will not result in the destruction of a device.

2.5.4. Collapsed Membranes and Leaking Devices

In balancing the sealing of a device and minimizing the bowing (pressure), devices can have slow leaks that result in a loss of liquid during the pumping process. This can lead to the absence of bulk liquid within the imaging region. A rule of thumb to check if this is the case is to look for a change in intensity between the edge of a device and the center once in the electron microscope. If there is no intensity gradient, then the device is likely empty or contains a large bubble. Devices experiencing this type of failure can be redeemed simply by refilling. It is important to note that electrical actuation should not be applied for a device that is empty, as it will likely result in the breaking of the window.

2.5.5. Beam Induced Deposition

Beam effects resulting in the formation of nanocrystal can be a focus of study, however, they can also fill the field view and block imaging. This is especially problematic during electrodeposition experiments, where the deposits can also modify the growth morphology. Beam deposits have been found to be electrically conductive, but often will not be etched during electrochemical stripping cycles. A video sequence taken during copper electrodeposition experiments shows copper being etched under galvanostatic conditions is available **Appendix Video B.3** with stills from the sequence shown in **Figure 10**. The etching is taking place near a liquid vapor interface, which is why the background intensity varies on the two sides of the interface. During the etching, the beam deposits are left behind even though the electrodeposit is readily removed. This is likely due to the beam deposits having some other composition (potentially alloyed or an oxide) that does not etch as easily as the plain copper.

If the goal of the study is to investigate the morphological evolution during elec-

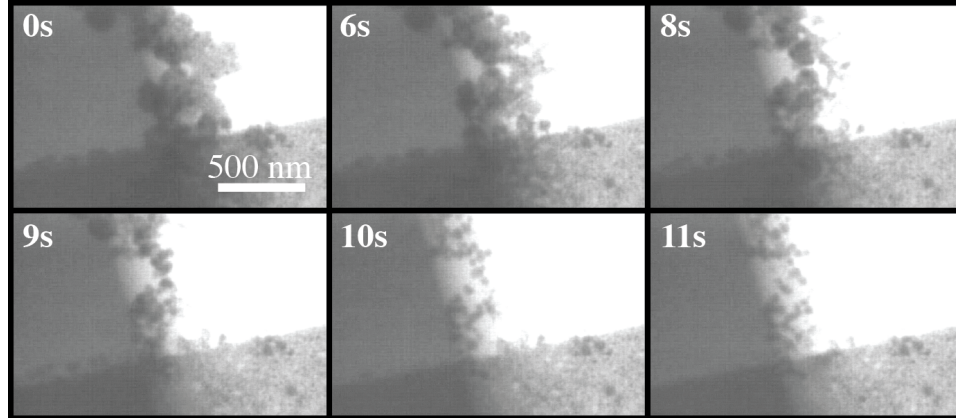


Figure 10: Etching of copper electrodeposit under galvanostatic conditions. Copper electrodeposition was performed around particles grown via beam deposition. The particles are not etched by the applied current and are instead left behind.

trodeposition, then the beam deposits will be a detrimental issue. However, the deposits could be exploited as a means to study the incorporation of a second, colloidal phase into an electrochemically grown phase. In the former case, the experiments will have to end when the beam induced deposition abstracts the morphological study. Fortunately, these nanocrystals are often loosely bound to the silicon nitride membrane. A consequence of this is that moving interfaces can push the particles away from the viewing region [14]. **Figure 11** shows a time sequence where the liquid vapor interface first advances moving the particles toward the right, then recedes pulling the particles back toward the left. The entire video sequence can be seen in **Appendix Video B.4**. A similar process may occur when cleaning the device, meaning there is some chance to reclaim and reuse a nanoaquarium suffering from significant beam induced crystal growth as long as the presence of these particles is not an issue in future experiments.

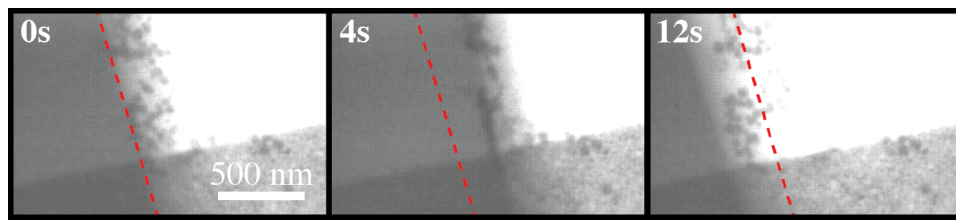


Figure 11: Advancing liquid vapor interface pushes particles toward the right, then receded and drags the particles back toward the left. A red dashed line illustrates the initial location of the bulk liquid phase.

CHAPTER 3 : Understanding Liquid Cell Results - Image Processing

In recent years, in-situ electron microscopy has emerged as a powerful technique for real-time imaging of dynamical processes with the nanometer resolution of the electron microscope. Modern electron detectors allow one to monitor processes with frame rates ranging from a few Hz to kHz, producing very large data sets. Automated image processing algorithms are needed to extract useful quantitative measures of the observed phenomena. In this chapter, we outline image processing workflows for the quantitative analysis of evolving phases imaged in liquid cell electron microscopy. We first account for variations in the imaging system in order to properly evaluate intensity data in a way that accounts for the physics of the observed system. Many of the relevant algorithms have been implemented in Mathematica and MATLAB, and are posted on the web [?].

3.1. Understanding Micrographs

3.1.1. What is a Micrograph? A Digital Image

A micrograph is an image defined by a two-dimensional function, $f(x, y)$, where x and y are spatial coordinates making up a plane. The amplitude of f at a given (x, y) coordinate pair is called the *intensity* or *gray value* of the image. **Figure 12** shows a sample micrograph from within our liquid cell consisting of a measure of the beam intensity as processed by the sensor and imaging system along with an imposed overlay with the timestamp and metadata from instrumentation. Although images can be continuous function in x , y , and amplitude f , modern imaging systems employed in (S)TEM use digital sensors for spatial recording in the (x, y) coordinate space and quantization of the amplitude. The result is a *digital image* with finite and

discrete values in amplitude and space. We consider monochromatic images and do not need to consider multiple channels at the same time. (Unless otherwise stated, the micrographs collected are reported as brightfield images.)



Figure 12: Typical Nanoaquarium Micrograph

Monochromatic digital images are conveniently represented as an $M \times N$ matrix, where M is the rows and N is columns in whole numbers. The intensity at a given pixel location is conventionally stored as either a floating point number on $[0, 1]$ or an unsigned integer between 0 and $2^{\text{bit-depth}} - 1$ that represents the quantized gray value. The bit-depth of an image is equal to the number of bits used in generating the quantized form of the intensity function and is often 8 bits (giving images with gray values from 0 to 255). In this work we shall conform to the former definition and employ double precision floating point numbers where mathematical operators passed over regions of the image are straight forward. We therefore can write the image f as

$$f = \begin{bmatrix} f(1,1) & f(1,2) & \cdots & f(1,N) \\ f(2,1) & f(2,2) & \cdots & f(2,N) \\ \vdots & \vdots & \ddots & \vdots \\ f(M,1) & f(M,2) & \cdots & f(M,N) \end{bmatrix} \quad (3.1)$$

3.1.2. Background Intensity

The Hitachi H9000 TEM used for experiments at IBM has a thermal emission electron source that is subject to temporal variations in the number of electrons produced as the filament’s temperature cycles as a function of microscope parameters. In order to account for drift (or applied shifts) in the beam intensity incident on the detector, we perform an analysis of the image *background intensity*. Where we define the “background” of an image as a region in the nanoaquarium where the beam passes through the minimum set of materials. That is, the background is a region of the viewing window where the beam passes through the two nitride windows and the supporting solution only. In the case of a metallic salt solutions, such as those used during electrodeposition, the background has no solid metal phase (no Pt electrode, no beam induced nanocrystals, and no electrodeposit) and is away from the silicon edge of the device.

Figure 12 shows a typical view from an electrodeposition experiment. Upon investigation, four separate regions are easily identified. First, we notice the edge of the silicon wafer near the right edge of the image. Second, we see the electrode splitting the scene nearly horizontally, with the darker region in the top half of the image being the Pt electrode. The bottom left portion (the brightest in these bright

field images), is a region that consists only of the two silicon nitride windows separated by the solution. The background image, is the most accurate estimate of the beam intensity drift as the region's composition changes the least during the course of an experiment. During electrodeposition, the solution contrast will change as a function of the local concentration of dissolved ions, however, given other contrasting agents in the system, the change is small and below the detection limit after accounting for noise within the image.

Using electrodeposition data, we select a rectangular subset of N_B total pixels that remains in the background region (i.e., does not see metal deposition during the experiment), and take their average value for each frame of the video. The region is denoted in the inset of **Figure 13** by the the black, opaque rectangle with the white outline. This is background intensity, $I_B(t)$, for the frame t is plotted in **Figure 13** for typical imaging conditions and a region where $N_B = 6600 \text{ pixels}$. There is a slight decay in the background intensity, however, the beam remains fairly constant for the duration of the experiment.

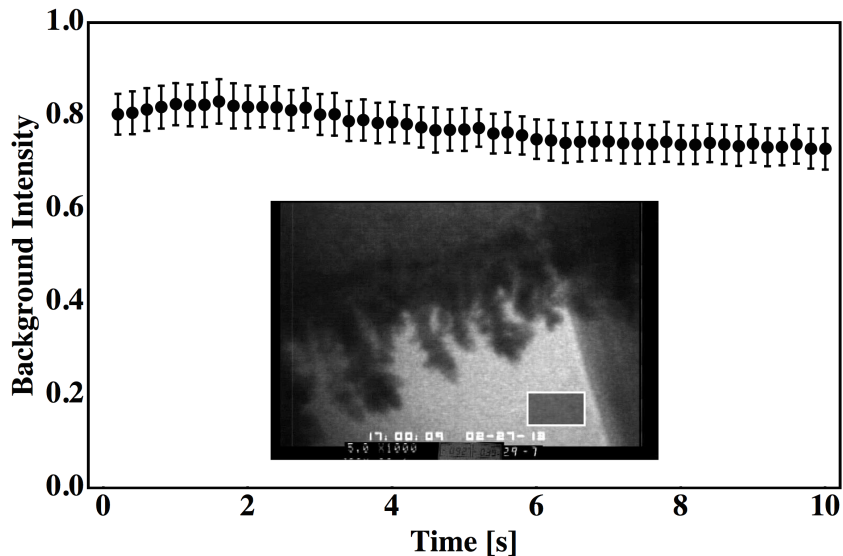


Figure 13: Typical Background Intensity

Since we can calculate $I_B(t)$ for each frame, we can adjust an entire image sequence for any variation in the beam intensity. We define an *image normalization factor*, $\gamma(t)$, to adjust a given image sequence by the variation in beam intensity. We scale $I_B(t)$ by its maximum value and take its inverse to get,

$$\gamma(t) = \left(\frac{I_B(t)}{\text{Max}[I_B(t)]} \right)^{-1}, \quad (3.2)$$

where we let t span all of the time covered by the image sequence. Note that, since we have a fixed frame rate, both $I_B(t)$ and $\gamma(t)$ are discrete functions with a single value for each frame. This factor can be applied to each frame as a scalar multiple in order to adjust the sequence brightness for any intensity drift during the experiment. **Figure 14** shows a plots where an adjustment was made to the beam or the gain on the sensor during the recording. The normalization factor is used simply by multiplying all of the pixel values in an image at time t by $\gamma(t)$. This is especially important when directly comparing intensity values between frames, or in cases where the beam intensity is changed during an experiment.

Noise Estimation

Imaging conditions are chosen to minimize electron dose required to form an image as a means to mitigate beam effects. A consequence of this choice is images with low signal to noise ratio. It is therefore desirable to estimate the strength and nature of noise in our imaging system. The part of the image identified as the background region serves as a means to deduce the type of noise and its level. By considering the histogram of intensities in the background region, we identify the statistical distribution that best fits the intensity record. We assume that noise is superimposed on top of the *truth image*, which, in the case of the background, is assumed to be

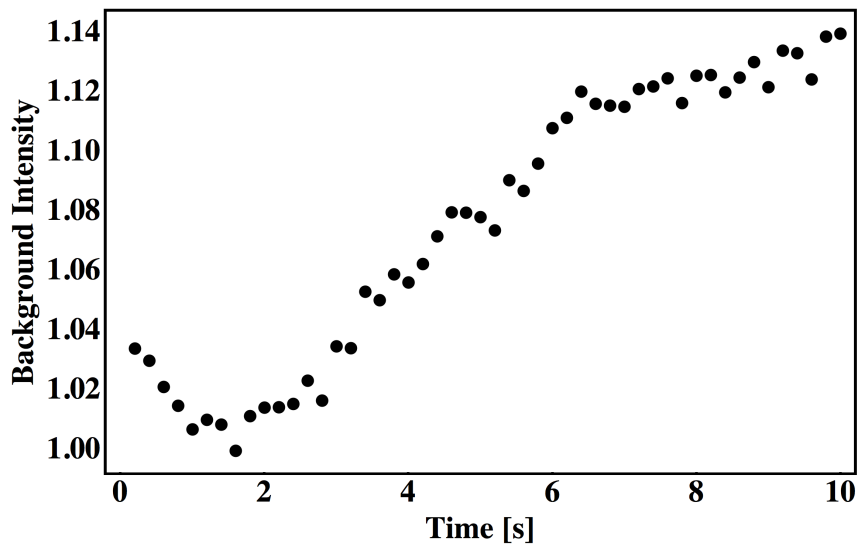


Figure 14: $\gamma(t)$ for Typical Electrodeposition Sequence

a constant grayvalue. We plot a typical histogram in **Figure 15** obtained from the region defined in the image sequence of **Figure 13**, which reveals a noise model most closely fit with a normal distribution.

The normal distribution is consistent with the dominant source of intensity variation being due to the natural fluctuations in the electron beam while imaging with a minimal dose. The error bars in **Figure 13** represent the standard deviation of the fitted normal distribution in each frame. The noise remains essentially constant for the duration of the experiment. In this particular case, the signal mean value is 0.75 and the standard deviation $\sigma = 0.04$. Knowledge of the noise model is also useful when using noise filtering algorithms as discussed later in the text.

3.1.3. Intensity Consistency Between Image Regions

Before we utilize these results broadly, we want ensure variations are actually due to beam fluctuations and not due to the system itself changing. To this end, we notice the existence of four regions in a typical micrograph scene demarcated by the edges of

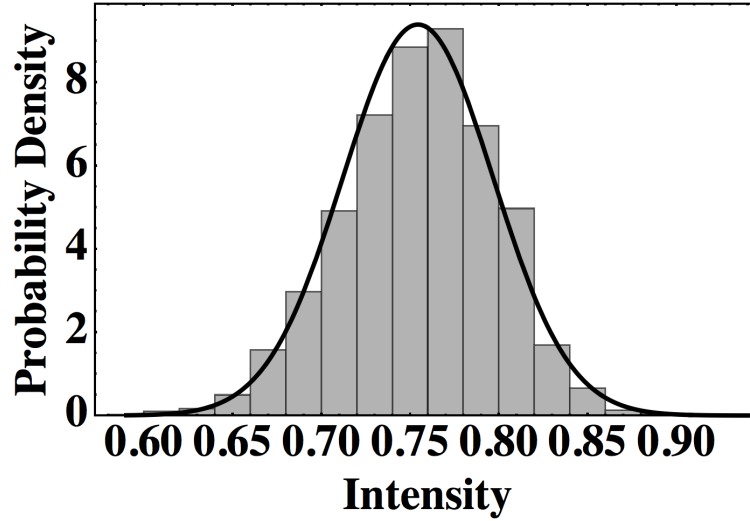


Figure 15: Best Fit Model to Background and Noise of sample frame from **Figure 13** (Best fit: $\mu = 0.75$ and $\sigma = 0.04$)

the silicon and the electrode. We refer to these regions as the *window off-electrode*, R_1 (background), the *window on-electrode*, R_2 , the *silicon off-electrode*, R_3 , and the *silicon on-electrode*, R_4 . Average intensity of each of these regions is tracked in a similar fashion as the background intensity for the regions identified in **Figure 16**. The four intensity curves are plotted in **Figure 17** as functions of time to see how they vary. The four curves follow patterns consistent with whether or not they see any electrodeposition of the copper where R_2 and R_4 rapidly decrease in value as the copper grows. The intensity in regions that includes the Si edge is lower than those in the absence of silicon both on and off of the electrode. The background intensity, as one might *a priori* assume, is the greatest (or brightest) as the electrons passing through this region see the lowest average atomic density. Note that these are bright field images, and so brighter intensities corresponds to regions with lower atomic density which results in less elastic scattering.

The relative changes in each of these regions is measured by taking ratios. First,

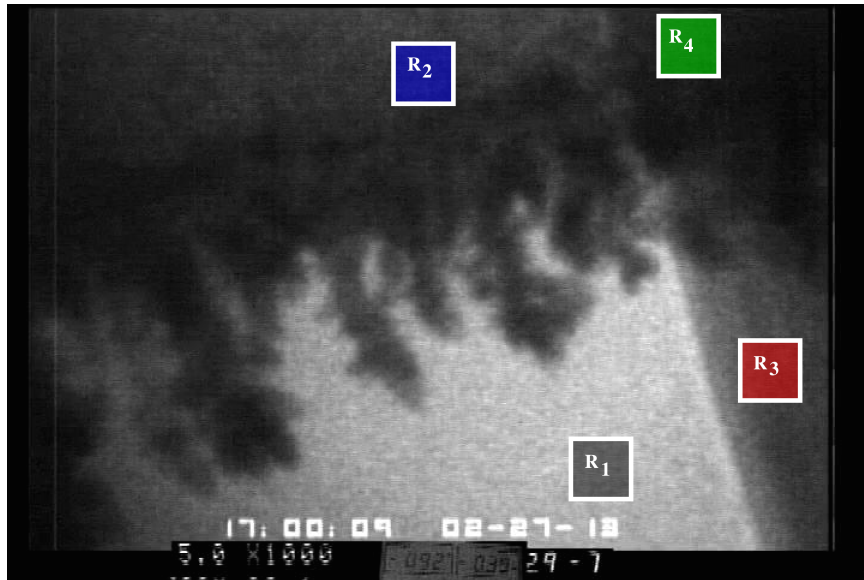


Figure 16: Definition of Image Regions

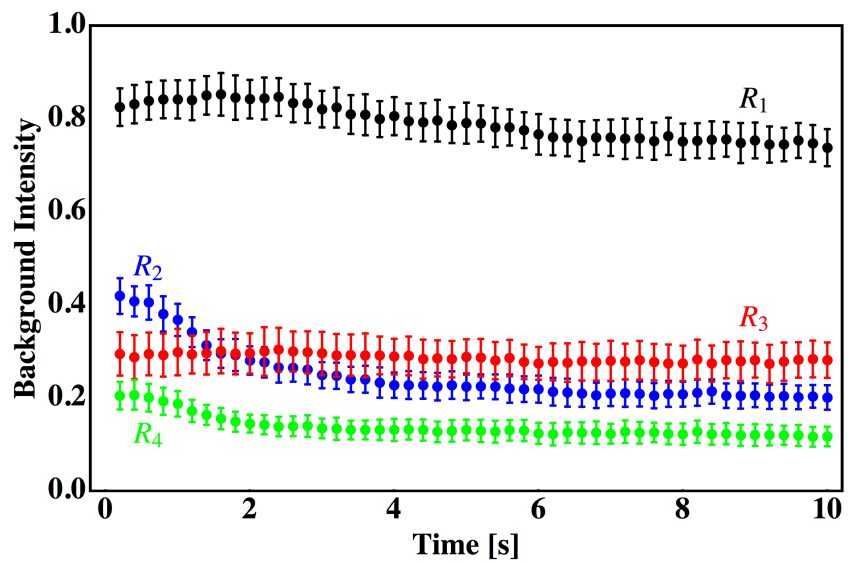


Figure 17: Average Intensity of Image Regions where 0 and 1 correspond, respectively, to black and white grayvalues

we extract the behavior of the deposition by taking the ratios of what is happening on and off the electrode, *viz.*, we plot $\frac{R_2}{R_1}$ and $\frac{R_4}{R_3}$ as functions of time in **Figure 18**. In this we see the two curves with the same shape, where the ratio decreases with time as the copper grows on the electrode during the experiment. This reduction is due to the copper deposition and shows that the being under the silicon or in the window region does not affect the results.

Next, we compare the electrodeposit in the window region and under the Si edge by plotting $\frac{R_3}{R_1}$ as a function of time in **Figure 18**. For completeness we also plot $\frac{R_4}{R_2}$ as a function of time. Here we again see the two curves, but this time maintaining a constant value. This is indicative of their being uniform deposition on the electrode in both the window region and under the silicon (in the field of view) for $\frac{R_3}{R_1}$. The ratio of $\frac{R_4}{R_2}$ confirms that there is little variation in the liquid layer in the window region compared to under the edge (i.e., no additional bowing of the nitride membrane window near the edge of the silicon during the deposition).

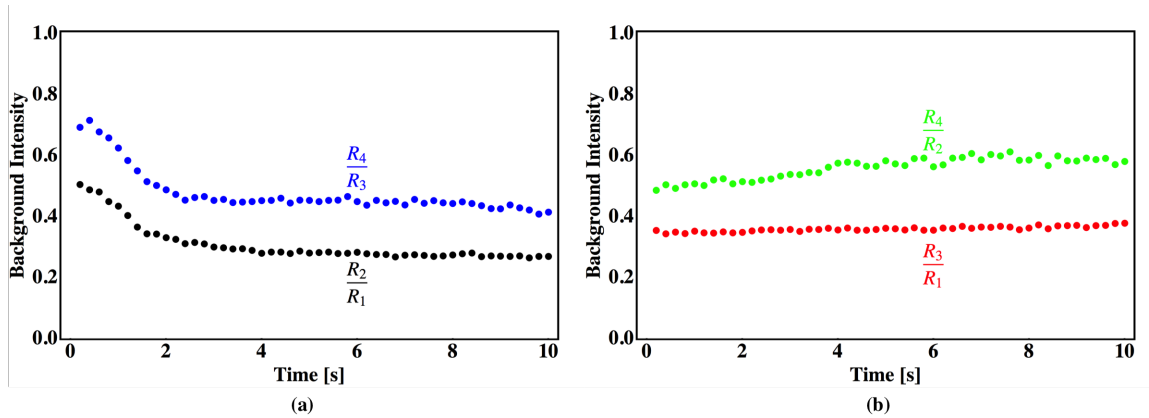


Figure 18: Intensity Ratios during electrodeposition. (a) Intensity Ratio On and Off Electrodeposit (b) Intensity Ratio between Window and Silicon Regions

3.1.4. Beam Spatial Consistency

Vignetting

Imaging systems are subject to phenomena that lead to the attenuation of signal away from the optical system’s center axis. This results in non-uniform intensity seen as a darkening near the edge of an image, called vignetting. Although the vignetting affect can be artistically pleasing, it proves to be an issue for computer vision algorithms that are dependent on the image intensity function. This is particularly a challenge for feature detection, such as the edges we wish to extract from our micrographs.

Vignetting is the result of several factors. The most prominent, off-axis illumination, is a result of camera systems themselves. If one were to imagine the simple case of a point source, say from a pin-hole, the light emerging from this source would spread spherically. If we place our planar sensor a finite distance away from the source, we will see that only one point on the sensor has the shortest distance from the source. All illumination hitting other parts of the sensor must travel further than the distance traveled along the optical axis (closest point), leading to a reduction in the flux of intercepted energy and a dimmer image near the edges of the sensor. If one were to solve this geometry problem, one would find that the intensity falls off as \cos^4 as one moves away from the sensor’s center [17, 18]. The simplest case, when the sensor is perpendicular to the optical axis, is illustrated in **Figure 19**.

The best way to correct for vignetting is to first image a “white” background and extract the vignetting function, however, given the physical constraints of our device and holder, this is not an option. To correct a single image, the brute force method is to fit the calculated intensity curve and force a constant intensity in the background. Alternatively, one can employ algorithms for single image correction, such as those

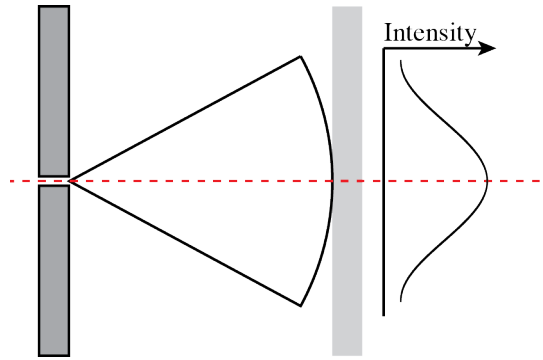


Figure 19: Vignetting is an optical aberration caused by geometry.

distributed by Zheng *et. al.* [17] and implemented in MATLAB. Their algorithm uses an iterative technique to estimate the vignetting function and then remove spurious variations from the intensity function. The input image is segmented, and an energy function is defined and minimized in order to estimate the vignetting. A typical output for the micrographs is shown in **Figure 20**.

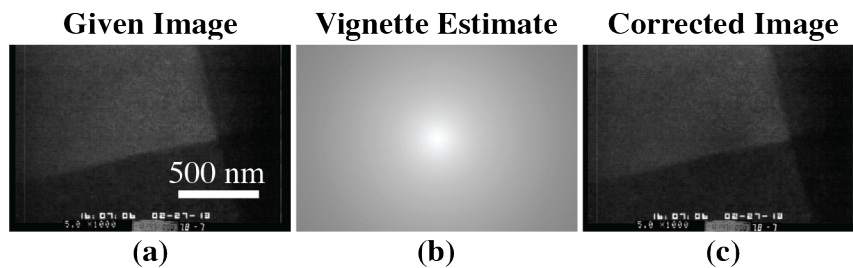


Figure 20: Single image vignette correction results showing the given image (a), the estimated vignetting (b), and the corrected image (c).

3.2. Automation of Image Processing

Now that we have an understanding of our imaging system of choice, the TEM, it is time to focus on the processing of experimental results. Given the large data sets generated (30+ hours of imaging at 30 *fps* at IBM alone), it is necessary to automate data analysis. We have developed predominately unsupervised, non-parametric image processing work flows to analyze digital images from several systems of interest.

The following sections will outline the work flow as it is relevant to the illustrative experimental results.

3.2.1. Raw Data

To perform automated analysis of image sequences, raw data should be in a consistent, easy to modify form. Since video file formats are often the default form of raw data storage, we shall assume the raw data is in a video format, readable by Mathematica. Non-video, image sequences can be handled with simple modifications to the code. Virtualdub [19] (Windows Only) and ImageJ [20] are useful open source software packages for basic video editing and format conversion, if needed. Once the raw data is in an acceptable video file format, we select a reference frame and manually define the rotation, if any; crop indices; and/or background for subtraction. It is necessary to crop out any time stamp or experimental overlay prior to the automated processes described below, as they will interfere with image thresholding. Rotation is particularly useful in the case of electrodeposition to ensure that the working electrode is horizontal to simplify post processing, however, rotation is not required. **Figure 21a** and **b** show, respectively, a raw image with overlaid crop indices and rotation angle and the resulting, rotated, cropped image. From here on, we shall refer to images of the form found in **Figure 21b** as the *sub image*.

3.2.2. Unsupervised Edge Detection

Detailed understanding of the dynamic evolution of interfaces is of both scientific and practical interest in many disciplines. The understanding of the evolution and control of interfaces is also of immense technological importance. Morphological instabilities, particularly dendrite formation, can cause potentially catastrophic failure in rechargeable batteries, and lower the quality of electroplated coatings [21–23], yet

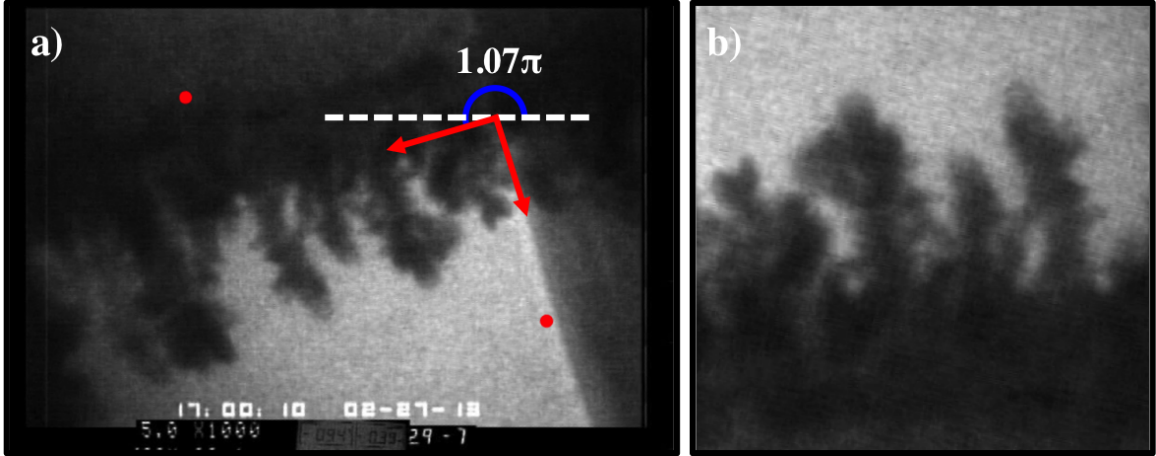


Figure 21: Example data of copper electrodeposition with a) overlaid crop indices (Red disks) and the defined angle of rotation and the b) resulting, cropped, rotated image. We refer to b) as the *sub image* throughout the rest of the text. Experimental methods for copper electrodeposition can be found later in the text.

they may be useful in forming porous deposits such as porous electrodes. During the formation of nanocrystals, controlling geometry is essential for tuning mechanical, electrical and optical properties [24, 25]. Thus it is important to develop strategies to understand and control the nanoscale phenomena that affect interface evolution. Liquid cell electron microscopy allows us to image in real time and with nanoscale resolution the evolution of the solid-liquid-vapor interfaces during electrochemical deposition and etching, nanocrystal formation and dissolution, and bubble nucleation, growth, and migration [2, 3, 7, 26–31]. This provides insight into the fundamental mechanisms controlling morphology and mass transport.

In this work, we develop a general use, interface-tracking algorithm, demonstrate its use in a few selected applications, extract several quantitative measures of dynamical processes, and outline the algorithm details for easy adaptation of the open source software [32] to other experimental systems. The processes employed in the workflow are illustrated with experimental data from electron beam induced formation of gold nanoprisms [30] and copper electrodeposition [31]. The first application

of the algorithm is in the study of the electrode-electrolyte interface during copper electrodeposition from an acidified copper solution [31] where we extract the growth front location as a function of time. The data is used to calculate the projected area in order to estimate the mass of the deposition, the RMS roughness to identify the growth regime, local normal velocity distribution (akin to current density) to obtain the relationship between geometry and point-wise growth rate, and the wavelengths associated with interface morphology as their control is important for structured surface manufacturing. The second demonstration of the algorithm is to analyze growing and dissolving single-crystal nanoparticles, a process mediated by the electron beam in liquid cells [7, 30]. Tracking growth velocities of crystals has applications in measuring the effects of surfactants, nucleation conditions, and shape selection. The algorithm is further extended to adjust for particle translation based on center of mass (area) and define ways to extract particle orientation in order to properly determine growth kinetics of single particles. Lastly, we consider nanobubble nucleation, growth, and migration [8, 29], where we extract bubble radius and position as a function of time. These measurements are necessary to separate effects due to radiolytic growth and confinement between two membranes. Each of the above measures could be performed by hand for a given frame sequence, however, automation of the process allows for analysis of large data sets over long times for better statistics of the underlying physical phenomena.

Noise Filtering and Background Subtraction

When attempting to minimize damage caused by the electron beam, it is conventional to operate at the minimum dose rate required to form a visible image. This results in images with a relatively low signal-to-noise-ratio (SNR). The Rose criterion requires the SNR to be about 5 for an image to be detectable by the human visual system

[33, 34]. It is therefore useful to take precautions to reduce the apparent noise in each frame of the video sequence. We achieve this reduction through background subtraction and the application of a Total Variation Filter (TV filter). We apply this technique to analyze experimental results from beam-induced gold nanocrystal formation from Park *et. al.* [30].

De-noising is necessary when high accuracy object extraction is desired. Since we are interested in tracking interfaces, which are seen as edges or intensity discontinuities in images, we choose an image restoration algorithm that maintains the fidelity of edges. The TV filter pioneered by Rudin *et. al.* [35, 36] poses noise removal as a constrained optimization problem. The method assumes that noise is additive (superimposed on top of real object image, or “truth image”) with a known statistical distribution. Assuming Gaussian noise (as established from background intensity data), **Figure 22a, b, and c** show, respectively, a nanocrystal sub image, filtered image and the difference between the two. Notice that to the eye, the filtered version looks almost unaltered, which is desirable. The smoothing provided by this filter mitigates false positives during unsupervised binarization and edge detection.

Background subtraction is useful for increasing contrast of dynamic objects in scenes imaged in a fixed laboratory frame. Several algorithms have been developed to estimate the “background model” using temporal information [37]. Carefully designed experiments to capture reference images can provide a frame or an average of a few frames for the background model. Using the nanocrystal of **Figure 22**, we select a frame before the nucleation of the particle for the background model. **Figure 22d, e, and f** (middle column) show, respectively, the background model, the frame of interest, and the foreground image. The image difference is a pixel-by-pixel

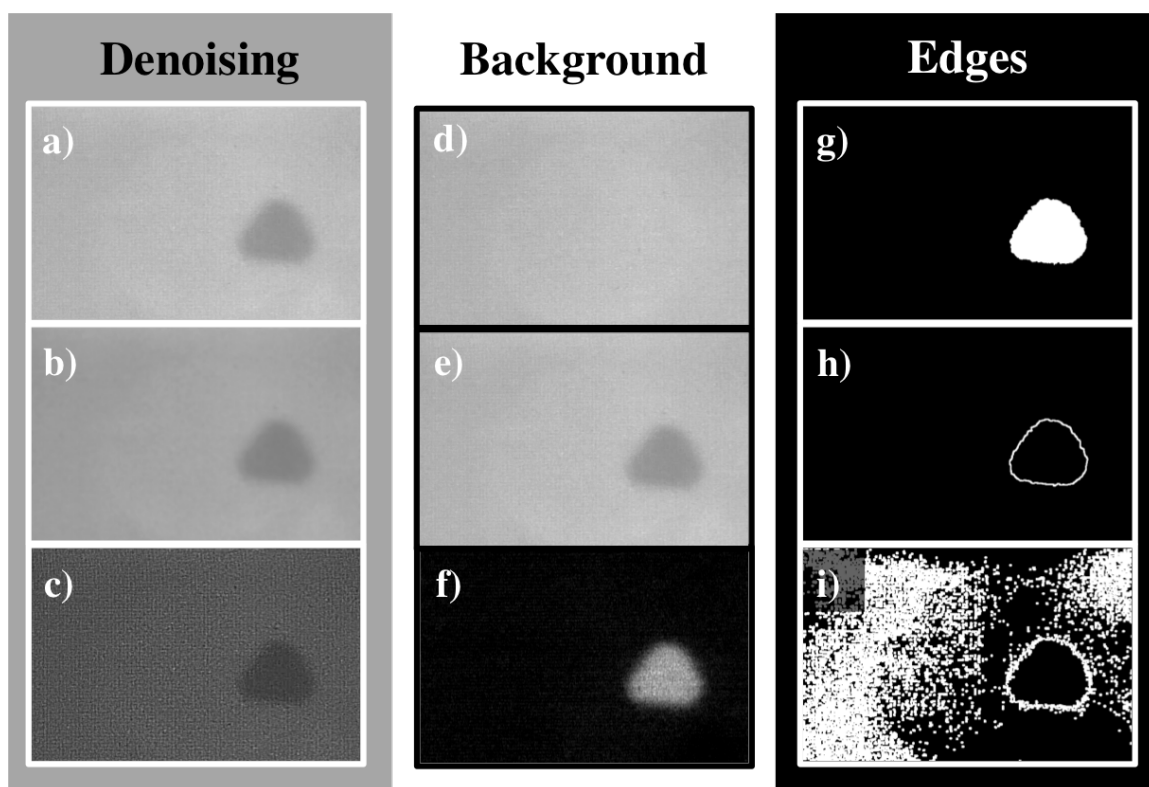


Figure 22: The denoising column shows a) a nanocrystal sub image, b) the same image after TV filter application, c) and the difference between the two. The second column shows d) the image used as the background model, e) the frame of interest, and f) the foreground image. The edge detection column shows g) a thresholded foreground image (with TV filter), h) the extracted edges from the prepared foreground image, and i) the extracted edges without image preparation (undesired).

subtraction of the image intensities,

$$I_F(x, y, t) = I(x, y, t) - I_0(x, y) \quad (3.3)$$

where, $I(x, y, t)$ is the intensity of pixel (x, y) at time t , and I_0 refers to the background model. The foreground image is then rescaled to have intensity levels between 0 and 1 as shown in **Figure 22f**, where 0 represents black in a digital image.

Thresholding and Edge Detection

Once noise and contrast are optimized, edge detection can be performed. Edge detection works best on a binary image, and so thresholding is first performed. The standard Otsu's method [38] is utilized to convert the grayscale image into one with only two values (additional gray levels can be included when needed). This process once again casts the image analysis as an optimization problem, where now we assume the image can be classified into two classes, the foreground and background, with maximized separability. That is, the image is assumed to have a bi-modal histogram and the algorithm tests all possible threshold values, where the chosen threshold value is the one where the sum of the variances of the classes is minimal. **Figure 22g** shows a binarized foreground image that was TV filtered prior to thresholding. Once the binary image is generated, it is time to find the edges of the object. The edges will be a direct measure of the interface as projected from the image plane. A Canny style edge detector [39] is extremely robust for images of the type found in **Figure 22g**. Edges are defined as local maximum in the first-order directional Gaussian gradient of the intensity function. Since the image has already been denoised and binarized, the edges are extracted with great fidelity as is seen in **Figure 22h**. Had the image not been prepared via the TV filter and background subtraction, many false positives

would have been identified by the edge detection. **Figure 22i** is the result of edge detection without preparation, notice many false edges in the background and around the object.

Translation Correction and Object Centroids

Often, image sequences suffer from drift and/or migration of the object being imaged. We therefore present one means for the correction of translation for a single object, say a bubble or nanocrystal growing. This process has the added benefit of tracking the area centroid of the object(s), which can be a separate measure of the system. The code can be extended to systems of multiple dynamic objects via particle tracking algorithms such as the methods of Crocker and Grier [40], which can readily be found as open source for a variety of several computation platforms. The particle tracking will statistically relate entities across frames via their displacement, giving a connected particle track. For the sake of simplicity, we will only extract the positions of particles subjected to translation.

Using the same nanocrystal growth from **Figure 22**, we now consider the entire video sequence from **Appendix Video B.5**. Once the binary image is generated (**Figure 22g**), the centroid of the foreground pixels is identified for each frame according to the formula

$$(x_c, y_c)_\Omega = \left(\frac{1}{n} \sum_n x, \frac{1}{n} \sum_n y \right) \quad (3.4)$$

where Ω is the region of pixels identified as the object (white pixels in **Figure 22g**), n is the number of pixels in Ω , and the pixel location is the (x, y) pair. This can either be hard coded into the algorithm, or the built in function of Mathematica called

MorphologicalComponents can be passed on the image with the option of “Centroid”. By looping over every frame, we obtain the area centroid of the nanocrystal as a function of time. By fixing the origin of the coordinate system for each frame at the center of the particle, we map our video from the laboratory frame to a frame of reference at the centroid of the object,

$$I_{Mapped}(x, y, t) = I(x - x_c, y - y_c, t). \quad (3.5)$$

3.3. Applications

3.3.1. Growth Front Tracking During Electrodeposition

The first application of our image-processing algorithm is the extraction of the growth edge morphology during copper electrodeposition. Since many transport processes work simultaneously during deposition, it is important to identify and understand the driving physics during the evolution of the solid-electrolyte interface. Spatially averaged electrical measurements are able to identify the dominant growth mechanisms, but fail to fully account for the local, nanoscale evolution. Liquid cell electron microscopy allows us to image, in real time and with nanoscale resolution, the surface evolution [2,3,26,31]. Quantitative analysis provides key insights into the mechanisms leading to diffusive instabilities and into the efficacy of measures employed to control electrodeposited morphology.

The algorithm described here robustly extracts quantitative measures of the growth front morphology. **Figure 23a** shows frames of the growth. The **Appendix Video B.6** shows the footage obtained from an experiment that resulted in a diffusive instability. From the extracted edge, we can further post-process the data to obtain figures

of merit describing the growth. The first and simplest metrics are the average height, the maximum height, and the minimum height of the solid film as functions of time, as shown in **Figure 23b**. Consistent with galvanostatic conditions, we see a nearly linear advancement of the average height after an initial transience associated with growth on top of the electrode (prior to the 2D growth regime). At the transition to the diffusive regime (~ 12 frames), the minimum height stagnates and the maximum height grows at a higher rate in order to maintain the average growth speed (and conserve charge/mass). Eventually, all of the growth stops, as some asperity outside the imaged region consumes all of the incoming ions. We can further describe the interface by its amplitude and wavelength. The RMS roughness, which is classically used in Kinetic Roughening Theory [41,42] to describe electrodeposition, is a measure of the amplitude of the surface, and is defined as

$$RMS(t) = \sqrt{\frac{1}{L} \sum_{i=1}^L [h(i,t) - \bar{h}(t)]^2}. \quad (3.6)$$

where L is the length of the domain, $h(i,t)$ is the height in pixel column i at time t , and $\bar{h}(t)$ is the average height at time t . We plot the RMS roughness as a function of time in **Figure 23c**.

The lateral wavelength(s) of the interface can also be extracted as a function of time. In this particular case, the viewing area is small (i.e., the wavelengths present are on the order of the window size), so we choose the autocorrelation or the cross correlation of the surface with itself in space at each time to identify this metric. The autocorrelation

$$R_h(t, \lambda) = \frac{\sum_{i=1}^{L-\lambda} (h(i,t) - \bar{h}(t)) (h(i+\lambda,t) - \bar{h}(t))}{\sum_{i=1}^L [h(i,t) - \bar{h}(t)]^2}, \quad (3.7)$$

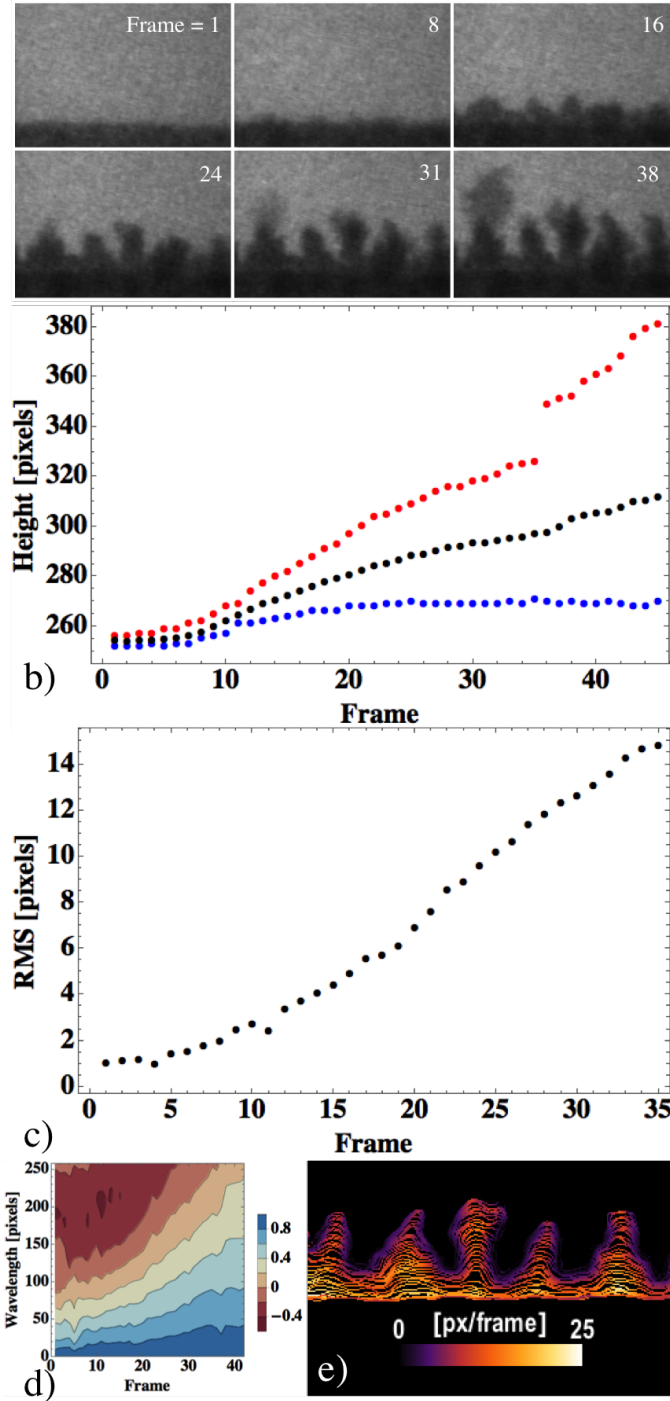


Figure 23: a) Stills from electrodeposition seen in **Appendix Video B.6**. b) Maximum, minimum, and average growth height as a function of frame number. c) RMS roughness of growth as a function of time. d) Contours of the autocorrelation function of the surface roughness as a function of wavelength (spatial shift) and frame number. e) A heat map of the normal growth speed each frame. The green line represents the surface morphology at the transition time.

where λ is the wavelength in pixels, $0 < \lambda < L$, and L is the image's width. This metric will always have a peak of 1 when $\lambda = 0$. Many wavelengths exist and interact dynamically and so no obvious, dominant wavelength is seen in the autocorrelation in **Figure 23d**. This behavior is consistent with what has previously been proposed for the evolution of electrodeposited surfaces [42].

We have so far extracted average parameters from our growth front, however, the nanoscale resolution of the electron microscope can be exploited further through local measurements. Morphology during electrodeposition is directly controlled by the normal current density at any given point [43,44], which is in turn, directly related to the normal local speed of the interface via a mass balance (with appropriate assumptions about the deposition efficiency). It is thus desirable to obtain the point-wise normal velocity of the extracted edge, which, from the calculus of moving surfaces, is defined as [45]

$$v_N(i, t) = \lim_{dt \rightarrow 0} \left(\frac{S_{t+dt}(i_N) - S_t(i)}{dt} \right), \quad (3.8)$$

where $v_N(i, t)$ is the normal velocity at point i and time t along the temporally evolving interface, S_t . The velocity will be determined by the vector distance between the point of interest, i , and the point that lies along the normal to $S_t(i)$, denoted i_N , on the interface S_{t+dt} . Essentially this problem is reduced to the task of finding the distance from a point on the current surface to a point of intersection between the normal to S_t and the surface after it has evolved for time dt . The diagram in **Figure 24a** shows this visually.

The real problem is slightly more complicated as we have a 2D point cloud with unknown noise. **Figure 24b** illustrates this reality. We have implemented two methods

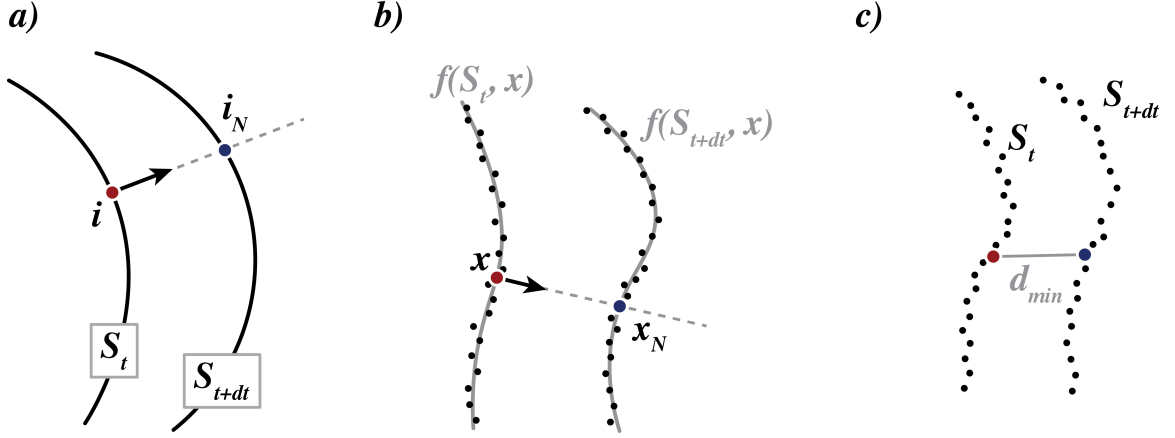


Figure 24: Illustrations of normal velocity extraction for a) a general surfaces, b) the moving least squares algorithm, and c) the minimum distance approach.

for extracting the normal direction to the surface. The first method is a moving least square algorithm [46], where the curve is locally fit via least squares method with the polynomial $f(S_t, x)$, and then the normal is determined by calculus. Mathematically, we take n points centered around the point of interest i on S_t and fit those values to the polynomial $P_m = \sum_{j=0}^m a_j x^j$ of degree m . The coefficients a_j are obtained by minimizing the penalty function

$$r^2 = \sum_{k=i-\frac{n-1}{2}}^{k=i+\frac{n-1}{2}} [S_t(k) - P_m(x_k, a_0, a_1, \dots, a_m)]^2. \quad (3.9)$$

Where n is an odd integer number of points from the extracted edge's point cloud centered about i . This method works best for low noise data, and cases where the frame rate is low (i.e., the interface moves more than a few pixels per frame).

An alternative method is to exploit the fact that the shortest distance from a point to a curve lies along the normal to the curve. If point i is the point of interest along the curve at time t and we find the point j at $t + dt$ for small dt , that i on S_t will be closest to i_N on S_{t+dt} , the vector distance between points i and j will automatically

give the normal direction over dt for point i at t . **Figure 24c** illustrates the results of this process. Mathematica has built in routines to quickly find which point from a point cloud (ordered or not) is closest to a point of interest. This proves to be a very effective and fast means for the extraction of point-wise normal direction, especially in the presence of noise. **Figure 23e** shows a “heat map” (contour plot) of the normal speed at each spatial, temporal point along the growth of **Appendix Video B.6**. Initially, we see uniform distribution of speeds and therefore uniform current density. As the roughness increases due to natural fluctuations, the current density becomes less uniform locally, leading to continued of the roughness. This process is even apparent before the transition to the diffusive regime. Comparing the velocity as a function of time at specific points, such as at the tips of the asperities, enables detailed models to be applied to predict phenomena such as tip splitting.

3.3.2. Facet-Dependent Growth and Dissolution Rates in Nanoparticles

Size and morphology control of nanocrystals are essential to tailoring the physical and chemical properties of the resulting structures [24, 25]. Liquid phase synthesis is convenient, low cost and very versatile since solution chemistry can be tuned to give specific morphology. A fundamental understanding of the driving force and principles that govern morphologies throughout nucleation, growth, and shape control is essential to optimize existing synthesis methods and to discover novel ones. The imaging processes described here enable quantitative analysis of single nanocrystal morphology and particle dynamics. Measuring growth or etching of specific points on a nanoparticle tell us about the atomic level processes that control shape.

Appendix Video B.7 shows beam-induced dissolution of gold nanorods. Focusing on a single nanorod undergoing dissolution, we use the vertices of the minimum bounding box to obtain both the particle’s aspect ratio and orientation as functions

of time. **Figure 25a** shows the image sequence of the nanorod after binarization and with the superposition of the minimum bounding box vertices. The minimum bounding box is used due to the nearly rectangular shape of the particles projections and the straight forward geometry problem that can be solved with Toussaint's rotating caliper method [47] (a brute force search for the four points making a minimum bounding box of a convex hull). Alternative geometric shapes and minimum area algorithms can be selected for other particle morphologies. Many of the convex hull algorithms, including the minimum bound box algorithms, are included with the Mathematica library and are straightforward to use. **Figure 25b, c, and d** depict, respectively, the particles aspect ratio, perimeter, and rotation from the initial orientation as functions of time. Interestingly, the particle etching is not isotropic, as is seen in the non-monotonic aspect ratio. The particles first etch along thier circumference before a more uniform etching begins to take place **Figure 25c**. The perimeter of the particle decreases linearly with time, consistent with a reaction limited etching induced by radiolysis products produced during water irradiation, particularly in the presence of CTAB which contributes bromine and radiolytically formed bromine ions and radicals known to etch gold [7]. We track the rotation of the particle for a more pragmatic reason. The particle's rotation can be used along with the center of mass of the particle to extend the code to extract the point-wise normal etching (or growth) velocity. This is a simple combination of the processes outlined throughout this paper.

3.3.3. Bubble Nucleation, Growth, and Migration

The dynamics of gas-liquid interfaces play an important role in many physical processes such as high efficiency phase change heat transfer. In recent years, the existence and stability of nanobubbles have been debated [48–51]. The surface-bound nanobub-

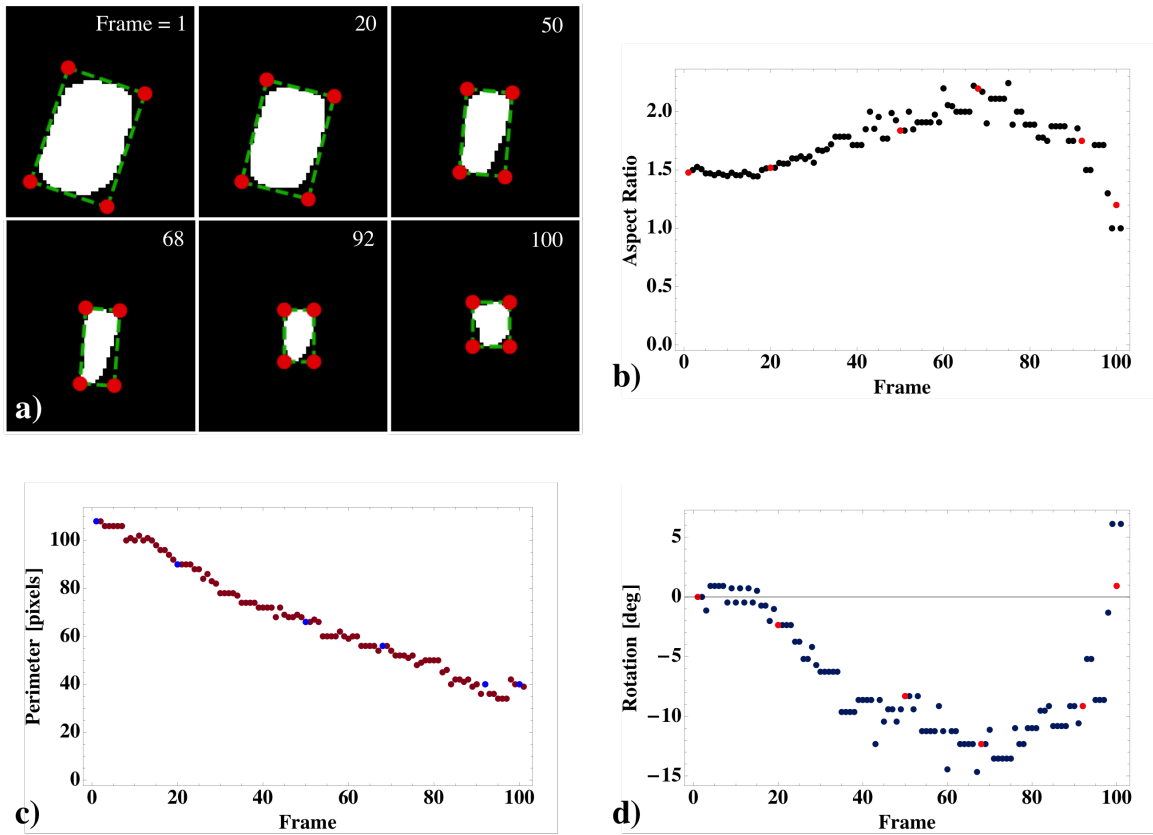


Figure 25: a) Image sequence of gold nanorod dissolution after image binarization and with the superposition of the minimum bounding box vertices (red) and connecting lines (green). b) Aspect ratio of particle as a function of frame. c) Perimeter of binarized convex hull. d) Right-handed rotation of particle from initial orientation.

ble hypothesis began as a result of indirect measurements; several investigators found that the force between two hydrophobic surfaces immersed in water varied in a step-wise manner at the sub-micron scale - a review of the findings can be found in Parker et al [52]. Recently, atomic force microscopy (AFM) measurements have confirmed the existence and unraveled the geometry of nanobubbles [48, 49, 51, 53]. However, such measurements are temporally restricted by the scanning rate of the AFM tip and there is the additional concern that the mechanical perturbation applied by the cantilever is too invasive. For this reason, studying the fundamentals of nanobubbles and their role in physical processes remains somewhat decoupled. For example, anomalous scrubbing of interfaces under ultra sound [54, 55] has been attributed to nanobubbles, as has the ease with which heterogeneous nucleation of vapor bubble occurs after repeated cycles [56]; however direct observations of them performing these roles is unavailable. As chemically and morphologically bespoke surfaces are created using state of the art micro and nanofabrication techniques, there is a need to assess the performance of the interfaces and contact line in real time at the level of a single bubble. Liquid cell electron microscopy helps bridge this gap.

The movement and growth of nanobubbles sandwiched between two partially wetting substrates is governed by wetting and de-wetting at the three-phase contact line. Identifying the interfaces of single bubbles and tracking their trajectories may enable us to obtain fundamental information on contact line dynamics. In this case, both the distribution of contact line velocities and centroid's trajectory are of interest. For the former, the edge detection scheme described is utilized. For the latter, sequences of bubble positions can be stitched together using a version of Crocker's [40] particle tracking code. The script is able to parse the trajectories of multiple bubbles present in the same frame.

The **Appendix Video B.8** shows the nucleation, growth, and migration of a nanobubble we wish to analyze. We first extract the effective radius of the bubble by finding the circular area equivalent radius from the binarized image

$$r = \sqrt{\frac{A_{Binarized}}{\pi}}, \quad (3.10)$$

where the area can be obtained by counting the number of pixel in the binary convex hull of the bubble object. **Figure 26a** shows the bubble radius as a function of the frame number. Additionally, we wish to track the bubble's location throughout the growth process. Instead of taking the area's centroid, we better account for the curvature and 3-dimension shape of the bubble by taking the intensity weighted centroid, where each pixel is multiplied by its intensity value. This serves to find the centroid most closely aligned with the center of mass of the vapor bubble, given the 2-dimension projection in the image. To accomplish this, we use the binary image as a mask to generate an image solely of the vapor bubble via image multiplication (pixel-by-pixel multiplication of the sub image intensity by the binary intensity, which reduces the background pixel values to 0). **Figure 26b** shows a comparison of a raw image, the binary image and their masked version. The extracted intensity weighted centroid is illustrated in **Figure 26c** with the edge of the bubble also drawn for each frame.

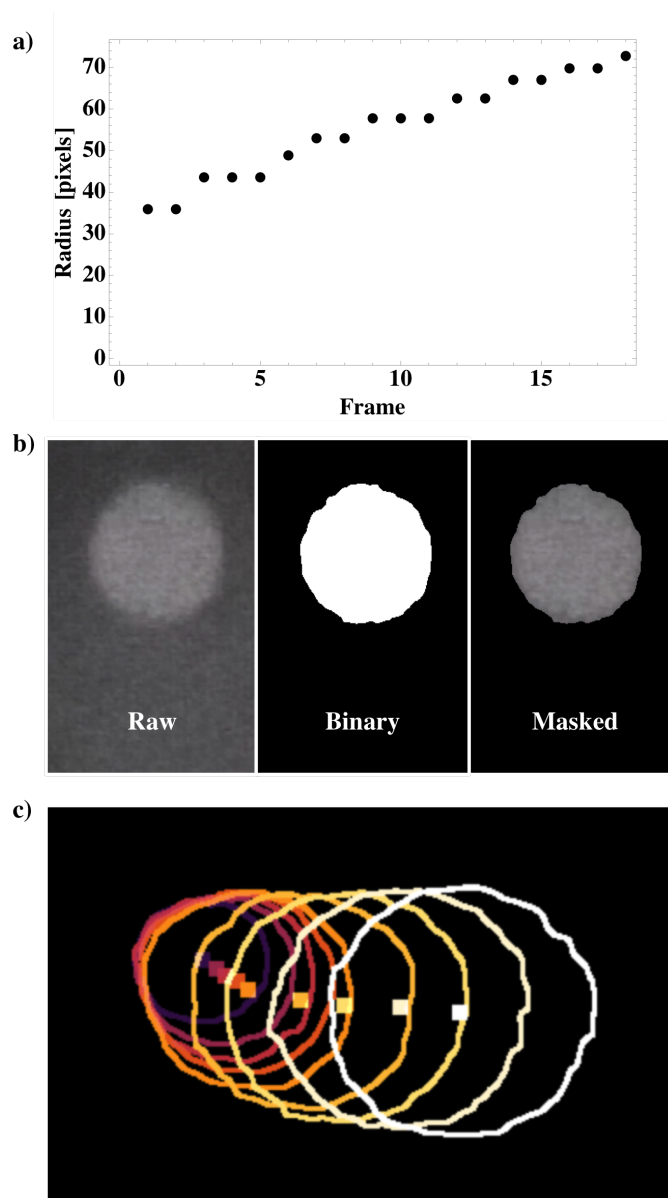


Figure 26: a) Bubble radius as a function of frame. b) Comparison of Raw, Binary, and Masked image. c) Bubble intensity weighted centroid (squares) with bubble edge outline, color-coded in time.

CHAPTER 4 : Beam-Sample Interactions

4.1. Introduction

The advent of liquid cells [2, 3] has made possible the direct imaging of processes in liquids with the nanometer resolution of the electron microscope. The samples are, however, subject to high dose rate radiation in the form of the electron beam. [7, 8] A detailed understanding of the interactions between the irradiation and the suspending medium is necessary to interpret, suppress, and exploit beam-mediated phenomena. The field of study of the chemical effects due to irradiation is called Radiation Chemistry, a field that has been studied intensively for its importance in medical imaging, nuclear energy, atmospheric science, and food preservation.

Ionizing radiation (photons, γ rays, x-rays, electrons, etc.) readily transfers energy to the irradiated medium with effects that are relatively independent of the type of radiation. Deposited energy excites and dislodges orbital electrons resulting in the generation of heat and changes in chemical composition. In this chapter, we will discuss the theoretical background necessary to understand the effects of radiolysis in liquid cells, heating, changes in solution chemistry with and without diffusion, and their implications for experimentally observed phenomena.

4.2. Electron Energy Loss in Liquids

Dose is the measure of the average amount of energy adsorbed by a mass exposed to ionizing radiation. The SI derived unit for dose is the Gray (Gy) and is defined as the adsorption of one joule of energy per kilogram of matter. The dose rate is the dose per unit time (Gy/s). It is important to distinguish this measure from the oft-reported electron flux (e^-/nm^2s), which is a measure of the ionizing radiation

itself, not the energy transferred to the sample. Here, we will consider dose rate due to an electron beam incident upon a thin layer of water in order to estimate heat generation and radiation chemistry in Liquid Cell Electron Microscopy. Water is used as the normative example due to its prevalence, however, other liquids can be considered by choosing their appropriate material properties.

Electrons passing through matter lose energy due to their interactions with nuclei and atoms of the irradiated media. Electrons elastically scattered by nuclei may be scattered at large angle, but lose little energy. Due to both excitation and ionization, electrons will lose energy to media electrons in addition to being scattered. As the electrons pass, the average rate of energy loss is given by dE/ds , which is called the (mean) stopping power. An electron will come to rest once it has lost all of its energy after a path length of

$$R = \int \left(\frac{dE}{ds} \right)^{-1} dE, \quad (4.1)$$

where R is the (mean) range [57]. The real process of energy loss is stochastic and the irradiation will deposit energy about the average rate dE/ds with some range of variation, known as straggle. These variations in energy are also manifested in the range, causing actual particles to travel more or less than the average. It is convenient, however, to consider only the mean, and this is called the Continuous Slow Down Approximation (CSDA). The straggle about the CSDA range is only about 10% - 15% [58]. For example, the mean range for electrons in liquid water under atmospheric conditions at 20kV, 30kV and 300kV is 8.6 μm , 18 μm and 840 μm , respectively. [59] **Figure 27a** illustrates the shape of electron trajectories. From here on we shall only consider the average.

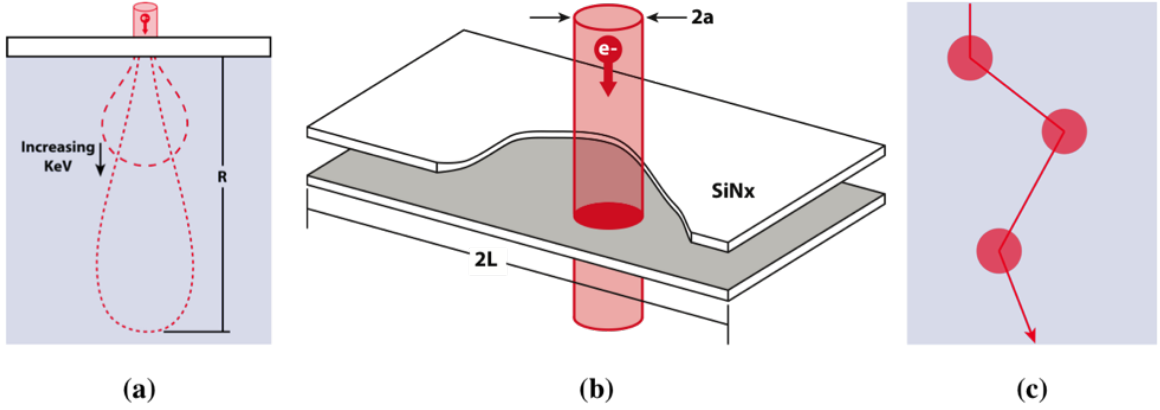


Figure 27: Illustration of shape taken by electron trajectories (a). Schematic of cylindrical irradiated volume (b). Spurs as bead on a string following electron trajectory spaced, on average, by mean free path (c).

Electrons lose energy in two predominant ways, via *Bremsstrahlung* and *collisions*. First, electrons lose energy due to Bremsstrahlung, or radiation released while the charge particle accelerates (slows down). The radiative stopping power, S_R , is the energy lost by an electron in this manner. Bremsstrahlung becomes the dominate form of energy loss above the critical energy, or the energy where radiative and collisional losses are equal. For water, the critical energy is 90.8MeV as seen in **Figure 28** showing stopping power data from the NIST ESTAR database [59]. Collisional stopping power, S_C , is the energy lost by electrons due to excitation and ionization processes as it passes through the medium. This is the dominant form of energy loss for the low acceleration voltages seen in electron microscopy. Lastly, for completeness, the total stopping power is the sum of all forms of stopping power,

$$S_{Total} = \frac{dE}{ds} = S_R + S_C = \rho S, \quad (4.2)$$

and is often reported as the density-normalized stopping power, $S(MeV\ cm^2/g)$, which we will refer to simply as stopping power from here on.

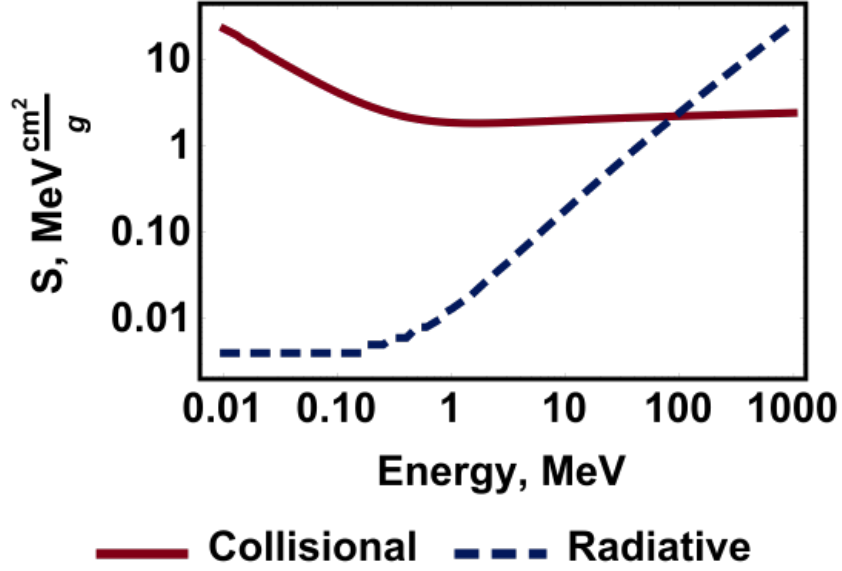


Figure 28: Collisional and Radiative Stopping Power for Electrons in Water.

In Liquid Cell Electron Microscopy we need to estimate the total energy deposited in the solvent, liquid water. We can use the stopping power to perform this approximation. The average energy lost (deposited in the surrounding media) by a single electron will be the product of the average energy loss per track length and the average distance travelled,

$$\langle dE_{e^-} \rangle = \frac{dE}{ds} \langle s \rangle \text{ (MeV)}, \quad (4.3)$$

where $\langle s \rangle$ is the average track length. The dose adsorbed by the water will be the energy deposited per mass, or,

$$[dose_{e^-}] = \frac{\frac{dE}{ds} \langle s \rangle}{\rho V_I} \text{ (MeV/g electron)}, \quad (4.4)$$

where ρ is density and V_I is the irradiated volume. Notice that this is really the stopping power over the volume. By substituting **Equation (4.2)** we get the dose of

a single electron to be

$$[dose_{e-}] = \frac{S_{Total} \langle s \rangle}{V_I} (MeV/g \text{ electron}). \quad (4.5)$$

To retrieve the dose rate for an electron beam, we break the volume up into the product of irradiated area, A_I (cm^2) and sample thickness, t , and multiply by the number of electrons per second, J , to obtain the dose rate, ψ ,

$$\psi = \frac{S \langle s \rangle}{A_I t} J (MeV/g \text{ s}). \quad (4.6)$$

Next, we convert into the proper units for dose rate of Gy/s , replace the irradiated area with an assumed circular beam geometry measured in m^2 instead of cm^2 , and convert the electron flow into beam current, $I(C/s)$. This results in a multiplicative factor of 10^5 ($m^2 \text{ electron Gy g/cm}^2 \text{ MeV C}$) and the dose rate given by microscope parameters as

$$\psi = \frac{10^5 S \langle s \rangle}{\pi a^2 t} I (Gy/s), \quad (4.7)$$

where a is the beam radius.

In the limit a thin sample, the average path length is assumed to be equal to the sample thickness, retrieving the expression from Grogan et. al. [8] of

$$\psi = \frac{10^5 S I}{\pi a^2} (Gy/s). \quad (4.8)$$

For a 300kV beam of $1 \mu m$ radius and $1 nA$ current, **Equation (4.8)** gives a dose rate of 7.5×10^7 (Gy/s), a value many orders of magnitude higher than ranges studied in medical physics and nuclear reactor design (10^{-2} to 10^3 Gy/s). In this estimate,

a thin sample is defined in relation to the mean free path of the incident particle in the particular material. LaVerne and Pimblott [60] report the mean-free-path of electrons in water. Their results are reproduced in **Figure 29**. Common electron acceleration voltages in the (S)TEM range from 10kV to 300kV, which have mean free paths on the order of 10's to 100's of nanometers. For example, the mean free path lengths for 20kV, 30kV and 300kV are 45.4 *nm*, 62.6 *nm* and 267.2 *nm*, respectively. A consequence of these mean free path lengths is that spurs will form along the electron trajectory like beads on a string as illustrated in **Figure 27c**. It is also important to note that the mean free path is much shorter than the range of electrons in water. When compared to the thickness of the sample of a few hundred nanometers, the estimation in **Equation (4.8)** is nearly valid. However, it is important to include the path lengthening multiple scattering that occurs at low acceleration voltages and in thicker samples to increase the accuracy of predictions.

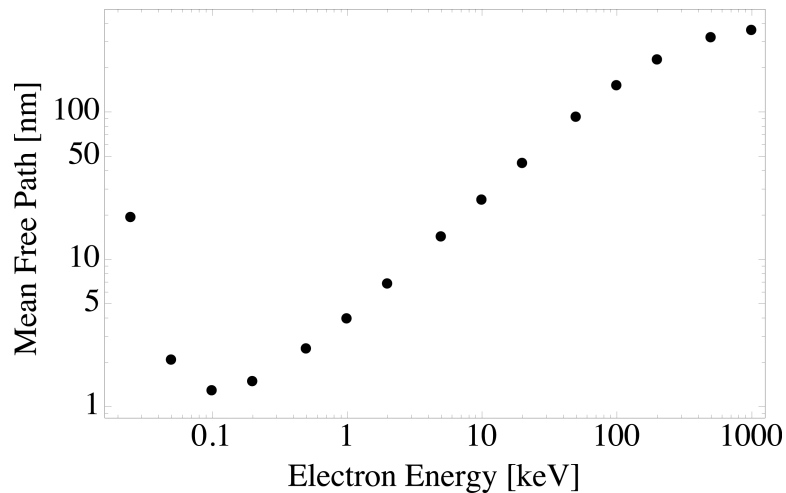


Figure 29: Electron Mean Free Path in Water. Produce from data presented in LaVerne and Pimblott.

Many researchers have considered the problem of multiple scattering in thin foils [61, 62]. In the limit where the total range R of an incident electron is much greater than the foil thickness t , the average path length $\langle s \rangle$ can be accurately estimated by

the first order approximation [62]

$$\langle s \rangle = t \left(1 + \frac{t}{\lambda} \right) (m), \quad (4.9)$$

where λ is the mean free path of the incident electron in the media being transversed and is a function of beam energy. Higher order corrections can be made when the sample thickness approaches the total range. In Liquid Cell Electron Microscopy, the layer thicknesses often range from 100's of nanometers to a few micron, and the ranges for electrons of acceleration voltages 20kV, 30kV and 300kV are, respectively, $9 \mu m$, $18 \mu m$ and $842 \mu m$, in liquid water [60]. The thinness of the sample compared to the range of electrons implies **Equation (4.9)** provides an appropriate estimation of the average path length through samples used in Liquid Cell Electron Microscopy.

We can divide **Equation (4.9)** by the device thickness to get the factor by which the electron track is extended due to multiple scattering events

$$\frac{\langle s \rangle}{t} = \left(1 + \frac{t}{\lambda} \right). \quad (4.10)$$

By substituting **Equation (4.10)** into **Equation (4.7)**, the first order estimate of dose rate becomes

$$\psi = \frac{10^5 SI}{\pi a^2} \left(1 + \frac{t}{\lambda} \right) (Gy/s), \quad (4.11)$$

which now accounts the effect of scattering on the average path taken by an electron (and the consequentially deposited energy). For a typical TEM experiment, where the beam is operated at 300kV and the liquid thickness is 100 nm , **Equation (4.11)** would estimate a dose rate of 1.4 times greater than the zeroth order estimate of

Equation (4.7). However, when the sample is $1\ \mu\text{m}$ thick, the first order dose rate would now be 4.8 times greater. Meaning, the thickness of the sample plays a strong role in the energy deposition process.

Additionally, surfaces within the liquid cell will locally alter the dose rate. Window material can cause scattering events and the emission of secondary electrons that increase the local dose rate. Since the range of these low energy electrons is extremely short, this effect will be limited to a region within a few nanometers of the surface itself. The same will be true for electrode materials. The extent of these effects on dose rate change can be investigated via electron trajectory simulation softwares such as CASINO [63].

4.2.1. Obtaining Dose Rate from Electron Trajectory Simulations

Driven by the need for more quantitative understanding of EM results coupled with the availability of computations power, researchers have developed open source softwares to simulate the passage of high energy electrons through materials [63–68]. The simulation calculates the energy lost by each electron as it passes through the material, or, conversely, the energy adsorbed by the medium. This energy is our dose [rate]. We can employ these simulations in order to check under which conditions the assumption made in our dose rate calculation are valid. Further, these softwares allow for multiple materials and geometries, so we can account for the nitride windows in addition to accounting for the thickness of the water layer - giving more accurate predictions of the behavior of the real system.

We consider a simple geometry as an example to understand the spatial dose rate. **Figure 30a** shows a nominal liquid cell composition with a $200\ \text{nm}$ thick water layer sandwiched between $50\ \text{nm}$ silicon nitride windows. Using the Casino software

v2.42 [63], we implement this geometry and subject it to a 5 nm radius electron beam at 30kV. We simulate 6241 electron trajectories and show the resulting screen shot in **Figure 30b**. These conditions are akin to a 1 nA beam irradiating for 1 μs, which represents realistic values for a STEM beam current and dwell time. The software is very robust and can be used with a wide array of parameters employed during liquid cell electron microscopy. **Figure 30b** shows that at lower acceleration voltage the beam experiences broadening by the time it reaches the bottom of this thin device, which will have implications for both radiolysis and the obtainable resolution. This phenomena will be more pronounced as the liquid layer thickness increases and should be considered.

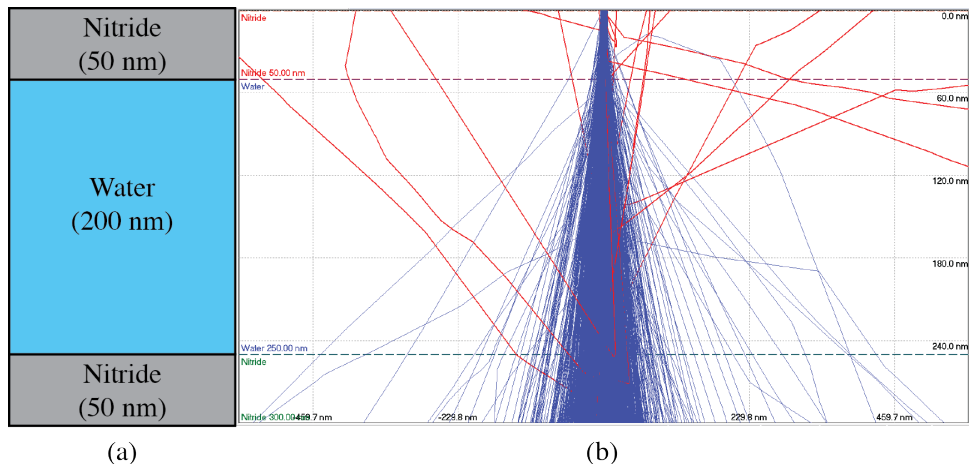


Figure 30: Electron trajectory simulation for nominal liquid cell with 200 nm of water sandwiched between two 50 nm silicon nitride windows illustrated in (a) and the resulting trajectories from Casino software (b).

The next step is use the extracted dose or energy adsorbed by the material and convert it to a dose rate. The software exports the energy adsorbed in keV per simulated volume whose geometry is defined by the user. Using the geometry and the desired beam current, calculating the dose rate from the extracted energy density distribution is a straight forward problem. The dose rate at the point (x, y, z) is given

by

$$\psi(x, y, z) = \frac{e^2 n_e}{IV_{\text{voxel}}} \text{EnergyDensity}(x, y, z) (\text{Gy/s}) \quad (4.12)$$

where e is the elementary charge, n_e is the number of simulated electrons, V_{voxel} is the simulated volume element, and the $\text{EnergyDensity}(x, y, z)$ is the energy density distribution at the discrete point (x, y, z) . This is a spatially varying dose rate that will be more accurate than the previous estimations of ψ . For the conditions simulated in **Figure 30** and taking the projection in the xz -plane, we obtain the spatial dose rate distribution shown in **Figure 31**. There are some interesting facets to these results. Mainly, the localization of high dose rates at interfaces (Nitride/Water) as this will be very important in nucleation and growth observations. Second, we notice that the dose rate is distributed over a geometry that is not the explicit cylinder that we assume in the theoretical estimate. The consequence of this is that there are actually gradients in the dose rate. The total dose rate, calculated with the total energy loss of all electrons simulated, is on the same order of magnitude as the dose rate obtained with **Equation (4.8)**.

4.3. Electron Beam Heating

4.3.1. Calculating of Heating Profiles

Energy deposited into the sample from the electron beam will result in heating. The amount of heating during liquid cell experiments has been investigated and found to be small in typical TEM liquid cells [8, 69] and is included here for completeness. However, thermally isolated samples can still experience significant heating. To estimate the heating, the volumetric rate of energy deposited in the sample is given

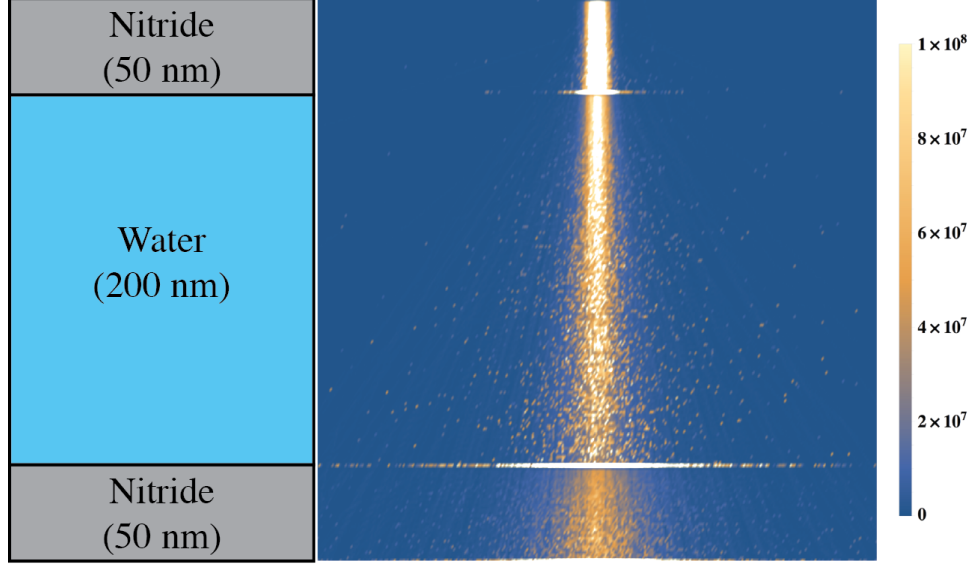


Figure 31: Spatial dose rate (Gy/s) as calculated using electron energy loss and simulation parameters from Casino software.

by

$$q = 10^3 \rho \psi \left(\frac{W}{m^3} \right), \quad (4.13)$$

where ρ is the density, $10^3 (cm^3 J/g m^3 Gy)$ accounts for unit conversions, and Φ is the dose rate as given by **Equation (4.7)** or **(4.11)**. In order to estimate the rise in temperature in the sample due to the beam, we must balance heat generation with conduction away from the beam region [8, 69, 70].

For simplicity, the heat transfer is modeled in one-dimension. The irradiated domain is a cylindrical volume of radius a subject to uniform heat generation q given by **Equation (4.13)** [8]. Radiation heat transfer is neglected as conduction is always the dominant means of heat transfer. Furthermore, we assume that the surfaces in contact with the vacuum environment of the microscope act as insulators and that there are no significant temperature variations in the vertical direction (conduction/convection and radiation heat transfer through the vacuum is small). By considering the case

where the beam is centered in the window region we retrieve the maximum temperature rise. This is a consequence of the center of the window experiencing the highest thermal resistance as is the furthest away from the bulk silicon and holder, and thus the greatest thermal resistance for conduction. The silicon chip used in most liquid cells acts as an effective heat sink due to the high thermal conductivity of silicon, its relatively large thermal mass, and its thermal connection to the holder. This leads to a constant temperature assumption for the boundary condition at the silicon (T_0 at $r = L$).

The temperature rise can be found by solving the dimensionless heat equation,

$$\begin{aligned} \frac{\partial \tilde{\theta}}{\partial \tilde{t}} - \nabla^2 \tilde{\theta} &= 1 \quad (\text{inside beam, } 0 \leq \tilde{r} \leq 1) \\ \frac{\partial \tilde{\theta}}{\partial \tilde{t}} - \nabla^2 \tilde{\theta} &= 0 \quad (\text{outside beam, } 1 < \tilde{r}). \end{aligned} \tag{4.14}$$

Quantities with a tilde are dimensionless while plain letters represent dimensional quantities. In **Equation (4.14)**, temperature rise ($T - T_0$) is scaled by $a^2 q 10^{-6} / \alpha_{th} C_p \rho$ to get dimensionless temperature rise $\tilde{\theta}$, where C_p is the specific heat at constant pressure, α_{th} is the thermal diffusivity of water, and 10^{-6} (m^3/cm^3) accounts for unit conversions to express ρ in g/cm^3 . Length is scaled by the beam radius a and time is normalized by the diffusive time a^2/α_{th} . The boundary conditions include symmetry at the origin ($r = 0$), and the constant temperature at the silicon $\tilde{\theta}(\tilde{L}, \tilde{t}) = 0$. We also assume the initial temperature to be equal to the ambient temperature, $\tilde{\theta}(\tilde{r}, 0) = 0$. Temperature throughout the system will evolve until a maximum is reached when the system has established a steady-state ($\tilde{t} \rightarrow \infty$). An analytical expression for the steady-state temperature profile can readily be obtained in dimensionless form both

inside and outside the irradiated region [8] as

$$\begin{aligned}\tilde{\theta}_{SS} &= \frac{1}{4} (1 - \tilde{r}^2) + \frac{1}{2} \ln [\tilde{L}] & (0 \leq \tilde{r} \leq 1) \\ \tilde{\theta}_{SS} &= \frac{1}{2} \ln \left[\frac{\tilde{L}}{\tilde{r}} \right] & (0 \leq \tilde{r} \leq \tilde{L})\end{aligned}\quad (4.15)$$

The maximum temperature rise will be at the beam's center, and is given, now in dimensional form, as a function of dose rate by substituting **Equation (4.13)** into the dimensional form of **Equation (4.15)** and setting $r = 0$

$$\Delta T_{max} = \frac{a^2 10^{-3}}{\alpha_{th} C_p} \psi \left(\frac{1}{4} + \frac{1}{2} \ln \left[\frac{L}{a} \right] \right). \quad (4.16)$$

4.3.2. Effect of Beam Current and Sample Thickness

The maximum change in temperature given in **Equation (4.16)** is a linear function of dose rate. By substituting **Equation (4.8)** or **(4.11)** for the dose rate, we retrieve an expression for temperature rise as a function of material and microscope parameters:

$$\Delta T_{max} = \frac{S 10^2}{\pi \alpha_{th} C_p} \left(1 + \frac{t}{\lambda} \right) \left(\frac{1}{4} + \frac{1}{2} \ln \left[\frac{L}{a} \right] \right). \quad (4.17)$$

where 10^2 ($m^2 \text{ electron } J/cm^2 \text{ MeV } C$) accounts for unit conversions. **Equation (4.17)** is a linear function of beam current I and the liquid thickness, t . The temperature rise, however, will have a non-linear relationship with beam energy and beam radius. The temperature rise, ΔT_{max} , is shown in the contour plot **Figure 32** as a function of beam current and beam radius in the case of a thin sample ($t/\lambda \rightarrow 0$) for the acceleration voltages of 300kV and 30kV. We take $L = \frac{2}{\sqrt{\pi}} 50 \times 10^{-6} \text{ m}$, $\alpha_{th} = 1.4 \times 10^{-7} \text{ m}^2/s$, and $C_p = 4.18 \text{ J/g} - K$. Under typical TEM conditions,

the temperature rise will only be a few °C, but can be much greater for low energy focused beams, such as a stationary STEM beam at 30kV with beam currents on the order of a few tens of nA. The temperature increase calculated here is to be an overestimate of the true heating as we neglect heat transfer through the membrane, which, for silicon nitride, has a thermal conductivity greater than water.

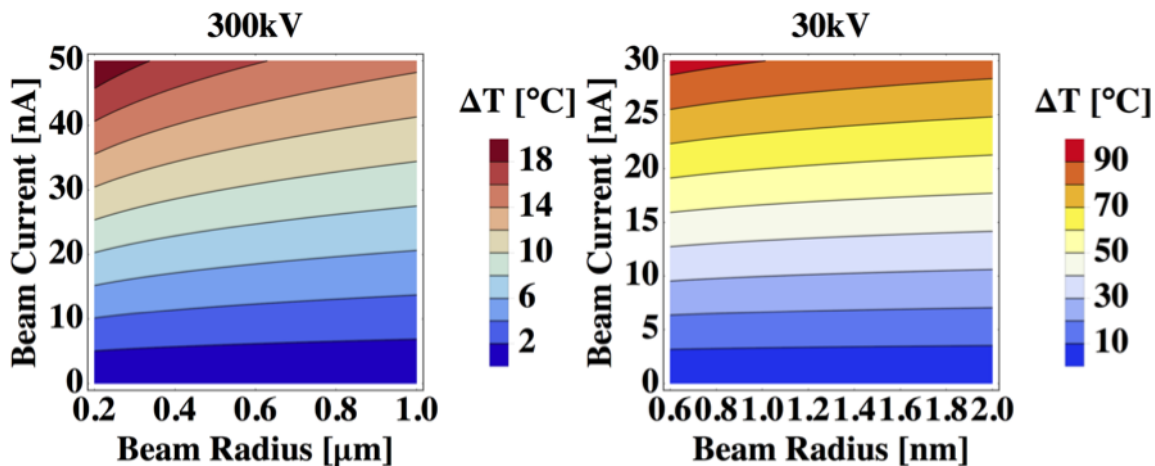


Figure 32: Estimated temperature rise in a water layer as functions of beam radius and beam current due to electron beam-induced heating under typical TEM (left) and lower acceleration voltage STEM (right).

4.4. Introduction to the Radiation Chemistry of Water

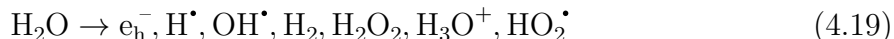
4.4.1. Energy transfer and short and long time kinetics

Shortly after an energy deposition event (10 ps) by incident electrons, individual ionized water molecules and their ejected electrons decompose surrounding water molecules into radical and molecular species, including hydrated (solvated) electrons e_{h}^- , hydrogen radical H^\bullet , hydroxyl radical OH^\bullet , and H_2 . The energy loss per collision is proportional to the stopping power (S_{Total}), the inelastic cross section (σ), and the

atomic number density (N) as

$$E_{collision} = \frac{S_{Total}}{N\sigma}, \quad (4.18)$$

which, for typical beam conditions, gives an energy deposition on the order of 20 eV, allowing the formation of highly reactive radicals. The short lived radical species are highly reactive and quickly interact with the surrounding media. The most reactive species, the hydrated electron, is a free electron surrounded by a cage of water molecules. These reaction products, known as the *initial yield*, are concentrated inhomogeneously along the track of the ionizing radiation in discrete volumes, called spurs [5, 8, 71–77]. As the spur evolves in short times ($< 1 \mu s$) the species participate in further reactions and diffusion to yield the primary products: [5, 6, 71, 73–78]



About $1 \mu s$ after the energy transfer event, the primary species are assumed to be uniformly distributed within the irradiated region [5]. The rate of generation (or destruction) of the primary products at this time is given as a constant called the G-value, first introduced by Burton in 1947 [79]. The G-value is defined as the number of molecules created or destroyed per 100eV of energy deposited. The G-values for a particular media depend on the type of radiation (electrons, heavy ions, gamma rays, etc.), its energy, and solution composition. G-values have been computed and measured for a variety of systems [4, 5, 77]. G-values can be experimentally measured by monitoring the absorption bands associated with a particular species generated during ionization. Since the production of all species is coupled, the addition of scavengers (additives known to quickly consume a particular species) to the solution is exploited as a means to decouple production of individual components. For sufficiently

low dose rate, the energy transfer is linear and reported G-values for LET (linear energy transfer) radiation are a good measure of the production rates [5, 8]. At higher dose rates, the spurs, which can be assumed to be spheres that form along the path of ionizing radiation like beads on a string, will begin to overlap. The overlap leads to an increase in the likelihood that radical species react to form the more stable molecular species (H_2 , O_2 , H_2O_2 , and recombined H_2O). The number of spurs produced during time T is given by

$$n_{spur} = \frac{tIT}{\lambda e}, \quad (4.20)$$

where e is the fundamental charge. The average volume containing a single spur is simply the irradiated volume divided by the number of spurs, or $\pi a^2 \lambda e / IT$. Assuming each volume is spherical, the average distance between spur centers is given by [8]

$$d_{spur} = \left(\frac{6e\lambda a^2}{IT} \right)^{1/3}. \quad (4.21)$$

In reality, spurs have Gaussian concentration profiles of the radiolytic products with variance σ_{spur}^2 . For most species in water, $\sigma_{spur} \sim 1.2 \text{ nm}$ [80]. In order to ensure there is no spur overlap, the average distance between spurs should be greater than $5\sigma_{spur}$, or $d_{spur} \leq 6 \text{ nm}$ [8]. The time of interest is the lifetime of a spur of $\sim 1 \mu\text{s}$, and so **Equation (4.21)** can be used to identify when spur overlap is likely given the proposed criteria. In the case of a rastering beam, such as in STEM, the average distance between spur centers is given by [8]

$$d_{spur,Rastering} = \left(\frac{12e\lambda av}{\pi I} \right)^{1/3}, \quad (4.22)$$

where v is the beam rastering velocity. Spur overlap should be considered when modeling radiolysis during liquid cell electron microscopy, as it will have strong effects on the G-values.

As longer times are approached ($> 1 \mu s$), the primary products participate in a cascade of slower chemical reactions, creating additional species such as O_2 . At these longer times, it is necessary to consider large numbers of interrelated kinetic reactions to describe the underlying changes in solution chemistry. To account for the evolution of solution chemistry that occurs on the time scales associated with Liquid Cell Electron Microscopy (seconds to hours), a kinetic model with dozens of reactions are needed. For neat water alone, 79 kinetic reactions are used to model the complex chemistry occurring in the system system and the time evolution of the 16 species [5, 7, 71].

4.4.2. Formation, Diffusion, and Consumption Rates of Radiolysis Species

Rate equations are constructed from the kinetic model and implemented in conservation of mass in order to obtain a reaction diffusion equation for each species. As long as the dominate reactions and their associated rates are known for an irradiated system, a balanced kinetic model can be formed, making simulation possible. The coupled equations, when solved, give the concentration fields of the various species as functions of space (\vec{x}) and time (t). The evolution of the concentration $C_i(\vec{x}, t)$ of species i is described by:

$$\frac{\partial C_i}{\partial t} = D_i \nabla^2 C_i - \sum_j k_{ij} C_i C_j + \sum_{j,k \neq i} k_{jk} C_j C_k + R_i \quad (4.23)$$

where the first term on the RHS represents diffusion and D_i is the diffusivity of species i in water. The second and third terms represent destruction and production

of species i through chemical reactions, respectively, and k_{ij} is the associated reaction rate constants. The last term,

$$R_i = \frac{\rho\psi G_i}{F} (M/s) \quad (4.24)$$

is the volumetric production rate of species i due to irradiation in the region illuminated by the beam. G_i is non-zero only for the primary products within the irradiated region. In **Equation (4.24)**, ρ is the media density (g/cm^3), F is the Faraday constant, and ψ is the dose rate given by **Equation (4.8)** or **(4.11)**.

To complete the model, initial and boundary conditions must be prescribed. Prior to exposure, the initial concentration of any species is uniform throughout the domain,

$$C_i(\vec{x}, 0) = C_{i,0} \quad (4.25)$$

When carrying out calculations for neat water, $C_i(\vec{x}, 0) = 0$ for all species other than H_2O , H^+ , and OH^- . When considering aerated solutions, we also have $C_{O_2}(\vec{x}, 0) > 0$ to represent the initial oxygen concentration. Nominally, we have initial conditions $C_{H_2O}(\vec{x}, 0) = 55.56 (M)$ and $C_{H^+}(\vec{x}, 0) = C_{OH^-}(\vec{x}, 0) = 10^{-7} M$ for neat water. For solutions that are not deaerated prior to use, we also have the saturation concentration of oxygen as calculated with a Henry's Law constant of $0.0013 \text{ mol/kg} - \text{bar}$ [81] is $255 \mu M$.

To the first order of approximation, we assume that all confining surfaces are chemically inert and, therefore, impermeable to all species, i.e.,

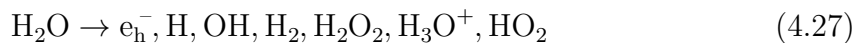
$$\nabla C_i \cdot \hat{n}|_{wall} = 0 \quad (4.26)$$

where \hat{n} is a unit vector normal to the surface.

4.5. Kinetic Model

To compute the concentrations of radiolysis products of water, we use the kinetic model of Elliot and McCracken [71]. This model accounts for the primary products (e_h^- , H, OH, H₂, H₂O₂, H₃O⁺, HO₂) through the G-values and the long-time kinetic reactions through conservation of mass for each species, accounting for production.

Table 1 lists the 79 reactions and rate constants included in our model. Reaction 1,

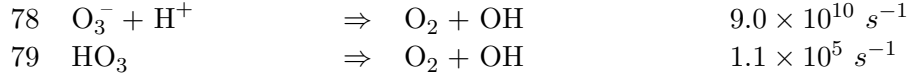


describes the production of the primary products with the rates defined by **Equation (4.24)**. Rate constants for these and additional reactions can be found in NIST Solution Kinetics database [82].

Table 1: Water Radiolysis Kinetic Model

Formation Reactions			
1	H_2O	\Rightarrow	$e_{\text{h}}^-, \text{H}, \text{OH}, \text{H}_2, \text{H}_2\text{O}_2, \text{HO}_2$
Equilibria Reactions			pK_a
2	H_2O	\Leftrightarrow	$\text{H}^+ + \text{OH}^-$ 13.999
3	H_2O_2	\Leftrightarrow	$\text{H}^+ + \text{HO}_2^-$ 11.65
4	OH	\Leftrightarrow	$\text{H}^+ + \text{O}^-$ 11.9
5	HO_2	\Leftrightarrow	$\text{H}^+ + \text{O}_2^-$ 4.57
6	H	\Leftrightarrow	$\text{H}^+ + e_{\text{h}}^-$ 9.77
Chemical Reactions			Rate Constant ($M^{-1}s^{-1}$ unless specified)
7	$\text{H}^+ + \text{OH}^-$	\Rightarrow	H_2O 1.4×10^{11}
8	H_2O	\Rightarrow	$\text{H}^+ + \text{OH}^-$ $k_7 \times \frac{K_2}{[\text{H}_2\text{O}]} s^{-1}$
9	H_2O_2	\Rightarrow	$\text{H}^+ + \text{HO}_2^-$ $k_{10} \times K_3 s^{-1}$
10	$\text{H}^+ + \text{HO}_2^-$	\Rightarrow	H_2O_2 5.0×10^{10}
11	$\text{H}_2\text{O}_2 + \text{OH}^-$	\Rightarrow	$\text{HO}_2^- + \text{H}_2\text{O}$ 1.3×10^{10}
12	$\text{HO}_2^- + \text{H}_2\text{O}$	\Rightarrow	$\text{H}_2\text{O}_2 + \text{OH}^-$ $k_{11} \times \frac{K_2}{K_3 \times [\text{H}_2\text{O}]}$
13	$e_{\text{h}}^- + \text{H}_2\text{O}$	\Rightarrow	$\text{H} + \text{OH}^-$ 1.9×10^1
14	$\text{H} + \text{OH}^-$	\Rightarrow	$e_{\text{h}}^- + \text{H}_2\text{O}$ 2.2×10^7
15	H	\Rightarrow	$e_{\text{h}}^- + \text{H}^+$ $k_{16} \times K_6 s^{-1}$
16	$e_{\text{h}}^- + \text{H}^+$	\Rightarrow	H 2.3×10^{10}
17	$\text{OH} + \text{OH}^-$	\Rightarrow	$\text{O}^- + \text{H}_2\text{O}$ 1.3×10^{10}
18	$\text{O}^- + \text{H}_2\text{O}$	\Rightarrow	$\text{OH} + \text{OH}^-$ $k_{17} \times \frac{K_2}{K_4 \times [\text{H}_2\text{O}]}$
19	OH	\Rightarrow	$\text{O}^- + \text{H}^+$ $k_{20} \times K_4 s^{-1}$
20	$\text{O}^- + \text{H}^+$	\Rightarrow	OH 1.0×10^{11}
21	HO_2	\Rightarrow	$\text{O}_2^- + \text{H}^+$ $k_{22} \times K_5 s^{-1}$
22	$\text{O}_2^- + \text{H}^+$	\Rightarrow	HO_2 5.0×10^{10}
23	$\text{HO}_2 + \text{OH}^-$	\Rightarrow	$\text{O}_2^- + \text{H}_2\text{O}$ 5.0×10^{10}
24	$\text{O}_2^- + \text{H}_2\text{O}$	\Rightarrow	$\text{HO}_2 + \text{OH}^-$ $k_{23} \times \frac{K_2}{K_5 \times [\text{H}_2\text{O}]}$
25	$e_{\text{h}}^- + \text{OH}$	\Rightarrow	OH^- 3.0×10^{10}
26	$e_{\text{h}}^- + \text{H}_2\text{O}_2$	\Rightarrow	$\text{OH} + \text{OH}^-$ 1.1×10^{10}
27	$e_{\text{h}}^- + \text{O}_2^+ \text{H}_2\text{O}$	\Rightarrow	$\text{HO}_2^- + \text{OH}^-$ $1.3 \times 10^{10} / [\text{H}_2\text{O}] M^{-2}s^{-1}$
28	$e_{\text{h}}^- + \text{HO}_2$	\Rightarrow	HO_2^- 2.0×10^{10}
29	$e_{\text{h}}^- + \text{O}_2$	\Rightarrow	O_2^- 1.9×10^{10}
30	$e_{\text{h}}^- + e_{\text{h}}^- + 2\text{H}_2\text{O}$	\Rightarrow	$\text{H}_2 + {}_2\text{OH}^-$ $5.5 \times 10^9 / [\text{H}_2\text{O}]^2 M^{-3}s^{-1}$
31	$e_{\text{h}}^- + \text{H} + \text{H}_2\text{O}$	\Rightarrow	$\text{H}_2 + \text{OH}^-$ $2.5 \times 10^{10} / [\text{H}_2\text{O}] M^{-2}s^{-1}$
32	$e_{\text{h}}^- + \text{HO}_2^-$	\Rightarrow	$\text{O}^- + \text{OH}^-$ 3.5×10^9
33	$e_{\text{h}}^- + \text{O}^- + \text{H}_2\text{O}$	\Rightarrow	$\text{H}_2 + {}_2\text{OH}^-$ $2.2 \times 10^{10} / [\text{H}_2\text{O}] M^{-2}s^{-1}$
34	$e_{\text{h}}^- + \text{O}_3^- + \text{H}_2\text{O}$	\Rightarrow	$\text{O}_2 + \text{OH}^- + \text{OH}^-$ $1.6 \times 10^{10} / [\text{H}_2\text{O}] M^{-2}s^{-1}$

35	$e_h^- + O_3$	\Rightarrow	O_3^-	3.6×10^{10}
36	$H + H_2O$	\Rightarrow	$H_2 + OH$	1.1×10^1
37	$H + O^-$	\Rightarrow	OH^-	1.0×10^{10}
38	$H + HO_2^-$	\Rightarrow	$OH + OH^-$	9.0×10^7
39	$H + O_3^-$	\Rightarrow	$O_2 + OH^-$	1.0×10^{10}
40	$H + H$	\Rightarrow	H_2	7.8×10^9
41	$H + OH$	\Rightarrow	H_2O	7.0×10^9
42	$H + H_2O_2$	\Rightarrow	$H_2O + OH$	9.0×10^7
43	$H + O_2$	\Rightarrow	HO_2	2.1×10^{10}
44	$H + HO_2$	\Rightarrow	H_2O_2	1.8×10^{10}
45	$H + O_2^-$	\Rightarrow	HO_2^-	1.8×10^{10}
46	$H + O_3$	\Rightarrow	HO_3	3.8×10^{10}
47	$OH + OH$	\Rightarrow	H_2O_2	3.6×10^9
48	$OH + HO_2$	\Rightarrow	$H_2O + O_2$	6.0×10^9
49	$OH + O_2^-$	\Rightarrow	$OH^- + O_2$	8.2×10^9
50	$OH + H_2$	\Rightarrow	$H + H_2O$	4.3×10^7
51	$OH + H_2O_2$	\Rightarrow	$HO_2 + H_2O$	2.7×10^7
52	$OH + O^-$	\Rightarrow	HO_2^-	2.5×10^{10}
53	$OH + HO_2^-$	\Rightarrow	$HO_2 + OH^-$	7.5×10^9
54	$OH + O_3^-$	\Rightarrow	$O_3 + OH^-$	2.6×10^9
55	$OH + O_3^-$	\Rightarrow	$O_2^- + O_2^- + OH^-$	6.0×10^9
56	$OH + O_3$	\Rightarrow	$HO_2 + O_2$	1.1×10^8
57	$HO_2 + O_2^-$	\Rightarrow	$HO_2^- + O_2$	8.0×10^7
58	$HO_2 + HO_2$	\Rightarrow	$H_2O_2^- + O_2$	7.0×10^5
59	$HO_2 + O^-$	\Rightarrow	$O_2 + OH^-$	6.0×10^9
60	$HO_2 + H_2O_2$	\Rightarrow	$OH + O_2 + H_2O$	5.0×10^{-1}
61	$HO_2 + HO_2^-$	\Rightarrow	$OH + O_2 + OH^-$	5.0×10^{-1}
62	$HO_2 + O_3^-$	\Rightarrow	$O_2 + O_2 + OH^-$	6.0×10^9
63	$HO_2 + O_3$	\Rightarrow	$HO_3 + O_2$	5.0×10^8
64	$O_2^- + O_2^- + 2H_2O$	\Rightarrow	$H_2O_2 + O_2 + {}_2OH^-$	$1.0 \times 10^2/[H_2O]^2 M^{-3}s^{-1}$
65	$O_2^- + O^- + H_2O$	\Rightarrow	$O_2 + {}_2OH^-$	$6.0 \times 10^8/[H_2O] M^{-2}s^{-1}$
66	$O_2^- + H_2O_2$	\Rightarrow	$OH + O_2 + OH^-$	1.3×10^{-1}
67	$O_2^- + HO_2^-$	\Rightarrow	$O^- + O_2 + OH^-$	1.3×10^{-1}
68	$O_2^- + O_3^- + H_2O$	\Rightarrow	$O_2 + O_2 + 2OH^-$	$1.3 \times 10^{-1}/[H_2O] M^{-2}s^{-1}$
69	$O_2^- + O_3$	\Rightarrow	$O_3^- + O_2$	1.5×10^9
70	$O^- + O^- + H_2O$	\Rightarrow	$HO_2^- + OH^-$	$1.0 \times 10^9/[H_2O] M^{-2}s^{-1}$
71	$O^- + O_2$	\Rightarrow	O_3^-	3.6×10^9
72	$O^- + H_2$	\Rightarrow	$H + OH^-$	8.0×10^7
73	$O^- + H_2O_2$	\Rightarrow	$O_3^- + O_2$	5.0×10^8
74	$O^- + HO_2^-$	\Rightarrow	$O_2^- + OH^-$	4.0×10^8
75	$O^- + O_3^-$	\Rightarrow	$O_2^- + O_2^-$	7.0×10^8
76	$O^- + O_3$	\Rightarrow	$O_2^- + O_2$	5.0×10^9
77	O_3^-	\Rightarrow	$O_2 + O^-$	3.3×10^3



4.5.1. G-Values

The formation reactions require G-values for each of the primary products. The G-values used during simulations were obtained from Hill and Smith's results for high energy electrons in water [77]. Since G-values are not independent (as we need to satisfy conservation of mass during the reactions) and occasionally G-values had to be obtained from graphs, it is important to make sure that the values are self-consistent. The consistency of G-Values was checked by carrying out atomic balances for both the hydrogen and oxygen atoms produced from water destruction. The hydrogen atomic balance yields

$$-G_{\text{H}_2\text{O}} = 0.5 (G_{\text{H}} + 2G_{\text{H}_2} + G_{\text{OH}} + 2G_{\text{H}_2\text{O}_2} + G_{\text{HO}_2} + G_{\text{H}^+} + G_{\text{OH}^-}), \quad (4.28)$$

and the oxygen balance gives

$$-G_{\text{H}_2\text{O}} = G_{\text{OH}} + 2G_{\text{H}_2\text{O}_2} + 2G_{\text{HO}_2} + G_{\text{OH}^-}. \quad (4.29)$$

In our code, we equated the RHS of **Equation (4.28)** and **(4.29)** to confirm that the G-values are consistent with the resulting atomic balance. For example, **Table 2** lists the G-values for 300kV electrons in liquid water taken from graphs in Hill and Smith [77]. The values listed in the table are consistent with **Equation (4.28)** and **Equation (4.29)**.

Table 2: G-Values for 300kV electrons in liquid water

Species	G-value [molecules/100eV]
e_h^-	3.47
H^\bullet	1.00
H_2	0.17
OH^\bullet	3.63
H_2O_2	0.47
HO_2^\bullet	0.08
H_3O^+	4.42
OH^-	0.95

Table 2: G-values [molecules/100eV] for primary products produced during water radiolysis. Values are obtained from Hill and Smith [77] for high energy electrons in water.

4.6. Implementation of Homogeneous Model

The kinetic reactions (**Table 1**) were modeled as a system of 16 coupled, ordinary differential equations in the form of **Equation (4.23)** without the diffusion term. These 16 equations were coded in Mathematica, MATLAB, and COMSOL and solved via the built in NDSolve function in Mathematica, ODE23 solver in MATLAB, and Paradiso solver in COMSOL. The reaction rates, dose rate, and initial conditions were appropriately defined in the code. All three codes yielded nearly identical results for identical conditions. Documented Mathematica and MATLAB source codes are available on the public source code repository GitHub [83].

4.7. Homogeneous Irradiation

If the entire liquid is irradiated homogeneously, there will be no spatial concentration gradients, and the diffusion term of **Equation (4.23)** will drop out. A situation

akin to graphene cells [84, 85] where small pockets of liquid are isolated between the two sandwiched graphene membranes. This leaves a set of 16 coupled ordinary differential equations (one for each species) when considering neat water. This system can readily be implemented in numerical solvers to obtain the temporal evolution of the solution composition. This implementation has been performed in Mathematica and MATLAB [7] and released as open source code available for download on GitHub [83].

Using these or similar implementations, the system of equations can be integrated numerically with the initial conditions $C_{\text{H}_2\text{O}}(t=0) = 55.56 \text{ (M)}$ and $C_{\text{H}^+}(0) = C_{\text{OH}^-}(0) = 10^{-7} \text{ M}$. The model uses G-values for high-energy electrons in neat water [77, 86] that are assumed, to the first order of approximation, to be independent of solution composition. The temporal evolution of a subset of species deemed most relevant to processes taking place during liquid cell electron microscopy are presented. The concentrations of all species can be obtained with the programs [83].

Figure 33 depicts the concentrations of e_{h}^- , H^\bullet , H_2 , H_2O_2 , OH^\bullet , and O_2 as functions of time. The simulation was carried out for the dose rate of $7.5 \times 10^7 \text{ (Gy/s)}$ associated with a 300kV beam of $1 \mu\text{m}$ radius and 1nA current according to **Equation (4.8)**. At time $t=0$ irradiation begins and is maintained continuously thereafter. Concentrations of H_2 , H_2O_2 , OH , and O_2 increase rapidly from zero to achieve steady state values within about 1 ms after the start of the irradiation. The concentrations of e_{h}^- and H^\bullet initially increase, peak, and then decline to their steady state values within the same time frame. A key result being that the system rapidly reaches a steady state, and the concentrations of the radiolysis products do not grow without bound. Reverse reactions convert radiolysis products back to water, enabling the establishment of this steady state.

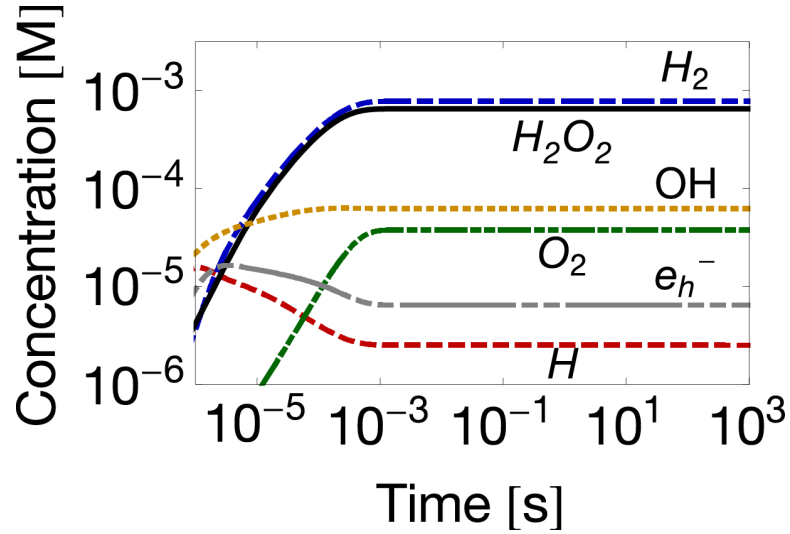


Figure 33: The concentrations of e_h^- , H^\bullet , H_2 , H_2O_2 , OH^\bullet , and O_2 as functions of time. Initially neat, deaerated water is irradiated continuously at a dose rate of 7.5×10^7 (Gy/s).

The calculation can be repeated for the range of dose rates typical in liquids cells and a steady state is always observed. Both the magnitude of the steady state concentration and the time that it takes to reach steady state depends, however, on the dose rate. **Figure 34** depicts the steady state concentrations of various species as functions of dose rate. The results of **Figures 33** and **34** suggest that the concentrations of radiolysis products as functions dose rate can be fit using power laws. For the dose rates commonly associated with liquid cell electron microscopy, the dependence of the steady state concentration on dose rate is approximated with a power law [7]

$$C_{SS,i} \sim \alpha_i \psi^{\beta_i} (M) \quad (10^6 < \psi < 10^{10} \text{Gy/s}). \quad (4.30)$$

Table 3 lists the values of α_i and β_i ($0.37 < \beta_i < 1.21$) obtained by fitting **Equation (4.30)** to the numerical results.

A time to steady state t_{ss} (ignoring initial fluctuations) is defined as the time needed for the concentration to achieve 95% of its steady state value, i.e., $\left[\frac{C_i(t_{ss}) - C_i(\infty)}{C_i(\infty)} \right] =$

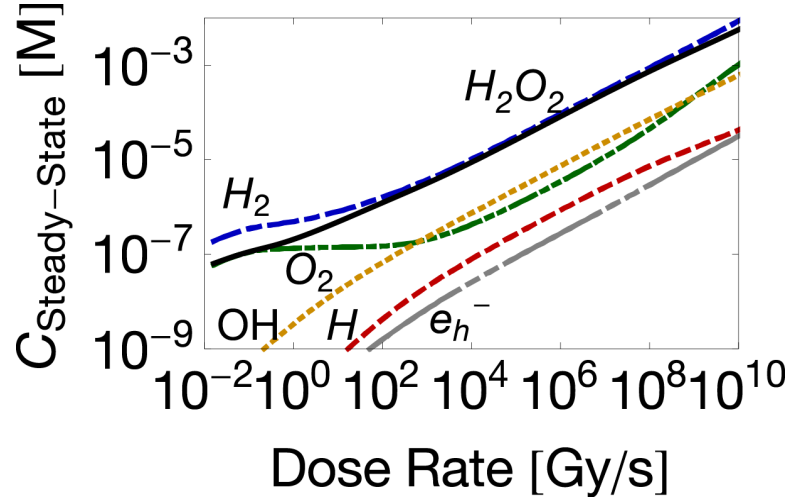


Figure 34: Steady state concentrations of e_h^- , H^\bullet , H_2 , H_2O_2 , OH^\bullet , and O_2 as functions of dose rate. De-aerated, neat water subjected continuous irradiation.

0.95. The dependence of t_{ss} on dose rate can also be approximated with a power law [7]

$$t_{SS,i} \sim a_i \psi^m (s) \quad (10^6 < \psi < 10^{10} Gy/s), \quad (4.31)$$

where the exponent $m = 0.50 \pm 0.01$ for all species. The coefficients a_i are of order 1 and are listed in **Table 3**. For a dose rate of $7.5 \times 10^7 (Gy/s)$, the time to steady state is on the order of 1 *ms* - a time scale much shorter than typical experiments. Due to the very high rate of energy deposition, the system is driven very quickly toward its steady state. In the case where diffusion is present, concentrations of all species will be on the same order as their long time value within this millisecond range, but the time it takes the entire system (including the non-irradiated volume) to reach a steady state will be dominated by the diffusion time as discussed in the next section.

Equation (4.30) and **Table 3** provide approximate estimates of the steady state concentrations of radiolysis products as functions of dose rate in the absence of diffusion and solutes. Concentrations of almost all radiolysis products increase sub-linearly ($\beta_i < 1$) with dose rate, and so, doubling the dose rate leads to less than a twofold

increase in concentration of most radiolysis products. Finally, the time it takes to establish a steady state in a continuously irradiated medium scales inversely as the dose rate to the power $\sim 1/2$, meaning that at the high dose rates common to electron microscopy ($10^6 - 10^{10} Gy/s$), the homogeneous system reaches steady state rapidly.

Table 3: Steady State Concentration Power Law Parameters

Species	Homogeneous			Heterogeneous		
	α_i	β_1	a_i	α_i	β_i	
e_h^-	2.49×10^{-10}	0.51	3.18	1.02×10^{-9}	0.50	
H^\bullet	6.31×10^{-9}	0.38	5.92	2.61×10^{-8}	0.33	
H_2	8.88×10^{-8}	0.50	3.55	1.88×10^{-7}	0.52	
H_2O_2	2.20×10^{-7}	0.44	3.16	4.43×10^{-7}	0.45	
HO_2^\bullet	2.39×10^{-11}	0.71	7.04	8.90×10^{-12}	0.85	
HO_2^-	4.34×10^{-12}	0.72	2.30	2.91×10^{-12}	0.85	
HO_3^\bullet	2.32×10^{-18}	1.21	4.43	4.53×10^{-19}	1.50	
H^+	2.07×10^{-9}	0.51	6.52	6.83×10^{-9}	0.48	
O_2	2.11×10^{-10}	0.67	6.99	2.54×10^{-10}	0.77	
O_2^-	8.21×10^{-10}	0.51	6.49	5.55×10^{-10}	0.63	
O_3^\bullet	7.96×10^{-16}	0.84	6.42	4.45×10^{-17}	1.17	
O_3^-	2.10×10^{-15}	0.83	5.72	1.77×10^{-16}	1.13	
OH^\bullet	1.45×10^{-8}	0.46	0.40	4.28×10^{-8}	0.46	
OH^-	1.20×10^{-8}	0.37	4.12	1.87×10^{-8}	0.43	
O^-	4.56×10^{-13}	0.69	4.67	1.87×10^{-13}	0.84	

Table 3: The coefficients α_i and β_i in the correlation for the steady state concentration $C_{SS,i} \sim \alpha_i \psi^{\beta_i}$ (M) of species i and the pre-factor a_i in the correlation $t_{SS,i} \sim a_i \psi^m$ for the time to steady state of species i for dose rates relevant to EM in the range from 10^6 to $10^{10} Gy/s$. In the case of the heterogeneous model, the concentrations are at the beam's center. The beam radius is $1 \mu m$ and the liquid cell's sidewalls are $50 \mu m$ away from the beam's center.

4.7.1. Code Verification

Comparison with Published Low Dose Rate Results

Data for the concentrations of radiolysis products at the high dose rates encountered in electron microscopy is not available. Instead, we reproduced the published data of Pastina and LaVerne [5] for low dose irradiation. In our simulations, we used the appropriate G-values for gamma radiation at the specified dose rate with the initial conditions prescribed in the reference. **Figure 35** depicts our computed concentrations of a few radiolysis products as functions of time when the dose rate is 0.25 Gy/s . **Figure 35** is qualitatively very similar to figure 1 of Pastina and LaVerne [5]. Steady state values obtained with our simulations agree within 20% with values in figures 1 and 2 of Pastina and LaVerne. The discrepancy may be due to the fact that data was not available in tabular form and was extracted from graphs.

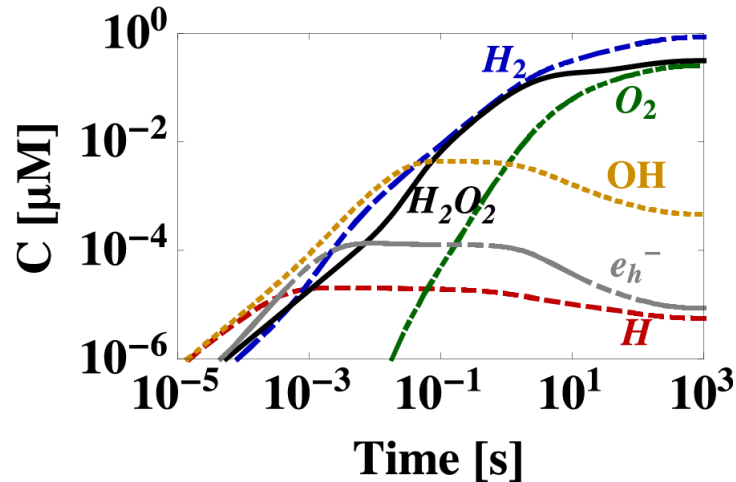


Figure 35: Temporal evolution of radiolysis products for γ radiolysis at 0.25 Gy/s of neat water.

Verification of the Constant Water Concentration Approximation

Next, we consider the assumption of constant water concentration. We use the homogeneous model to calculate water consumption when the water mass is allowed to vary. **Figure 36** depicts the percent water consumption as a function of dose rate compared to the initial neat water concentration of 55.56 M . The data is correlated with a power law of the form $4.55 \times 10^{-7} \psi^{0.48}$ (%). In the range of dose rates expected in liquid cell electron microscopy, water remains well within 1% of its initial concentration. For example, at the extremely high dose rate of 10^{13} Gy/s , ~ 0.8 % of the water molecules are consumed.

When comparing predictions of non-water species concentrations from a model that accounts for water consumption to the predictions of a model that assumes a fixed water concentration, we find the average percent difference of the steady state concentrations (amongst all non-water species) to be 5×10^{-6} % with a standard deviation of 7.0×10^{-6} %. These simulations were carried out with the homogeneous model at the high dose rate of 10^{13} Gy/s . The small percent differences imply that the approximation that the water mass remains constant is applicable.

Comparing Numerical Solvers

The three numerical solvers were compared to check for consistency. We examined the average deviation among each codes' predictions for all 16 species, and focused on H_2 and O_3^- in particular. The discrepancies among various codes' predictions were the largest at the highest dose rate considered during liquid cell electron microscopy (10^{10} Gy/s). **Figure 37** depicts the relative difference between MATLAB and Mathematica predictions (red) and between COMSOL and Mathematica pre-

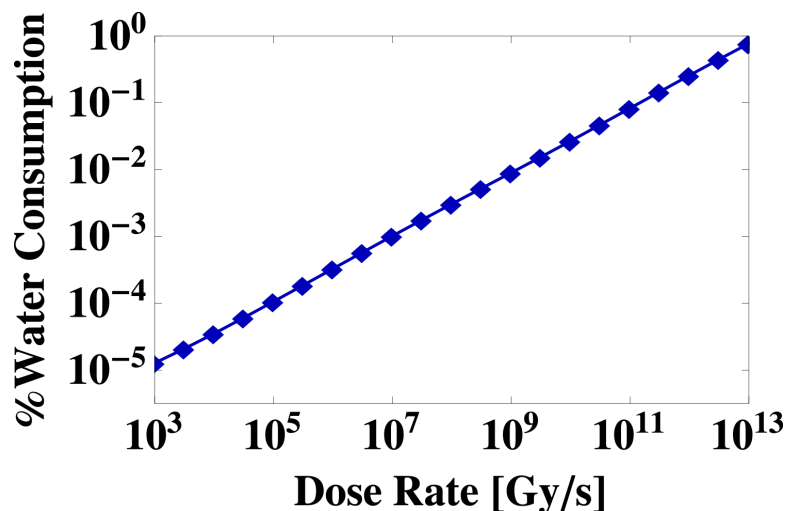


Figure 36: Percent consumption of water as a function of dose rate.

dictions (blue) as functions of the dose rate for H_2 (a) and O_3^- (b). We elected to consider H_2 since it is the most stable and abundant species and O_3^- due to it being one of the least abundant species. The concentration of the water was held constant in the COMSOL simulations, but is allowed to vary in Mathematica and MATLAB. The discrepancies between MATLAB, COMSOL, and Mathematica predictions were always smaller than 3.5%. The error can perhaps be attributed to differences in the numerical precision (number of significant digits) of each code.

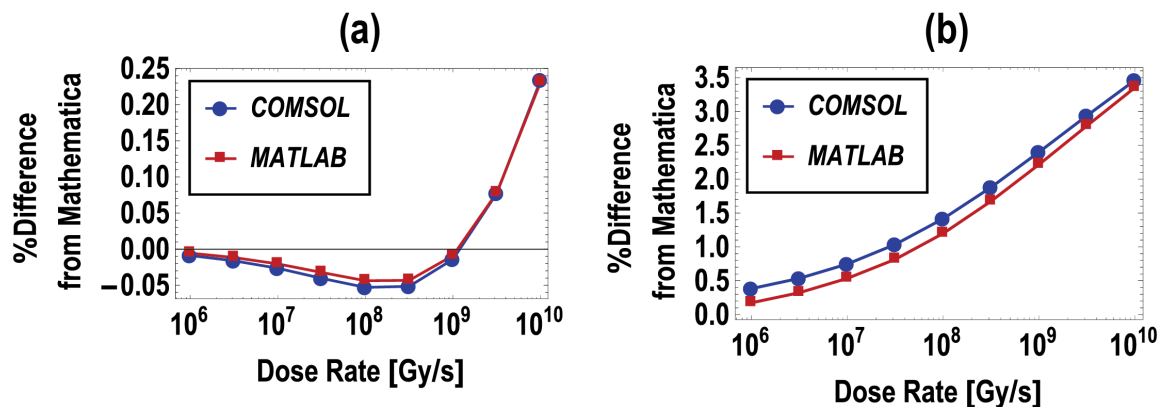


Figure 37: Percent difference between COMSOL and MATLAB relative to Mathematica for H_2 (a) and O_3^- (b) during homogeneous simulations.

4.8. Finite Beam Irradiation with Diffusion

In most Liquid Cell Electron Microscopy experiments, only a fraction of the liquid in the cell is irradiated. Radiolysis products generated within the irradiated region will diffuse out and continue to react outside the irradiated volume. To examine the effects of diffusion, a model system, similar to the one used in the temperature rise analysis is employed. The system is comprised of a cylindrical electron beam of radius a located in the center of a one-dimensional radial chamber of radius W . For the calculations presented in this section, $a = 1 \mu m$ and $W = 50 \mu m$. It is important to note that W may be as large as a few mm in practice. We focus here on circumstances relevant to TEM, where the electron beam is maintained at a fixed position for a prescribed time interval.

In the irradiated domain $0 < r < a$, the equations include the relevant source terms R_i . In the region outside the beam $a < r < W$, $\psi = 0$ (and therefore $R_i = 0$). **Figure 38** (left column) depicts H_2 , e_h^- , O_2 , and H^+ concentrations as functions of the radial position r at various times. **Figure 38** (right column) depicts the concentrations of the species at the beam's center ($r = 0$), the beam's edge ($r = a$), and at the device's outer, impermeable surface ($r = W$) as functions of time.

All species reach steady state concentrations within seconds - much longer than the equilibration time in the homogeneous case. This longer equilibration time results from the slow diffusion process that takes place over time scales on the order of the diffusion time, $t_{D,i} \sim W^2/D_i$. Typical diffusion coefficients of solutes in water are on the order of $10^{-9} m^2/s$, and so it is easy to estimate the order of magnitude of the time to steady state by using the diffusion time scale. Due to the chemical reactions between species, the actual steady state concentration is a function of position within

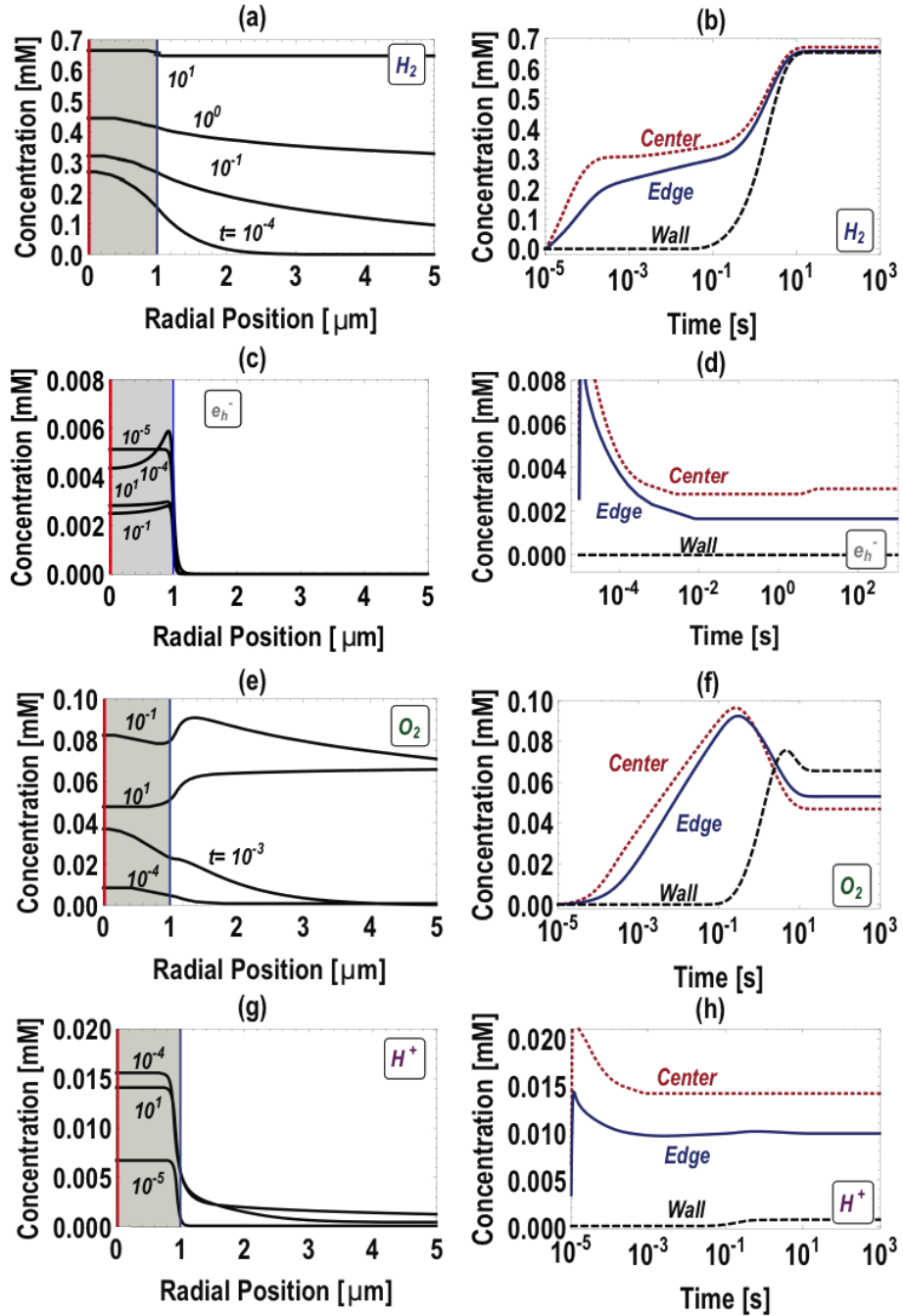


Figure 38: Heterogeneous model predictions for the spatial and temporal evolutions of H₂ (a and b), e_h⁻ (c and d), O₂ (e and f), and H₃O⁺ (H⁺) (g and h). The left column depicts the concentrations of the selected radiolysis products of neat water as functions of the radial distance from the center of the irradiated region at various times. The right column depicts the concentrations of the same products at the center and edge of the irradiated region and at the perimeter of the liquid cell. The beam and liquid cell radii are, respectively, 1 μm and 50 μm. The dose rate is 7.5×10^7 Gy/s.

the liquid cell.

It is very important to make two notes about the time it takes to establish a steady state. First, although it may take minutes or hours to reach the long time steady state in a large device, the species concentrations within the irradiated volume will be on the same order of magnitude as their long time values extremely quickly (milliseconds as described in the homogenous case). This means that changes in the local chemistry are unavoidable even for a large liquid cell. Consequently, a second caveat is that flowing the solution through the cell is also unlikely to help mitigate beam-induced phenomena, as the flow rate required to sweep away primary products would need to be large. We can estimate when flow will be important via the Damköhler number, the ratio of the production rate to the advective mass transfer rate. When

$$Da = \frac{R_i l}{C_i v} \quad (4.32)$$

is less than unity, then flow will have a significant role in the solution chemistry. Here, l is the length scale (irradiated volume radius $\sim 1 \mu m$) and v is the flow velocity. Setting $Da = 1$, we solve for velocity under the conditions of $C \sim 10^{-6}$ (M), $l \sim 10^{-6}$ (m), $\psi \sim 10^7$ (Gy/s), and $G \sim 1$ ($molecule/100eV$) to get $v \sim 1$ (m/s). Meaning the flow rate will have to be sufficiently high to make the fluid velocity greater than 1 (m/s) in the irradiated volume for advection to be dominant. This large flow velocity requirement means the radiolysis products will likely play the dominant role in solution chemistry.

Figure 38 illustrates the spatial and temporal behavior of some species. The most well-behaved (least reactive) species, H_2 , is continuously produced within the irradiated region and diffuses away (**Figure 38**). At early times ($t < 10^{-4}s$), the

production exceeds the diffusion and the H_2 concentration increases rapidly at the beam's center. At later times, the production is balanced by diffusion, which is reflected by the plateau in $C_{\text{H}_2}(0, t)$ (**Figure 38b**). As the H_2 concentration outside the beam builds up and the diffusive flux decreases, the H_2 concentration in the irradiated region resumes its growth to eventually approach its maximum, equilibrium value.

The more reactive radiolysis products, such as e_{h}^- , H^\bullet , OH^\bullet , H_3O^+ , and O_2 exhibit more complex behaviors than H_2 . The highly reactive e_{h}^- , H , and OH persist mainly in beam region and their concentrations drop quickly outside thereof. As they diffuse away from the irradiated region they are consumed through chemical reactions and drop rapidly to zero (**Figure 38c**). The somewhat complex behavior of e_{h}^- (**Figure 38c and d**) can be understood by considering its interactions with O_2 (**Figure 38e and f**), the dominant scavenger of e_{h}^- in neat water (via $e_{\text{h}}^- + \text{O}_2 \Rightarrow \text{O}_2^-$). Oxygen production is delayed somewhat, and initially the e_{h}^- concentration in the irradiated region increases rapidly. Once the production of O_2 ramps up ($t > 10^{-5}\text{s}$), the O_2 scavenges e_{h}^- and reduces its concentration. As a result, the concentration of e_{h}^- as a function of time exhibits a peaks at $t \sim 5\mu\text{s}$. As time increases further, the e_{h}^- concentration declines to its equilibrium value. The peak in the spatial distribution of e_{h}^- next to the edge of the irradiated region at intermediate times (*i.e.*, $t \sim 10^{-4}\text{s}$) is attributable to the mass transfer of O_2 by diffusion away from the irradiated region. The temporal and spatial distributions of the oxygen concentration, causally, exhibit opposing trends to that of e_{h}^- .

H_3O^+ (or H^+ , **Figure 38g and h**) behaves similarly to the other radical products, but with somewhat higher concentration outside the irradiated region than e_{h}^- . After the onset of irradiation, the H_3O^+ concentration in the irradiated region quickly

peaks and then drops to a steady state. Outside the irradiated region, the H_3O^+ concentration grows slowly by diffusion. Eventually the entire liquid cell will have an increased H_3O^+ concentration and reduced pH. For a neat water initially at pH 7 exposed to a $1 \mu\text{m}$ radius beam of 1 nA at 300kV (a dose rate of $7.5 \times 10^7 \text{ Gy/s}$), the steady state the pH will drop to ~ 4.9 within the irradiated region and ~ 6.1 outside the irradiated region.

As in the homogeneous case, we can fit a power law similar to the one in **Equation (4.30)** to specify the concentrations of radiolysis products at the beam's center as functions of the dose rate. The calculations were carried out for a liquid cell with radius $W = 50 \mu\text{m}$, but the results should be approximately applicable for any sufficiently large W (i.e., $W > 10 \mu\text{m}$). The pre-factor α_i and the exponent β_i ($0.3 < \beta_i < 1.5$) are listed in **Table 3**.

4.8.1. Diffusion Coefficients

When solving the heterogeneous problem, we need to account for mass transfer by diffusion. For the reader's convenience, we reproduce the diffusion coefficients of radiolysis products in water at room temperature in **Table 4**.

4.9. COMSOL Implementation

We used the multi-physics, finite element program COMSOL to solve both the homogeneous case and the heterogeneous case. In the latter, we account for mass transfer by diffusion. The kinetic equations (**Table 1**) were implemented in the *reaction chemistry module*. The spatial domain was defined in the diffusion of dilute species module using 1D, axisymmetric cylindrical coordinates (**Figure 39**). The radial coordinate is r , and the beam's center is at the origin ($r = 0$). The diffusion module is

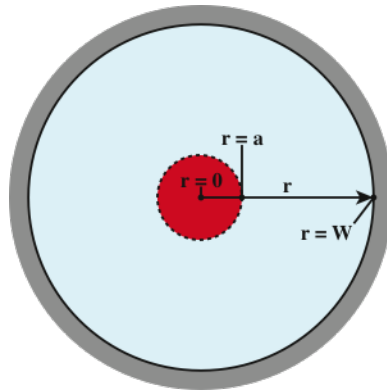
Table 4: Diffusion Coefficients of Radiolysis Products

Species	D [$10^{-9} \text{ m}^2/\text{s}$]	Species	D [$10^{-9} \text{ m}^2/\text{s}$]
e_h^-	4.5	O_2	2.1
H^\bullet	7.0	O_2^-	2.1
H_2	4.5	O_3^\bullet	1.89
H_2O_2	1.4	O_3^-	2.0*
HO_2^\bullet	2.0	OH^\bullet	2.8
HO_2^-	1.4	OH^-	5.0
HO_3^\bullet	2.0*	O^-	2.8
H_3O^+	9.0		

Unless otherwise stated the data was obtained from Hill and Smith [77].

*Estimated

directly linked to the reaction physics module. The domain consisted of two regions, the irradiated, beam region $r \leq a$, where relevant source terms were included, and the bulk region, $0 \leq r \leq W$, where reactions continue but there is no generation. The simulation was carried out after selecting a fine enough element size to assure mesh-independence. In the homogeneous case, COMSOL results agreed within 3.5% with Mathematica results.

**Figure 39:** COMSOL Simulation Domain

CHAPTER 5 : Effects of Radiolysis

The beam-sample interaction outlined in the previous chapter have important consequences when interpreting liquid cell results. Additionally, we can exploit our quantitative understanding of the radiation-induced processes to use the electron beam as a tool to study interesting nanoscale phenomena. In this chapter we look at a few examples including bubble formation, the effects of aeration solution, the effects of variations in solution pH, and beam-induced metallic crystal formation.

5.1. Hydrogen and Bubble Formation

Bubble nucleation and growth is frequently observed during liquid cell experiments, [8, 87–90] occasionally with adverse effects. The ability to predict the conditions needed for bubble formation improves our capacity to design experiments that avoid bubble formation or that allow bubbles to form under controlled conditions. The experimental observations also support the existence of a steady state predicted by numerical models.

Prolonged irradiation under moderate dose rates is possible without the formation of bubbles, which suggests the existence of reverse reactions that prevent the concentrations of the gaseous radiolysis products H_2 and O_2 from growing without limit and therefore greatly exceeding their saturation concentrations [7, 8]. Second, at relatively high dose rates, reproducible nucleation and growth of nanobubbles has been observed [8]. The periodic behavior observed in this experiment strongly suggests the existence of a steady background concentration field far from the bubble, consistent with steady state conditions. The nucleation, growth, and migration of one of these bubbles can be seen in **Figure 40**, where, fortuitously, a defect in the silicon nitride

membrane serves as a nucleation site. The nucleation site allows for heterogeneous nucleation of nanoscale bubbles in a repeatable pattern [8]. In the absence of a nucleation site, homogeneous nucleation is expected which will often lead to the rapid formation of a large bubble (radius on the order of 10's of microns).

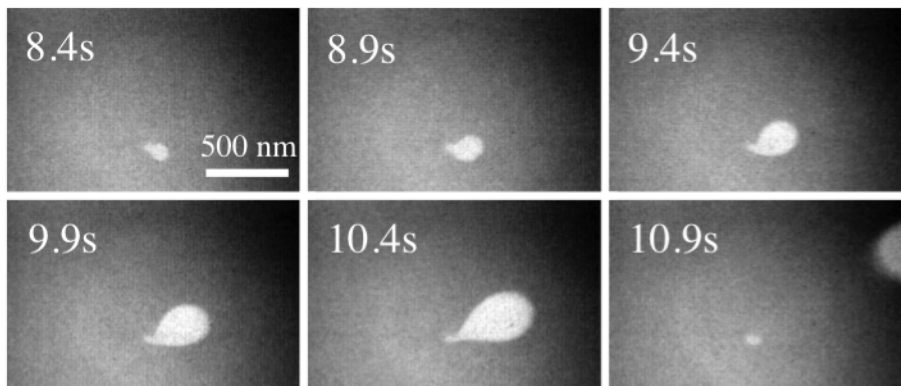


Figure 40: Nucleation, growth, and migration of radiolytic bubbles at a serendipitous nucleation site.

In most circumstances bubbles are undesired as they interfere with imaging. It is important to calculate the expected steady state concentrations of the gaseous radiolysis products H_2 and O_2 under the experimental conditions used, so that one can estimate whether they will exceed their saturation concentrations by an amount sufficient to facilitate bubble nucleation. To form bubbles, one would need to exceed the saturation concentration by many times [91]. Using Henry's law, and assuming realistic values of the pressure in the liquid cell, one can estimate the supersaturation of the gaseous species. For neat water radiolysis, the supersaturation of H_2 will always be greater than that of O_2 , and so bubble nucleation will usually be due to hydrogen. (Though, once a bubble is nucleated, its composition must consist of a mixture of all gases species in diffusion communication with the bubble.) **Figure 41** depicts the concentration of radiolytic H_2 at the center of the irradiated region as a function of time in a liquid cell with an effective diameter of $50 \mu m$ and $1000 \mu m$.

The horizontal lines in **Figure 41** mark the saturation concentrations at the various indicated pressures. The actual pressure in a liquid cell depends on the design of the cell, the loading conditions, and the extent of the bowing of the windows. Typical pressures are in the range of a tenth to a few atmospheres, and due to the deflection of the electron transparent membranes, the pressure inside the device will often drop below atmospheric once the liquid cell is inserted in the high vacuum of the electron microscope. Calculations similar to those shown in **Figure 41** can be used to identify the maximum dose rate that allows for indefinite bubble-free imaging or, alternatively, the imaging time available for bubble-free operation at a given dose rate. For the moderate dose rate of **Figure 41**, prolonged, bubble-free imaging is attainable even at atmospheric pressure, as the supersaturation needed for bubble formation is likely much greater than the predicted steady state concentration.

The presence of a bubble will also play a role in the local radiolysis. The concentration of species at the interface and mass flux associated with a growing or dissolving bubble will alter solution chemistry and therefore the steady state concentrations of all species. Radiolysis will also occur in the gas phase (including any water vapor), however, the production will be much lower than in the liquid phase as the dose rate scales linearly with density. A bubble could be implemented in a numerical simulation to directly study these effects as long as the device pressure, the size of the bubble, and an estimate of surface concentration are known.

5.2. Radiolysis of Aerated Water

Solutes can play a strong role in the steady state concentrations of radiolysis products [72, 74]. Oxygen is one solute of particular importance. Since it is not practical to deaerate solutions in most liquid cell experiments, one will often encounter solutions

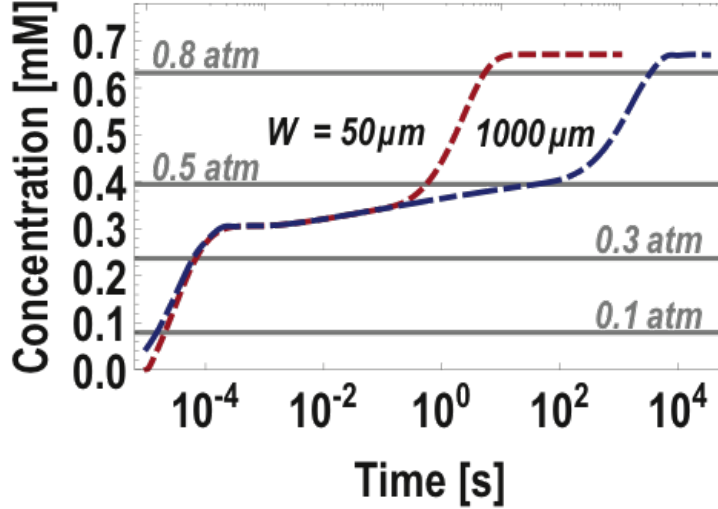


Figure 41: The concentration of H_2 at the beam's center in the heterogeneous case for device radii sizes of $50 \mu m$ (red line) and $1000 \mu m$ (blue line) and the saturation concentration of H_2 in water at various pressures (horizontal lines). Initially neat, deaerated water is irradiated continuously at a dose rate of $7.5 \times 10^7 Gy/s$. The beam radius is $1 \mu m$.

with dissolved oxygen. It is simple to account for the effect of dissolved oxygen in the solution on the concentrations of the radiolysis products by changing the initial conditions in the numerical simulation. Aerated water is defined here as neat water saturated with oxygen at atmospheric conditions without any dissolved CO_2 or N_2 . The saturation concentration of oxygen is $0.255 mM$ as calculated with a Henry's Law constant of $0.0013 mol/kg - bar$ [81]. **Figure 42** depicts the ratios of the steady state concentrations of e_h^- , H^\bullet , H_2 , H_2O_2 , OH^\bullet , and O_2 in irradiated water initially oxygen-saturated (aerated) and in oxygen-free (deaerated) water as functions of the dose rate.

The changes in steady state concentration is a strong function of dose rate. For sufficiently high dose rates ($> \sim 10^8 Gy/s$), the steady state oxygen concentration in the deaerated solution exceeds the initial saturated oxygen concentration leading to all species being nearly independent of the initial oxygen concentration. In other words, all the ratios in **Figure 42** asymptotically approach the value of 1 as the dose

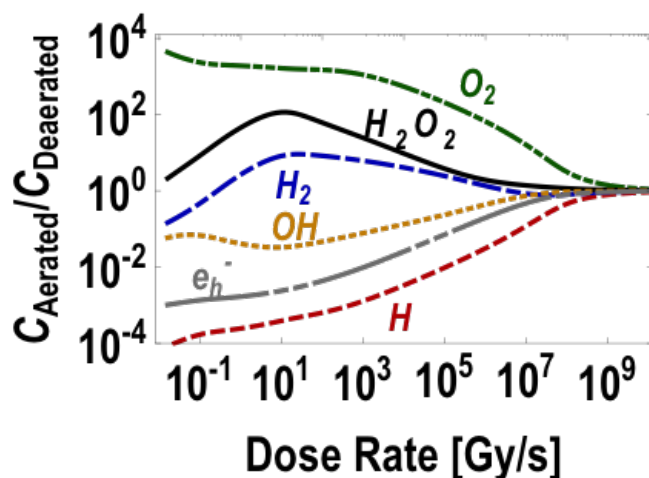


Figure 42: Ratio of aerated to deaerated steady state concentrations of e_h^- , H^\bullet , H_2 , H_2O_2 , OH^\bullet , and O_2 as functions of dose rate.

rate increases. However, at lower dose rates, the presence of initial oxygen in solution plays an important role on the steady state concentrations of radiolytic species.

5.3. Changes in pH; Effect of pH on Radiolysis Yields

One extremely important consequence of irradiation is strong changes in the local pH of an irradiated volume [7]. **Figure 43** depicts the steady state pH as a function of dose rate and initial pH of deaerated water. When the dose rate is low ($< 10^3$ Gy/s), the pH of the solution is nearly unaffected by irradiation and is independent of the dose rate. For higher dose rates, the system is always driven toward being more acidic. This is particularly important for alkaline solutions, as the pH will become rather acidic.

These changes in pH will play a strong role in many process including electrochemistry and colloidal stability. Grogan et al., [87] Li et al., [12] and Woehl et al., [92] among others, have shown that otherwise stable colloidal suspensions aggregate during electron microscope imaging. The aggregation seen in the experiments is

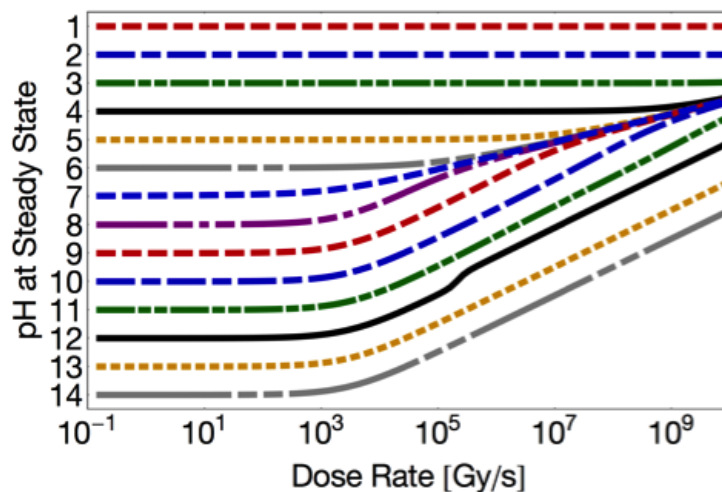


Figure 43: Steady state pH as a function of dose rate and initial pH prior to irradiation. Deaerated water.

most probably due the change in pH caused by the beam moving the colloids' surface charge closer to their isoelectric point, causing their destabilization. Given the experimental conditions [87], the solution pH would drop from a pH of 7 to 3.25 within the irradiated volume, causing the aggregations.

It is clear from the above that at any given dose rate, the steady state pH (or H_3O^+ concentration) depends on the initial pH of the solution pre-irradiation. Since the concentrations of all radiolysis products are interrelated, the steady state concentrations of the other radiolysis products also depend on the initial pH. These effects are important to consider since strong acids and bases are frequently employed in liquid cell experiments to improve salt solubility. **Figure 44a** depicts the equilibrium concentrations of e_h^- , H^\bullet , H_2 , H_2O_2 , OH^\bullet , and O_2 as functions of the initial solution pH in deaerated water. **Figure 44b** depicts the ratios of radiolysis products in aerated and deaerated water as functions of the initial pH. These simulations assume that the conjugate pairs to the protons/hydroxides of the added acid/base (e.g., SO_4^{-2} in sulfuric acid and K^+ in potassium hydroxide) do not significantly participate in

the various reactions. At moderate pH ($5 < \text{pH} < 9$), the steady state concentrations of all radiolysis products is nearly independent of the initial pH value as reflected by the plateaus in **Figure 44a**. This is consistent with prior reports on radiolysis at low dose rates. [5,6] For strong acids and strong bases, however, the steady state concentrations of radiolysis products are greatly altered and needs to be considered. **Figure 44b** compares the effect of initial pH in aerated and deaerated solutions and shows that aeration becomes less important in strong acids or strong basis.

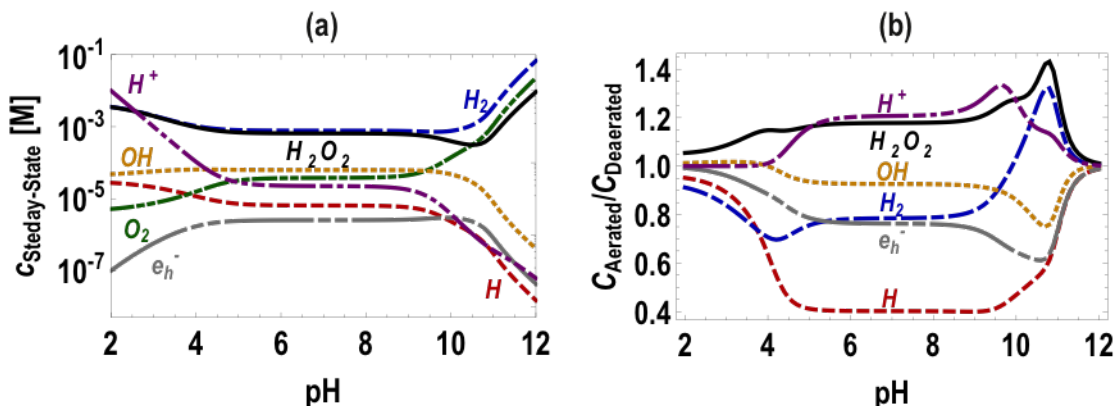


Figure 44: (a) Steady state concentrations of e_h^- , H^\bullet , H_2 , H_2O_2 , OH^\bullet , and O_2 as functions of the pH value prior to irradiation for deaerated water under uniform irradiation (homogeneous case). (b) The ratio of radiolytic products concentrations in initially oxygen-saturated water ($C_{\text{O}_2}(0) = 0.255 \text{ mM}$) and in deaerated water as functions of initial pH. The dose rate is $7.5 \times 10^7 \text{ Gy/s}$.

5.4. Hydrated Electrons; Particle Nucleation, Beam Writing, Etching vs. Growth

One often observed beam-induced phenomena is the nucleation and growth of nanocrystals in metal salt solutions [7,28,93–96]. When an aqueous salt solution is irradiated, radiolysis products that are reducing agents, such as hydrated electrons, may reduce cations and induce precipitation under certain conditions [86, 97, 98]. The rate of mass transfer can control the crystal growth habit [99], by controlling the dose rate one can obtain different types of crystal geometries and control whether materials

are formed by single atom addition or by coalescence of clusters (oriented assembly) [9, 11, 69, 93, 95].

Since hydrated electrons are extremely reactive, they are present at significant concentrations only within the irradiated region. Precipitation will take place, therefore, mainly in the illuminated region, allowing patterning of deposits using the electron beam as a “pencil”. Grogan et. al. [8] used the electron beam to precipitate gold nanowires from gold solution, writing the names of the authors’ institutions. An additional level of control can be achieved by applying electric fields [28].

In addition to reducing agents, radiolysis will also produce strong oxidizers. During imaging of Au nanorods in water, particles were observed etching, growing and remaining unaltered as a function of dose rate. At low dose rates, growth occurred. By changing the dose rate, they were able to transition repeatedly between etching and growth regimes. Since the radiolysis products include both strong reducing and oxidizing agents, the observed behavior reflects changes in the relative concentrations of the reducing and oxidizing agents. To determine whether growth or etching would take place, one must consider the rates of the corresponding reactions. Components other than water must also be considered as the situation is further complicated by the presence of Br^- (from the CTAB used in the particle synthesis), and products resulting from the interaction of radiation with Br^- such as $\text{Br}_2^{\bullet-}$, Br_3^- , and Br_2 that react with gold [98] and for neat water radiolysis does not account.

5.5. The Role of Hydrogen Peroxide on Liquid Cell Radiolysis

Additives to the initial solution are known to alter radiolysis product formation. Here we examine the effect of hydrogen peroxide, an important additive in oxidation and reduction reactions, on the production of radiolytic species in liquid cell electron mi-

croscopy. We computed the concentrations of radiolysis products as functions of initial hydrogen peroxide concentration, beam current, beam size, and time. Our calculations predict that the concentration of oxygen increases greatly as the concentration of hydrogen peroxide in the pre-irradiated solution increases. Bubble nucleation is a function of the saturation concentration, which is fixed by the pressure within the device. The pressure inside the device was controlled during the filling of our closed cell, the nanoaquarium, and then estimated, *in situ*, by considering the deflection of the silicon nitride windows based on transmitted beam intensity. The predictions are consistent with experimental observations in a liquid cell indicating that the presence of hydrogen peroxide lowers the critical dose rate required to nucleate bubbles as a result of the higher radiolytic production of oxygen.

5.5.1. H_2O_2 as an Additive

Imaged systems often exhibit unexpected/undesirable behavior when exposed to the extremely high dose rates encountered during liquid cell electron microscopy. Hydrogen peroxide, a useful solute, encourages bubble formation. **Appendix Video B.9** shows the nucleation and growth of a very large gaseous bubble within the nanoaquarium for a solution containing 3% wt H_2O_2 . The bubble is initiated by zooming in to increase the dose rate within the imaged volume. Once a sufficient dose rate is reached, the local solution chemistry supports homogeneous nucleation of the gaseous phase. The nucleating species is *a priori* unknown, but radiolysis simulation reveal that O_2 is the most likely culprit [but we also have H_2]. Although, in the limit of an ideal solution, the bubble nucleation is controlled by a single species, the post nucleation bubble composition will naturally contain both gaseous hydrogen and oxygen. Knowing how to avoid the formation of bubbles is essential when trying to use liquid cell electron microscopy as a tool to study the growth mechanisms of nanoparticles in

bulk solution. We therefore investigate the nucleation of gaseous bubbles when H_2O_2 is an additive due to its importance in nanocrystal formation [100].

5.5.2. Varying Initial Concentration

The neat water radiolysis model previously developed can be used to estimate hydrogen peroxide concentration as H_2O_2 is already one of the primary products of water radiolysis. We merely need to specify the initial concentration of this one species to see to what extent the solution chemistry is altered by its initial presence in the solution. **Figure 45** shows the ratio of the steady state concentration of important species as a function the initial (pre-irradiated) concentration of H_2O_2 normalized by their steady state concentration of neat water ($C_{\text{H}_2\text{O}_2}(t = 0) = 0$). The simulation was carried out at the typical TEM conditions with associated dose rate of $7.5 \times 10^7 \text{ Gy/s}$. For very dilute initial H_2O_2 concentration, all ratios are unity. As the initial concentration increases above $10 \mu\text{M}$, the resulting concentrations of the molecular products increase while those of the radical products decrease. This means that the hydrogen peroxide helps to scavenge the radical species and encourages the formation of the more stable, molecular products. This implies that it can be exploited to control the oxidation and reduction reactions that occur with metallic ions as e_{h}^- and H^\bullet are generally the primary reducers and OH^\bullet is the primary oxidizer.

5.5.3. Bubble Formation

In the context of bubble formation, an important consequence of the addition of H_2O_2 to the pre-irradiated solution is the increase the steady state concentration of O_2 can be amplified. For neat water, we showed that bubble nucleation will likely be governed by the levels of hydrogen formation, as the super saturation of hydrogen is always larger than that of oxygen during neat water radiolysis. However, when

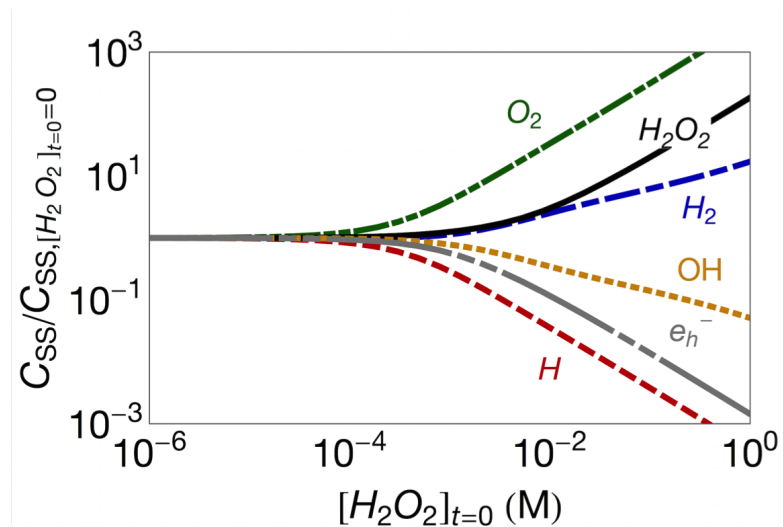


Figure 45: Ratios of steady state concentrations of select species as functions of initial H_2O_2 concentration compared to their neat water values during typical TEM imaging conditions ($7.5 \times 10^7 Gy/s.$)

the solution contains a significant amount of hydrogen peroxide, the oxygen super saturation will greatly surpass that of molecular hydrogen - making it the most likely cause for bubble nucleation.

In order to test the results of the simulation, we prepared devices containing controlled initial concentrations of hydrogen peroxide. The devices were loaded into the STEM at Penn and imaged under low dose rate to obtain the intensity as a function of position over the entire window. This intensity data was then used to estimate for liquid thickness. The bowing of the membrane (as dictated by the bright field intensity) is fit to the membrane deflection equation and used as an estimate of the device pressure.

The saturation concentration of oxygen is calculated using Henry's law for the pressure in the device prior to bubble formation (the pressure will increase post nucleation due to the density difference between the liquid and the gaseous phase). The dose rate is then increased by changing microscope parameters until a large bubble forms

within the first 30 seconds of irradiation. Bubbles often form instantaneously once the beam parameters are changed. The time waited is short compared to the diffusion time associated with the device size (hours), implying the nucleation is driven by the local solution. Using the results of the homogenous radiolysis model, we estimate the supersaturation for the dose rate associated with the conditions where the bubble nucleated. In the cases where the concentration of hydrogen peroxide is low and the microscope is incapable of supplying a high enough dose rate to nucleate a bubble, we calculate the maximum supersaturation obtained in the system. The results of each of these cases are plotted in **Figure 46**, where the “X” markers identify cases where there was no nucleation and the “O” marker identify the cases when a bubble did nucleate.

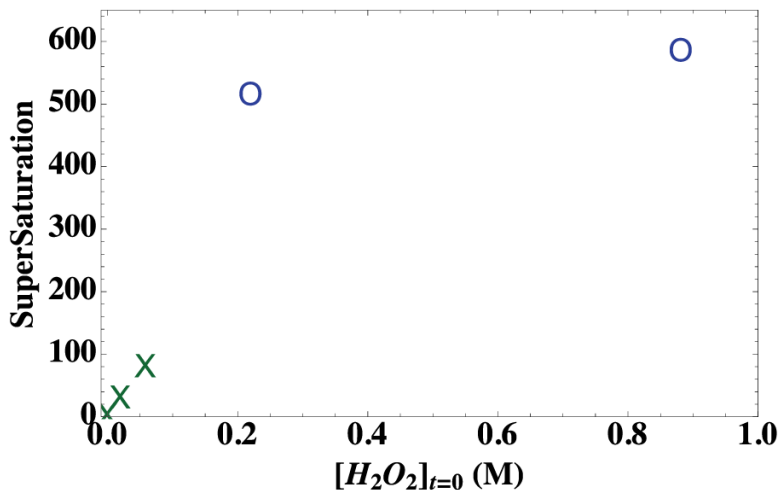


Figure 46: Estimated supersaturation of O₂ for homogeneous bubble nucleation “O” and for cases where no nucleation occurred under maximum possible dose rate “X” as a function of initial (pre-irradiation) H₂O₂ concentration.

Figure 46 shows that for low supersaturation (< 100), a bubble does not form. However, once the supersaturation is on the order a few hundred, a large bubble instantly nucleates. These conditions are consistent with homogeneous nucleation, where a very high level of supersaturation is required before the formation of a second

phase [91]. Presumably, if there were nucleation sites on the silicon nitride windows, bubbles would have formed sooner than what was seen here. The existence of a regime where bubble nucleation is not instant (it may still happen after long times), gives the usable range of initial H_2O_2 concentrations when studying its role in the formation of metallic nanostructures or other physics outside of bubble formation.

5.6. Other Aqueous Solutions with Additional Chemistries

Further species can be included in the water radiolysis simulations to provide more accurate quantitative results in the presence of additional solutes. If the reaction pathways and associated rate constants are all known, the implementation of an augmented water radiolysis kinetic model is merely a matter of extending the set of equations to include new species and reactions according to **Equation (4.23)**. Practically speaking, one could find all of the reactions utilizing resources such as the NIST Solution Kinetics database [82] and published works, identify the dominate set of reactions, and implement the new reaction scheme in a numerical solver. Park et. al. [Park] performed this task when they included the role of chloride and its radiolytic constituents to explain the formation of gold nanocrystals in a solution containing chloroauric acid. The model did not, however, directly include gold as a species since the necessary reaction rates are still unknown. Even so, they found accounting for the solution chemistry with chloride reactions and the appropriate pH was essential to obtain quantitative agreement between the model and experimental observations as described in the following section.

5.6.1. Beam Induced Gold Nanoprism Formation

Solution-phase particle synthesis is an important manufacturing technique for the creation of nanomaterials. *In Situ* measurements of growth provide mechanistic infor-

mation that is useful in designing and synthesizing new materials. Here, we briefly investigate a model system of gold nanocrystal formation within a well controlled irradiated environment. Gold chloride solution is loaded in a liquid cell for imaging during electron microscopy. The beam also serves as the radiation source of reducing species. Radiolytically formed hydrated electrons reduce gold ions in solution. The neutralized gold atoms precipitate to form nanocrystals. **Figure 47** shows the beam-induced growth of a gold nano prism during liquid cell electron microscopy. We measure growth rates for individual crystals under conditions that favor well-faceted Au nanoprism formation, and find that each crystal grows linearly with time at a rate unaffected by its shape or proximity to neighbors. Furthermore, solid phase growth requires a threshold dose rate (or beam current), suggesting competition between reduction and oxidation processes in the solution. Above this threshold, growth follows a power law with dose rate. **Figure 48** shows the growth rate's dependence on beam current (scalar multiple of dose rate). The growth rate, S , is the area growth rate of the imaged gold prisms. Post hoc AFM analysis showed the crystals to be of constant thickness, making the area growth rate a direct measure of the particle volume. To account for the dose rate dependence we show that a radiolysis model is required that includes the chemistry of the chloride brine solution. For neat water radiolysis, the simulated concentration of e_h^- scales as dose rate raised to the power of 0.51, however, when chloride is included along with the pH of the solution (~ 2), e_h^- scales as dose rate raised to the power of 0.79, much closer to the experimentally determined 0.76. The model results show the necessity of considering all species present when interpreting kinetic data obtained from beam-induced processes.

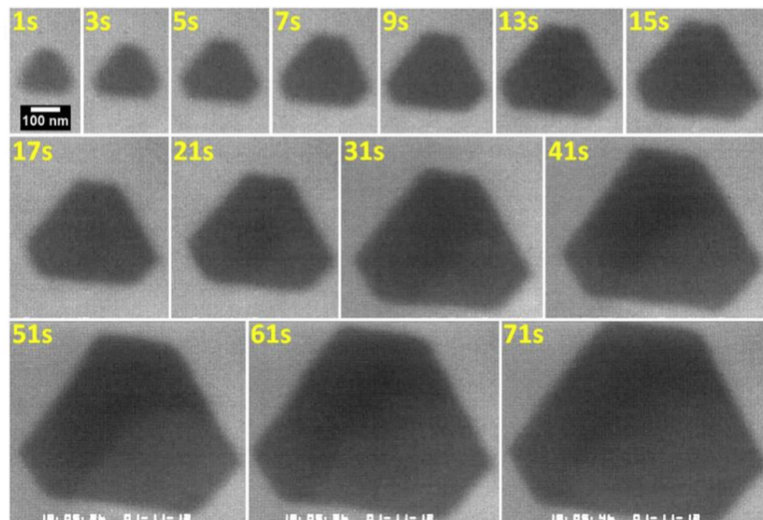


Figure 47: Bright field TEM images of beam induced Au crystal growth in 20 *mM* HAuCl₄, acquired at times *t* indicated after irradiation began at *t*₀. Dose rate of 6.0×10^8 Gy/s calculated with a beam current of 8.0 nA spread over 1 μ m radius. Figure generously provided by Dr Jeung Hun Park.

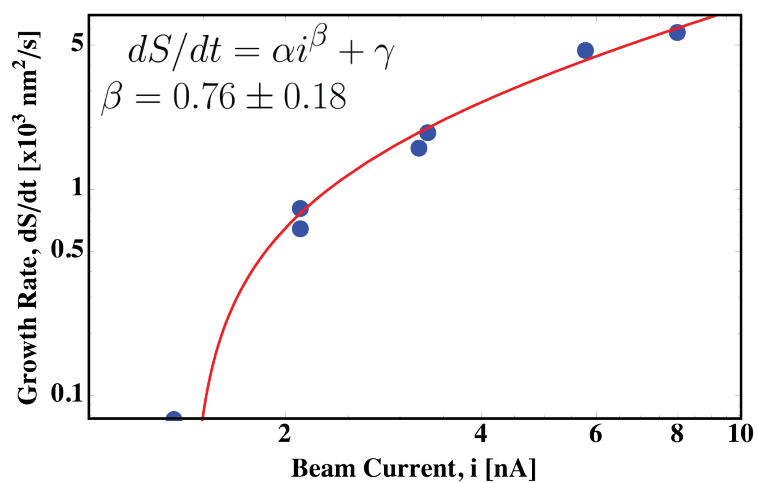


Figure 48: Growth rate dS/dt vs. beam current with each data point showing measured growth rate individual Au crystals. The beam current *i* varied from 0.1 nA to 8.0 nA over 1 μ m radius beam. The solid line is the least-squares fit and yields a growth exponent of $\beta \sim 0.76$.

Radiolytic Gold Reduction Mechanism

The reduction mechanisms of HAuCl_4 solutions are complicated but the overall chemical pathway for radiolytic reduction has been established [98,101]. Au(III) is ultimately reduced to Au(0) primarily through reactions with hydrated electrons, the strongest and fastest reducing agent among radiolytic byproducts. However, the production of Au(0) is non-linear, even at constant dose rate, in the sense that there is an induction time for Au(0) formation [98]. Irradiation of HAuCl_4 solution below the dose required for a total reduction of Au(III) to Au(0) does not result in the nucleation and growth of gold nanocrystals. The reason for this induction time is that the reaction proceeds up to the formation of Au(I) in the form of Au(I)Cl_2^- , [102] but this species is relatively stable and is not reduced further until the less stable Au(III) ions are substantially consumed, requiring the solution to absorb a critical dose [98]. Essentially, the reduction of Au(III)Cl_4^- “screens” the reduction of Au(I) until the ratio of Au(I) to Au(III) approaches unity [98]. This scenario is supported by the higher reduction potential of Au(I)Cl_2^- compared to Au(III)Cl_4^- [101]. Another key feature of the reaction sequence is that the intermediate reduction step of $\text{Au(II)Cl}_3 \rightarrow \text{Au(I)Cl}_2^-$, a disproportionation reaction, is mediated via chloride complexes [98,102], implying that, without the presence of chloride, the Au would never be fully reduced. This means that tracking e_h^- and including Cl^- are both essential to modeling the growth kinetics. We therefore extend our TEM water radiolysis model to include Cl^- to quantitatively address the observed physical phenomena of time-dependence, dose rate-dependence and the existence of a threshold dose rate.

Extending Radiolysis to Chloride Brine

To compute the concentrations of radiolysis products in the presence of chloride, we augmented the water radiolysis model to include the dominant reactions and species associated with the irradiation of chloride brine. **Table 5** lists the 8 additional reactions needed to incorporate species resulting from the presence of chloride (Cl , Cl^- , Cl_2^- , ClOH^-), along with appropriate rate constants. The reaction set in **Table 5** is taken from Atinault *et. al.* [103]. The rate constants for these and additional reactions can be found in NIST databases [82]. The source code for neat water radiolysis was distributed by Schneider *et. al.* [7] on GitHub [83]. We utilized our Mathematica implementation extended it with the appropriate reaction scheme for chloride interactions. The Mathematica code with the additional 8 reactions is also available in GitHub [83].

Table 5: Additional Reactions Required for Chloride

	Chemical Reactions	Rate Constant at 25°C ($M^{-1}s^{-1}$)
1	$\text{Cl}^- + \text{OH} \rightarrow \text{ClOH}^-$	4.3×10^9
2	$\text{ClOH}^- \rightarrow \text{Cl}^- + \text{OH}$	6.1×10^9
3	$\text{ClOH}^- + \text{H}^+ \rightarrow \text{Cl}^- + \text{H}_2\text{O}$	2.1×10^{10}
4	$\text{ClOH}^- + \text{e}_h^- \rightarrow \text{Cl}^- + \text{OH}^-$	1.0×10^{10}
5	$\text{Cl}^- + \text{Cl} \rightarrow \text{Cl}_2^-$	2.1×10^{10}
6	$\text{Cl}_2^- + \text{e}_h^- \rightarrow 2 \text{Cl}^- + \text{H}_2\text{O}$	1.0×10^{10}
7	$\text{Cl}_2^- + \text{H} \rightarrow 2 \text{Cl}^- + \text{H}^+$	8.0×10^9
8	$\text{Cl} + \text{H} \rightarrow \text{Cl}^- + \text{H}^+$	1.0×10^{10}

5.6.2. Non-Aqueous Solvents

Radiation chemistry in solvents other than liquid water can be treated by means analogous to the treatment of water here. If the degradation pathways are known

for the system, kinetic models can be designed to account for the radiation-induced changes in chemistry. Extensive knowledge as to radiation's effect on matter has been generated for gases, aprotic solvents, ionic liquids, and more [72, 74, 104, 105]. Ionic liquids are a solvent of particular interest due to their promising material properties, especially in lithium ion batteries [106]. Ionic liquids are molten salts made of a combination of organic and/or inorganic cations and anions that are liquid at low temperatures, have low vapour pressures, are combustion resistant, and have other properties making them amenable to engineered materials processing. Many of these materials have been studied for their radiolytic behaviour and recently reviewed by Mincher and Wishart [105]. Similar to water, the primary form of energy deposition is in the form of ionization that cascades into the creation of radicals, excess electrons, holes, and excited states. The resulting chemistry will be derived from the constituents in the ionic liquid, and each individual material will therefore have its own radiation-induced behaviour. This behaviour must be accounted for via the kinetics for proper understanding of in situ observations in the electron microscope.

CHAPTER 6 : Electrochemistry with the Nanoaquarium

6.1. Geometry of Experimental Apparatus

The manufacture of a liquid cell for electron microscopy results in non-trivial geometries that must be understood before analyzing data. The nanoaquarium, made with standard lithography processing [13], is equipped with four platinum electrodes on a titanium adhesion layer. The electrodes are formed via thermal evaporation followed by a lift-off patterning step. The outcome is a polycrystalline thin film (30 nm total) on top of the silicon nitride layer with well-controlled geometry. The top view of the electrode and nanochannel layout are depicted in the schematic **Figure 49**, where the electrode labeling corresponds to the standard setup used during electrochemical experiments (which can be changed). The portions of the working and reference electrode exposed to solution has an area of $2.4 \times 10^{-8} \text{ m}^2$ and a perimeter of 1380 μm . The counter electrode is nominally 1500 μm away with total exposed area of $2.9 \times 10^{-7} \text{ m}^2$.

6.2. Copper Growth Modes

Growth progresses in several stages during electrode deposition. At early times, copper nucleates predominately on top of the platinum electrode. The nuclei grow and quickly form a hard packed film. The hard packed film grows vertically until it reaches a steady thickness dictated by the thickness of the liquid cell (200 nm in this case). Once it mostly occupies the thickness of the channel, the growth becomes essentially two-dimensional. **Figure 50** illustrates the growth where gray scale is representative of time with lighter gray value being later times. This view is supported by the bright field intensity images as discussed in then next section.

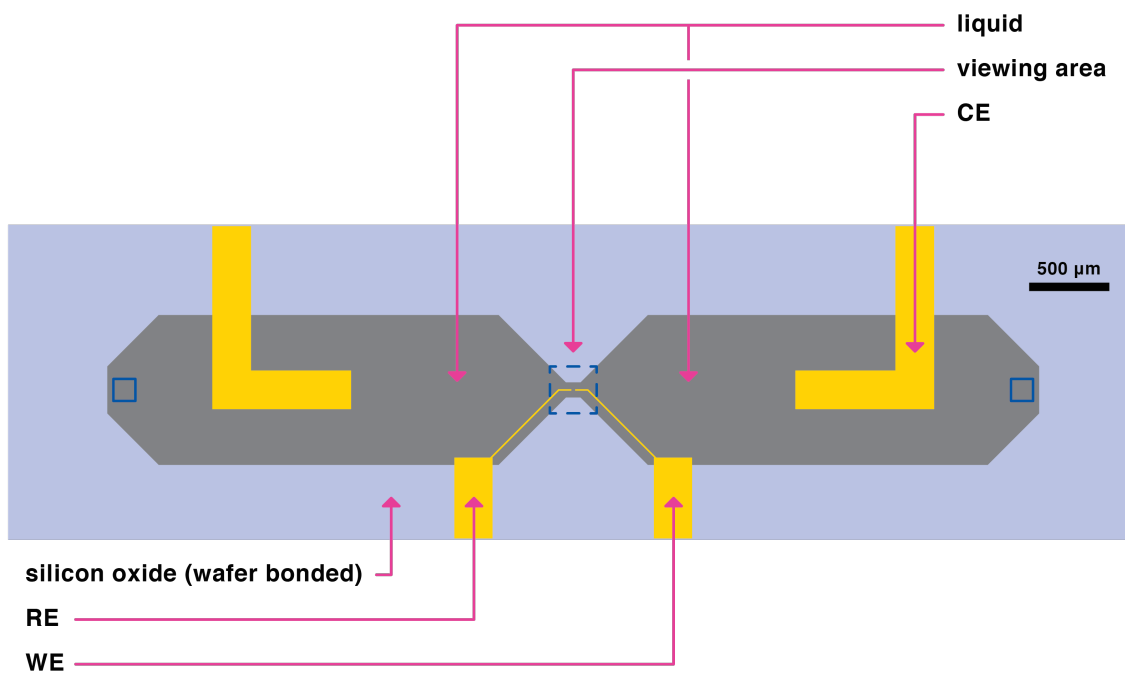


Figure 49: Schematic of electrode configuration with standard 3-electrode setup labeled with the Working (WE), Reference (RE), and Counter (CE) Electrodes. The gray area represents the nanochannel where the solution is loaded.

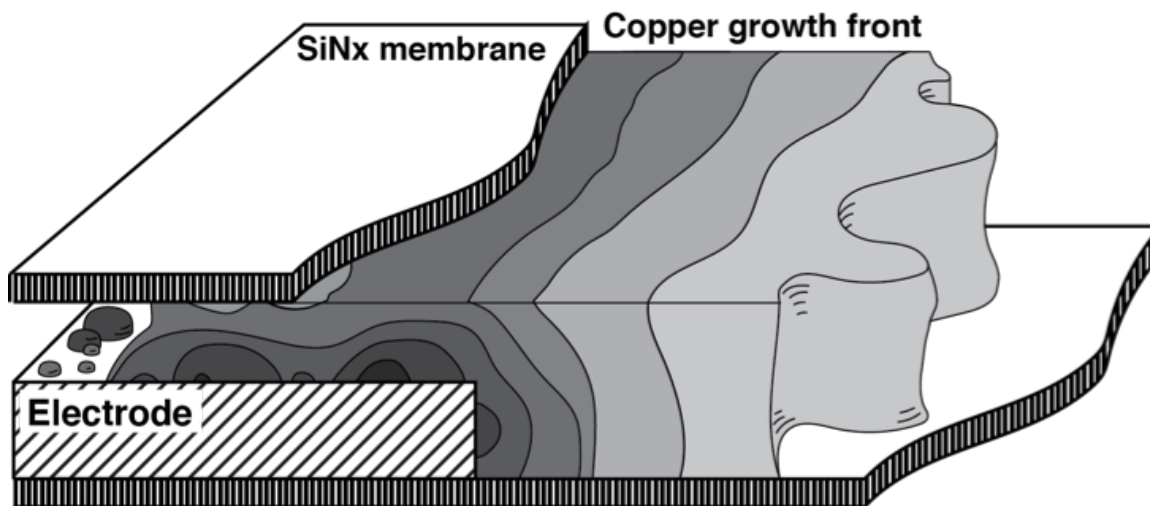


Figure 50: Illustration of Copper growth modes. The copper first nucleates at arbitrary sites, then forms a hard packed film which grows vertically until it reached the top of the device where it then grows perpendicular to the electrode in a essentially 2D fashion.

6.3. 2D Growth - Constant Height Assumption

Next, we consider the predominately two-dimensional growth assumption. That is, the copper deposited on the electrode, grows upward to the liquid cell ceiling and then grows out laterally from the electrode with a constant height. We investigate the intensity map of the deposition to establish this fact. We measure the intensity along a line perpendicular to the electrode as illustrated in **Figure 51a**. The measurement is averaged over 10 pixels in the direction transverse to this line (parallel to the electrode) at each time instance during the deposition to minimize noise. The intensity profile is extracted for each frame and plotted in the contour plot of **Figure 51b**. The lower the intensity (the darker the image), the greater the thickness of the copper deposited. The contour plot supports the hypothesis that the copper reaches a constant thickness and continues to grow in an essentially two-dimensional fashion. **Figure 51c** depicts the normalized intensities as functions of time at a representative location on the electrode and off the electrode. The intensity has been normalized by the background intensity (blue line in **Figure 51b**) to adjust for drift in the electron beam. The black line, depicting intensity at the electrode location, drops quickly from its initial value and most of the copper is deposited within the first 1 s. The copper continues to thicken at a much slower rate that we take as negligible. The off electrode region has to wait for the interface to progress before its intensity is lowered by the presence of copper. Once the interface has travelled through the probed location, the signal intensity quickly drops.

6.3.1. Confirming Imaging Sensor is Not Saturated

Since it is possible to saturate the sensor in an imaging system either toward white or black, it is necessary to ensure that intensity values are meaningful. Seeing if

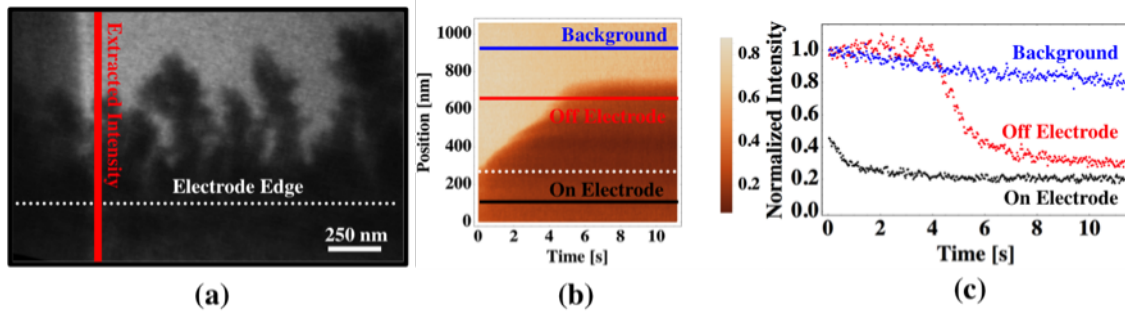


Figure 51: Sample frame from electrode deposition at 400 nA from **Appendix Video B.10** indicating (a) image intensity extraction location as red vertical line. White dotted line represents electrode edge location. (b) Contour plot of extracted intensities as a function of distance from the electrode (along the vertical line in (a)) and time. The black line is located on the electrode, the red is off the electrode, the blue line is the background intensity, and the white dotted line represents the electrode edge. (c) Normalized intensities as functions of time for the points indicated in **Figure 51b**. Black and red points correspond to intensity normalized by the background intensity of each frame. Blue points represent the background intensity normalized by the initial frame intensity to illustrate the decay in the electron beam (due to the thermal emission source).

the intensity measurements in the region analyzed lie between the maximum and minimum intensity level can serve as this check. **Figure 52a** the time history of the intensity at the four regions indicated in **Figure 52a**. We plot the mean and standard deviation of each region in **Figure 52b**. First, we notice the edge of the silicon wafer near the right edge of the image. Second, we see the electrode splitting the scene nearly horizontally, with the darker region in the top half of the image being the Pt electrode. The bottom left portion (the brightest in these bright field images), is a region that consists only of the two silicon nitride windows separated by the solution. We refer to these regions as the *window off-electrode*, R_1 (background), the *window on-electrode*, R_2 , the *silicon off-electrode*, R_3 , and the *silicon on-electrode*, R_4 . By tracking signal intensities in these regions as functions of time, we find that the region over the electrode and under the silicon edge always has a lower intensity value than any other region, implying that the intensity measures used in the other regions have not saturated the sensor toward its black level (0).

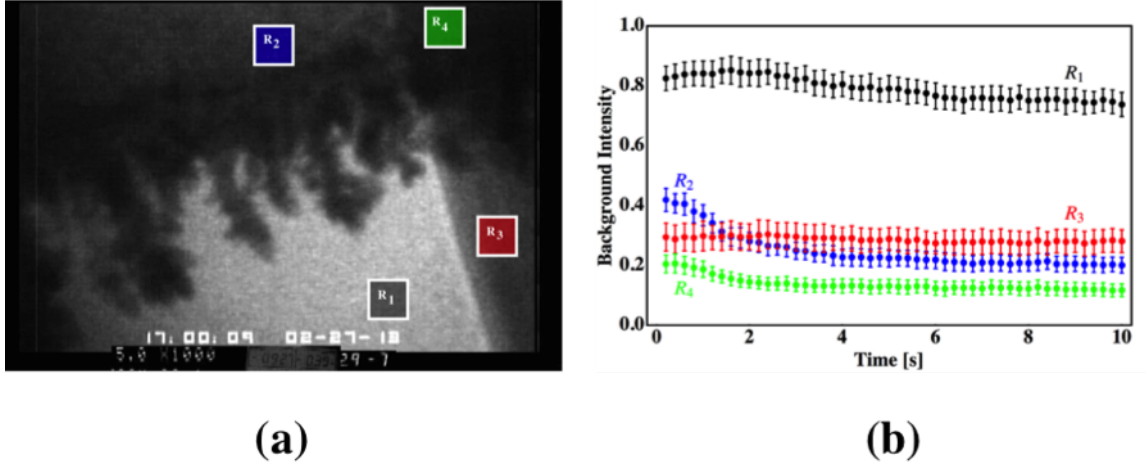


Figure 52: Further probing of intensities to ensure proper white balancing of image system (no saturation of detector). Identification of image regions (a) and their associated mean intensities and standard deviation as error bars (b).

6.4. Time for Growth to Become 2D

In this work we focus on the growth mode when the interface is two-dimensional, however, it is important to establish that the growth is actually 2D. We can do this by tracking the time it takes for the copper to grow on the electrode, until it reaches the height of the channel. Incoming ions will then preferentially deposit near the edge protruding into the bulk solution as previously discussed. By creating figures akin to **Figure 51c** for several applied currents, we see that the time it takes to become 2D decreases rapidly as the total applied current increases. **Figure 53** depicts the transition time to 2D growth as a function of the applied current.

6.5. Copper Thickness Estimate

Linear Estimate

The bright field intensity profile can also provide information about the thickness of copper deposited. We use the known electrode thickness (platinum on titanium

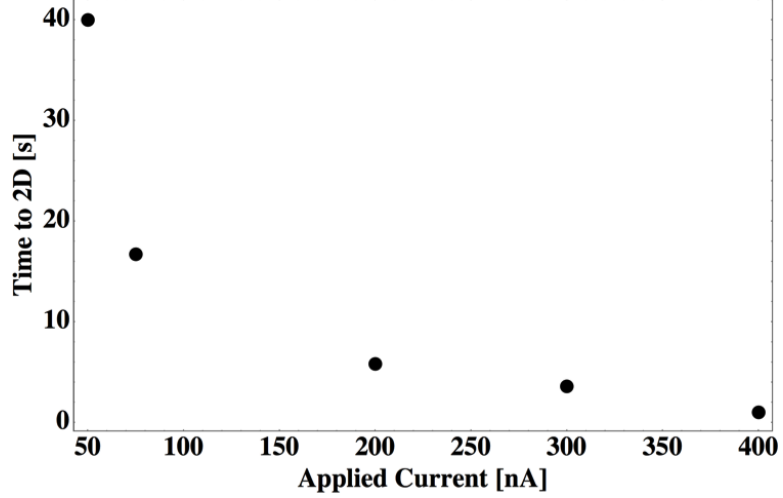


Figure 53: Total required deposition time until growth becomes essentially 2D as a function of applied current as extracted from the bright field intensity in the electrode region.

adhesion layer) to enable us to convert the intensity data into a thickness estimate. By taking the average intensity in a region on and off of the electrode prior to copper deposition and neglecting the effect of the ions in solution, we establish the attenuation due to the ~ 30 nm of Pt and its Ti adhesion layer. We assume that the attenuation is directly proportional to a material's atomic number, Z , the thickness of the deposited material, and that the electrode is 25 nm Pt on 5 nm Ti. This gives an average weighted atomic number of $Z_{ave} = \frac{Z_{Pt}T_{Pt} + Z_{Ti}T_{Ti}}{T_{Pt} + T_{Ti}} = 68.7$. The attenuation per unit thickness of the electrode is defined as

$$\delta_{electrode} = \frac{f_{background} - f_{Pt}}{t_{electrode}}, \quad (6.1)$$

where $0 < f < 1$ is the intensity measured over the location identified by the subscript and t is the thickness of the material at the measured location. We estimate the intensity drop of the copper, δ_{Cu} , by scaling the measured $\delta_{electrode}$ with the atomic

number ratio, giving

$$\delta_{Cu} = \frac{Z_{Cu}}{Z_{electrode}} \delta_{electrode}. \quad (6.2)$$

Finally, we estimate the thickness of copper at any point by measuring the intensity drop at that location (taking care to normalize the images when beam conditions vary) as

$$t_{Cu} = \frac{\Delta f}{\delta_{Cu}} = \frac{Z_{electrode}}{Z_{Cu}} \frac{\Delta f}{\delta_{electrode}}. \quad (6.3)$$

Equation (6.3) estimates an average copper thickness of $\sim 122 \text{ nm}$ in the regions off of the electrode, which is reasonable given the height of the device is defined by the lithography as 200 nm . This means that the maximum thickness of the copper should be limited to 200 nm by the silicon wafer. Since imaging is performed directly next to the edge of the window, the liquid layer is also close to 200 nm in the imaged region.

Exponential Estimate

Another estimate of the thickness can be made by using the exponential form of the decay in bright field intensity due to multiple scattering. As electrons pass through the material, the probability of being scatter increases exponentially [34]. The bright field intensity will go as

$$\frac{f}{f_0} = \exp[-t/l], \quad (6.4)$$

where f is the bright field intensity at a point, f_0 is the incident beam intensity (no material between beam and sensor), t is the thickness of the material, and l is akin to the mean free path. By taking the average intensities in regions with and without copper deposition, the thickness of copper can be estimated given the mean free path of electrons in copper. Taking the ratio of a region where copper grows to the background region (no growth) gives

$$\frac{f_{\text{Cu}}}{f_{\text{Background}}} = \exp[-t_{\text{Cu}}/l_{\text{Cu}}]. \quad (6.5)$$

Using a Rutherford scatter model, we estimate the mean free path of 300kV electrons in solid copper to be 828 nm [34]. Solving **Equation (6.5)** for the thickness of copper, t_{Cu} , to be 1091 nm . Meaning, the real copper thickness is likely to be between the linear estimate of 122 nm and the exponential estimate here. This implies the copper film is on the order of a few hundred nanometers, or nearly the thickness of the device.

6.5.1. Liquid Thickness Estimate in Imaged Region

For a device at 1 *atm* of pressure, the bowing of the membranes into the vacuum of the microscope adds 100 nm to the liquid thickness at the far edge of the viewing window as calculated using the solution to the membrane deflection of Maier-Schneider et al. [15]. **Figure 54a** shows a contour plot of the calculated liquid thickness around a typical viewing area. The location (0,0) represents the point where the electrode protrudes into the window region at a right angle to the silicon edge defined by the KOH back etch during manufacturing.

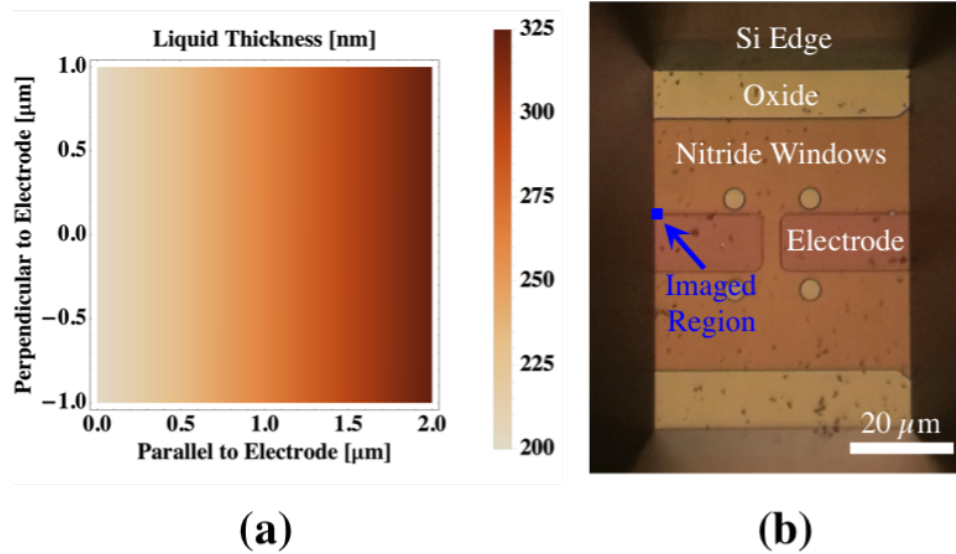


Figure 54: Calculated liquid thickness in the imaged region (a) due to membrane bowing when nanoaquarium is loaded into microscope. Illustration of image region compared to entire window region as imaged in an optical microscope (b) where the small blue box is the region typically imaged during electron microscopy. The device is unfilled in the optical image.

6.6. Control and Understanding Electrodeposit

In order to directly control the mass of copper deposited, galvanostatic conditions are selected when carrying out experiments. This allows quantitative comparison of the total current to the changes observed via bright field TEM. By assuming 100% of the current goes into the primary reaction of copper reduction, conservation of mass (or charge) gives the explicit number of fully reduced copper atoms without having to account for the complex, non-linear kinetics.

We compare the mass of material within the imaged region to the total charge passed by the potentiostat. The total volume of deposited copper can be calculated as

$$\Delta V_{Total} = \frac{MW}{\rho} \frac{I}{nF} T_{dep}, \quad (6.6)$$

where MW is the molecular mass, ρ is the density of the deposited material, F is the Faraday constant, $n = 2$ is the number of electrons per ion in the reduction reaction, I is the total current, and T_{dep} is the deposition time. The 100% efficiency assumption makes this the upper limit of the total copper reduced. The above calculation also assumes that the copper film is well-packed (zero porosity).

The local growth volume can also be calculated using parameters extracted from the imaging. The simple product of the estimated thickness and the area of the deposition gives the volume, mainly,

$$\Delta V_{local} = \Delta \bar{h} t_{Cu} w. \quad (6.7)$$

In **Equation (6.7)**, $\Delta \bar{h}$ is the measured change in average height within the window assuming we are in the 2D grow regime. The copper thickness t_{Cu} is estimated with the linear estimate, and w is the width of the imaged region.

To compare the volumes found in **Equation (6.6)** and **Equation (6.7)**, we normalize each quantity by the appropriate electrode width. Locally, we normalize by the width of the window, and globally we use the perimeter of the working electrode. The ratio of these two quantities, call it γ , is a measure of how evenly distributed the deposition is along the electrode overall, and takes the form

$$\gamma = \frac{V_{global}}{P_{WE}} \left(\frac{V_{local}}{w} \right)^{-1}. \quad (6.8)$$

P_{WE} is the perimeter of the working electrode as defined by the fabrication ($\sim 1380 \mu m$). For plain copper experiments, γ ranges from 1.6 to 7.5, implying that our estimates of mass are of the right order of magnitude and that deposition is fairly uniform along the perimeter of the electrode. Differences here can be attributed

to less than 100% efficiency deposition, non-uniformity in current density along the electrode, and geometric screening.

6.7. Current Densities

Current density is a useful quantity for describing electrodeposition, as it is a simple measure that can classify what type of growth is expected. There are several ways one might *a priori* estimate this quantity. The naive approach would be to divide the total current by the total area of the working electrode. For our cell geometry and the geometric screening that occurs during the 2D growth phase, this is a gross under estimate of the real current density. A better estimate would use the active area of the electrode, which is a much smaller region when the growth has reached the 2D mode of growth. Under 2D growth with a uniformly distributed current, the current density will be the total current over an area defined by the perimeter of the channel and the thickness of the device. This proves to be a more reasonable *a priori* estimate of the current density. In order to confirm this, we must first calculate the experimentally observed current density and check for consistency.

6.8. Estimating Local Current Density from Average Growth Rate

We estimate the current density as a function of position based on the rate of deposition. We assume that all the current is due to the reduction of copper, there are no side reactions involved, and the deposited material is solid copper (zero porosity). A mass (or charge) balance at the growing interface suggests that the volume growth rate of the solid phase is

$$\dot{V} = \frac{MW}{\rho} \frac{I}{nF}, \quad (6.9)$$

where MW is the molecular mass, ρ is the density of the deposited material, F is the Faraday constant, $n = 2$ is the number of electrons per ion in the reduction reaction, and I is the total current. When the growth is two-dimensional and takes place along area A , the growth rate of the interface \dot{h} satisfies the equation

$$\dot{h} = \frac{MW}{\rho} \frac{i}{nF}, \quad (6.10)$$

where i is the current density.

In our experiments, we record the position of the electrode-electrolyte interface as a function of time. If we consider the average interface height as measured from the electrode edge, we can check to see if the amount of copper deposited is consistent with the charge passed into the system. To do this, we estimate the average current density, which is the applied current divided by the active electrode area. Since the copper grows up on the electrode and then out in a 2D fashion, the average current density during the 2D portion of the growth will be the applied current over an area associated with the perimeter of the electrode multiplied by the height of the liquid cell ($2.76 \times 10^{-10} \text{ m}^2$).

6.8.1. Local Current Density from Experimental Observations

The local (measured) current density can be extracted directly from the experimental data using **Equation (6.10)** with the experimentally recorded growth rates. The local current density is given as

$$i_{local} = \frac{\rho n F}{MW} \dot{h}, \quad (6.11)$$

where \dot{h} is the experimentally measured local average interface velocity of the imaged region. The average velocity is extracted during 2D growth for several applied currents and a total of 94 separate observations. Using **Equation (6.11)**, we plot the local current density (i_{local}) as a function of applied current in **Figure 55**. We overlay a best fit line to the curve $i_{local} = aI$, where the intercept is fixed at 0. I is the total applied current. The reciprocal $\frac{1}{a} = 4.37 \times 10^{-10} \text{ m}^2$ is the effective area of the electrode. This is of the same order of magnitude as the area defined by the perimeter of the electrode ($\sim 1380 \text{ } \mu\text{m}$) and the device thickness (200 nm) of $2.76 \times 10^{-10} \text{ m}^2$.

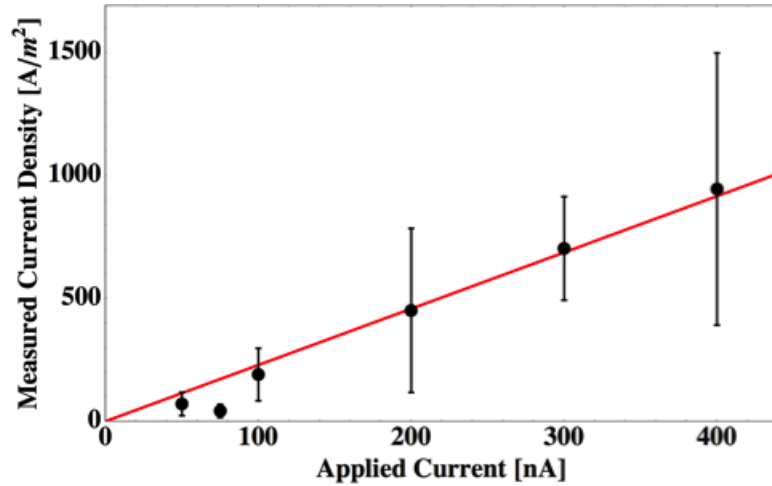


Figure 55: Measured Current Density as a function of applied current for Plain Copper deposition. The solid line is best-fit $i = aI$, where $a = 2.29 \times 10^9 \text{ (m}^2\text{)}$.

A particular example of each discussed current density is summarized in **Table 6** for the case in **Appendix Video B.10** at 400 nA total applied current.

Table 6: Estimated Current Density Using Various Methods

	Area	Average Velocity	i @ 400nA
<i>Entire Electrode</i>	$2.76 \times 10^{-8} \text{ [m}^2\text{]}$	-	$14.5 \text{ [A/m}^2\text{]}$
<i>Edge of Electrode</i>	$2.76 \times 10^{-10} \text{ [m}^2\text{]}$	-	$1450 \text{ [A/m}^2\text{]}$
<i>Average Velocity</i>	-	55.0 [nm/s]	$1500 \text{ [A/m}^2\text{]}$

6.8.2. Relating Interface Normal Velocity to Point-Wise Current Density

The spatial and temporal resolution afforded by liquid cell electron microscopy can be exploited further through local measurements. Morphology evolution during electrodeposition is governed by the normal current density at any given point [43, 44], which is in turn, directly related to the normal local speed of the interface via a mass balance. Similar to **Equation (6.11)**, we can define the point wise current density as

$$i(s, t) = \frac{\rho n F}{MW} v_N(s, t), \quad (6.12)$$

where $i(s, t)$ is the “point-wise current density” for a point s along the interface at time t , and $v_N(s, t)$ is magnitude or speed of that point in the direction normal to the surface at time t . The point wise normal velocity of the electrode-electrolyte interface is automatically extracted using our in-house interface tracking software.

6.9. Other Potential Mass Transport Mechanism

It is necessary to establish that diffusion is actually the dominant transport mechanism in our system in order to ensure the observed phenomena are properly analyzed. Several effects can facilitate convection and the motion of ions in solution and ought to be addressed. In this section, we establish that electromigration, electroosmosis, surface conduction, and advection are all negligible.

6.9.1. Full Supported Electrolyte (Negligible Electromigration)

Electrical migration adds significant complication in modeling the transport process of a depositing species. When the species being deposited is also transferring the current in solution, the mass transport is a function of the electrical field, which is

coupled with the concentration distribution. The use of a supporting electrolyte can decouple the distribution of depositing species (copper) and the electrical field as long as the solution is fully supported to the point where the supporting electrolyte is carrying most of the current in solution. The fraction of the migration current carried by a species in solution is given by the transference number,

$$t_j = \frac{z_j^2 D_j c_j}{\sum_k z_k^2 D_k c_k}, \quad (6.13)$$

where, z_j is the charge, D_j is the diffusion coefficient, and c_j is the concentration of ionic species j .

For the solution of 0.1 M CuSO₄ and 0.18 M H₂SO₄ used in our experiments, we find that the transference number of copper ions is 0.03, allowing us to make the simplifying assumption of a fully supported electrolyte as H⁺ and SO₄²⁻ carry 97% of the current passed through the solution. **Table 7** details the constants used for each species.

Table 7: Physical Constants of Species in Solution.

	Cu ²⁺	SO ₄ ²⁻	H ⁺
t_j	0.03	0.15	0.82
z	2+	2-	1+
D	$0.71 \times 10^{-9} \text{ m}^2/\text{s}$	$1.065 \times 10^{-9} \text{ m}^2/\text{s}$	$9.312 \times 10^{-9} \text{ m}^2/\text{s}$
c	0.1M	0.280 M	0.360 M

6.9.2. Electroosmosis Does Not Contribute Significantly

The existence of an electric double layer on the silicon nitride membrane exposed to the electrolyte can lead to several phenomena that result in relative motion of the fluid in the channel when an electric field is present. These transport mechanism can

aid or hinder diffusion's ability to supply reducible ions to the electrode interface.

The first mechanism we wish to consider is electroosmotic flow. This flow is generated when the electric field is parallel to the channel walls and ions in the electric double layer experience shear forces. The resulting motion of the ions is transmitted to the fluid via viscous interactions and creates bulk motion within the channel. To see if this flow is important, we consider the ratio of this advective transport rate to the diffusive rate, or the Peclet number. The Peclet number will take the form of

$$Pe = \frac{V_S l_D}{D}, \quad (6.14)$$

where V_S is the Smoluchowski slip velocity (or the effective velocity of ions near the slip layer experiencing the electroosmotic shear force), l_D is the diffusive length scale, and D is the diffusion coefficient. We can estimate the magnitude of the Smoluchowski slip velocity by [?]

$$V_S = \frac{\varepsilon \varepsilon_0 E \zeta}{\mu}, \quad (6.15)$$

with ε being the relative permittivity of the solvent (water), ε_0 is the vacuum permittivity, E is the electric field, ζ is the zeta potential of the silicon nitride, and μ is the solvent viscosity. For water at $25^\circ C$, an electric field on the order of $1 V/mm$, and a zeta potential of $25 mV$ [107] at a $pH \sim 2$, the Smoluchowski velocity is a few tens of $\mu m/s$. If we take the diffusive length scale to be $\sqrt{2Dt}$ with a time scale on the order of seconds, **Equation (6.15)** gives a Peclet number of 1.05. This means that the flow caused by electroosmosis is of the same order of magnitude as the diffusive transport rate.

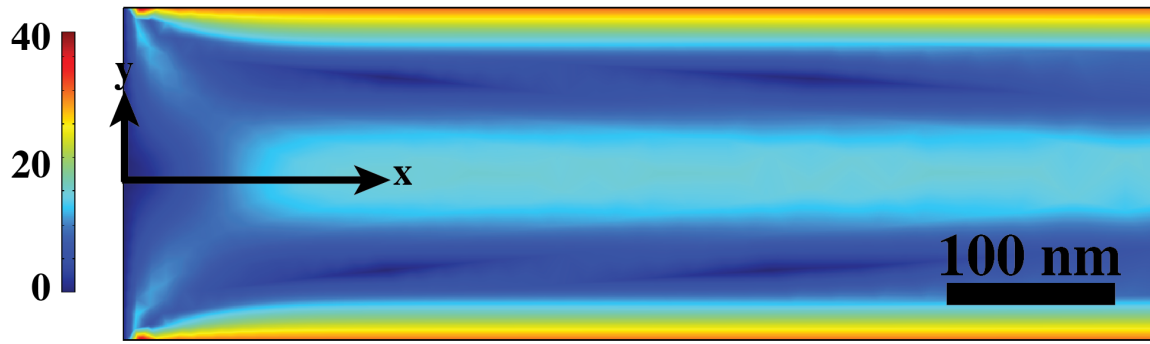
To obtain more detailed information on the role of electroosmosis, we turn to the

finite element program COMSOL. We consider a long, thin, rectangular channel with height fixed as the thickness of the experimental nanochannel (200 nm). For the transport of the copper ion, we apply a flux out of the system on one of the short edges as a function of applied current density. At the other, far end, we prescribe a constant concentration of the depositing ion (Cu^{2+}). The long, top and bottom walls have no flux boundary conditions. This is implemented in COMSOL’s Transport of Dilute Species Module. For fluid flow, we utilize the Laminar Flow version of the Single Phase Fluid Flow Module. The estimated Smoluchowski velocity, $30 \mu\text{m}/\text{s}$, is implemented as a slip boundary condition on the long walls, and all four walls are impermeable to fluid flow.

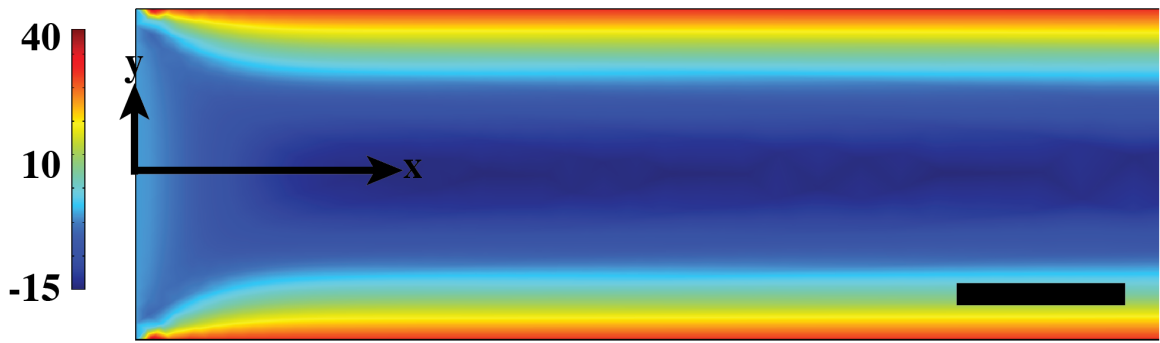
We run the simulation for a couple of applied current densities, and for the cases of when the slip velocity toward wall representing the electrode where deposition occurs, in the opposite direction, and the case where the slip velocity is 0. We extract the resulting time it takes to reach zero concentration of the depositing ion on the wall with the flux boundary as a measure of the Sand time. By comparing the cases with and without a slip velocity, we see very small differences in the Sand time, implying electroosmosis is not important for the transition to the diffusion limited regime of growth. However, it may still be important in other transport processes when an electric field is present and should be considered. The results from the COMSOL simulation are tabulated in **Table 8**. The resulting velocity profile near the depositing wall is also illustrated in **Figure 56** for the case of flow toward the right, or positive x-direction.

6.9.3. Surface Conduction

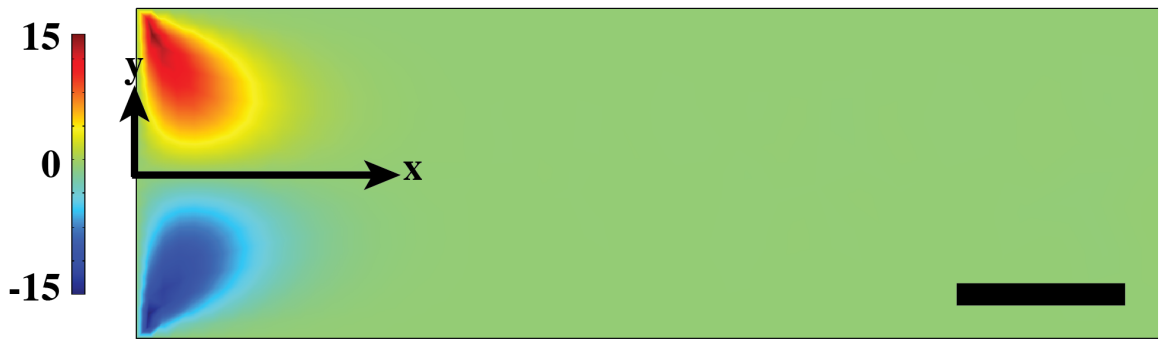
A second transport process facilitated by the electric double layer is surface conduction. In this phenomenon, the electric double layer acts as a “short circuit” path for



(a) Velocity Magnitude ($\mu\text{m/s}$)



(b) x-velocity ($\mu\text{m/s}$)



(c) y-velocity ($\mu\text{m/s}$)

Figure 56: Resulting velocity profile from COMSOL for a slip velocity of $30 \mu\text{m/s}$ at the top and bottom walls. Deposition occurs on left wall ($y = 0$). The figures show the (a) magnitude of velocity, (b) x component, and (c) y component near the depositing wall.

Table 8: Sand Time in 2D Rectangular Channel with Electroosmotic Flow

Current Density] [A/m ²]	Sand Time: Slip Velocity Toward WE of 30 [μm/s]	Sand Time: No Slip Velocity	Sand Time: Slip Velocity Away from WE of 30 [μm/s]
100	23 s	23 s	23 s
1000	0.24 s	0.24 s	0.24 s

the depositing ions, allowing counter ions (compared to the surface charge) to migrate along the electric field Han:2014in. Since silicon nitride has a positive zeta potential, SO₄⁻ counter ions will be conducted toward the counter electrode (CE) in a process that could hinder the diffusion of Cu²⁺ to the working electrode (WE). Following the analysis of Han et al [108], we can estimate the current associated with surface conduction to see how important its role is in the transport process. The current due to surface conductance

$$I_{SC} = \sigma_{SC}V, \quad (6.16)$$

where V is the applied voltage, and σ_{SC} is given by [108]

$$\sigma_{SC} = \frac{zeDA\varepsilon_p\sigma_s}{\tau Lk_bTh_p} \quad (6.17)$$

with z being the valency of the transported ion, e the elementary charge, D the diffusion coefficient, A the area of the electrode, ε_p the porosity of the channel (1 in the case of flat plates), σ_s is the surface charge density, τ is the tortuosity of the pores (1 for flat plates), L is the distance between electrodes, k_bT is the thermal energy, and h_p is the effective pore size. We estimate σ_s in the simplified Debye-Huckel limit

as

$$\sigma_S = \frac{\varepsilon\varepsilon_0\zeta}{\lambda}, \quad (6.18)$$

with ε being the relative permeability of the solvent (water), ε_0 is the vacuum permeability, ζ is the zeta potential of the silicon nitride, and λ is the Debye screening length. We estimate λ as a function of the ionic strength of the solution with

$$\lambda = \sqrt{\frac{\varepsilon\varepsilon_0RT}{F^2 \sum z_i^2 C_i}}, \quad (6.19)$$

where N_A is Avogadro's number, R is the gas constant, T is temperature, and C_i is the concentration of ionic species i with valency z_i . For the aqueous solutions of 0.1 M copper sulfate with 0.18 M sulfuric acid solutions at 25°C, an assumed zeta potential of 25 mV , and voltage of 1 V , **Equation (6.16)** gives a current associated with surface conductance of 6.6 nA , which is at least an order of magnitude smaller than the lowest currents used during this study. This implies that transport due to surface conduction is negligible for the present study, but should be considered for low current situations where the over potential is still order 1.

6.10. O₂ Production at Counter Electrode

Another possible cause of convection could be due to the production of oxygen at the Pt counter electrode. In order to estimate the worst-case scenario, we assume that the counter electrode is Pt only (no Cu coating, which is not always true as copper can be deposited during the etching cycles), and does not etch. Which is to say, that the production of O₂ is 100% efficient at the counter electrode. Next we consider the highest total current in our experiments 400 nA , and a duration of 10s.

This equates to the production of 6.24×10^{12} oxygen molecules. If we assume this generates a gaseous bubble instantly and assume a device pressure of 0.5 atm , the O_2 would increase the total volume in the device by $5.1 \times 10^{-13} \text{ m}^3$, or about 0.05% of the total device volume.

If we assume the volume of oxygen generated is converted into flow toward the working electrode, we can obtain an estimate of the average fluid velocity \bar{u} . For a device height of 200 nm , channel width of 1 mm , and experimental time of 10 s , $\bar{u} \sim 10^{-4}$. To see if the convection of ions due to this velocity is important, we calculate the Peclet number as

$$Pe = \frac{l\bar{u}}{D} \quad (6.20)$$

where we take the characteristic length scale of the experiment, l , to be on the order of 100 nm , and the diffusion coefficient of copper to be $0.71 \times 10^{-9} \text{ m}^2/\text{s}$. This results in $Pe \sim 10^{-2}$, implying diffusion is the dominant form of mass transfer.

6.11. Etching By The Solution is Negligible

Some of the copper may be oxidized by reactive species in the solution, especially during the off time in pulse plating. Using the data from the low current density deposition, we find the background etch rate and show that it is small compared to the deposition. For the 35 growth cycles (10 seconds each at 75 nA total applied current), the average interface velocity is $2.42 \pm 1.04 \text{ nm/s}$. During the 10 second off times between growths, the average interface velocity is $-0.14 \pm 0.31 \text{ nm/s}$. The results show that the off time growth is on average an etching of the interface at a rate that is an order of magnitude slower than the deposition.

6.12. Ohmic Heating in the Electrode is Negligible

Given the thinness of our electrode, it is important to ensure that the current passed does not cause significant heating. Ohmic heating takes the form

$$Q_{ohmic} \sim I^2 R T_{current}, \quad (6.21)$$

where I is the current, R is the resistance of the current conductor, and $T_{current}$ is the total time current is passed. We can estimate the resistance of the exposed electrode by assuming it takes the form of a rectangular extrusion made of platinum with a 30 nm thickness, 20 μm width, and a total length of 700 μm . This will serve as an over estimate of the resistor due to the fact the current will be transmitted out of the electrode along the whole perimeter and not just the tip of the electrode. The resistance will be given by

$$R = \rho_E \frac{l}{A}, \quad (6.22)$$

with ρ_E is the electrical resistivity (105 $n\Omega - m$), l is the length of the conductor, and A is the cross-sectional area. For our geometry and the highest total current of 400 nA over 20 s, we estimate the joule heating from **Equation (6.21)** and **Equation (6.22)** to be on the order of $Q_{ohmic} \sim 10^{-10} J$. We next estimate the temperature rise in the absence of any heat dissipation, a gross over estimate given much of the electrode would dissipate heat through the silicon which acts as a relatively large thermal mass, as

$$\Delta T = \frac{Q_{ohmic}}{\rho C V}, \quad (6.23)$$

where ΔT is the temperature rise, ρ is the electrode density (21.45 g/cm^3), and C is the heat capacity ($0.133 \text{ J/g} - K$). **Equation (6.23)** gives a temperature rise of 0.33 K for the case discussed, implying the ohmic heating is negligible.

6.13. Ohmic Heating in the Electrolyte is Negligible

Given the geometry of the liquid channel, it is important to ensure that the current passed does not cause significant heating in the solution. Ohmic heating can be estimated using **Equation (6.21)** using the appropriate resistance for the solution conductivity and cell geometry. We can estimate the resistance of the electrolyte by assuming it takes the form of a rectangular conductor made the copper sulfate solution with conductivity $\kappa \sim 1 \text{ S/m}$, 200 nm thickness, channel width of $1000 \mu\text{m}$, and distance between electrodes of $1500 \mu\text{m}$. The resistance will be given by **Equation (6.22)**. For the highest total current of 400 nA over 20 s , we estimate the joule heating in the solution to be on the order of $Q_{ohmic} \sim 10^{-5} \text{ J}$. We next estimate the temperature rise in the absence of any heat dissipation, a gross over estimate given much of the electrode would dissipate heat through the silicon which acts as a relatively large thermal mass, with **Equation (6.23)** and taking ρ , the electrolyte density, to be 1 g/cm^3 , C , the heat capacity, to be that of water or $4.183 \text{ J/g} - K$, and V , the volume, to be the volume of liquid in the cell or 1 nL . **Equation (6.23)** gives a temperature rise of 0.006 K for the case discussed, implying the ohmic heating of the solution is also negligible.

6.14. Sand Time

A useful metric employed by electrochemists when estimating when the diffusive regime will set in is the Sand time. The Sand time, in electrodeposition, is defined as the time it takes for the surfaces excess concentration of the depositing species to

drop to zero. This explicitly gives the conditions where the mass flux to the surface is dependent of transport processes other than the surface reaction. That is, the system is being driven fast enough that the surface reaction is not the limiting factor in the system. The simplest form of the Sand time comes from solving a one-dimensional diffusion problem with a constant (current density dependent) flux prescribed at a flat, plane in a semi-infinite media. The initial concentration is set to the bulk concentration and allowed to deplete according to the heat equation near the wall under the flux boundary condition, and the solution concentration remains fix far away from the wall. The solution for the time where the surface excess concentration goes to zero for galvanostatic deposition is [109]

$$\tau = \frac{\pi D}{4} \left(\frac{C_0 n e}{i_0} \right)^2, \quad (6.24)$$

where D is the diffusion coefficient, C_0 is the bulk concentration of depositing species, n is the valency of depositing species, and i_0 is the current density.

We can go further by accounting for a two-dimensional geometry and applying more realistic boundary conditions to solve the problem of when the local concentration is depleted. We consider a half wavelength of a sinusoid to imitate the roughness we see during electrodeposition. The amplitude (500 nm) and wavelength (500 nm) are taken to be similar to those observed in experiments. We are still neglecting to account for the moving boundary and the time evolution of the roughness, but can none-the-less begin to investigate the effect of geometry on depletion along the electrode. We apply Bulter-Volmer kinetics to the wall with the constraint that the total average current is held constant (the integral of the current density normal to the surface is a constant). The problem is implemented in COMSOL and solved with the described Butler-Volmer kinetics on the sinusoidal wall where there is deposition,

symmetry at the side walls (enforced with no flux), and fixed far field concentration. The equilibrium potential for copper deposition is taken to be -0.33 V [121], the heterogeneous rate constant is taken as 0.001 m/s [121], and the cathodic transfer coefficient is assumed to be 0.5. We solve the time-dependent problem and extract the surface concentration at the peak and valley each as a function of time. An example of the evolution of the surface concentrations are illustrated in **Figure 57** for a total average current density of 500 A/m^2 and a snapshot of the 2D concentration profile is seen in **Figure 58**. We see that the valley concentration remains below that of the peak until the concentrations go toward zero. We identify a sand time when the valley concentration (always the lower valley since it is partially screened) drops below $1\text{ }\mu\text{M}$.

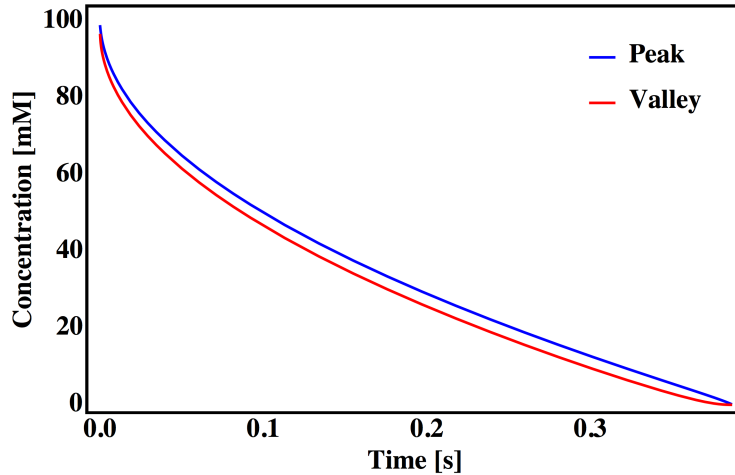


Figure 57: Surface concentration of copper at peak and valley of half-wavelength sinusoid for total average current density of 500 A/m^2 . The amplitude is 500 nm and wavelength is 500 nm .

In order to compare to a one-dimensional case, we also perform the calculations for the same conditions for a flat plate wall - akin to the traditional Sand time calculation, but with the more complicated Butler-Volmer type kinetics. We compile several simulations across the range of current densities in our experiments for a fully

Concentration (M)

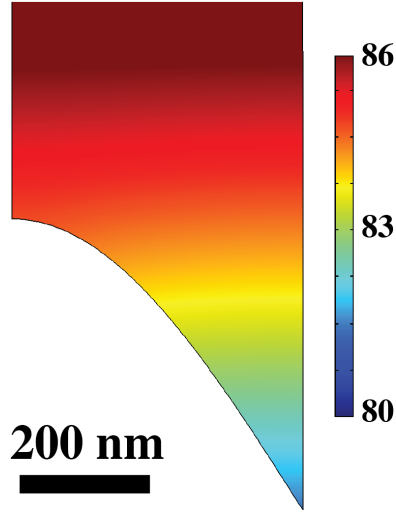


Figure 58: Concentration of copper near half-wavelength sinusoid after 0.01 s at total average current density deposition of 500 A/m^2 . The amplitude is 500 nm and wavelength is 500 nm.

supported copper solution in **Table 9**. We find that the flat plate case has a sand time that is ~ 3 times longer than that of the sine wave case and will be related to the increased arc length of the surface.

Table 9: Sand Time given Butler-Volmer Kinetics with Constant Total Average Current on a Sinusoid and Flat Plate

Current Density [A/m^2]	Sine Wave	Flat Plate	Ratio
288	1.15 s	3.53 s	3.07 s
500	0.39 s	1.17 s	3.00 s
1000	0.098 s	0.29 s	2.96 s
1500	0.044 s	0.13 s	2.95 s

6.15. C-Rate

When studying battery cycling, the C-Rate is a convenient metric to describe the charging rate. A C-Rate of 1 is defined as the rate in which a given battery is fully

charged in one hour. This measure normalizes for varying capacities and geometries. For the version of the nanoaquarium used in our experiments, it would be useful to calculate the C-Rate as a function of applied current and solution concentration. For this calculation we need to know the total volume of the device, which could be complicated by the solution trapped within the o-rings just outside the nano channel. Since our experiments are on the order of 10 seconds in length, we compare the diffusion time from the inlet to window region with experimental time to see if diffusion from these reservoirs is significant.

Next, we calculate the required total current to achieve a C-Rate of 1. This will merely be the current required to fully reduce all of the copper atoms within the cell in 1 hour (assume 100% efficiency in the reduction). For a 100 *mM* solution of CuSO_4 and a device volume of 1 *nL*, the current associated with a C-Rate of 1 is 5 *nA* total applied current. This means the depositional C-Rate employed in experiments in this work ranges from 10 to 100 and the discharge (etching rate) is often 10.

If we consider one-dimensional diffusion, then the diffusion time will be given by

$$t_{diff} = \frac{x^2}{2D}, \quad (6.25)$$

where x is the length scale from the device inlet to the working electrode, and D is the diffusion coefficient of copper. The distance from the inlet to the standard working electrode is on the order of 1 *mm*, and copper's diffusion coefficient is $0.71 \times 10^{-9} \text{ m}^2/\text{s}$. This gives a diffusion time of over 700 seconds. Since this time is an order of magnitude greater than our experimental time scales, we assume that diffusion from the inlets is slow compared to our depletion rate, and we define our C-Rate based on the volume within the device, and do not consider the solution trapped in the o-rings.

CHAPTER 7 : Morphological Evolution During Copper Electrodeposition

Despite its importance, critical questions still remain in understanding the transition from roughening regimes to diffusion-limited growth during electrodeposition. Electrochemical processes play a pivotal role in nanoscale science, from nanomanufacturing to battery technologies. Detailed nanoscale observations of the metal-electrolyte interface evolution during deposition and stripping provide crucial insight into the onset of growth instabilities. Morphological instabilities can lower the quality of electroplated coatings and cause catastrophic failure during the cycling of rechargeable batteries, yet are also useful in forming porous and patterned structures. Liquid cell electron microscopy allows for real-time, nanoscale imaging of metal-electrolyte interfaces during deposition [2, 3, 21–23, 26–28]. In this chapter, we gain insights into the mechanisms leading to the onset of instability utilizing kinetic roughening theory as a means to understand our quantitative data. We study these processes with a unique tool (the nanoaquarium) that facilitates real-time imaging of nanoscale processes in liquid media in situ with the high resolution of the electron microscope. In this chapter we describe the results in which we directly observe the onset of growth instabilities. We see a transient roughening regime prior to the formation of large asperities. Our nanoscale resolution allows us to measure the normal growth velocity along the interface during the early transient phase, providing a clear picture of the current density distribution along the imaged interface. We further investigate two means of controlling morphology through the use of pulse plating and the addition of lead as an inorganic additive to suppress the formation of large asperities.

7.1. Copper Growth Regimes

The electrodeposition of copper will follow three primary regimes. For low overpotentials, copper will nucleate as distinct islands that grow in nearly hemispheres. An example of growth in this regime is found in **Figure 59** for low current galvanostatic deposition. If the overpotential is increased, say to increased current flow, then the copper will begin to grow as a hard packed film since the number of nucleation sites grows exponentially with overpotential [27]. This type of film growth is shown in **Figure 60**. Lastly, for high current density (and larger overpotential) deposition, the growth will become diffusion limited and result in large asparities as is seen in **Figure 61**. In the following sections, we focus on the latter two growth regimes and the relationship between the two.

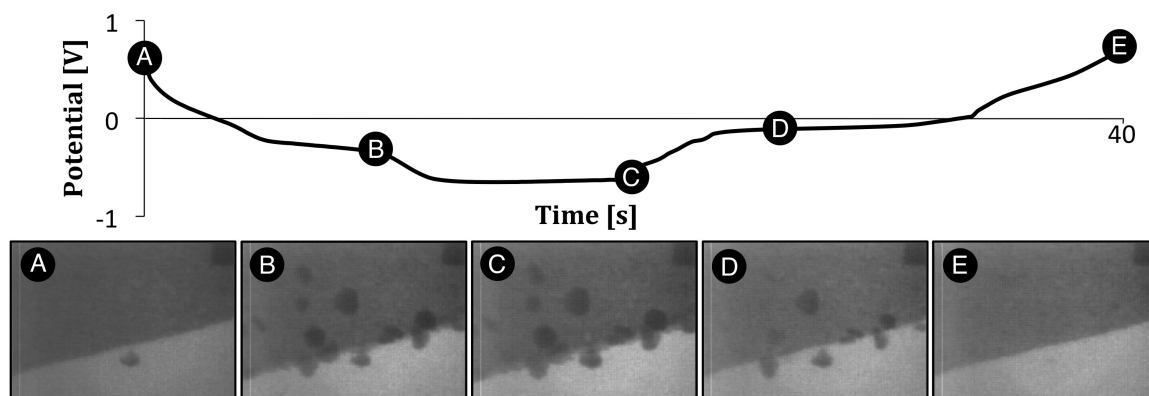


Figure 59: Galvanostatic deposition and etching at 50 nA for 20 s each in 0.1 M CuSO_4 and $0.18 \text{ M H}_2\text{SO}_4$. This deposition results in island or nucleate growth. Insets: TEM bright field images recorded at time of A) 0, B) 10, C) 20, D) 27, and E) 40 s since the start of current flow. Each image is $1.8 \mu\text{m}$ horizontally.

7.2. Transition to Diffusion Limited Growth

Morphological instabilities can lower the quality of electroplated coatings and cause catastrophic failure during the cycling of rechargeable batteries, yet are also useful in forming porous and patterned structures. For this reason it is important

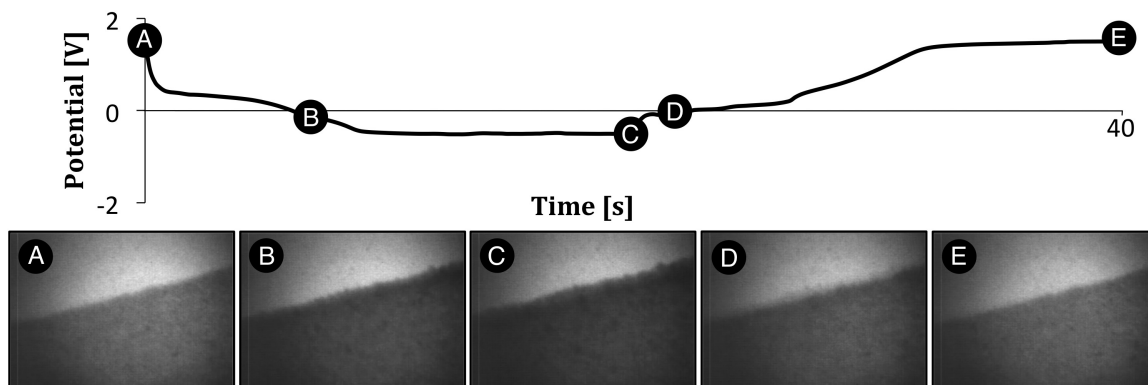


Figure 60: Galvanostatic deposition and etching at 100 nA for 20 s each in 0.1 M CuSO_4 and $0.18\text{ M H}_2\text{SO}_4$. This deposition results in compact growth. Insets: TEM bright field images recorded at time of A) 0, B) 7, C) 20, D) 22, and E) 40 s since the start of current flow. Each image is $1.8\text{ }\mu\text{m}$ horizontally.

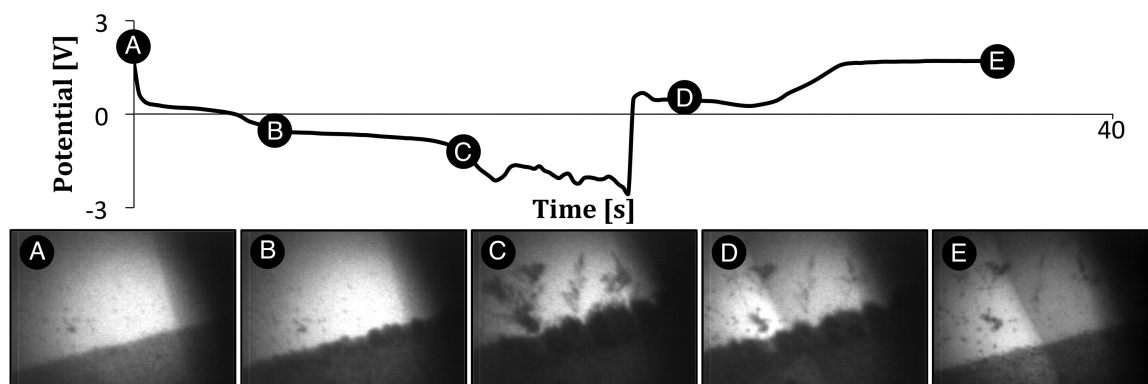


Figure 61: Galvanostatic deposition and etching at 200 nA for 20 s each in 0.1 M CuSO_4 and $0.18\text{ M H}_2\text{SO}_4$. This deposition results in dendritic growth. Insets: TEM bright field images recorded at time of A) 0, B) 7, C) 15, D) 23, and E) 36 s since the start of current flow. Each image is $1.8\text{ }\mu\text{m}$ horizontally.

to develop an understanding of different growth regimes and develop strategies to modify growth interface stability during deposition. Liquid cell electron microscopy allows for real-time, nanoscale imaging of metal-electrolyte interfaces during deposition [2, 3, 21–23, 26–28]. We have therefore used this technique to gain insights into the mechanisms leading to the onset of instabilities and means for controlling the resulting morphologies.

The governing physics of growth instabilities and their temporal evolution has been studied intensely as it is key to controlling the structure and composition of deposited materials. Modeling the linear stability of solid-liquid interfaces is a well established field for both solidification and electrodeposition [99, 110, 111]. However, these analyses are limited to nearly steady-state conditions and do not account for the complex transient interaction between multiple wavelengths [42]. The initial stages are critical, but have been difficult to access experimentally prior to the development of liquid cell electron microscopy. The length and time scales associated with this technique enable direct observation [21, 31, 112–114], suggesting that it should be possible to measure deposition physics during these critical moments. Here, we use liquid cell electron microscopy to quantify the transient growth of interfaces during galvanostatic deposition of copper from acidic electrolytes. We extract the explicit electrode-electrolyte interface as a function of time, which gives, among other measures, the normal growth velocity at each point along the interface, a direct measure of the point-wise current density on a time and a length scale previously inaccessible. We find that initial stages of growth can be understood through Kinetic Roughening Theory [41, 42, 115–117]. At longer times, we identify a transition in growth mode and show that this is consistent with the onset of diffusion limited growth. The non-uniform distribution of current density along the interface ultimately leads to a

rapid increase in the amplitude of surface asperities [118], and we show that this is the critical component for understanding the onset of diffusive instability. Based on these results for the transition between regimes, we discuss the use of two strategies for controlling instabilities by delaying the onset of diffusion limited growth: active modulation of the current by periodically pausing current flow, and the use of Pb as an inorganic additive to mediate the deposition reaction passively and avoid large asperities.

Figure 62a and **Appendix Video B.10** show the development of interface instability during the deposition of copper from an acidified copper sulphate solution. The copper first grows up from the electrode and quickly becomes two-dimensional with growth primarily in the direction perpendicular to the electrode. Analysis of the intensity implies that the growth is essentially two-dimensional after ~ 0.83 s. From here, we consider the two-dimensional growth where an initial roughening regime, the onset of the diffusive instability, and the initial development of nanoscale ramified growth are visible. Galvanostatic deposition conditions were used, and calibrations were carried out to understand the reproducibility of this type of data and the relationship between the macroscopic parameter of applied current and the local current density as discussed in **Section 6.8.1**. As a means to quantifying the growth, we developed an unsupervised, non-parametric image-processing algorithm [Schneider Imaging] to robustly extract the electrode-electrolyte interface from the image sequence. The resulting edge is shown as an overlay in **Figure 62a**. In particular, the videos enable one to estimate the local current density by converting the local growth rate (rate of advancement) normal to the local interface (**Section 6.8.2**). In **Figure 62**, the measured average growth rate of 55 nm/s implies a local current density of 1500 A/m². We can also calculate a device-averaged value, 1450 A/m², obtained by

dividing the total current (400 nA) by the electrode perimeter ($1380 \text{ }\mu\text{m}$) and active thickness (200 nm , the nominal thickness of the liquid cell) for the two-dimensional portion of the growth. The similarity in the magnitudes of these two values suggests that the electrode behaves similarly in the region under observation and the regions outside the liquid cell viewing window.

Figure 62b shows that the growth appears to proceed in two distinct regimes that would be otherwise veiled in the qualitative images. We distinguish these regimes by tracking the position of the interface perpendicular to the Pt electrode's edge (defined by lithography) into the electrolyte and showing the maximum, minimum and average height, respectively. At $\sim 3.1 \text{ s}$, the minimum height goes essentially stagnant, while the maximum height grows more rapidly than at earlier times. Note that the average height continues to grow at a constant rate - this is expected, given the galvanostatic conditions, and is a consistency test for the experiment. Because of the high spatial resolution, we can go further and explicitly track the normal growth velocity point-wise along the interface. **Figure 62c** shows a colored version (heat map) of the normal speed at each point during growth. As growth proceeds, the initially uniform growth velocities become more varied with the peaks having the highest velocities and the valleys growing slowly or not at all. Kinetic roughening models do not address these types of spatially-resolved features of growth, but instead model average parameters like the root mean square (RMS) roughness [41,42,115–117]. To guide our modeling, we therefore also plot the RMS roughness in **Figure 62d**. The roughness appears to scale as a power law in time with two distinct growth exponents, indicated on the graph. In the early stages, during the predominantly planar phase, roughness grows slowly with an exponent of 0.3, but after the transition at 3.1 s , the exponent increases dramatically with the rapid asperity growth and stationary valleys leading

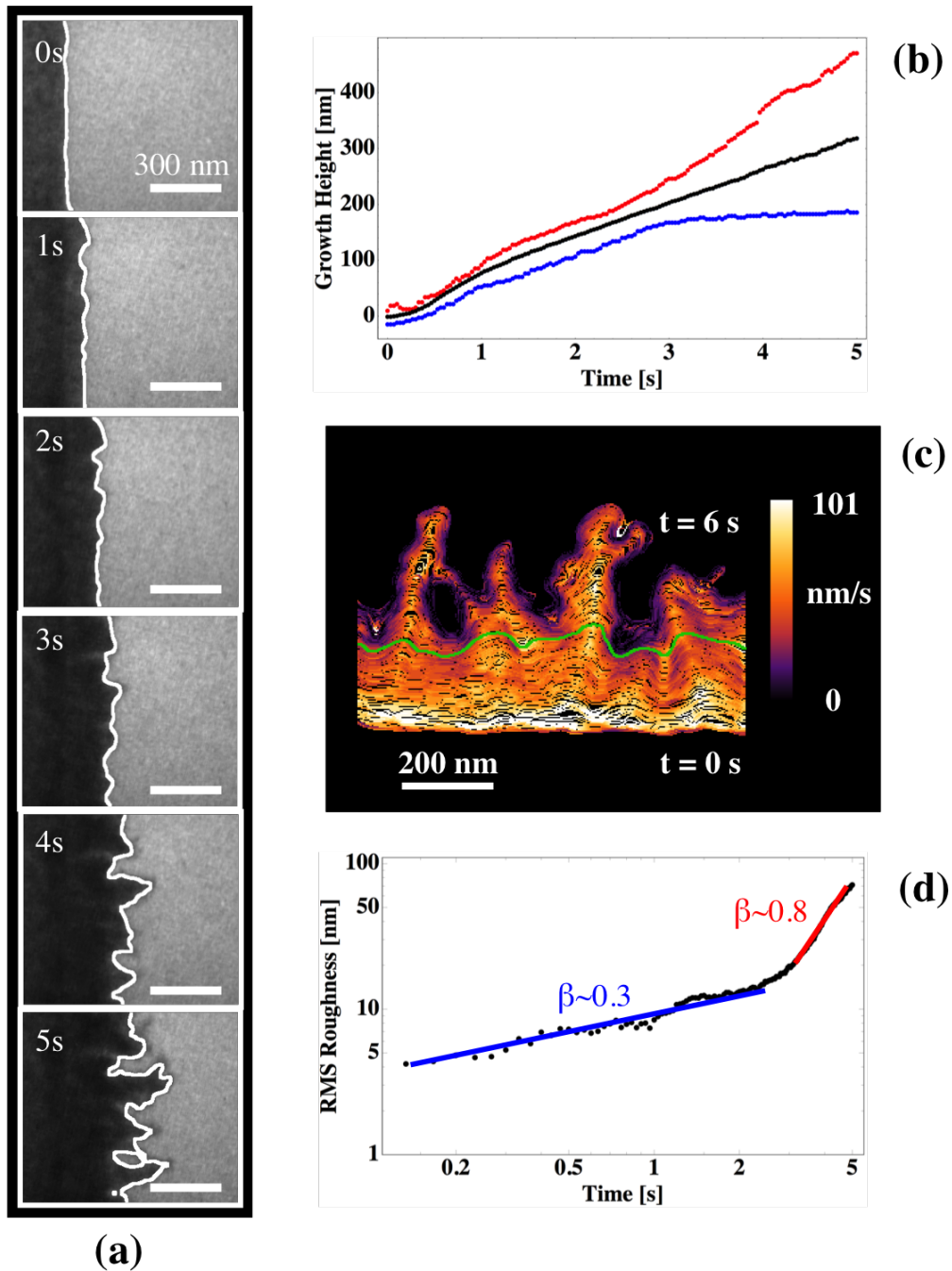


Figure 62: Galvanostatic deposition with average current density of 288 A/m^2 and local average growth rate of 67 nm/s (equivalent to 1823 A/m^2) in 0.1 M CuSO_4 and $0.18 \text{ M H}_2\text{SO}_4$. (a) Images recorded in bright-field conditions. Times in seconds since current flow began. The transition time is $\sim 3.1 \text{ s}$. (b) Average, maximum, and minimum growth height as a function of time. (c) “Heat Map” of normal growth speed with white being fastest and blue/purple being slowest (d) Log-log plot of RMS roughness of interface as a function of time. Best fitting straight lines are shown with exponents indicated.

to a value around 0.8.

The morphological development and the growth exponents appear consistent with a transition between two well known growth modes, an initial kinetic roughening regime followed by diffusion-limited growth. In kinetic roughening, growth takes place by the random arrival of material. This causes the surface to roughen stochastically (at least, at early times). Smoothing forces may be present, and if so the roughness will not continue to increase, but will saturate. In diffusion-limited growth, incoming ions from the bulk solution follow the path of highest conductivity and deposit on the highest local asperity (called screening). Low points on the growth front are deprived of incoming ions. Asperities thus develop and consume a disproportionate amount of the depositing ions causing an acceleration of maximum height. The growth exponent characterizes the nature of the underlying physics. As a point-of-reference, an exponent of $\frac{1}{2}$ results from a Poisson process, or one with a purely random, uniform deposition [115]. Values below $\frac{1}{2}$ imply the presence of driving forces that smooth the surface such as surface diffusion and surface tension [116]. Values above $\frac{1}{2}$ imply the growth asperities are compounded. The values 0 and 1 bound the growth exponent, making the Poisson process value of $\frac{1}{2}$ a good dividing line for determining the controlling physics (reactions limited vs diffusion limited) [115]. The early stage of growth in **Figure 62**, having a growth exponent of 0.3, implies random deposition but with forces acting to smooth the surface, presumably surface diffusion. The later development of large asperities and the exponent of 0.8 suggests the onset of diffusion-limited growth, with spatial variation in current density becoming dominant in leading to preferential deposition at the peaks of the growth.

We would expect the transition to diffusion limited growth to occur at a time given by the Sand equation [119], which solves for the time it takes to reach zero

surface concentration at an electrode given a constant, uniform current density (in one dimension). For the solution chemistry (0.1 M Cu^{2+}) and parameters of **Figure 62** (1450 A/m^2 , obtained by applying 400 nA over an electrode perimeter of $1380\text{ }\mu\text{m}$ and active width of 200 nm), the Sand equations estimates the transition time of 0.1 s , starkly different from the measured time it takes for the troughs to go stagnant of 3.1 s . The videos provide local current density directly by converting the local growth rate (increase in area of the deposit) to a number of deposited atoms over the projected length of the interface, as detailed in the supplement. The extracted average growth rate of 55 nm/s results in a measured current density of 1500 A/m^2 , consistent with the device averaged current density.

Although the transition to the diffusively controlled regime is clear in the data, an important fundamental question remains; how, not just when, does the transition emerge? Direct simulation is difficult since the point-wise normal growth speed or current density distribution controls the subsequent interface geometry, but conversely, the morphology governs the current density distribution. However, the coupled relationship between geometry and current density has been solved for the case of a growing sinusoidal surface [118], leading to an expression relating the deviation from the average current density to deviation from the mean height. **Figure 63a** shows this relationship (solid line) along with the point-wise current density normalized with the average current density as a function of the deviation of the asperity's height from the average displacement of the interface. for the data in **Figure 62**. Data is shown at time from the start of deposition at 0.0 (black points), 2.0 (blue points), 3.0 (green points), and 3.8 (red points) seconds. Data from before the transition of 3.1 s is strongly clustered: there is small deviation from the mean height (standard deviation of 4 and 20 nm at times 0 and 3 s , respectively), and velocities are similar along the

growth front (standard deviation of 1 and 11 *nm* at times 0 and 3 *s*, respectively). As the onset approaches, the data spreads: points deviate from the mean and their current density also deviates in a way that is consistent with the model in [118]. Points that protrude further into the solution grow faster and their counterparts closer to the electrode grow more slowly, screened from incoming ions. At the transition time the valleys go stagnant and the peaks continue to grow. This is also clear from **Figure 63b**, which shows the maximum and minimum current densities normalized by average current density as a function of time. The distinguishing feature of the onset of diffusion-limited growth appears to be that the minimum current density approaches zero. The maximum current density does not increase very rapidly, as one might expect given the lack of growth of the valleys. This is presumably because asperities extending into the solution gain access to additional ions, but eventually transition once again to a new growth mode - the tip splitting regime where perturbations at the tip undergo roughening and then diffusion limited growth. This process is the origin of the fractal nature of dendrites where self-similar geometries are observed on many length scales. To characterize the asymmetry of the current distribution, **Figure 63c** shows the relative growth rate of the highest quartile of points along the growth front. Initially the top 25% of the growth front consumes $\sim 30\%$ of the incoming ions. After the transition, the top 25% consumes over 50% of the incoming ions. This is an important difference compared to the kinetic regime of growth discussed next.

We would expect, based on the equations governing diffusion, that growth at a lower average current density should take longer to transition into the diffusion-limited regime (in the absence of convection). In **Figure 64** we show the results of growth under lower current density conditions. **Appendix Video B.11** showing the complete data set is available in the supplement. In this case, the total current is

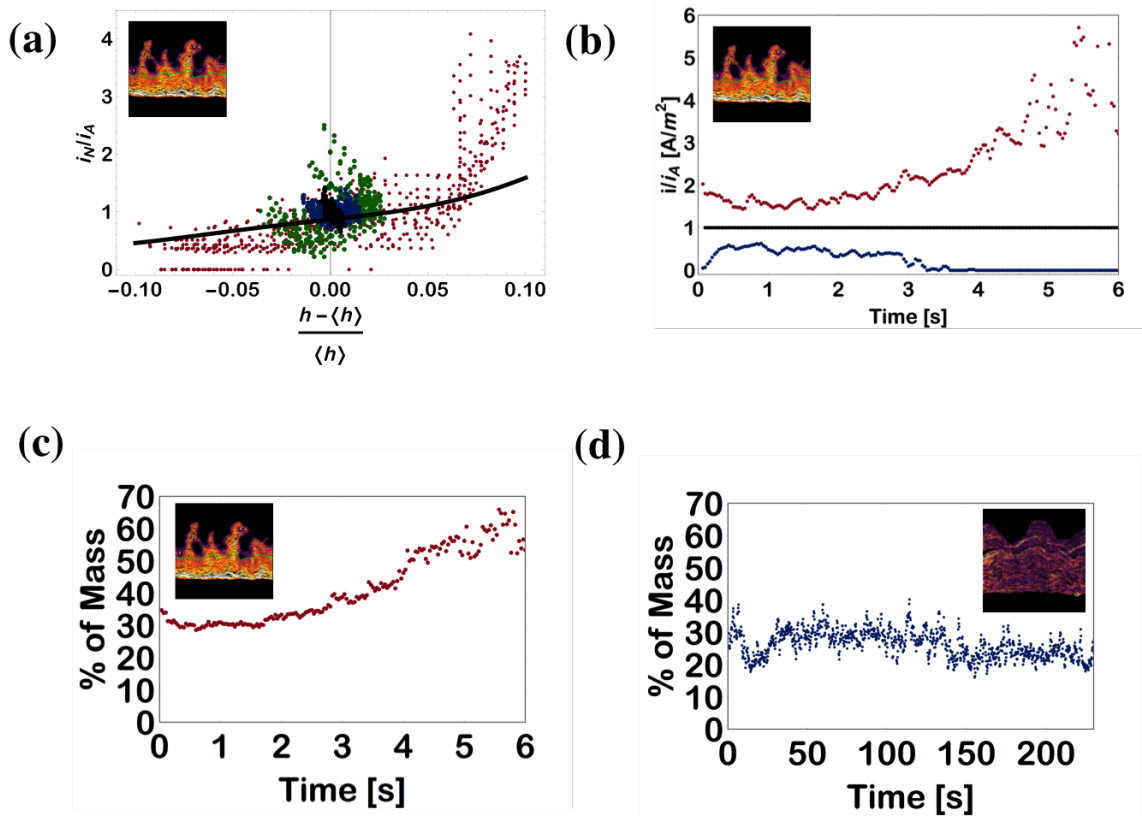


Figure 63: a) Current density normalized by average current density as a function of deviation from the mean height for growth of **Figure 62**. b) Max, Min, and average current density normalized by limiting current for the experiment shown in **Figure 62**. Percent of mass consumed by top quartile of points during growth during the experiments in c) **Figure 62** and d) **Figure 64**.

5x lower than in **Figure 62** (75 rather than 400 nA) and, in addition, the current is interrupted for 10 s after every 10 s of growth to allow for diffusion to replenish the ions next to the growth front. These deposition parameters keep us far from the diffusion limited regime throughout the entire set of deposition cycles in order to isolate the reaction limited physics governing growth when there is always sufficient surface excess concentration. **Figure 64b, c** and **d** show the same measures as in **Figure 62**, i.e., the surface evolution and current density distribution, the peak and valley heights, and the RMS roughness. These parameters are qualitatively different from those in **Figure 62**. The RMS roughness (**Figure 64d**) initially increases with growth exponent of 0.3, a value similar to that in the first regime of **Figure 62** and consistent with values reported in the literature [41], but then reaches a plateau (growth exponent ~ 0). The peaks and valleys continue to advance (**Figure 64b**); the valleys do not stagnate. The peak-valley separation reaches a nearly constant value after the initial stages of growth. The normal growth speed or current density (**Figure 64c**) is more uniformly distributed than in **Figure 62**. The percent consumption of mass by the top quartile of points (**Figure 63d**) is similar to the initial value in the higher current density growth, with the top 25% of points receiving about 30% of the incoming mass, but unlike **Figure 63c**, this number remains constant throughout deposition, implying that there is little inequality in mass distribution even though the surface is initially roughening with the same growth exponent.

The low current density growth overall appears to follow the behavior expected for ballistic deposition [115]. At early times, the exponent below 0.5 suggests random growth with some smoothing. After a time the roughness saturates as the growth is left in the reaction-limited regime.

Comparing the high and low current density data, it appears that both start with a

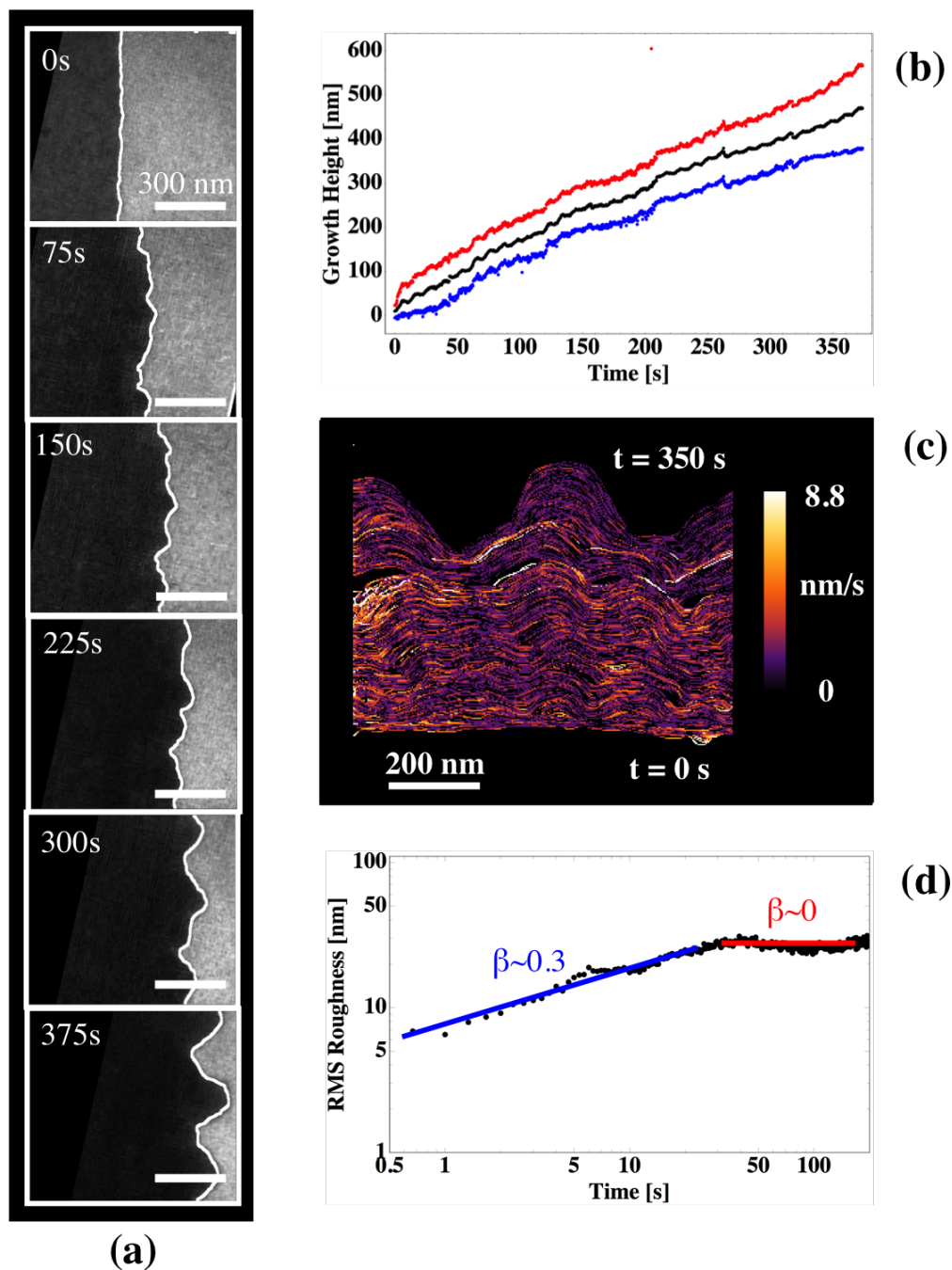


Figure 64: Galvanostatic deposition with average current density of 54 A/m^2 and local average growth rate of 1.3 nm/s (equivalent to 35 A/m^2) in $0.1M \text{ CuSO}_4$ and $0.18 M \text{ H}_2\text{SO}_4$. (a) Images recorded in bright-field conditions extracted from the video sequence found in the **Appendix Video B.11** with detected edge as overlay. Times in seconds since current flow began. (b) Average, maximum, and minimum growth height as a function of time. (c) “Heat Map” of normal growth speed with white being fastest and blue/purple being slowest (need to redo with a color scale) (d) Log-log plot of RMS roughness of interface as a function of time. Best fitting straight lines are shown with exponents indicated.

regime that is consistent with kinetic roughening models. At low current density with pausing, growth remains in this regime: the growth front roughens then saturates. At higher current density the same initial roughening occurs, but the asperities formed grow rapidly in an unstable manner. What causes the low current density growth to stay in the reaction limited regime? The surface excess concentration of copper ions is never driven close to zero, ensuring there are always ions available to deposit at all points along the electrode interface. This is evident in the measure of point-wise normal velocity (current density), where the uniformity in velocities implies uniform current density, which, assuming Butler-Volmer type kinetics, implies uniform, non-zero concentrations of copper ions along the interface. It therefore appears that the growth regime is dictated by the macroscale diffusion physics, while the morphology is the direct consequence of the local current density distributions.

7.3. Means of Morphology Control

A practical consequence of the behavior observed at higher current density is that the instabilities grow from random perturbations caused by the initial kinetic roughening regime. This implies that growth stability can not be improved by, for example, starting from a very smooth surface. To suppress instabilities, other strategies must therefore be used. We have examined two strategies, pulse plating and additives, and describe below nanoscale observations of each.

Pulse plating is a well-known electrodeposition technique for improving surface roughness [120]. **Figure 65** and **Appendix Video B.12** show a set of pulsed experiments where the current is on for one second followed by a five second waiting time with no applied current. The off time allows diffusion to replenish the solution near the electrode, which in turn allows for uniform growth during subsequent pulses

of times less than the transition time. The current density used implies a transition time of over 3 s from the previously observed experiments. **Figure 65a** shows that growth instabilities do not develop, even with asperities present on the underlying substrate. By tracking the max, min, and average height in **Figure 65b**, we see there is initially little growth in distance between the max and min when pulsing. Further confirmation comes when considering the point-wise normal speed distribution, which is shown in **Figure 65c**. The RMS roughness shown in **Figure 65d** has an average growth exponent, which includes the off time, of 0.48 during the four total cycles. This growth exponent is approximately akin to random uniform deposition and means the surface is governed by physics that should not develop large asperities like its continuous growth counterpart. The local current density increases from 142 A/m^2 to 539 A/m^2 for the last four cycles shown based on the rate of average height growth for the total period including off time. We include the off time in the velocity calculation as the diffusive behavior is governed by the total time. This increase in growth rate is due to a bubble that moves into the imaging region after the first 4 cycles (i.e., at 24 s) (it ultimately can be seen at the end of **Appendix Video B.12**), causing the liquid layer to thicken as the silicon nitride membranes bow out into the vacuum. The data in **Figure 65** show that pulse plating can be used to grow in a stable mode. By varying the applied current, the period, and on/off time ratio, one can vary independently the diffusive limit and the reaction kinetics [120].

Additives can be used to control growth morphology during electrodeposition. Here, we show the effects of lead on copper plating. **Figure 66a** and **Appendix Video B.13** shows a set of experiments where the electrolyte includes saturated $PbSO_4$; the surface appears smooth, compared to **Figure 62**. The growth rate is constant during deposition as seen in **Figure 66b** and stagnant when the current

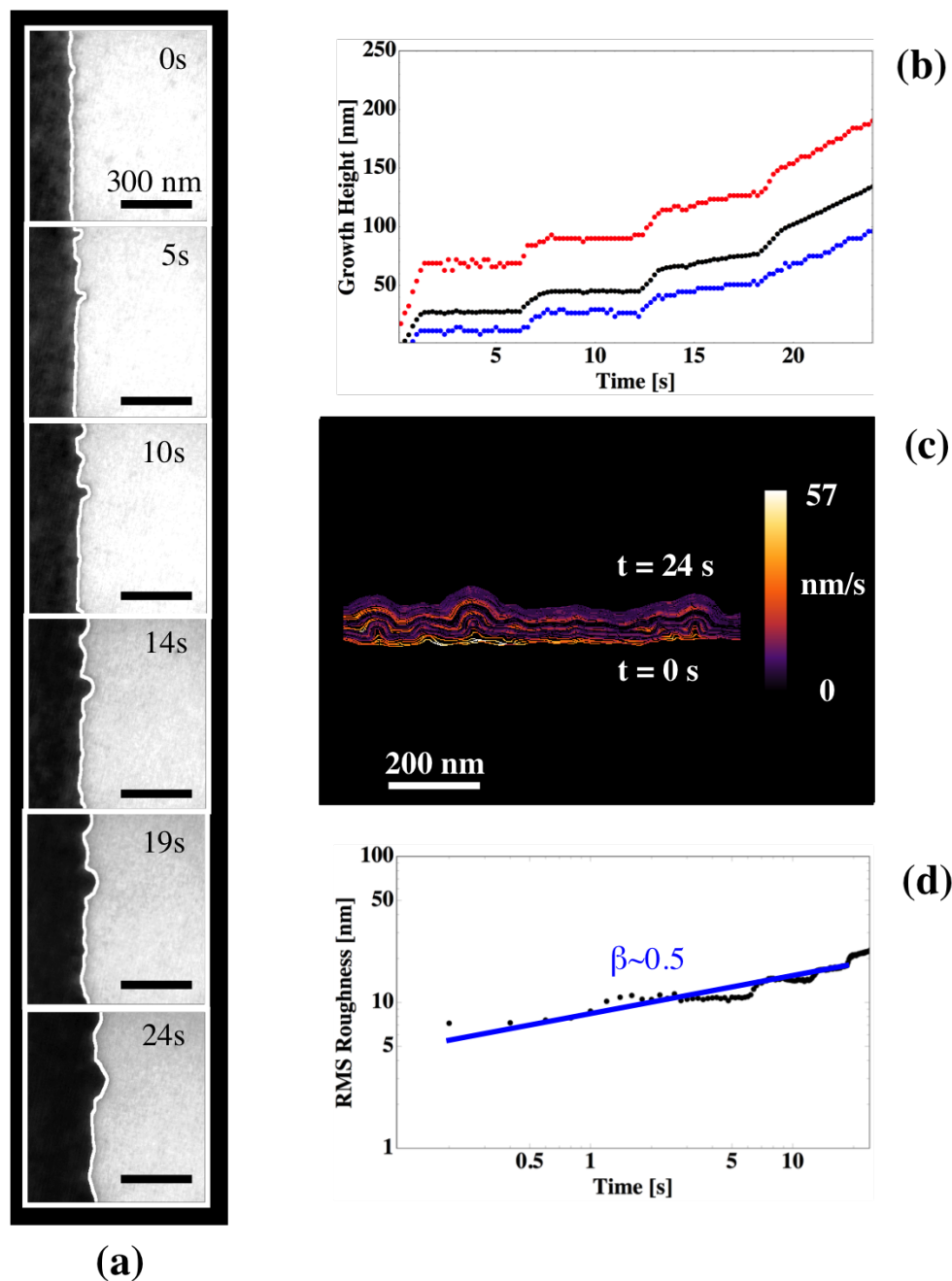


Figure 65: Galvanostatic Pulsed deposition with average current density of 288 A/m^2 and local average growth rate of 13 nm/s including off time (equivalent to 340 A/m^2) in 0.1M CuSO_4 and $0.18\text{M H}_2\text{SO}_4$. The local current density when only considering the pulse on time is 2040 A/m^2 . (a) Images recorded in bright-field conditions extracted from the video sequence found in the **Appendix Video B.12**. Times in seconds since current flow began. (b) Average, maximum, and minimum growth height as a function of time. (c) “Heat Map” of normal growth speed with white being fastest and blue/purple being slowest (need to redo with a color scale) (d) Log-log plot of RMS roughness of interface as a function of time. Best fitting straight lines are shown with exponents indicated.

is off, with a constant difference between the max and min heights. **Figure 66c** reveals a very consistent point-wise growth velocity along the entire edge. The RMS roughness calculation shown in **Figure 66d** has an average growth exponent of 0.02, and even shows an initial smoothing of the substrate. The growth clearly does not have a large amplification. Presumably the lead is acting as a surfactant that slows the reaction rate, keeps the system reaction limited, and allowing surface tension to continue to smooth the surface. This hypothesis is supported by the fact that the local current density as measured via the growth rate is lower when lead is present compared to when plain copper. See the supplement for details.

In conclusion, we have quantified the transition to morphological instability during the early stages of electrodeposition of copper, using liquid cell electron microscopy to provide the spatial and temporal resolution necessary to probe the critical early stages of growth. We have further quantified the exploitation of the initial roughening regime via pulse plating and the use of additives as a means to postpone the onset of these diffusive instabilities. Quantitative analysis of the videos shows we can pinpoint the onset of diffusion limited growth explicitly, even when macroscale approximations fail to account for local variations in current density. The quantitative measures also reveal the growth mode prior to the transition time where the surface roughens in a reaction limited growth regime. This suggests that an initially flat surface can not help to suppress instabilities and other means must be used. Detailed understanding of early stage growth will lead to the development of control schemes and geometries to be exploited in nanofabrication.

Figure 63b shows δi for the low current density deposition given in **Figure 64**. The key result seen in this figure is that δi is essentially constant throughout the entire deposition and never shows a rise. Although the absolute value of δi is larger

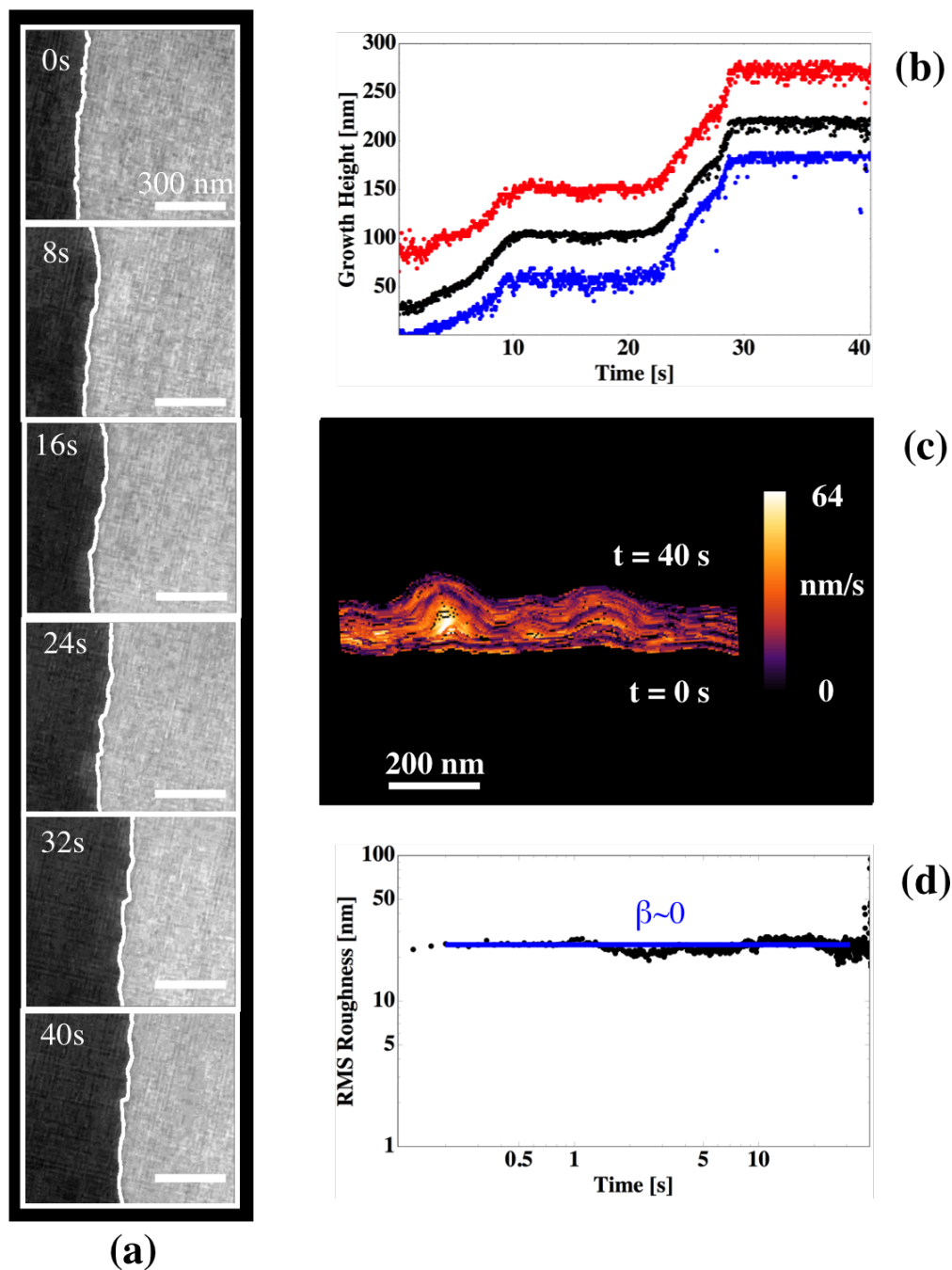


Figure 66: Galvanostatic deposition with average current density of 216 A/m^2 for 10 s followed by 10 s of no current, repeated. Average local growth rate is 14 nm/s (equivalent to 381 A/m^2) in 0.1 M CuSO_4 and $0.18 \text{ M H}_2\text{SO}_4$ saturated with PbSO_4 (a) Images recorded in bright-field conditions extracted from the video sequence found in the Supplemental **Appendix Video B.13** with detected edge as overlay. Times in seconds since current flow began. (b) Average, maximum, and minimum growth height as a function of time. (c) “Heat Map” of normal growth speed with white being fastest and blue/purple being slowest (need to redo with a color scale) (d) Log-log plot of RMS roughness of interface as a function of time. Best fitting straight lines are shown with exponents indicated.

compared to the high current density case, the relative value and time derivative are what provide insight into an oncoming diffusive instability. This also shows that the initial phase of the growth shown in **Figure 62** is the transient, reaction-limited regime theorized to exist before the onset of diffusion limited growth where we have roughening, but not the formation of ramified features.

7.3.1. Copper Electrodeposition Partial Conclusions

We have investigated and quantified the transition to morphological instabilities during the electrodeposition of copper. Liquid cell electron microscopy with devices like the nanoaquarium provide access to the spatial and temporal resolutions necessary to probe the critical early stages of growth. Quantitative analysis of the obtained videos shows we can pinpoint the onset of diffusion limited growth explicitly, even when macroscale approximations fail to account for local variations in current density. By considering the variations in point-wise current density (as measured by the speed of the normal velocity along the interface), we can see the rise of the diffusive instability well before the transition is visible in the interface. The quantitative measures also reveal the phase of growth prior to the transition time where the surface roughens in a reaction limited growth regime. Detailed understanding of early stage growth will lead to the development of control schemes and geometries to be exploited in nanofabrication.

7.4. Methods

Experiments were carried out with our custom made liquid cell, the nanoaquarium [13], operating in a three terminal configuration with Pt electrodes controlled by a Gamry potentiostat. The interface morphology evolution was simultaneously imaged at video rate (30 images per second) in a Hitachi H-9000 TEM at 300kV. Bright field

imaging conditions were used. Aqueous solutions of 0.1 M copper sulfate with 0.18 M sulfuric acid solutions were prepared by dissolution in doubly deionized water.

7.5. Electrical Data for Discussed Videos

The experimental setup allows for traditional spatially averaged measures of the electrodeposition. Since we apply galvanostatic conditions, potential is the measured quantity. In this section, we show the electrical data for the four cases explored in detail. It is important to note that the reference electrode used in these experiments is primarily made of platinum and serves as a pseudo reference. (The change in potential is reliable, but absolute value of the potential measurements will vary over time due to the electrical instability of platinum).

7.5.1. Transition to Diffusion Limited Growth (400nA)

The potential during copper electrodeposition resulting in diffusion limited growth is plotted in **Figure 67**. This data corresponds to the experiment shown in **Appendix Video B.10**. The potential drops from the OCP of ~ 70 mV as the copper begins to grow. There is a slight inflection in the potential around 2 s where the growth becomes 2D, but then continues to drop until about 6 s , which corresponds to the time where the growth within the imaged regions stops. From here the potential remains around 1 V , implying a secondary reaction may also be occurring, such as the formation of hydrogen at that working electrode.

7.5.2. Low Current Density Deposition (75nA)

The potential and applied current during copper electrodeposition during low current density growth is plotted in **Figure 68**. This data corresponds to the experiment shown in **Appendix Video B.11**. The first cycle contains an electrode strip-

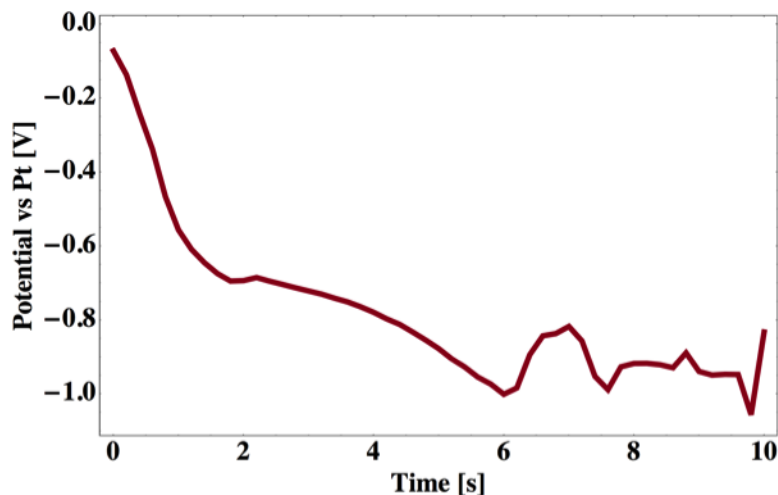


Figure 67: Potential as a function of time for deposition shown in **Appendix Video B.10**. Total applied current of 400 nA was turned on at time 0 and held constant.

ing/cleaning cycle of 15 s by applied a stripping current. After this one cleaning step, a deposition current with magnitude of 75 nA is cycled on and off for 10 s periods. The total deposition time is 350 s . The potential cycle is extremely repeatable with a shape expected for galvanostatic cycling [109]. The variations in the magnitude of the potential during each cycle can be attributed to the stability of the Pt electrode.

7.5.3. Pulse Plating (400 nA for 1 s , 0 nA for 5 s)

The potential and applied current during copper electrodeposition during pulse plating growth is plotted in **Figure 69**. This data corresponds to the experiment shown in **Appendix Video B.12**. Deposition current with magnitude of 400 nA is cycled on for 1 s followed by 5 s of no current. We again see classical galvanostatic cycling curves for the resulting potential. The magnitude of the deposition current increases with each cycle due to using platinum as the electrode. In this particular experiment, a two electrode configuration was used (the working electrode served as both the working and reference electrodes), which is why the magnitude of the potential is large.

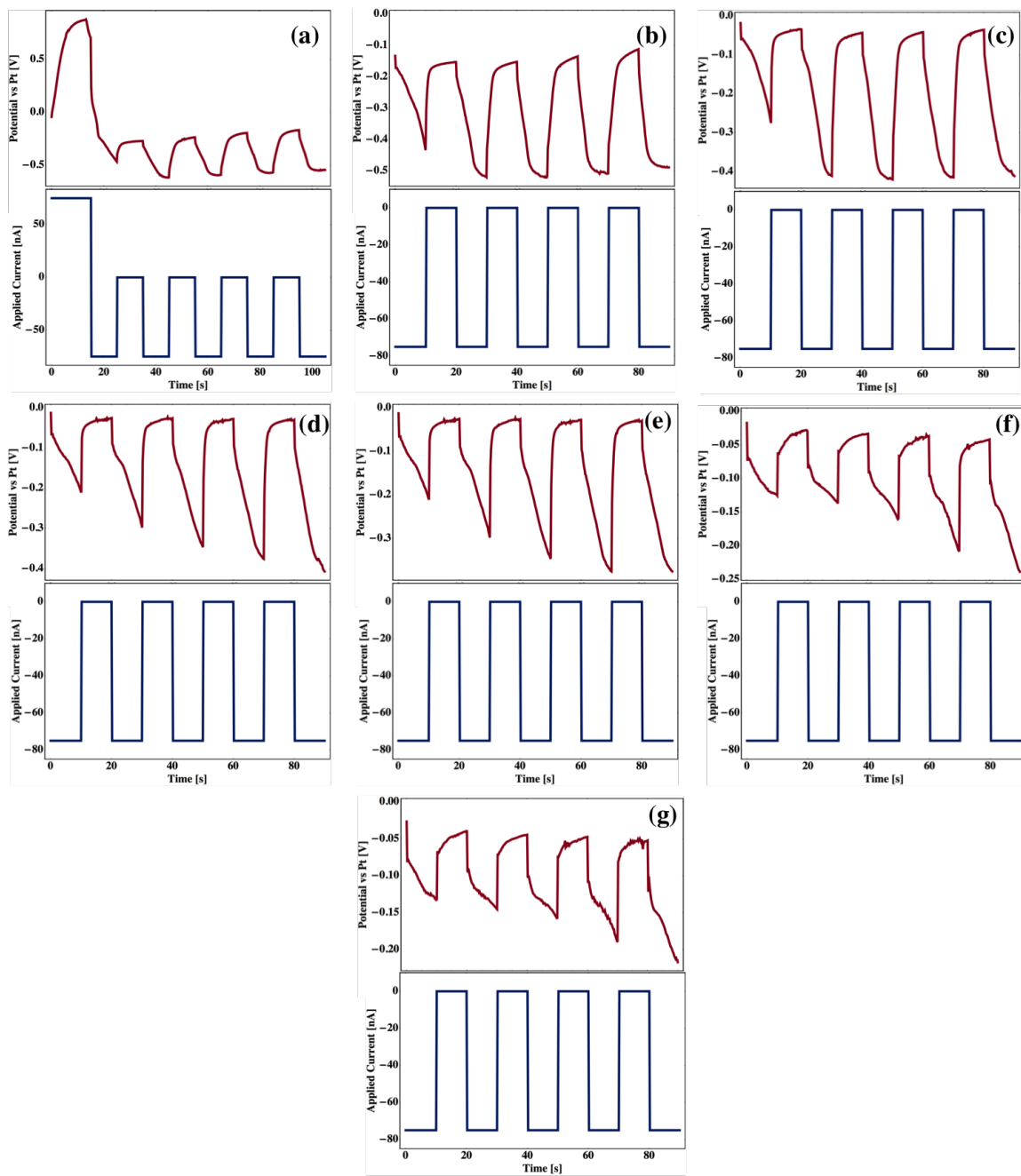


Figure 68: Potential and applied current as a function of time for deposition shown in **Appendix Video B.11**. Current is cycled on and off for a total of 35 periods with short pauses to restart the potentiostat after every 5 cycles (due to limitation in the software).

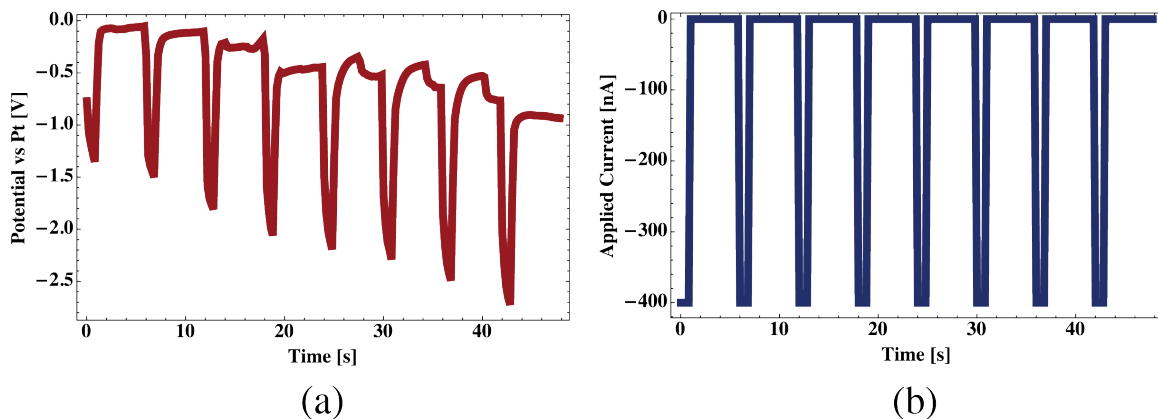


Figure 69: Potential and applied current as a function of time for deposition shown in **Appendix Video B.12**. Current is cycled on for 1 s and off for 5 s and repeated.

7.5.4. Lead Additive (300nA)

The potential and applied current during copper with lead additive electrodeposition is plotted in **Figure 70**. This data corresponds to the experiment shown in **Appendix Video B.13**. Deposition current with magnitude of 300 nA is cycled on and off for 10 s each. The potential follows an expected pattern for galvanostatic cycling.

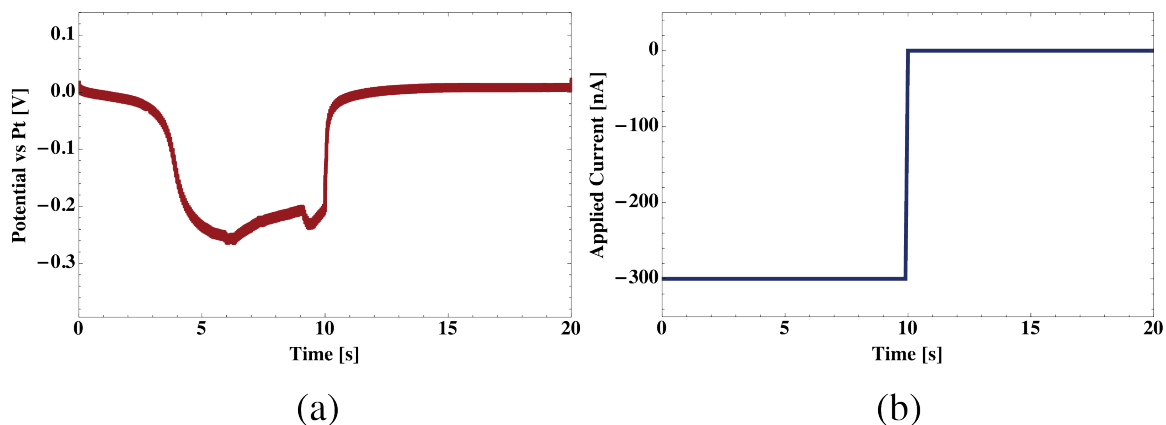


Figure 70: Potential and applied current as a function of time for deposition shown in **Appendix Video B.13**. Current is cycled on for 10 s and off for 10 s.

7.6. Ex Situ Hull Cell Experiments with Pb Additive

The fidelity of the observed differences between the plain copper sulfate and the copper sulfate saturated with lead sulfate solutions must be confirmed outside of the liquid cell. Ex situ experiment ensure that the observations, though already repeatable amongst separate devices, is not the result of contamination. We employ a simple flat plate Hull Cell to examine the onset of dendritic growth in the two solutions.

A typical Hull Cell was designed according to the layout in West [121]. The cell was manufactured out of glass slides of 25.4 *mm* width patterned with 200+ *nm* thick thermally deposited gold electrodes. The gold was cleaned in a nitric acid bath, followed by an acetone bath, followed by an IPA bath, and finally rinsed in DI water prior to assembly to clean any contaminates. **Figure 71a** depicts a schematic of the cell, which was assembled with clean working electrodes for each of the solutions (0.1 *M* CuSO₄ + 0.18 *M* H₂SO₄ and 0.1 *M* CuSO₄ + 0.18 *M* H₂SO₄ saturated with PbSO₄). Once assembled, the counter electrode was coated at low current density with copper foil serving as the counter electrode and a copper source. Galvanostatic conditions with 200 *mA* total (depositional) current were applied for 300 *s* in each solution. These conditions give an average current density, i_{ave} , of 20 *A/m*².

Post growth, the resulting structures were measured along the mid-width of the working electrode to avoid edge effects. We identify location with the same roughness between the two solutions and use that point to calculate the current density experienced. The location is defined by the position where the asperities are greater than the depth of field ($\sim 1.5\mu m$). **Figure 71b** and **c** show optical micrographs of the same location at two different levels of focus for the same sample as an example

of the location identified.

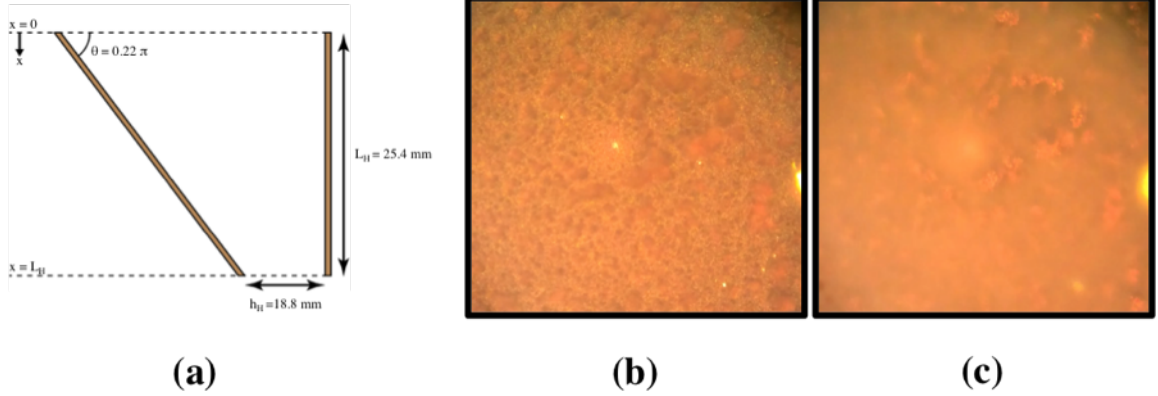


Figure 71: Schematic of Hull Cell design (a). Illustrative example of substrate in focus (b) compared to tips of dendrites in focus (c) at the same location. The circle represents the same location containing asperities that protrude out of the depth of field.

Table 10: Hull Cell Results between Plain Copper and Lead Saturated Solutions

	Location	Current Density
	[mm]	[A/m ²]
Cu	2.2 ± 0.4	44
CuPb	0.6 ± 0.4	75

The measured location of the onset of diffusion-limited growth is directly related to a particular current density as defined by the Hull Cell geometry. For our cell geometry, the current density as a function of positions was given by West [121] as

$$\frac{i(x)}{i_{ave}} = \frac{(x/L_H)^{1.2733}}{(1 - x/L_H)^{0.359}} (1.733 - 0.763x/L_H), \quad (7.1)$$

where, L_H and x are defined in **Figure 71a**, i_{ave} , is the average applied current density (20 A/m^2), and $i(x)$ is the current density and position x . **Table 10** summarizes the findings for the Hull Cell experiments. The Cu solution saturated with Pb has a current 1.7 times greater than the Cu solution for the same roughness, supporting

the in situ observations where dendritic growth is suppressed by the lead additive. The lead is likely acting as a surfactant resulting in an overall slower reduction rate.

CHAPTER 8 : Conclusions and Outlook

8.1. Conclusions

The limitation of standard electron microscopy, the required high vacuum environment, that precludes imaging of systems containing high vapor pressure liquids has been overcome through the use of hermetically sealed nanofluidic platforms. Liquid Cell Electron Microscopy has proven to be a useful tool across a large spectrum of scientific endeavors. A home brewed device, dubbed the nanoaquarium, invented by Grogan and Bau [13,14] at Penn, has been employed as a tool to study the morphological evolution of the electrode-electrolyte interface during copper electroplating, the onset of diffusive instabilities in electrodeposits, beam-mediated nucleation, growth, and dissolution of metallic nanoparticles, the nucleation and growth of nanobubbles, and the fundamentals of the electron-water interaction (Radiation Chemistry). Electron microscopy is often a qualitative art. In this work we go beyond our fundamental result, qualitative images, and dig deeper into the quantitative aspects of the physics. Automated image analysis algorithms to map intensity images obtained during experiments to physical measures of interests have been developed. Particularly, we extract interfacial dynamics between solid, liquid, and vapor phases during liquid cell electron microscopy. The source codes to these processes are freely distributed to aid researchers in analyzing their results.

Understanding the fundamental beam-sample interactions during Liquid Cell Electron Microscopy is necessary to interpret, suppress, and exploit beam-mediated phenomena. Employing a kinetic model is a powerful tool for quantifying how irradiation alters the underlying solution chemistry in the observation region. Models developed for the study of water radiation chemistry in medical imaging and nuclear reactor

safety have been leveraged and extended to the extremely high dose rate regime found in liquid cell imaging. We focused primarily on water as a suspending media, but other material systems are investigated, such as ionic liquids, similar accounting must be made for ubiquitous effects of irradiation.

The electron beam used for imaging can change the local temperature, solution chemistry, and, of particular importance to colloidal and electrochemical aqueous systems, the pH in the imaged region. In most TEM experiments, temperature rise is small due to conduction through the liquid layer [8]. Additional changes to the local chemical makeup can be significant depending on the imaged processes and are always present, even if not visible. A key result is that theory always predicts a steady state that is rapidly approached. In the usual case where only a small fraction of the cell volume is irradiated, the final steady state will be achieved on time scales associated with diffusion, however, the solution concentrations within the beam will be on the same order of magnitude as its final value within milliseconds. The consequences of radiolysis will, therefore, always be present in observed phenomena.

The kinetic model described here is useful for designing experiments that minimize unwanted artifacts, as well as exploit desired artifacts. Most importantly, the model, which has been release as open source code [7, 83], assists in interpreting experimental observations obtained with Liquid Cell Electron Microscopy. Liquid cells are a powerful tool that can also be used to study fundamental radiolysis and the behavior of materials under extreme conditions.

Additionally, we have quantified the transition to morphological instability during the early stages of electrodeposition of copper, using liquid cell electron microscopy to provide the spatial and temporal resolution necessary to probe the critical early stages of growth. We have further quantified the exploitation of the initial roughening

regime via pulse plating and the use of additives as a means to postpone the onset of these diffusive instabilities. Quantitative analysis of the videos shows we can pinpoint the onset of diffusion limited growth explicitly, even when macroscale approximations fail to account for local variations in current density. The quantitative measures also reveal the growth mode prior to the transition time where the surface roughens in a reaction limited growth regime. This suggests that an initially flat surface can not help to suppress instabilities and other means must be used. Detailed understanding of early stage growth will lead to the development of control schemes and geometries to be exploited in nanofabrication.

8.2. Outlook

Liquid Cell Electron Microscopy is a fast growing field with many opportunities for discoveries in fundamental science. Areas of particular interest include the controlled nucleation and growth of nanostructures, electrochemical deposition and etching of materials for fabrication and battery applications, the study of materials until hostile and high radiation dose environments, and fundamental radiation chemistry. Here we briefly discuss some of these future applications, particularly those within reach.

8.2.1. Automated Electron Beam Control

In this work we have shown that the electron beam can have a strong effect on the the local solution chemistry. Although this can often lead to unwanted artifacts, it can also be exploited as a manufacturing process. The process of beam induced reduction of species in liquid phase solutions is an example of one process that can used to generate controlled structures. Grogan *et. al.* [8] showed that by controlling the dose rate and exposed volumes one can generate maskless patterns. **Figure 72** shows the resulting structure “penciled” to spell the names of the author’s institutions. By

designing a control algorithm for the electron beam, more controlled geometries can be designed. Replacing the solution with a new material system will allow for the design of devices that take advantage of connecting dissimilar materials (and not just metallic).

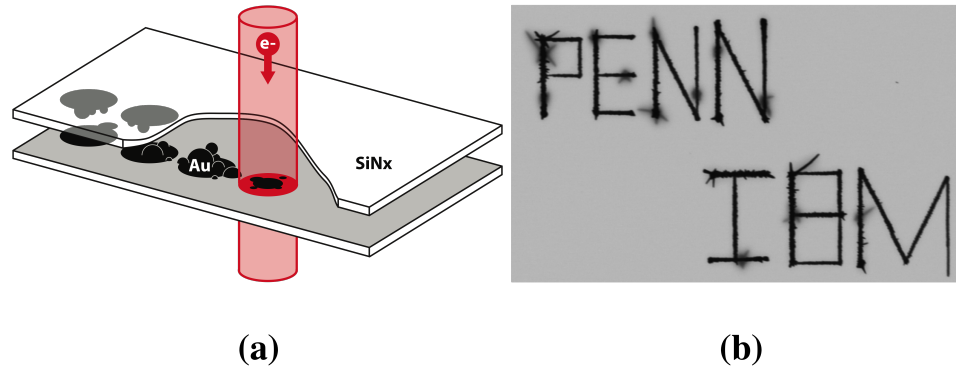


Figure 72: Illustration of beam-induced deposition (a). (Figure generously provided by Michael Norton) Exploitation of the fact that highly reducing species do not persist outside the beam region allows for mask-less patterning by the electron beam (b).

The explicit control of the beam has uses beyond maskless patterning. The same concept will work for the controlled formation of controlled colloids, core shelled particles, and radiation induced phase changes within structures. Beyond the manufacturing of materials, the converse can also be employed. If the goal is to image a structure with minimal total dose, then the algorithm used to control the beam could be used to apply a transient dose rate. This can be achieved by several means; the beam radius can be pulsed to change the exposed area and thus alter the dose rate; the beam, in the case of a STEM style control, can be rastered in a non-linear fashion that minimizes the overall dose [rate] while still providing enough electrons to form an image. The simplest approach would be to raster the beam in a random fashion, however, one could do better by solving the an optimization problem that globally minimizes the absorbed dose and minimizes the changes of local chemistry (through a coupled radiolysis simulation) throughout the imaged region. Ultimately,

the explicit control of the dose rate at every point in a liquid cell allows the resulting radiation chemistry to be exploited as a manufacturing process, a means to mitigate beam induced damage, and as an analytical tool via the regulation of local chemistry.

8.2.2. Electrochemical processes

Multicomponent Electrodeposition

Electrodeposition enables economic and scalable manufacturing of nanostructures with great design flexibility. Examples range from the production of interconnects in high density microelectronics; to low-cost photovoltaic cells; to thin film ferromagnetic inductors for energy storage for integrated circuits, containing on-chip power management. The physical, mechanical, and electrical properties of electroplated films depend critically on their morphology and composition. Control of the structure requires detailed understanding of how the material deposits, including the factors that affect nucleation, texture, grain boundary structure and surface roughness. The nanoaquarium and liquid cell electron microscopy have proven to be excellent platforms for the study of these processes. Despite the wealth of experimental results, however, a full understanding of the temporal evolution during transient electrodeposition is still poorly understood, especially for complex systems with multiple depositing species.

A recent and more challenging application of this manufacturing technique is the development of inductive DC-DC conversion devices [122, 123]. This is driven by a key problem in microelectronics, the need to reduce heat generation and leakage currents during chip operation. The development of voltage convertors would enable different voltages to be supplied at different regions of an integrated circuit, offering significant power savings in those parts of the circuit that can operate at lower

supply voltage. DC-DC voltage conversion is achieved using inductors, and the application therefore places both magnetic and electrical (resistivity) demands on the materials used in these inductors, a challenging task. Electrochemical deposition is a possible means to produce the inductors, which are based on magnetic materials such as Cu/NiFe, NiFeCo and CoW alloys. Control of nucleation density and grain size, interface planarity, and composition are required for optimizing performance. Yet in these materials, “anomalous codeposition” is common, where the electrochemically less noble element (Fe in the case of Ni-Fe alloys) deposits preferentially under most plating conditions. The codeposition process is extremely complex, poorly understood, and requires a lengthy development process. A basic understanding of the processes at work would help to design and control the codeposition process and optimize the product. The understanding of multicomponent deposition physics is applicable to other important codeposition processes in the engineering of materials. The ability to codeposit materials with composition controlled down to nearly atomic scale would open wide opportunities for materials with even more highly customized properties [124].

The nanoaquarium is well suited for the study of these systems. We have already established that solutions containing copper and nickel can be loaded into the device and deposited. **Figure 73** shows electrodeposited structures from one such solution. Our setup, however, suffers from one major disadvantage; we are currently unable to perform simultaneous or even post mortem chemical analysis of the resulting structures. A necessary next step is to incorporate “multi-modal” analytical microscopy, where structures are probed for more than their morphology, but also their chemical and electrical states through techniques such as EDX (chemical) and electron holography (electrical).

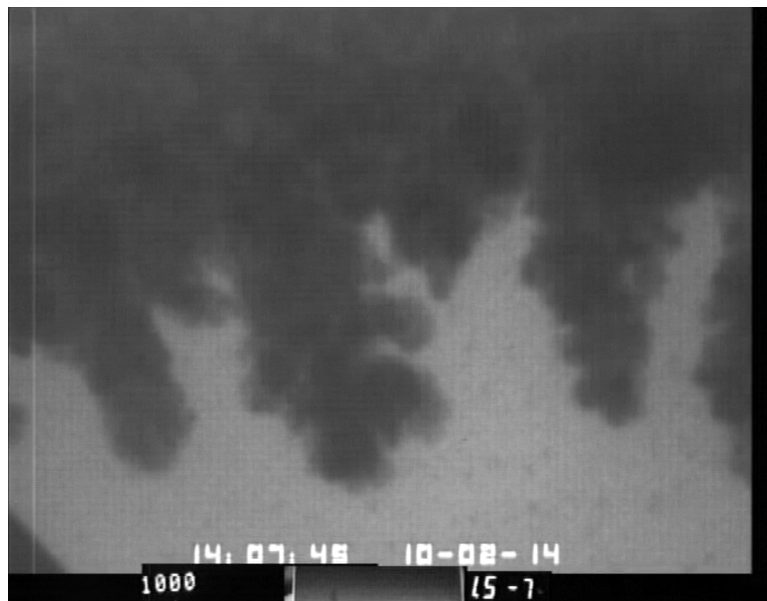


Figure 73: Galvanostatically deposited Copper-Nickel structure from 0.1 M NiSO₄ 0.18 M H₂SO₄ and 0.02 M CuSO₄

Alternative Electrode Geometries

The nanoaquarium platform can be further extended with customization. Alternative electrode and window designs can be employed to investigating strategies of morphological control. Since the nanoaquariums are fabricated by wafer bonding in a batch process where each set of bonded wafers yields 52 devices, this provides us the opportunity to include a rich variety of electrode and window configurations in each fabrication run. Some of the recommended designs are shown in **Figure 74**. These include: (i) Parallel electrodes. (ii) Hull configuration, consisting of two diverging planar electrodes, allowing for known variations in current density along the length of the electrodes. The Hull configuration will allow us to investigate the effect of current density on deposit properties [121]. This is especially valuable in the case of co-deposition where each element is deposited differently depending on voltage and current density. (iii) The Hele-Shaw configuration, consisting of a circular disk or

a different shaped electrode centered within a large ring electrode. In this configuration, the current density decreases as the electroplated layer grows radially. (iv) Saw-tooth style electrodes will enable us to study the onset of morphological instabilities at deliberately introduced asperities. (v) We will also examine electroplating around conducting objects (“floating” electrodes) of various shapes placed between two parallel electrodes. This will provide the first in-situ views of bipolar electrodeposition, where one side of a conductive object in a field acts as an anode while the other side acts as a cathode [125]. Bipolar electrochemistry is useful, for example, for the production of Janus particles, which are of interest for variety of applications, and for which high throughput fabrication techniques are still lacking. The control of bipolar morphology is key to these applications. (vi) Asymmetrical placement of electrodes in an elongated observation chamber to encourage bubbles resulting from gaseous reaction products to move away from the electrode area. Our experience to date is that the formation of a bubble over the working electrode (e.g. of hydrogen, formed during prolonged high current density deposition when the metal ion concentration is too depleted to supply the entire current) limits the duration of liquid cell electrochemistry experiments. The idea here is that the thickness of the liquid cell will increase slightly along the length of the window. To minimize their free energy, bubbles will tend to migrate to thicker regions of the liquid cell. (vii) Pillar designs far from the electrodes have been included in our existing nanoaquariums to control window bowing. In some cases, we will place pillars close to the electrodes to mimic the presence of colloidal particles in the electroplating solution. These pillars will block the path of the deposit as it grows and allow us to examine the effects of such blocks on the development of morphology during deposition. The pillars will also mimic presence the effects of suspended particles on electroplating.

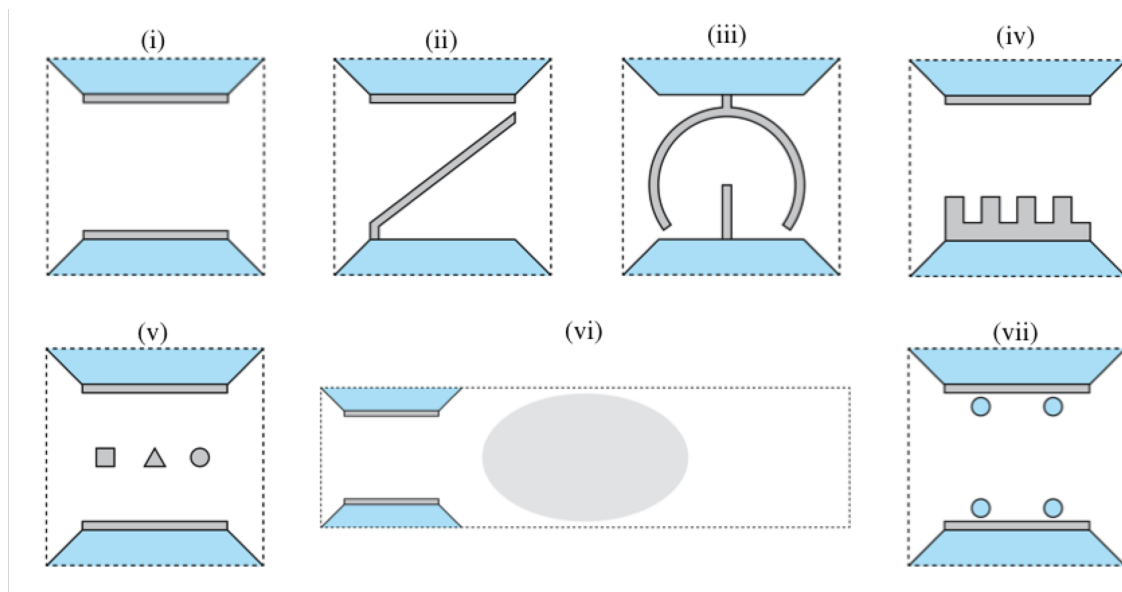


Figure 74: Schematic illustration of a few electrode configurations: standard parallel (i); Hull cell design enabling deposition subject to varying current densities (ii); Hele Shaw (iii); sawtooth to study deposition on vertical structures and trench filling (iv); and bipolar (v). The entire exposed working electrode is in the viewing window (dashed line). Elongated window design to encourage bubble (shown as a gray ellipse) migration away from the electrode region (vi). Pillars next to the electrodes to simulate the presence of colloids (vii). A single photolithographic mask can be used to pattern the various electrode configurations, enabling the manufacturing of nanoaquariums with different electrode configurations in a single run with minimal added cost.

APPENDIX -

APPENDIX - Device Preparation

The employed manufacturing process allows for wafer level production of the nanoaquarium [13,14]. This results in a batch of 52 devices per set of 4 *in* wafers. It is best to store devices in the state after the last level of lithography, which is to perform a KOH etch to define the windows, inlets, and scribe lines as well as expose the electrode connection pads. This means several microscope and experiment specific steps must be taken to prepare the devices for use in a particular study. The dexterity required for preparation is non-trivial, and so we have developed this section highlighting some best practices for the current version of the device.

N.B., Whenever one is working with one of these devices, gloves should be worn to protect oneself and the chips from harmful oils and debris.

A.1. Wafer Dicing

Lithography returns a wafer with predefined scribe lines that must be completed in order to retrieve individual devices. Hand dicing of the wafer is preferred as care is necessary to avoid breaking the free standing membranes. This process will require the following list of materials separate the nanoaquarium from its wafer:

- Nanoaquarium wafer and case
- Scotch Tape™
- Diamond tip scribe
- Compressed air/nitrogen (for dust removal)
- Razor
- Gel-Pak™ for device storage

First, identify a “column” of devices to be separated. Given the current design of the wafer, separating by column is easiest. Next, gently use the compressed air at a glancing angle to clean the wafer of dust and debris. Once the wafer is cleaned, take a strip of tape wide enough to span the inlets and place it down the center of the column as illustrated by the light blue overlay in **Figure 75a**. Place a second strip of tape on the backside of the wafer to cover the windows there. The backside of the wafer will essentially mirror the work done to the front throughout this process. These steps protect the window and intent membranes from the damage during the potentially rough dicing.

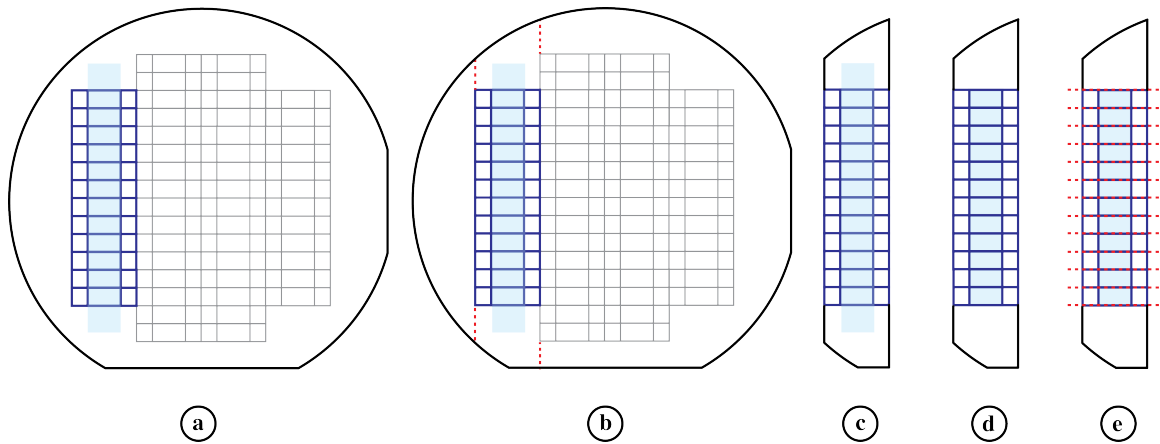


Figure 75: Illustration of wafer dicing steps

Using the diamond scribe, connect the KOH defined scribe lines to the top and bottom of the wafer (the primary flat is called the “bottom” of the wafer) as illustrated by the red dashed lines in **Figure 75b**. Again, mirror this operation on the backside for a total of 8 new scribes. Starting from the smallest piece, use two hands to snap the wafer by holding with one’s index finger and thumb on each side of the scribe line. In the illustration, it would be best to snap off the left side of the wafer with no devices first and then the column of desired devices. This part of the process should be done close to a clean surface in case the wafer breaks in additional, undesired locations. By

breaking off the smaller part of the wafer, one avoids accidentally dropping the wafer. Once divided, place the remaining wafer back in carrying case, leaving a section like **Figure 75c**.

The next step is to use the razor to cut the tape along the scribe lines by running the razor through the scribe line. This will serve to allow complete separation of devices as they are diced horizontally. Be sure to cut the tape on both the front and backside of the wafer so no devices are connected with tape as illustrated in **Figure 75d**. This process should be simple as the etched scribe lines provide a trench easily found with the tip of a razor.

Following the red dashed lines in **Figure 75e**, scribe along each device (while the wafer sits on a clean surface). Perform this step on both the front and back of the wafer. Note that this step is critical and care should be taken to ensure all scribe lines are complete. Failure to complete scribes will result in many windows breaking during the dicing. Once confident each device is properly scribed, start from the top of the wafer and snap each piece/device with the same two handed approach as before. This will result in separate devices covered in tape on the front and back. The last step is simply to remove the tape (a razor edge works well for this), and to place them in a gel pack for storage and additional preparation.

A.2. Inlet Etching

Now that individual devices are available, it is time to open the inlets by removing the silicon nitride membranes left after that back etch. It is important to note that one can “cheat” by physically breaking the inlets with the point of a set of tweezers. This will leave shards of nitride in the window region, which is problematic when loading solutions with particles. However, if the system to be studied does not have

particles, say in the case of a metallic salt or hydrogen peroxide experiments, then this quick-and-dirty method is acceptable. The advantage of this method is that one does not also etch the nitride on the bottom of the channel, exposing silicon, which may be important for special types of experiments. For most cases studied thus far, etching the nitride is preferable. This process will require the following materials:

1. Nanoaquarium devices (in Gel-Pak™)
2. Scotch Tape™
3. Razor
4. Tweezers
5. RIE Etcher with O_2 and SF_6

Take a long piece of tape and place it adhesive side up on a clean surface. It may be easier to tape down the ends of the tape provided there is sufficient tape between the edge of the device post placement and the edge of the tape. Place devices length wise on the tape bottom-down as illustrated in **Figure 76a** where the light blue is tape, black lines are device edges, blue lines are inlet edges, and the red lines are the window (which we do not want to etch).

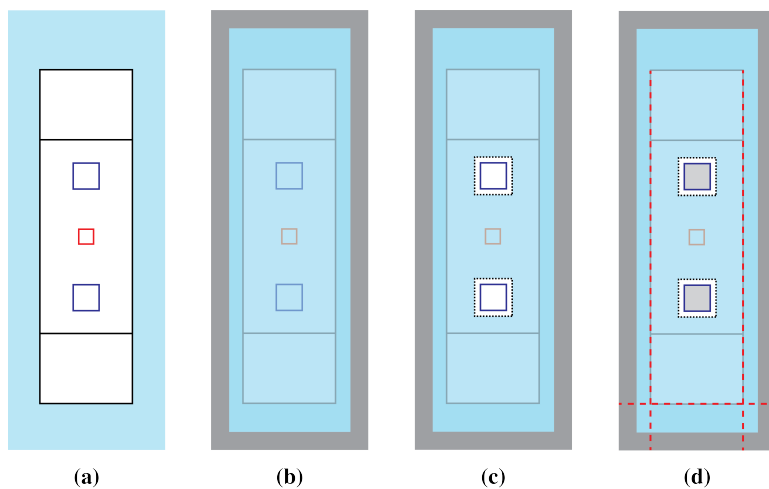


Figure 76: Illustration of inlet etching mask

Once the device is secured, place a second piece of tape long enough to cover all devices adhesive side down. Seal the tape to the bottom piece of tape around the devices as illustrated by the gray area around the tape in **Figure 76b**, entirely encapsulating each device. This is essential as we are preventing plasma from etching in undesired locations - mainly the observation window.

Next, using the razor, cut out a square around the inlets to expose the underlying nitride. Use the razor to flip up the edge of the square and use tweezers to remove the small squares of tape. Note that it is often convenient to make a tape role (ring of tape with outwardly exposed adhesive attached to the table) to remove the small squares from the tweezers or other surfaces. Care should be taken as it is easy to smear adhesive on the device with adverse effects and is a source of contamination. The result should look similar to the illustration in **Figure 76c** where tape covers all but a small region around the inlets. At this point, the device is ready to be etched open.

For etching at the University of Pennsylvania, the Technics at Quattrone Nanofabrication Facility in the Singh Center for Nanotechnology is used, however, any etcher with O_2 and SF_6 that allows the materials the device is made out of and the tape is sufficient. Place devices window side up with tape masks into the etcher and secure them appropriately (with more tape if needed). For the Technics, evacuate the chamber and run an etching cycle with 6 sccm SF_6 and ~ 100 sccm O_2 at a pressure of ~ 400 *mTorr*, with a power of 100 *W* for 1 *min*. Other process parameters can be used for reactive ion etching of nitride with O_2 and SF_6 chemistry.

After the inlets have been etched, use the razor to cut the bottom of the tape (short edge of device) off as illustrated by the horizontal, red, dashed line in **Figure 76d**.

This cut should be in the small, visible air pocked within the masked region and should be as close to the device as possible. After the bottom is removed, cut the tape along the long edges of the device. This opens the mask in a way that can be “peeled like a banana” with the help of tweezers and the razor edge. If adhesive is left behind from this process, an oxygen plasma can be used to clean the device. However, it is important to know that the O₂ plasma will make the surface of the device very wetting, making it difficult to load most aqueous solutions. Therefore, it is recommended to clean the device days before expected use so that the surface chemistry can return to its native, partially-wetting state. The chips should be placed back in the Gel-Paks for storage. For experiments not requiring electrical connection, the devices are now ready for use.

A.3. Electrical Leads

In order to gain access to the integrated electrodes in the nanoaquarium, we must provide a bridge lead from the device to the selected holder. In the case of the custom holder for the Hitachi H9000 transmission electron microscope at IBM T.J. Watson, we have adopted a straight forward procedure using copper tape and silver epoxy as the means to this end. In this section we detail the steps for the preparation. It is advised to prepare several devices at once, as this is a rate limiting step. The following is a list of materials needed to prepare the leads on nanoAquariums:

1. Diced and Opened nanoAquarium(s)
2. EPO-TEK™ H22 two-part silver epoxy
3. One-sided copper adhesive tape (6.35 *mm* width)
4. Tweezers
5. Razor

6. Glass Slides
7. Kapton Tape
8. Plastic Toothpicks
9. Hot Plate

A.3.1. Making Leads

Copper foil is used to make the bridge lead between the nanoaquirum and the custom holder at IBM as it is highly conductive, easy to work with, and inexpensive. First, cut a piece of copper foil tape to be approximately 5 *cm* in length. Crease the tape along center of long edge as illustrated in **Figure 77a** (easily done by bending against glass slide) so that the adhesive side is on the inside of the fold. Remove the backing to expose the adhesive and fold onto itself. Flatten the copper well with a smooth surface such as tweezer handles. Using the Kapton tape, secure the copper to a glass slide with any exposed adhesive facing up. The illustration in **Figure 77b** shows how this should look with the yellow transparent boxes representing Kapton, the dark brown copper, and the lighter brown adhesive. The foil is now ready to be cut into leads.

Take a second glass slide as a guide, and cut off any exposed adhesive with the razor. This is best done by holding the slide flat and firm on the copper and running the razor several times to slowly cut through the foil. Perform a second cut down the cent of the remaining copper foil. Once the two long cuts have been made, cut horizontally as to make 8-10 *mm* length strips of copper - these are the unshaped leads. The cutting lines are illustrated as red dashed lines in **Figure 77c**. Lastly, leads should be bent using tweezers into the shape of a stretched out “Z”. The shape can be seen in **Figure 77d** where the ends are ~ 2 *mm* in length and the midsection ~ 4 *mm*.

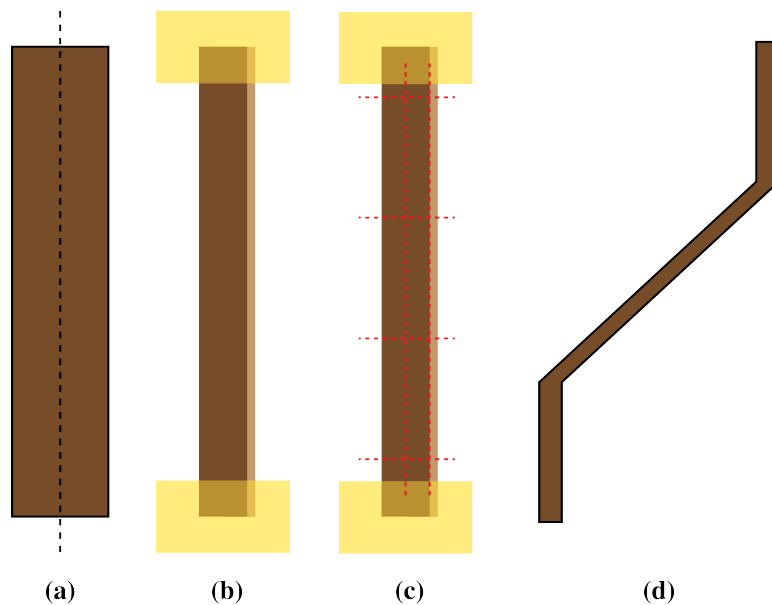


Figure 77: Steps for lead production from copper foil

Four leads should be produced per nanoaquarium.

A.3.2. Gluing Leads on Nanoaquarium

Once copper leads are ready, preheat hot plate to 150°C . Next, mix the two part silver epoxy with a toothpick on a glass slide. Note that one will not need much epoxy, and usually a volume the size of a pea is more than enough for ten or so devices. Test the epoxy by gluing a piece of copper to a spare glass slide. To do this, place a small amount of silver epoxy on slide and press copper to it with tweezers (a small “L” shaped piece of copper lead works well). Place glass slide on hot plate for ten minutes. After the curing time, remove the slide from the heat and allow to cool to room temperature. After cooling, test the copper and cured epoxy for electrical conductivity with a multimeter. Further test for mechanical strength - if the glass slide can be lifted by the glued tab, then the epoxy is mixed and cured well. If the conductivity or mechanical strength tests fail, this may be due to improper mixing or ratios of the two part epoxy. Adjust the mixed or make a new batch to correct the

issue.

Now that all of the preparation work has been completed, it is time to actually glue the leads to the devices. Cut Kapton tape into small squares ($\sim 6.35 \times 6.35 \text{ mm}$ works well) to use as a means to secure the devices on a glass slides. Ensuring the devices do not move during gluing is essential, so next, tape down the nanoaquarium in a fashion similar to the illustrated in **Figure 78a**. The goal is to have minimal Kapton tape on the devices while still holding their location firm.

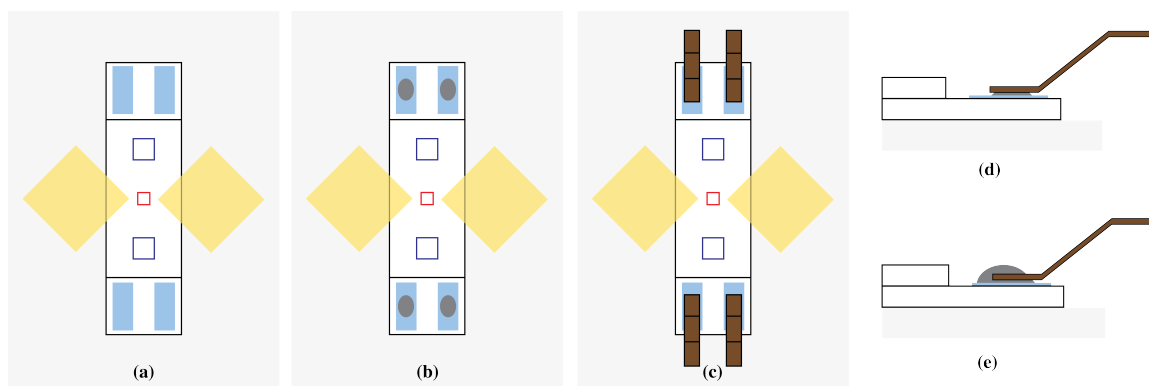


Figure 78: Gluing Leads to Nanoaquarium

The secured device is now ready for the first round of epoxy. Dip the end of the toothpick into the mixed epoxy from earlier allowing a small amount to accumulate on the end. Lightly dab a small drop onto each of the four electrode pad as illustrated in **Figure 78b**. This should be a small amount as too much will smear and cause electrical connection between the two electrode pads. The leads can now be placed on each pad (**Figure 78c** and the side view **Figure 78d**) extending off of the device. The long direction of the lead should be parallel with the long direction of the device. This can be done using two sets of tweezers where one pair moves the lead nearly in place and the second adjusts and presses the lead down on the pad.

Once all four electrode pads have leads attached, cure the epoxy on the hot plate

for 10 *min*. After the curing time, remove the slide from the heat and allow to cool to room temperature. Test the leads for mechanical strength by lightly tapping them with tweezers. Once set, apply an additional layer of epoxy on top of the copper and electrode pad (**Figure 78e**). This second layer provides additional mechanical support holding the leads during the clamping of the device in the holder. Cure the epoxy for another 10 *min* on the hot plate, remove and cool to room temperature. The device is now ready for use in conjunction with the IBM holder and should be stored in a sealed Gel-Pak until use.

A.4. IBM Holder

The nanoaquarium's footprint fits the design of the holder for the Hitachi H9000 at IBM. This allows us to readily prepare devices for experiments at IBM's microscope facility. The holder is equipped with four copper beryllium tabs that serve as the point of contact for electrical connections outside of the microscope for interfacing with electrical control equipment such as the potentiostats used during electrochemical experiments. The fabrication of leads as discussed in **Section A.3** is also designed to facilitate proper electrical connection. When assembling the holder with a device, the orientation of the nanoaquarium is important to ensure that the mapping of the electrical leads outside the microscope correspond to the desired electrodes within the liquid cell. Asymmetry has been designed into the device layout to aid in this process. The pads to which the leads are glued have two different lengths. The longer pads are associated with the electrodes extending into the window region (the electrodes selected as the default working and reference electrode). **Figure 79a** illustrates the electrode layout as it relates to the electrode pads, where we define the default orientation such that the longer pads point upward. The IBM holder's default orientation is such that the alignment pin is toward the left as illustrated in

Figure 79b.

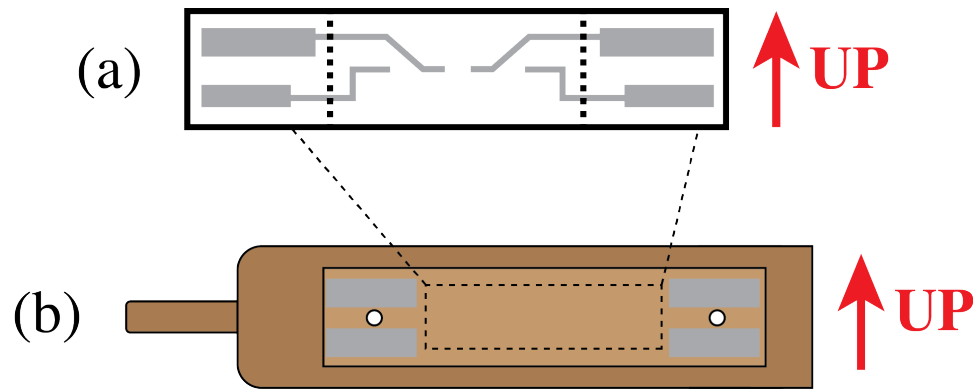


Figure 79: IBM holder assembly. Asymmetry designed into nanoaquarium to aid in proper orientation (a). Standard orientation of IBM holder when loading (b.)

Each of the electrical connections on the holder, chip, and external to the microscope are given a common name. The naming scheme is based on the reference frame of the holder and how it is loaded into the microscope. Assuming we are looking down the holder in the direction of the alignment pin, the four electrical connections can be divided by whether they are on the left or right side of the holder and by if they are toward the tip (alignment pin) or near the middle of the cartridge. This allows us to identify the connections as Right-Tip (R_{tip}), Right-Middle (R_{mid}), Left-Tip (L_{tip}), Left-Middle (L_{mid}). This notation is identified on the illustration in **Figure 79** and is used throughout any lab notes or digital databases with experimental metadata. During the clamping process, the nanoaquarium should be placed in the default position so that the electrical connection line up appropriately. This is an arbitrary configuration as the connections outside the microscope are interchangeable and can be arranged as desired. The device is placed in the holder, it is extremely important to ensure that the leads are cut short enough as to avoid being near the holes for the set screws. Since the set screws are electrically conductive, shifting during the clamping process can result in a short if the device leads are too long and come into contact with the screws. **Figure 80** shows a photo of a top view of the

IBM holder with a nanoaquarium prior to clamping where the leads are clearly short enough to avoid the holes for the set screws.

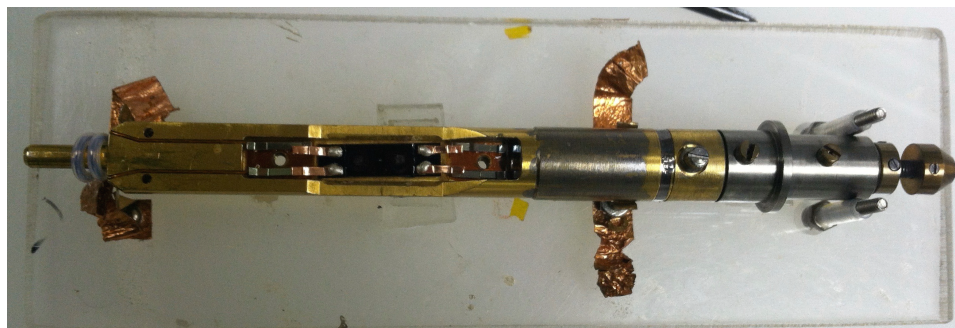


Figure 80: Top view of IBM holder with nanoaquarium prior to clamping. This holder is designed for the cartridge loading used by IBM's Hitachi H9000.

Once the device has been placed in the proper orientation on the holder and solution has been placed on both sets of inlets, it is time to seal the device. The lid of the holder has two recessed circular regions that fit o-rings. Capillary forces are strong enough to hold the o-ring, so place a small droplet of solution in each of the recessed wells. The o-rings can then be placed on the droplets and will stay in place. The lid will then hold the o-rings down as the set screws are moved into their holes. There are two different set screws, a brass set screw with a tall head, and an aluminum set screw with a thin machined head. The latter goes toward the tip of the holder and is designed to be thin to avoid contact with the poll piece of the microscope during loading. The lid should be dropped in place carefully by aligning the set screws. Using ones thumb to hold the first screw and lid in place makes it easier to engage the complementary set screw. At first, the screw should be lightly engaged followed by the sliding of ones thumb from the held screw. The second screw should be loosely engaged. Alternating between the fore and aft set screw, slowly tighten the holder until the device has been sealed. Observe the window periodically to make sure the windows are not over-bulged to avoid breaking. Once the lid has sealed the device,

place the entire holder in the desiccator for at least 5 minutes. Observe the window once again in the optical microscope. If the window has collapsed, tighten the set screws once again and iterate on this process until the device no longer leaks. Once the holder has been fully assembled and sealed, the sample is ready to be loaded into the microscope load lock and pumped down.

A.5. STEM Holder

An in house titanium fixture was designed for easy sealing of nanoaquarium devices [14] has a similar clamping procedure as the IBM holder. The STEM has not been used for electrochemical experiments, and so we shall only cover the loading of a device and not a process by which to gain access to electrical connections outside of the microscope. This functionality could, however, be obtained with the use of standard LEMO Connectors with custom wiring as the Quanta ESEM used at Penn has a panel with electrical pass-throughs. Once a device has been filled, it can be placed on the holder with the inlets facing upward. Capillarity can once again be used to hold the o-rings in place on the cover piece. The cover piece is then placed above the device and secured using the two set screws of the hold by once again alternating small adjustments. Periodic observation of the device window is need to ensure the device is not over pressurized. The fully assembled holder can be seen in the photograph in **Figure 81**.

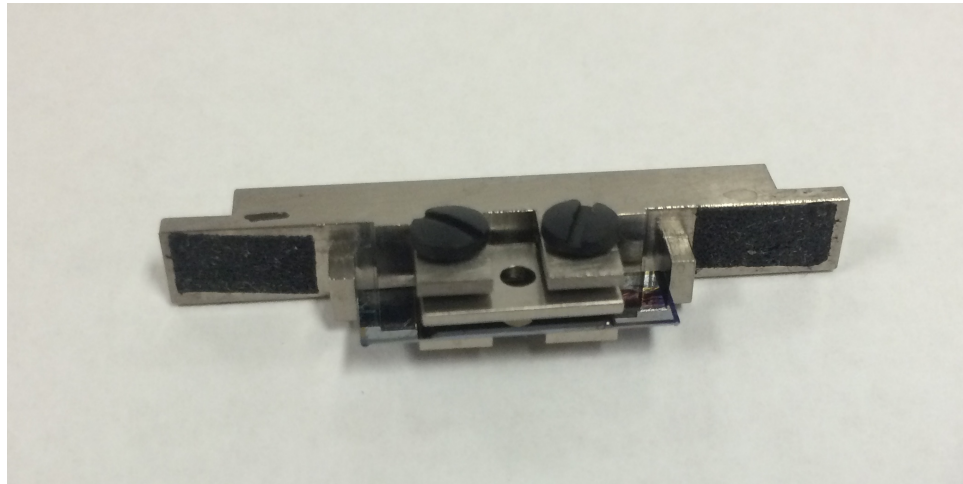


Figure 81: Photo of device loaded in STEM holder

APPENDIX - Videos

Several videos have been prepared to show illustrate the results of the work. These videos can be found on YouTube on Nicholas Schneider's channel, with a playlist available at: <http://bit.ly/NMSVideos>

B.1. Device Filling Sequence

Example video of nanoaquarium filling as imaged in an optical microscope. The device is filled with 3% wt H_2O_2 via the inlet toward the top of the video. Capillarity pulls the fluid into the device and fills the entire window region. Once the flow settles, the membranes begin to collapse and ultimately trap an air bubble. Notice that the liquid is still seen near the top of the window and along the edge of the silicon oxide. Once a second drop of solution is added to the complementary inlet (toward the bottom of the image), the fluid begins to separate the collapsed membranes and refills the image region. In this case, the air bubble dissolves and either remains as a dissolved gas, exits the device through the inlets, or migrates to another air pocket within the device.

B.2. Catastrophic Window Failure in NanoAquarium

Example video of the catastrophic failure of a nanoaquarium as imaged in the FEI Quanta ESEM in STEM mode. The device is filled with 3% wt H_2O_2 which, upon irradiation, forms a large radiolytic bubble. Instead of the silicon nitride membrane delaminating the pillars, the nitride ruptures and the solution begins to empty into the vacuum. Small bubbles can be seen as the solution undergoes a phase change.

B.3. Example of Beam Deposits not Etching

Etching of copper electrodeposit under galvanostatic conditions. Copper electrodeposition was performed around particles grown via beam deposition in 0.1. The particles are not etched by the applied current and are instead left behind. Aqueous solutions of 0.1M copper sulfate with 0.18M sulfuric acid solutions were prepared in doubly deionized water and were not deaerated before use. The morphology evolution was imaged at video rate (30 frames per second) in a Hitachi H-9000 TEM at 300kV.

B.4. Beam Deposited Particles moved by Liquid Vapor Interface

Advancing liquid vapor interface pushes particles toward the right, then receded and drags the particles back toward the left. Particles were formed through radiolytic reduction of copper from solution. Aqueous solutions of 0.1 M copper sulfate with 0.18 M sulfuric acid solutions were prepared in doubly deionized water and were not deaerated before use. The morphology evolution was imaged at video rate (30 frames per second) in a Hitachi H9000 TEM at 300kV.

B.5. Gold Nano Crystal Formation

Video of gold crystal growth using the nanoaquarium with transmitted beam current of 7.8 nA spread over 2 μm diameter in a Hitachi H9000 at 300kV. Stock solutions of chloroauric acid (Sigma Aldrich) were made by dissolving the salt in deionized (DI) water at concentration of 10mM. The solutions were stored in opaque glass bottles due to their light-sensitive nature.

B.6. Copper Electrodeposition Example

Copper electrodeposition in our custom made liquid cell, the nanoaquarium, operating in a three terminal configuration with Pt electrodes controlled by a Gamry potentiostat. The interface morphology evolution was simultaneously imaged at video rate (30 frames per second) in a Hitachi H9000 TEM at 300kV. Bright field imaging conditions were used. Aqueous solutions of 0.1 *M* copper sulfate with 0.18 *M* sulfuric acid solutions were prepared in doubly deionized water and were not deaerated before use.

B.7. Beam-Induced Etching of Gold Nanoparticles

This supplementary video features examples of beam-mediated etching of gold nanorods as a function of dose rate. The nanorods are suspended in water (pH \sim 7) with trace amounts of the surfactant cetrimonium bromide (CTAB) and chloroauric acid. The dose rate is controlled by changing the spot size, which controls beam current, and magnification. The imaging was carried with a FEI Quanta 600 in STEM mode (30kV) at beam currents ranging from 0.05 to 1.2 *nA*, beam radius ranging from 0.5 to 1.5 *nm*, and raster area of \sim 1 μm^2 .

B.8. Nucleation Growth and Migration of Nanobubbles

Nanobubble formation experiments were observed in an aqueous solution of gold nanorods with a measured pH \sim 7 and trace amounts of the surfactant cetrimonium bromide (CTAB). Imaging was performed with a Hitachi H9000 TEM (300kV) at beam current $<$ 1 *nA* and beam radius \sim 1 μm .

B.9. Large Bubble Formation in H₂O₂

Example video of the large bubble formation in the nanoaquarium as imaged in the FEI Quanta ESEM in STEM mode. The device is filled with 3% wt H₂O₂ which, upon irradiation, forms a large radiolytic bubble.

B.10. Transition to Diffusion Limited Growth (400 nA)

Copper electrodeposition in our custom made liquid cell, the nanoaquarium, operating in a three terminal configuration with Pt electrodes controlled by a Gamry potentiostat. The total applied current of 400nA was fixed for the duration of the experiment. The interface morphology evolution was imaged at video rate (30 frames per second) in a Hitachi H9000 TEM at 300kV. Bright field imaging conditions were used. Aqueous solutions of 0.1 M copper sulfate with 0.18 M sulfuric acid solutions were prepared in doubly deionized water and were not deaerated before use. The interfacial growth habit transitioned from a roughening regime to a diffusion limited regime.

B.11. Low Current Density Deposition (75 nA)

Copper electrodeposition in our custom made liquid cell, the nanoaquarium, operating in a three terminal configuration with Pt electrodes controlled by a Gamry potentiostat. Total applied current of 75 nA was applied on for 10 s and off for 10 s over a total of 35 cycles. The interface morphology evolution was imaged at video rate (30 frames per second) in a Hitachi H-9000 TEM at 300kV. Bright field imaging conditions were used. Aqueous solutions of 0.1 M copper sulfate with 0.18 M sulfuric acid solutions were prepared in doubly deionized water and were not deaerated before use.

B.12. Pulse Plating (400 *nA* for 1 *s*, 0 *nA* for 5 *s*)

Copper electrodeposition, operating in a three terminal configuration with Pt electrodes controlled by a Gamry potentiostat. Total current was pulsed at 400 *nA* for 1 *s* followed by a 5 *s* off time. The interface morphology evolution was simultaneously imaged at video rate (30 frames per second) in a Hitachi H9000 TEM at 300kV. Bright field imaging conditions were used. Aqueous solutions of 0.1 *M* copper sulfate with 0.18 *M* sulfuric acid solutions were prepared in doubly deionized water and were not deaerated before use. This growth shows no large asperities as the diffusion fields have sufficient time to relax between pulses as to never enter a diffusion limited regime.

B.13. Lead Additive (300 *nA*)

Copper saturated with lead electrodeposition operating in a three terminal configuration with Pt electrodes controlled by a Gamry potentiostat. Total current was applied at 300 *nA* for 10 *s* followed by a 10 *s* off time. The interface morphology evolution was simultaneously imaged at video rate (30 frames per second) in a Hitachi H-9000 TEM at 300kV. Bright field imaging conditions were used. Aqueous solutions of 0.1 *M* copper sulfate with 0.18 *M* sulfuric acid solutions were prepared in doubly deionized water and were saturated with PbSO₄. The solution was not deaerated before use. This growth shows no growth in roughness as the lead acts to help smooth the surface.

APPENDIX - Calibrations

C.1. Hitachi H9000 Magnification and Pixel Size

An essential metric in interpreting micrographs is the relationship between a pixel and its corresponding physical length. Here we include the calibration between magnitude and pixel size in the Hitachi H9000 at IBM. When working with any of the results presented here from this microscope, all that is needed is the magnification to know the physical dimensions. The magnification is recorded on the micrograph as an overlay, and so should be embedded in the raw data file. The measurements reported here were performed by Dr Jeung Hun Park. **Figure 82** shows the pixel size in nm as a function of the magnification in 1000's. Points represent measurements and solid line is a best fit giving $PixelSize = 15.17Mag^{-1}$, where Mag is the magnification is 1000's.

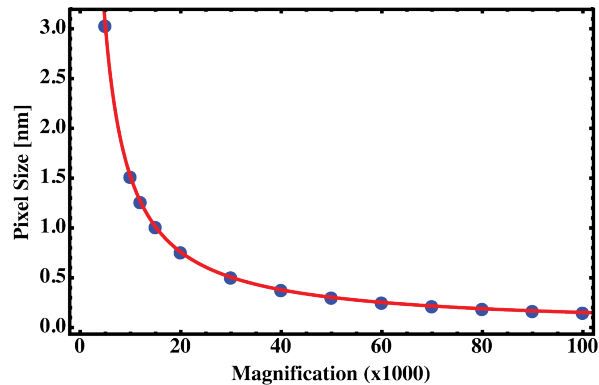


Figure 82: Pixel size (nm) as a function of Magnification (1000's) in IBM's Hitachi H9000. Points represent measurements and solid line is a best fit giving $PixelSize = 15.17Mag^{-1}$, where Mag is the magnification is 1000's.

C.2. Quanta Magnification and Pixel Size

We again need the relationship between a pixel and its corresponding physical length to interpreting micrographs from the FEI Quant ESEM at Penn. Here we include the calibration between magnitude and pixel size. When working with any of the results presented here from the Quanta, all that is needed is the magnification to know the physical dimensions. The magnification is recorded on the micrograph data bar, and so should be embedded in the raw video file. **Figure 83** shows the pixel size in nm as a function of the magnification in 1000's. Points represent measurements and solid line is a best fit giving $PixelSize = 250.0Mag^{-1}$, where Mag is the magnification is 1000's.

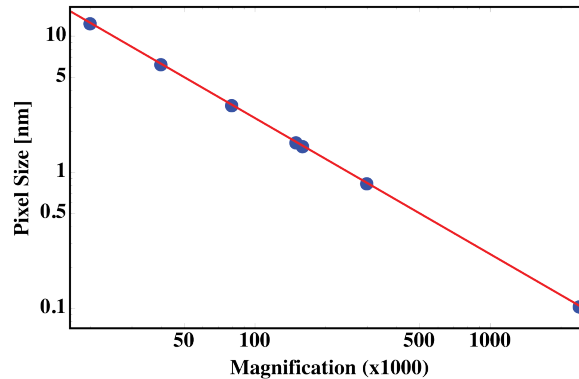


Figure 83: Pixel size (nm) as a function of Magnification (1000's) in Penn's FEI Quanta ESEM using STEM Detector. Points represent measurements and solid line is a best fit giving $PixelSize = 250.0Mag^{-1}$, where Mag is the magnification is 1000's.

C.3. Quanta Beam Current

The beam current on the Quanta is not explicitly controlled, instead it is a function of the microscope parameters. In practical use, the beam current will be governed by the Spot Size, which is the user control over the aperture used in the column. The software prescribes arbitrary numbers to the spot size from 1 to 7, where 7 allows

most of the beam to pass to the sample resulting in lower image quality due to the incident electrons being less collimated. The consequence is more electrons hitting the sample. Conversely, a small spot size will have a low beam current filled with mostly parallel electron paths. In order to know the dose rate, we must calibrate the beam current (independent of imaging conditions) as a function of this microscope parameter. We use a Faraday Cup to collect the entire beam and measure the current output. **Figure 84** shows the the beam current as a function of spot size. Points represent measurements and solid line is a best fit giving $Current = 2.323 \times 10^{-3} Spot^{-1}$ (nA), where $Spot$ is the software defined spot size.

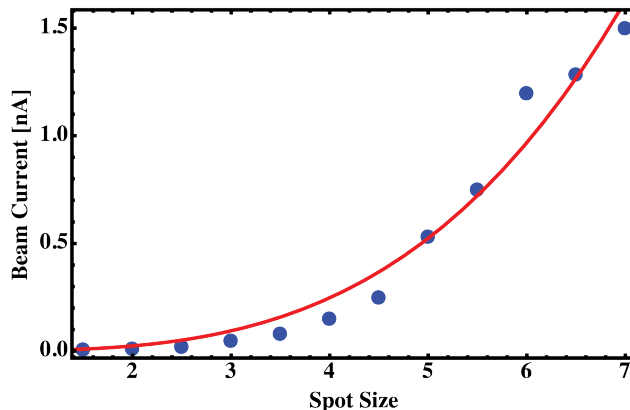


Figure 84: Beam current (nA) as a function of Spot Size in FEI Quanta ESEM using STEM Detector. Points represent measurements and solid line is a best fit giving $Current = 2.323 \times 10^{-3} Spot^{-1}$, where $Spot$ is software defined spot size.

REFERENCES

- [1] P. de Gennes, “Wetting: statics and dynamics,” *Reviews of Modern Physics*, vol. 57, no. 3, pp. 827–863, Jul. 1985.
- [2] N. de Jonge and F. M. Ross, “Electron microscopy of specimens in liquid,” *Nature Nanotechnology*, vol. 6, no. 11, pp. 695–704, Oct. 2011.
- [3] J. M. Grogan, N. M. Schneider, F. M. Ross, and H. H. Bau, “The Nanoaquarium: A New Paradigm in Electron Microscopy,” *Journal of the Indian Institute of Science*, vol. 92, no. 2, pp. 295–308, Dec. 2012.
- [4] A. O. Allen, *The Radiation Chemistry of Water and Aqueous Solutions*, 1961.
- [5] B. Pastina and J. A. LaVerne, “Effect of molecular hydrogen on hydrogen peroxide in water radiolysis,” *The Journal of Physical Chemistry A*, vol. 105, no. 40, pp. 9316–9322, 2001.
- [6] J. M. Joseph, B. S. Choi, P. Yakabuskie, and J. C. Wren, “A combined experimental and model analysis on the effect of pH and O₂(aq) on γ -radiolytically produced H₂ and H₂O₂,” *Radiation Physics and Chemistry*, vol. 77, no. 9, pp. 1009–1020, Sep. 2008.
- [7] N. M. Schneider, M. M. Norton, B. J. Mendel, J. M. Grogan, F. M. Ross, and H. H. Bau, “Electron–Water Interactions and Implications for Liquid Cell Electron Microscopy,” *The Journal of Physical Chemistry C*, vol. 118, no. 38, pp. 22 373–22 382, Sep. 2014.
- [8] J. M. Grogan, N. M. Schneider, F. M. Ross, and H. H. Bau, “Bubble and Pattern Formation in Liquid Induced by an Electron Beam,” *Nano letters*, vol. 14, no. 1, pp. 359–364, Jan. 2014.
- [9] H. Zheng, R. K. Smith, Y. w. Jun, C. Kisielowski, U. Dahmen, and A. P. Alivisatos, “Observation of Single Colloidal Platinum Nanocrystal Growth Trajectories,” *Science*, vol. 324, no. 5932, pp. 1309–1312, Jun. 2009.
- [10] J. M. Yuk, J. Park, P. Ercius, K. Kim, D. J. Hellebusch, M. F. Crommie, J. Y. Lee, A. Zettl, and A. P. Alivisatos, “High-Resolution EM of Colloidal Nanocrystal Growth Using Graphene Liquid Cells,” *Science*, vol. 336, no. 6077, pp. 61–64, Apr. 2012.
- [11] J. E. Evans, K. L. Jungjohann, N. D. Browning, and I. Arslan, “Controlled Growth of Nanoparticles from Solution with In Situ Liquid Transmission Electron Microscopy,” *Nano letters*, vol. 11, no. 7, pp. 2809–2813, Jul. 2011.

- [12] D. Li, M. H. Nielsen, J. R. I. Lee, C. Frandsen, J. F. Banfield, and J. J. De Yoreo, "Direction-Specific Interactions Control Crystal Growth by Oriented Attachment," *Science*, vol. 336, no. 6084, pp. 1014–1018, May 2012.
- [13] J. M. Grogan and H. H. Bau, "The Nanoaquarium: A Platform for In Situ Transmission Electron Microscopy in Liquid Media," *Microelectromechanical Systems, Journal of*, vol. 19, no. 4, pp. 885–894, 2010.
- [14] J. M. Grogan, "The nanoaquarium: A nanofluidic platform for in situ transmission electron microscopy in liquid media," 2011.
- [15] D. Maier-Schneider, J. Maibach, and E. Obermeier, "A new analytical solution for the load-deflection of square membranes," *Journal of Microelectromechanical Systems*, vol. 4, no. 4, pp. 238–241, 1995.
- [16] S. Sinha, M. P. Rossi, D. Mattia, Y. Gogotsi, and H. H. Bau, "Induction and measurement of minute flow rates through nanopipes," *Physics of Fluids (1994-present)*, vol. 19, no. 1, p. 013603, Jan. 2007.
- [17] Y. Zheng, S. Lin, C. Kambhamettu, J. Yu, and S. B. Kang, "Single-Image Vignetting Correction," *Pattern Analysis and Machine Intelligence, IEEE Transactions on*, vol. 31, no. 12, pp. 2243–2256.
- [18] E. Hecht, "Optics," Jul. 2013.
- [19] Welcome to virtualdub.org! - virtualdub.org. [Online]. Available: <http://www.virtualdub.org/index.html>
- [20] W. S. RASBAND, "ImageJ," *rsbweb.nih.gov*, 2008.
- [21] E. R. White, S. B. Singer, V. Augustyn, W. A. Hubbard, M. Mecklenburg, B. Dunn, and B. C. Regan, "In Situ Transmission Electron Microscopy of Lead Dendrites and Lead Ions in Aqueous Solution," *ACS nano*, vol. 6, no. 7, pp. 6308–6317, Jul. 2012.
- [22] T. Kraus and N. de Jonge, "Dendritic Gold Nanowire Growth Observed in Liquid with Transmission Electron Microscopy," *Langmuir*, vol. 29, no. 26, pp. 8427–8432, Jul. 2013.
- [23] M. Sun, H.-G. Liao, K. Niu, and H. Zheng, "Structural and Morphological Evolution of Lead Dendrites during Electrochemical Migration," *Scientific Reports*, vol. 3, pp. –, Nov. 2013.
- [24] A. R. Tao, S. Habas, and P. Yang, "Shape Control of Colloidal Metal Nanocrystals," *Small*, vol. 4, no. 3, pp. 310–325, Mar. 2008.

- [25] R. Jin, Y. Cao, C. A. Mirkin, K. L. Kelly, G. C. Schatz, and J. G. Zheng, “Photoinduced Conversion of Silver Nanospheres to Nanoprisms,” *Science*, vol. 294, no. 5548, pp. 1901–1903, Nov. 2001.
- [26] M. J. Williamson, R. M. Tromp, P. M. Vereecken, R. Hull, and F. M. Ross, “Dynamic microscopy of nanoscale cluster growth at the solid–liquid interface,” *Nature Materials*, vol. 2, no. 8, pp. 532–536, Jul. 2003.
- [27] A. Radisic, P. M. Vereecken, J. B. Hannon, P. C. Searson, and F. M. Ross, “Quantifying Electrochemical Nucleation and Growth of Nanoscale Clusters Using Real-Time Kinetic Data,” *Nano letters*, vol. 6, no. 2, pp. 238–242, Feb. 2006.
- [28] M. den Heijer, I. Shao, A. Radisic, M. C. Reuter, and F. M. Ross, “Patterned electrochemical deposition of copper using an electron beam,” *APL Materials*, vol. 2, no. 2, p. 022101, Feb. 2014.
- [29] M. Norton, J. Park, S. Kodambaka, F. Ross, and H. Bau, “Dynamics of Sub-Micron Bubbles Growing in a Wedge in the Low Capillary Number Regime,” *Bulletin of the American Physical Society*, vol. Volume 59, Number 20, Nov. 2014.
- [30] J. H. Park, J. M. Grogan, H. H. Bau, S. K. Kodambaka, and F. M. Ross, “Mechanism of Electron-Beam Induced Au Formation in Aqueous Solution,” *Microscopy and Microanalysis*, vol. 19, no. S2, pp. 486–487, Aug. 2013.
- [31] N. M. Schneider, J. H. Park, and J. M. Grogan, “Visualization of Active and Passive Control of Morphology during Electrodeposition,” *Microsc . . .*, 2014.
- [32] N. M. Schneider. NMSchneider/Quantitative-Image-Analysis. [Online]. Available: <https://github.com/NMSchneider/Quantitative-Image-Analysis>
- [33] A. Rose, “Television Pickup Tubes and the Problem of Vision,” in *Advances in Electronics and Electron Physics Volume 1*. Elsevier, 1948, pp. 131–166.
- [34] N. d. Jonge, D. B. Peckys, G. J. Kremers, and D. W. Piston, “Electron microscopy of whole cells in liquid with nanometer resolution,” *Proceedings of the National Academy of Sciences*, vol. 106, no. 7, pp. 2159–2164, Feb. 2009.
- [35] L. I. Rudin, S. Osher, and E. Fatemi, “Nonlinear total variation based noise removal algorithms,” *Physica D: Nonlinear Phenomena*, vol. 60, no. 1-4, pp. 259–268, Nov. 1992.

- [36] T. F. Chan, S. Osher, and J. Shen, “The digital TV filter and nonlinear denoising,” *Image Processing, IEEE Transactions on*, vol. 10, no. 2, pp. 231–241, Feb. 2001.
- [37] M. Piccardi, “Background subtraction techniques: a review,” in *2004 IEEE International Conference on Systems, Man and Cybernetics*. IEEE, pp. 3099–3104.
- [38] N. Otsu, “A Threshold Selection Method from Gray-Level Histograms,” *Systems, Man and Cybernetics, IEEE Transactions on*, vol. 9, no. 1, pp. 62–66, 1979.
- [39] J. Canny, “A Computational Approach to Edge Detection,” *Pattern Analysis and Machine Intelligence, IEEE Transactions on*, no. 6, pp. 679–698, 1986.
- [40] J. Crocker, “Methods of Digital Video Microscopy for Colloidal Studies,” *Journal of colloid and interface science*, vol. 179, no. 1, pp. 298–310, Apr. 1996.
- [41] D. P. Barkey, “Structure and pattern formation in electrodeposition,” *Advances in Electrochemical Science and Engineering*, vol. 7, pp. 151–192, 2002.
- [42] W. Schwarzacher, “Kinetic roughening of electrodeposited films,” *Journal of Physics: Condensed Matter*, vol. 16, no. 26, pp. R859–R880, Jun. 2004.
- [43] M. Haataja and D. Srolovitz, “Morphological Instability and Additive-Induced Stabilization in Electrodeposition,” *Physical review letters*, vol. 89, no. 21, p. 215509, Nov. 2002.
- [44] D. P. Barkey, R. H. Muller, and C. W. Tobias, “Roughness Development in Metal Electrodeposition II . Stability Theory,” *Journal of the Electrochemical Society*, vol. 136, no. 8, pp. 2207–2214, Aug. 1989.
- [45] P. Grinfeld, *Introduction to Tensor Analysis and the Calculus of Moving Surfaces*. New York, NY: Springer New York, 2013.
- [46] R. Kolluri, “Provably good moving least squares,” *ACM Transactions on Algorithms (TALG)*, vol. 4, no. 2, pp. 18–25, May 2008.
- [47] G. Toussaint, “Solving Geometric Problems with the Rotating Calipers,” 1983.
- [48] J. W. G. Tyrrell and P. Attard, “Atomic Force Microscope Images of Nanobubbles on a Hydrophobic Surface and Corresponding Force–Separation Data,” vol. 18, no. 1, pp. 160–167, Jan. 2002.

- [49] —, “Images of Nanobubbles on Hydrophobic Surfaces and Their Interactions,” *Physical review letters*, vol. 87, no. 17, p. 176104, Oct. 2001.
- [50] P. Attard, M. P. Moody, and J. W. G. Tyrrell, “Nanobubbles: the big picture,” *Physica A: Statistical Mechanics and its Applications*, vol. 314, no. 1-4, pp. 696–705, Nov. 2002.
- [51] P. Attard, “Nanobubbles and the hydrophobic attraction,” *Advances in Colloid and Interface Science*, vol. 104, no. 1-3, pp. 75–91, Jul. 2003.
- [52] J. L. Parker, P. M. Claesson, and P. Attard, “Bubbles, cavities, and the long-ranged attraction between hydrophobic surfaces.” *The Journal of Physical Chemistry*, vol. 98, no. 34, pp. 8468–8480, Aug. 1994.
- [53] S.-T. Lou, Z.-Q. Ouyang, Y. Zhang, X.-J. Li, J. Hu, M.-Q. Li, and F.-J. Yang, “Nanobubbles on solid surface imaged by atomic force microscopy,” *Journal of Vacuum Science & Technology B*, vol. 18, no. 5, pp. 2573–2575, Sep. 2000.
- [54] G. Liu, Z. Wu, and V. S. J. Craig, “Cleaning of Protein-Coated Surfaces Using Nanobubbles: An Investigation Using a Quartz Crystal Microbalance,” *The Journal of Physical Chemistry C*, vol. 112, no. 43, pp. 16 748–16 753, Oct. 2008.
- [55] G. Liu and V. S. J. Craig, “Improved Cleaning of Hydrophilic Protein-Coated Surfaces using the Combination of Nanobubbles and SDS,” *ACS Applied Materials & Interfaces*, vol. 1, no. 2, pp. 481–487, Jan. 2009.
- [56] R. Cavicchi and C. Avedisian, “Bubble Nucleation and Growth Anomaly for a Hydrophilic Microheater Attributed to Metastable Nanobubbles,” *Physical review letters*, vol. 98, no. 12, p. 124501, Mar. 2007.
- [57] N. J. Carron, *An Introduction to the Passage of Energetic Particles through Matter*. CRC Press, Nov. 2006.
- [58] H. A. Bethe and J. Ashkin, “Bethe: Passage of radiations through matter - Google Scholar,” *Experimental nuclear physics*, 1953.
- [59] M. J. Berger, J. S. Coursey, M. A. Zucker, and J. Chang. NIST Stopping-Power and Range Tables: Electrons, Protons, Helium Ions . [Online]. Available: <http://physics.nist.gov/PhysRefData/Star/Text/ESTAR.html>
- [60] J. A. LaVerne and S. M. Pimblott, “Electron energy-loss distributions in solid, dry DNA,” *Radiation research*, vol. 141, no. 2, pp. 208–215, 1995.
- [61] T. Tabata, “A Simple Calculation for Mean Projected Range of Fast Electrons,” *Journal of Applied Physics*, vol. 39, no. 11, pp. 5342–5343, 1968.

- [62] M. E. Rose, "Electron Path Lengths in Multiple Scattering," *Physical Review*, vol. 58, no. 1, p. 90, 1940.
- [63] D. Drouin, A. R. Couture, D. Joly, X. Tastet, V. Aimez, and R. Gauvin, "CASINO V2.42—A Fast and Easy-to-use Modeling Tool for Scanning Electron Microscopy and Microanalysis Users," *Scanning*, vol. 29, no. 3, pp. 92–101, May 2007.
- [64] D. C. JOY, "An Introduction to Monte-Carlo Simulations," *Scanning Microscopy*, vol. 5, no. 2, pp. 329–337, Jun. 1991.
- [65] Casino. [Online]. Available: <http://www.gel.usherbrooke.ca/casino/What.html>
- [66] P. Hovington, D. Drouin, and R. Gauvin, "CASINO: A new monte carlo code in C language for electron beam interaction —part I: Description of the program," *Scanning*, vol. 19, no. 1, pp. 1–14, Jan. 1997.
- [67] D. Drouin, P. Hovington, and R. Gauvin, "CASINO: A new monte carlo code in C language for electron beam interactions—part II: Tabulated values of the mott cross section," *Scanning*, vol. 19, no. 1, pp. 20–28, Jan. 1997.
- [68] P. Hovington, D. Drouin, R. Gauvin, D. C. Joy, and N. Evans, "CASINO: A new monte Carlo code in C language for electron beam interactions—part III: Stopping power at low energies," *Scanning*, vol. 19, no. 1, pp. 29–35, Jan. 1997.
- [69] H. Zheng, S. A. Claridge, A. M. Minor, A. P. Alivisatos, and U. Dahmen, "Nanocrystal Diffusion in a Liquid Thin Film Observed by in Situ Transmission Electron Microscopy," *Nano letters*, vol. 9, no. 6, pp. 2460–2465, Jun. 2009.
- [70] R. F. Egerton, P. Li, and M. Malac, "Radiation damage in the TEM and SEM," *Micron*, vol. 35, no. 6, pp. 399–409, Aug. 2004.
- [71] A. J. Elliot and D. R. McCracken, "Computer modelling of the radiolysis in an aqueous lithium salt blanket: Suppression of radiolysis by addition of hydrogen," *Fusion Engineering and Design*, vol. 13, no. 1, pp. 21–27, Aug. 1990.
- [72] A. O. Allen, "The radiation chemistry of water and aqueous solutions," 1961.
- [73] J. W. T. Spinks and R. J. Woods, *An introduction to radiation chemistry*. Wiley-Interscience, 1990.
- [74] I. Draganic, *The Radiation Chemistry of Water*. Elsevier, Dec. 2012.

- [75] H. A. Schwarz, "Applications of the spur diffusion model to the radiation chemistry of aqueous solutions," *The Journal of Physical Chemistry*, vol. 73, no. 6, pp. 1928–1937, Jun. 1969.
- [76] G. V. BUXTON, C. L. GREENSTOCK, W. P. HELMAN, and ROSS, AB, "Critical-Review of Rate Constants for Reactions of Hydrated Electrons, Hydrogen-Atoms and Hydroxyl Radicals (.Oh/.O-) in Aqueous-Solution," *Journal of Physical and Chemical Reference Data*, vol. 17, no. 2, pp. 513–886, 1988.
- [77] M. A. Hill and F. A. Smith, "Calculation of initial and primary yields in the radiolysis of water," *Radiation Physics and Chemistry*, vol. 43, no. 3, pp. 265–280, Mar. 1994.
- [78] H. Christensen, "Remodeling of the oxidant species during radiolysis of high-temperature water in a pressurized water reactor," *Nuclear Technology*, vol. 109, no. 3, Mar. 1995.
- [79] M. Burton, "Radiation Chemistry." *The Journal of Physical Chemistry*, vol. 51, no. 2, pp. 611–625, Feb. 1947.
- [80] S. M. Pimblott and J. A. LaVerne, "Molecular Product Formation in the Electron Radiolysis of Water," *Radiation research*, vol. 129, no. 3, p. 265, Mar. 1992.
- [81] J. Speight, *Lange's Handbook of Chemistry*. McGraw-Hill Professional, Dec. 2004.
- [82] W. G. Mallard, ROSS, AB, and W. P. HELMAN. NDRL/NIST Solution Kinetics Database on the Web: A compilation of kinetics data on solution-phase reactions. [Online]. Available: <http://kinetics.nist.gov/solution/>
- [83] "NMSchneider/Radiolysis."
- [84] Q. Chen, J. M. Smith, J. Park, K. Kim, D. Ho, H. I. Rasool, A. Zettl, and A. P. Alivisatos, "3D Motion of DNA-Au Nanoconjugates in Graphene Liquid Cell Electron Microscopy," *Nano letters*, vol. 13, no. 9, pp. 4556–4561, Sep. 2013.
- [85] H.-G. Liao, K. Niu, and H. Zheng, "Observation of growth of metal nanoparticles," *Chemical Communications*, vol. 49, no. 100, pp. 11 720–11 727, 2013.
- [86] E. J. Hart, "The Hydrated Electron: Properties and reactions of this most reactive and elementary of aqueous negative ions are discussed," *Science*, vol. 146, no. 3640, pp. 19–25, Oct. 1964.

- [87] J. M. Grogan, L. Rotkina, and H. H. Bau, “In situ liquid-cell electron microscopy of colloid aggregation and growth dynamics,” *Physical Review E*, vol. 83, no. 6, p. 061405, Jun. 2011.
- [88] U. Mirsaidov, C.-D. Ohl, and P. Matsudaira, “A direct observation of nanometer-size void dynamics in an ultra-thin water film,” *Soft Matter*, vol. 8, no. 27, pp. 7108–7111, 2012.
- [89] T.-W. Huang, S.-Y. Liu, Y.-J. Chuang, H.-Y. Hsieh, C.-Y. Tsai, W.-J. Wu, C.-T. Tsai, U. Mirsaidov, P. Matsudaira, C.-S. Chang, F.-G. Tseng, and F.-R. Chen, “Dynamics of hydrogen nanobubbles in KLH protein solution studied with in situ wet-TEM,” *Soft Matter*, vol. 9, no. 37, pp. 8856–8861, 2013.
- [90] K. L. Klein, I. M. Anderson, and N. de Jonge, “Transmission electron microscopy with a liquid flow cell,” *Journal of Microscopy*, vol. 242, no. 2, pp. 117–123, Jan. 2011.
- [91] S. Jones, “Bubble nucleation from gas cavities — a review,” *Advances in Colloid and Interface Science*, vol. 80, no. 1, pp. 27–50, Feb. 1999.
- [92] T. J. Woehl, J. E. Evans, I. Arslan, W. D. Ristenpart, and N. D. Browning, “Direct in Situ Determination of the Mechanisms Controlling Nanoparticle Nucleation and Growth,” *ACS nano*, vol. 6, no. 10, pp. 8599–8610, Oct. 2012.
- [93] K. W. Noh, Y. Liu, L. Sun, and S. J. Dillon, “Challenges associated with in-situ TEM in environmental systems: The case of silver in aqueous solutions,” *Ultramicroscopy*, vol. 116, no. 0, pp. 34–38.
- [94] J. Lee, A. Urban, X. Li, D. Su, G. Hautier, and G. Ceder, “Unlocking the Potential of Cation-Disordered Oxides for Rechargeable Lithium Batteries,” *Science*, vol. 343, no. 6170, pp. 519–522, Jan. 2014.
- [95] M. Bresin, B. R. Nadimpally, N. Nehru, V. P. Singh, and J. T. Hastings, “Site-specific growth of CdS nanostructures,” *Nanotechnology*, vol. 24, no. 50, p. 505305, Nov. 2013.
- [96] J. Park, S. Kodambaka, F. M. Ross, J. M. Grogan, and H. H. Bau, “In Situ Liquid Cell Transmission Electron Microscopic Observation of Electron Beam Induced Au Crystal Growth in a Solution,” *Microscopy and Microanalysis*, vol. 18, no. S2, pp. 1098–1099, Nov. 2012.
- [97] H. Remita, I. Lampre, M. Mostafavi, E. Balanzat, and S. Bouffard, “Comparative study of metal clusters induced in aqueous solutions by γ -rays, electron

- or C6+ ion beam irradiation,” *Radiation Physics and Chemistry*, vol. 72, no. 5, pp. 575–586, Apr. 2005.
- [98] W. Abidi and H. Remita, “Gold based Nanoparticles Generated by Radiolytic and Photolytic Methods,” *Recent Patents on Engineering*, vol. 4, no. 3, pp. 170–188, Nov. 2010.
- [99] W. W. Mullins and R. F. Sekerka, “Stability of a Planar Interface During Solidification of a Dilute Binary Alloy,” *Journal of Applied Physics*, vol. 35, no. 2, pp. 444–451, 1964.
- [100] H. Fujita, M. Izawa, and H. Yamazaki, “ γ -Ray-Induced Formation of Gold Sol from Chloroauric Acid Solution,” *Nature*, vol. 196, 1962.
- [101] E. Gachard, H. Remita, J. Khatouri, B. Keita, L. Nadjo, Belloni, and Jacqueline, “Radiation-induced and chemical formation of gold clusters,” *New Journal of Chemistry*, vol. 22, no. 11, pp. 1257–1265, 1998.
- [102] G. R. Dey, A. K. El Omar, J. A. Jacob, M. Mostafavi, and J. Belloni, “Mechanism of Trivalent Gold Reduction and Reactivity of Transient Divalent and Monovalent Gold Ions Studied by Gamma and Pulse Radiolysis,” *The Journal of Physical Chemistry A*, vol. 115, no. 4, pp. 383–391, Feb. 2011.
- [103] E. Atinault, V. De Waele, U. Schmidhammer, M. Fattahi, and M. Mostafavi, “Scavenging of and OH radicals in concentrated HCl and NaCl aqueous solutions,” *Chemical Physics Letters*, vol. 460, no. 4-6, pp. 461–465, Jul. 2008.
- [104] A. Mozumder, *Fundamentals of Radiation Chemistry*. Elsevier Science, 1999.
- [105] B. J. Mincher and J. F. Wishart, “The Radiation Chemistry of Ionic Liquids: A Review,” *Solvent Extraction and Ion Exchange*, vol. 32, no. 6, pp. 563–583, Jul. 2014.
- [106] J. Y. Huang, L. Zhong, C. M. Wang, J. P. Sullivan, W. Xu, L. Q. Zhang, S. X. Mao, N. S. Hudak, X. H. Liu, A. Subramanian, H. Fan, L. Qi, A. Kushima, and J. Li, “In Situ Observation of the Electrochemical Lithiation of a Single SnO₂ Nanowire Electrode,” *sciencemag.org*.
- [107] L. Bousse and S. Mostarshed, “The zeta potential of silicon nitride thin films,” *Journal of Electroanalytical Chemistry and Interfacial Electrochemistry*, vol. 302, no. 1-2, pp. 269–274, Mar. 1991.

- [108] J.-H. Han, E. Khoo, P. Bai, and M. Z. Bazant, “Over-limiting Current and Control of Dendritic Growth by Surface Conduction in Nanopores,” *Scientific Reports*, vol. 4, p. 7056, Nov. 2014.
- [109] A. J. Bard and L. R. Faulkner, *Electrochemical Methods*, ser. Fundamentals and Applications. Wiley, Dec. 2000.
- [110] D. P. Barkey, R. H. Muller, and C. W. Tobias, “Roughness Development in Metal Electrodeposition I. Experimental Results,” *Journal of the Electrochemical Society*, vol. 136, no. 8, pp. 2199–2207, Aug. 1989.
- [111] R. Aogaki, K. Kitazawa, Y. Kose, and K. Fueki, “Theory of powdered crystal formation in electrocrystallization—occurrence of morphological instability at the electrode surface,” *Electrochimica Acta*, vol. 25, no. 7, pp. 965–972, Jul. 1980.
- [112] R. R. Unocic, R. L. Sacci, G. M. Brown, G. M. Veith, N. J. Dudney, K. L. More, F. S. Walden, D. S. Gardiner, J. Damiano, and D. P. Nackashi, “Quantitative Electrochemical Measurements Using In Situ ec-S/TEM Devices,” *Microscopy and Microanalysis*, vol. 20, no. 02, pp. 452–461, Mar. 2014.
- [113] Z. Zeng, W.-I. Liang, H.-G. Liao, H. Xin, Y.-H. Chu, and H. Zheng, “Visualization of Electrode-Electrolyte Interfaces in LiPF₆/EC/DEC Electrolyte for Lithium Ion Batteries via In-Situ TEM,” *Nano letters*, p. 140120111747008, Jan. 2014.
- [114] N. M. Schneider, J. H. Park, J. M. Grogan, S. Kodambaka, D. A. Steingart, F. M. Ross, and H. H. Bau, “In Situ Electrochemical Measurements in the Nanoaquarium,” *Microscopy and Microanalysis*, vol. 19, no. S2, pp. 422–423.
- [115] A. L. Barabasi, H. E. Stanley, and L. M. Sander, “Fractal Concepts in Surface Growth,” *Physics Today*, vol. 48, no. 10, p. 68, 1995.
- [116] F. Family, “Dynamic scaling and phase transitions in interface growth,” *Physica A: Statistical Mechanics and its Applications*, vol. 168, no. 1, pp. 561–580, Sep. 1990.
- [117] F. Family and T. Vicsek, “Scaling of the active zone in the Eden process on percolation networks and the ballistic deposition model,” *Journal of Physics A: Mathematical and General*, vol. 18, no. 2, pp. L75–L81, Jan. 1999.
- [118] P. Fedkiw, “Primary Current Distribution on a Sinusoidal Profile,” *Journal of the Electrochemical Society*, vol. 127, no. 6, p. 1304, 1980.

- [119] H. J. Sand, “III. On the concentration at the electrodes in a solution, with special reference to the liberation of hydrogen by electrolysis of a mixture of copper sulphate and sulphuric acid,” *The London, Edinburgh, and Dublin Philosophical Magazine and Journal of Science*, vol. 1, no. 1, pp. 45–79, 1901.
- [120] M. S. Chandrasekar and M. Pushpavanam, “Pulse and pulse reverse plating—Conceptual, advantages and applications,” *Electrochimica Acta*, vol. 53, no. 8, pp. 3313–3322, 2008.
- [121] A. C. West, *Electrochemistry and Electrochemical Engineering: An Introduction*. CreateSpace Independent Publishing Platform, 2012.
- [122] P. Herget, N. Wang, E. J. O’Sullivan, B. C. Webb, L. T. Romankiw, R. Fontana, G. Decad, and Gallagher, “Limits to On-Chip Power Conversion With Thin Film Inductors,” *IEEE Transactions on Magnetics*, vol. 49, no. 7, pp. 4137–4143, Jul. 2013.
- [123] N. Wang, E. J. O’Sullivan, P. Herget, B. Rajendran, L. E. Krupp, L. T. Romankiw, B. C. Webb, R. Fontana, E. A. Duch, E. A. Joseph, S. L. Brown, X. Hu, G. M. Decad, N. Sturcken, K. L. Shepard, and W. J. Gallagher, “Integrated on-chip inductors with electroplated magnetic yokes (invited),” *Journal of Applied Physics*, vol. 111, no. 7, p. 07E732, Apr. 2012.
- [124] P. Allongue, F. Maroun, H. F. Jurca, N. Tournerie, G. Savidand, and R. Cortès, “Magnetism of electrodeposited ultrathin layers: Challenges and opportunities,” *Surface science*, vol. 603, no. 10-12, pp. 1831–1840, Jun. 2009.
- [125] G. Loget, D. Zigah, L. Bouffier, N. Sojic, and A. Kuhn, “Bipolar Electrochemistry: From Materials Science to Motion and Beyond,” *Accounts of Chemical Research*, vol. 46, no. 11, pp. 2513–2523, Nov. 2013.